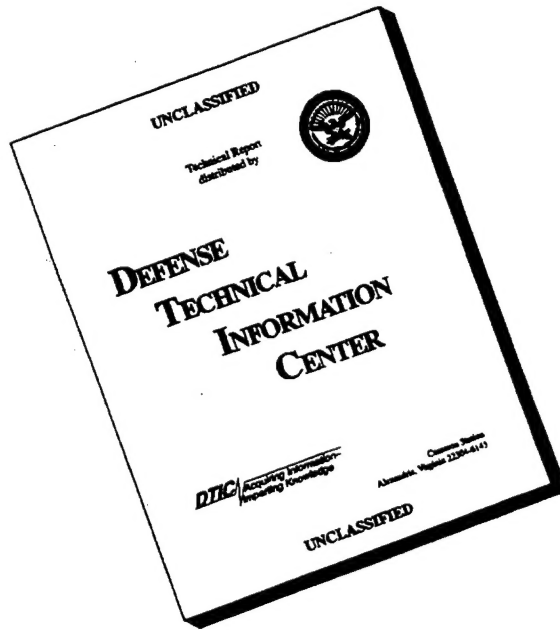


REPORT DOCUMENTATION PAGE			Form Approved OMB NO. 0704-0188
<p>Public reporting burden for this collection of information is estimated to average 1 hour per response, including the time for reviewing instructions, searching existing data sources, gathering and maintaining the data needed, and completing and reviewing the collection of information. Send comment regarding this burden estimate or any other aspect of this collection of information, including suggestions for reducing this burden, to Washington Headquarters Services, Directorate for Information Operations and Reports, 1215 Jefferson Davis Highway, Suite 1204, Arlington, VA 22202-4302, and to the Office of Management and Budget, Paperwork Reduction Project (0704-0188), Washington, DC 20503.</p>			
1. AGENCY USE ONLY (Leave blank)	2. REPORT DATE	3. REPORT TYPE AND DATES COVERED	
	January, 1996	Final 1 Jul 92 - 30 Sep 95	
4. TITLE AND SUBTITLE		5. FUNDING NUMBERS	
Fabrication of Nanostructures in Group IV Semiconductors		DAAL03-92-G-0290	
6. AUTHOR(S)			
Jason Xu and Andrew J. Steckl			
7. PERFORMING ORGANIZATION NAMES(S) AND ADDRESS(ES)		8. PERFORMING ORGANIZATION REPORT NUMBER	
Nanoelectronics Laboratory University of Cincinnati, ECECS 899 Rhodes Hall PO Box 210030 Cincinnati, OH 45221-0030		8. PERFORMING ORGANIZATION REPORT NUMBER	
9. SPONSORING / MONITORING AGENCY NAME(S) AND ADDRESS(ES)		10. SPONSORING / MONITORING AGENCY REPORT NUMBER	
U.S. Army Research Office P.O. Box 12211 Research Triangle Park, NC 27709-2211		ARO 29290.16-EL	
11. SUPPLEMENTARY NOTES			
The views, opinions and/or findings contained in this report are those of the author(s) and should not be construed as an official Department of the Army position, policy or decision, unless so designated by other documentation.			
12a. DISTRIBUTION / AVAILABILITY STATEMENT		12 b. DISTRIBUTION CODE	
Approved for public release; distribution unlimited.		19960523 038	
13. ABSTRACT (Maximum 200 words)			
<p>The objectives of this work combine a study of the fundamental mechanisms of light emission from porous silicon (PoSi) with the development of techniques for fabricating PoSi-based light emitting structures and devices. The incubation time of PoSi formation was found to have a strong dependence on the substrate doping type and concentration. Utilizing the incubation time difference and Ga<sup>+</sup> FIB implantation a process was successfully developed to fabricate selective light emitting Si structures embedded in a conventional Si substrate. Sub-micron resolution was achieved for the first time. It was observed that a minimum level of crystallinity is required for PoSi layers to exhibit visible PL. A unique correlation exists between the level of crystallinity of the starting Si film and the presence of surface oxyhydrides and photoluminescence after stain-etching. Visible LED's using stain-etched PoSi have superior electrical characteristics and achieved the best ideality factor, the highest rectifying ratio and the lowest EL onset current reported to date. The stain-etch process is much simpler than anodization and can be used to form sub-micron luminescent PoSi patterns and to produce luminescing poly-PoSi films on quartz and glass. These results demonstrate a very promising technique for fabrication of PoSi-based LED's.</p>			
14. SUBJECT TERMS		15. NUMBER OF PAGES	
Nanostructures, porous Si, stain-etching, LED		126	
		16. PRICE CODE	
17. SECURITY CLASSIFICATION OR REPORT		18. SECURITY CLASSIFICATION OF THIS PAGE	
UNCLASSIFIED		UNCLASSIFIED	
19. SECURITY CLASSIFICATION OF ABSTRACT		20. LIMITATION OF ABSTRACT	
UNCLASSIFIED		UL	

# DISCLAIMER NOTICE



THIS DOCUMENT IS BEST  
QUALITY AVAILABLE. THE  
COPY FURNISHED TO DTIC  
CONTAINED A SIGNIFICANT  
NUMBER OF PAGES WHICH DO  
NOT REPRODUCE LEGIBLY.

**FABRICATION OF NANOSTRUCTURES IN GROUP IV  
SEMICONDUCTORS**

**FINAL REPORT**

Jason Xu and Andrew J. Steckl, Principal Investigator

December, 1995

U.S. Army Research Office

Contract Number DAAL03-92-G-0290

University of Cincinnati

APPROVED FOR PUBLIC RELEASE  
DISTRIBUTION UNLIMITED

THE VIEWS, OPINIONS, AND/OR FINDINGS CONTAINED IN THIS REPORT ARE THOSE OF THE AUTHOR(S) AND SHOULD NOT BE CONSTRUED AS AN OFFICIAL DEPARTMENT OF THE ARMY POSITION, POLICY, OR DECISION, UNLESS SO DESIGNATED BY OTHER DOCUMENTATION.

## FOREWORD

This document is the final technical report for a contract sponsored by BMDO and monitored by ARO at the University of Cincinnati. The title of the project is "Fabrication of Nanostructures in Group IV Semiconductors" and the project period covered is from July 1, 1992 to September 30, 1995. The principal investigator on the contract was Prof. Andrew J. Steckl from the Department of Electrical and Computer Engineering and Computer Science at the University of Cincinnati. Together with Prof. Steckl, two graduate assistants, Jason Xu and Homi Mogul, were heavily involved in this contract. In the course of the contract both of these students obtained their Ph.D. and they are currently employed in the semiconductor industry in the United States.

The recent observations of the efficient room temperature photoluminescence and the blue shifted optical absorption in porous silicon have generated a flurry of interest in the fundamental mechanisms of light emission from porous silicon and in its potential applications in Si-based integrated optoelectronics. The overall objective of this work combines a study of the fundamental mechanisms of light emission from porous silicon with the development of techniques for fabricating porous Si-based light emitting structures, and ultimately with the fabrication of porous silicon light emitting nanostructures and devices.

Incubation time of porous silicon formation using pure chemical etching (stain-etching) in HF:HNO<sub>3</sub>:H<sub>2</sub>O was studied in detail and a strong dependence of the incubation time on the substrate doping type and concentration was consequently observed. Scanning electron microscopy study of the stain-etched porous silicon revealed the existence of a wide variety of surface morphology which is primarily affected by the substrate doping. No significant doping effect on the photoluminescence itself was observed. Utilizing the incubation time difference and Ga<sup>+</sup> focused ion beam implantation a process was successfully developed to fabricate selective light emitting silicon patterns and nanostructures embedded in a conventional silicon substrate with sub-micron resolution being achieved for the first time.

Luminescent porous polycrystalline silicon films were obtained by stain-etching poly-Si films on both oxidized silicon and quartz substrates deposited by low pressure chemical vapor deposition. Uniform light emission was achieved from patterned poly-Si films on oxidized Si with both sub-micron features and large area which offers potential application in porous-silicon-based flat panel display devices. Porous silicon from stain-etched Si thin films deposited on oxidized Si substrates at temperatures ranging from 540 to 640°C, designed to provide varying levels of crystallinity, was systematically studied by x-ray diffraction, photoluminescence and infrared transmission spectroscopy. It was observed that a minimum level of crystallinity in the as-deposited Si film is required for the subsequent porous silicon layer to exhibit visible photoluminescence, and it appears that there exists a unique correlation between the level of crystallinity of the starting Si film, and the presence of surface oxyhydrides and photoluminescence after stain-etching.

Visible light emitting diodes (LED) using stain-etched porous silicon thin films have been fabricated and characterized. The porous silicon film used in this work of only about 200 nm is the thinnest ever reported for a porous silicon LED. The devices have superior electrical characteristics and achieved the best ideality factor, the highest rectifying ratio and the lowest EL onset current reported to date along with improved EL linearity. Since the stain-etch process is much simpler than anodization and can be used to form sub-micron luminescent porous silicon patterns and to produce luminescing poly-porous silicon films on quartz and glass, these results demonstrate a very promising and advantageous technique for fabrication of porous-silicon-based LED's and poly-porous-silicon-based electroluminescent devices.

As a result of the research carried out in this contract, 14 publications have been written and numerous conference presentations have been given.

## Publications

1. A.J. Steckl, J. Xu, H.C. Mogul and S. Mogren, "Doping-Induced Selective Area Photoluminescence in Porous Silicon," *Applied Physics Letters*, Vol. 62, pp. 1982-1984, April 1993.
2. A.J. Steckl, J. Xu and H.C. Mogul, "Photoluminescence from Stain-Etched Poly-Crystalline Si Thin Films," *Applied Physics Letters*, Vol. 62, pp. 2111-2113, April 1993.
3. A.J. Steckl J. Xu and H.C. Mogul, "Submicron Selective Photoluminescence in Porous Si by Focused Ion Beam Implantation," *MRS Proceedings of Symposium on Semiconductor Heterostructures for Photonic and Electronic Applications*, Vol. 281, pp. 519-524, 1993.
4. A.J. Steckl, J. Xu and H.C. Mogul, "Relationship between Crystallinity and Photoluminescence in Stain-Etched Porous Si," *Journal of the Electrochemical Society*, Vol. 141, pp. 674-679, March 1994.
5. A.J. Steckl, J. Xu and H.C. Mogul, "Photoluminescence of Chemically Etched Polycrystalline and Amorphous Si Thin Films," *MRS Proceedings of Symposium on Silicon-Based Optoelectronics Materials*, Vol. 298, pp. 211-216, April 1993.
6. A.J. Steckl, J.N. Su, J. Xu, J.P. Li, C. Yuan, P.H. Yih and H.C. Mogul, "Characterization of Photoluminescence from Anodically Etched SiC/Si Heterostructures," *MRS Proceedings of Symposium on Silicon-Based Optoelectronics Materials*, Vol. 298, pp. 361-366, April 1993.
7. A.J. Steckl, J.N. Su, J. Xu, J.P. Li, C. Yuan, P.H. Yih and H.C. Mogul, "Selective-Area Room Temperature Visible Photoluminescence from SiC/Si Heterostructures," *Applied Physics Letters*, Vol. 64, pp. 1419-1420, March 1994.
8. H.C. Mogul, J. Xu, A.J. Steckl, S.J. Clarson, J.O. Stuart and C.L. Hoffman, "Light Emission and Related Materials Properties of Siloxene and Si-based Zeolites," *Proceedings of 1994 Electrochemical Society 7th International Symposium on Si Materials and Science and Technology*, Vol. 99-10, pp. 563-568, May 1994.
9. J. Xu and A.J. Steckl, "Visible Electroluminescence from Stain-Etched Porous Si Diodes," *IEEE Electron Device Letters*, Vol. 15, pp. 507-509, December 1994.
10. A.J. Steckl, J. Xu, H.C. Mogul and S.M. Prokes, "Si Hydrides on Stain-Etched Porous Si Thin Films and Correlation with Crystallinity and Photoluminescence," *Journal of the Electrochemical Society*, Vol. 142, pp. L69-71, May 1995.
11. J. Xu and A.J. Steckl, "Fabrication of Visibly Photoluminescent Si Microstructures by Focused Ion Beam Implantation and Wet Etching," *Applied Physics Letters*, Vol. 65, pp. 2081-2083, October 1994.
12. J. Xu, H.C. Mogul and A.J. Steckl, "Visible Photoluminescence from Stain-Etched Silicon Nanostructure," *Proceedings of the 2nd International Symposium on Quantum Confinement*, *Electrochemical Society Proceedings*, Vol. 94-17, pp. 231-239, 1994.

13. L. Wei, M. Vaudui, C-L. Hwang, G. White, J. Xu and A.J. Steckl, "Heat Conduction in Si Thin Films: Effect of Microstructure," *Journal of Materials Research*, Vol. 10, pp. 1889-1896, August 1995.
14. J. Xu and A.J. Steckl, "Stain-Etched Porous Si Visible Light Emitting Diodes," *Journal of Vacuum Science and Technology B*, Vol. 13, pp. 1221-1224, May/June 1995.

## Table of Contents

<b>Foreward</b> .....	<b>i</b>
<b>List of Publications From This Contract</b> .....	<b>iv</b>
<b>Table of Contents</b> .....	<b>vi</b>
<b>List of Tables</b> .....	<b>viii</b>
<b>List of Figures</b> .....	<b>ix</b>
<b>1. Introduction</b> .....	<b>1</b>
<b>2. Literature Review</b> .....	<b>6</b>
2.1 Band Structure and Optical Properties of Crystalline Silicon .....	6
2.2 Optical Processes and Luminescence Efficiency in Semiconductors .....	8
2.3 Engineering Luminescent Silicon .....	10
2.3.1 Defect Engineering in Silicon .....	10
2.3.2 Band Structure Engineering .....	13
2.3.3 Quantum Confinement Approaches .....	14
2.3.4 Hybrid Approaches .....	14
2.4 Porous Silicon .....	15
2.4.1 Porous Silicon Formation by Anodization .....	15
A. History Review .....	15
B. General Current-Voltage Characteristics of Si Anodization Process .....	16
C. Surface Dissolution Chemistries .....	19
D. Porous Silicon Formation Mechanism .....	20
2.4.2 Porous Silicon Formation by Stain-Etch .....	21
2.5 Properties of Porous Silicon .....	22
2.5.1 Morphology and Microstructure of Porous Silicon .....	22
2.5.2 Luminescence of Porous Silicon .....	25
<b>3. Experimental Techniques</b> .....	<b>30</b>
3.1 Focused Ion Beam Implantation Technology .....	30
3.1.1 System Specification and Operation .....	30
3.1.2 Fabrication Of Liquid Metal Ion Sources (LMIS) .....	33
3.2 Rapid Thermal Processing for Annealing and Oxidation .....	37
3.3 Wet Etching of Silicon .....	38
3.3.1 Anisotropic Etching of Silicon .....	39
3.3.2 Electrochemical Anodization .....	40
3.3.3 Stain-Etching .....	40
3.4 Metallization and Solid Contact by DC & RF Sputtering .....	41
3.5 Optical Characterization .....	42
3.6 Structural Characterization .....	44
3.6.1 X-Ray Diffraction Spectrometry (XRD) .....	44
3.6.2 Secondary Electron Microscopy (SEM) .....	44
3.6.3 Atomic Force Microscopy (AFM) .....	45
3.6.4 Fourier Transform Infrared Spectroscopy (FTIR) .....	46
3.6.5 Raman Spectroscopy .....	46
3.7 Electroluminescence Characterization .....	47
<b>4. Porous Si Light Emitting Pattern &amp; Nanostructures</b> .....	<b>49</b>
4.1 Doping Effect on Porous Si Formation and Fabrication of Embedded Photoluminescent Porous Si Patterns with Sub-Micron Resolution .....	49

4.1.1	Introduction .....	49
4.1.2	Experimental Results .....	49
4.1.3	Summary .....	62
4.2	Light Emitting Si Nanostructures .....	64
4.2.1	Introduction .....	64
4.2.2	Experimental Results .....	64
	A. Si Nanostructures .....	66
	B. Undercut and Annealing Effect .....	68
	C. Luminescing Si Nanostructures .....	71
4.2.3	Summary .....	74
<b>5.</b>	<b>Crystallinity, Photoluminescence &amp; Si Oxyhydrides in Stain-Etched Porous Silicon Films .....</b>	<b>76</b>
5.1	Photoluminescent Polycrystalline Si Thin Film Patterns .....	76
5.1.1	Introduction .....	76
5.1.2	Experimental Results .....	76
5.1.3	Summary .....	84
5.2	Crystallinity, Photoluminescence and Si Oxyhydrides in Stain-Etched Porous Si Films .....	85
5.2.1	Introduction .....	85
5.2.2	Experimental Procedures .....	85
5.2.3	Results and Discussions .....	86
5.2.4	Summary .....	106
<b>6</b>	<b>Porous Si Optoelectronic Devices .....</b>	<b>109</b>
6.1	Porous Si Light Emitting Diodes .....	109
6.1.1	Introduction .....	109
6.1.2	Experimental Procedures .....	110
	A. Fabrication Process .....	110
	B. Characterization .....	112
6.1.3	Results and Discussions .....	113
6.1.4	Summary .....	123
<b>7.</b>	<b>Conclusions and Suggestions for Future Work .....</b>	<b>125</b>
7.1	Conclusions .....	125
7.2	Suggestions for Future Work .....	126

## List of Tables

2.1	Common radiative and nonradiative processes in semiconductors .....	9
2.2	Radiative recombination at 300°K .....	9
2.3	Surface recombination velocities and area densities of traps for Si surface .....	10
2.4	Porous silicon formation models by anodization .....	16
2.5	Breakdown of the different electrochemical regions for the Si/HF system, summarizing the important features for each region .....	18
2.6	Summary of proposed porous silicon luminescence mechanism .....	26
3.1	Summary of FIB applications and related research directions at NanoLab .....	30
3.2	Focused ion beam system specifications .....	33
3.3	Advantages of atomic force microscopy .....	46
4.1	Resistivity & doping (hole) concentrations of samples used .....	50
5.1	Summary of the LPCVD films used in this work .....	86
6.1	Summary of porous silicon LED characteristics .....	109

## List of Figures

1.1.1	Photograph of the first light emitting porous silicon, under UV illumination, produced at University of Cincinnati .....	3
2.1.1	Band structures of Si, Ge, and GaAs .....	6
2.1.2	Absorption processes in indirect semiconductor (a), and relationship between absorption coefficient $\alpha$ and incident photon energy $h\nu$ (b) .....	7
2.1.3	Experimental absorption spectra for Si at several temperatures .....	8
2.3.1	Solid solubility of dopants in silicon .....	12
2.3.2	Brillouin zone folding of a Si-like band structure introduced by a superlattice with a period of $L = 5a$ .....	13
2.4.1	Schematic of an electrochemical cell for silicon anodization .....	16
2.4.2	"Typical" current-voltage relationships for <i>n</i> - and <i>p</i> -type silicon .....	17
2.4.3	Typical anodic <i>i</i> - <i>V</i> relationship for silicon anodization in HF showing three different regions .....	19
2.4.4	Porous silicon formed under different conditions .....	21
2.5.1	A select sampling of porous silicon samples showing the distinctive pore morphologies .....	23
2.5.2	XTEM micrographs showing the basic differences in the morphology among <i>n</i> , <i>p</i> , <i>n</i> <sup>+</sup> , and <i>p</i> <sup>+</sup> samples .....	24
2.5.3	XTEM of stain film formed by chromium trioxide and hydrofluoric acid on 0.01 $\Omega$ -cm <i>p</i> -type silicon .....	25
3.1.1	Electrical schematic of NanoFab 150 system .....	31
3.1.2	Schematic of the ion column in NanoFab-150 FIB system .....	32
3.1.3	Schematic of liquid metal ion source for NanoFab-150 FIB system .....	34
3.1.4	Experimental setup for LMIS tip fabrication .....	35
3.1.5	Schematic of the home-made vacuum working station for LMIS fabrication and testing .....	36
3.2.1	Schematic diagram of the NanoLab RV1003 RTA system .....	38
3.3.1	Schematic of the automated silicon anisotropic etching setup .....	39
3.3.2	Schematic of a single cell electrochemical etching setup .....	40
3.3.3	Stain etch setup for fabrication of porous silicon .....	41
3.4.1	Schematic of the Denton Vacuum DC-602 sputter deposition system .....	42
3.5.1	Block diagram of the optical characterization system .....	43
3.6.1	Principle of scanning probe microscopy .....	45
3.6.2	Schematic of the Raman spectroscopy system used in this work .....	47
3.6.3	Block diagram of the electroluminescence characterization system .....	48
4.1.1	Incubation time $t_i$ as function of resistivity .....	51
4.1.2	Incubation time as a function of hole concentration of Si substrates .....	52
4.1.3	Photoluminescence spectra of porous silicon on various substrates .....	53
4.1.4	PL peak and FWHM as a function of substrate resistivity for both <i>n</i> - and <i>p</i> -type Si etched for $t_i$ plus 2 min .....	54
4.1.5	SEM micrographs (plan-view) of porous silicon on various substrates .....	55
4.1.6	Process flow for selective fabrication of light-emitting porous silicon pattern .....	59
4.1.7	PL micrograph of FIB Ga <sup>+</sup> implantation-induced localized photoemission pattern of 500 $\times$ 500 $\mu\text{m}^2$ .....	60

4.1.8	PL micrograph of FIB $\text{Ga}^+$ implantation-induced localized line patterns with 3.5 and 0.5 $\mu\text{m}$ line widths implanted at 30 kV with $10^{14}/\text{cm}^2$ .....	60
4.1.9	PL micrograph of broad beam $\text{B}^+$ implantation-induced localized photoemission patterns .....	61
4.1.10	PL micrograph of a stain-etched as-implanted pattern .....	62
4.2.1	Overall process schematic of the fabrication of optically active Si micro- and nano-structures .....	65
4.2.2	SEM micrograph (tilted-view) of Si $4 \times 4 \mu\text{m}^2$ cantilevers: on-axis FIB, 30 min KOH etching of annealed sample in R1 at $71^\circ\text{C}$ .....	66
4.2.3	SEM micrograph (tilted-view) of Si $0.5 \mu\text{m} \times 50 \mu\text{m}$ air-bridges: off-axis FIB and 10 min KOH etching of annealed sample in R1 at $82^\circ\text{C}$ .....	67
4.2.4	SEM micrograph (tilted-view) of Si air-bridge of $2 \mu\text{m} \times 20 \mu\text{m}$ obtained by $25^\circ$ off-axis FIB implantation into (100) $n$ -Si and 1.5 min KOH etching of the as-implanted sample in R2 at $81^\circ\text{C}$ .....	67
4.2.5	SEM micrograph (tilted-view) of orientation dependence of undercut: 2 min etching of as-implanted sample in R2 at $82^\circ\text{C}$ .....	68
4.2.6	(a) SEM micrograph (tilted-view) of Si O-ring nanostructure right after KOH etching of the as-implanted sample; .....	69
	(b) SEM micrograph (tilted-view) of Si O-ring nanostructure after KOH etching of the as-implanted sample plus RTA at $600^\circ\text{C}$ for 30 sec; .....	70
	(c) SEM micrograph (tilted-view) of Si O-ring nanostructure after KOH etching of the as-implanted sample plus RTA at $600^\circ\text{C}$ for 30 sec plus 20 min modified RCA cleaning .....	70
4.2.7	SEM micrograph (tilted-view) of stain-etched Si nanostructures .....	71
4.2.8	Color microphotographs of photoemission image of stain-etched Si microstructures under UV excitation .....	72
4.2.9	Color microphotographs of photoemission image of stain-etched Si $4 \times 4 \text{ mm}^2$ under UV excitation with its PL spectrum shown in Fig. 4.2.10 .....	73
4.2.10	Room temperature PL spectrum of sample A under $\text{Ar}^+$ 488 nm excitation .....	74
5.1.1	SEM micrographs of as-deposited and stain-etched polycrystalline silicon thin films .....	77
5.1.2	Photoluminescence spectra : doped and undoped poly-Si on $\text{SiO}_2/\text{Si}$ stain-etched for 30 sec; undoped poly-Si on quartz stain-etched for 120 sec; $n$ -type c-Si stain-etched for $t_i$ plus 120 sec .....	81
5.1.3	Photoluminescence spectra of porous poly-Si films on quartz measured from both front and back sides .....	82
5.1.4	PL micrograph of light emitting patterns in stain-etched poly-Si on $\text{SiO}_2/\text{Si}$ .....	83
5.2.1	Film deposition rate as a function of temperature .....	87
5.2.2	X-ray diffraction spectra of as-deposited CVD Si films on quartz at temperatures of 580, 600 and $630^\circ\text{C}$ .....	88
5.2.3	SEM micrographs of as-deposited amorphous and polycrystalline silicon thin films .....	89
5.2.4	AFM area scan of as-deposited amorphous and polycrystalline silicon thin films .....	91
5.2.5	Surface roughness of as-deposited films as a function of the deposition temperature $T_D$ .....	93

5.2.6	SEM micrographs of 2 min stain-etched amorphous and polycrystalline silicon thin films .....	94
5.2.7	SEM micrographs of non-luminescent amorphous porous silicon stained-etched for 31 and 7 min .....	96
5.2.8	Relative weight loss during stain etching of CVD Si films deposited at different temperatures .....	97
5.2.9	Room temperature PL spectra of porous silicon formed in Si films deposited at 580, 600, 620°C .....	98
5.2.10	XRD spectra of Si film deposited at 600°C: (a) as-deposited; (b) stain-etched for 50 sec in HF/HNO <sub>3</sub> with 200:1 ratio; (c) after porous silicon removal by etching in KOH for 30 sec .....	99
5.2.11	Raman spectrum of as-deposited (at 630°C) and stain-etched (for 2 min) poly-Si film .....	100
5.2.12	Full range FTIR spectra showing distinct periodic fringes attributed to interference between the various layers of material present .....	101
5.2.13	FTIR spectra near the vicinity of 2260 wavenumbers from stain-etched polycrystalline Si films showing distinct peak due to Si-H stretching mode .....	102
5.2.14	FTIR spectra in the range of 500 - 1000 cm <sup>-1</sup> from both as-deposited and stain-etched poly-Si films with T <sub>D</sub> of 630°C .....	103
5.2.15	FTIR spectra (800-900 cm <sup>-1</sup> ) in the vicinity of Si oxyhydride peak (880 cm <sup>-1</sup> ) from porous silicon films deposited at several temperatures (540, 580, 600, 630°C) .....	104
5.2.16	Effect of deposition temperature on porous silicon materials properties: (a) photoluminescence - UV pumping at 365 nm ; (b) crystallinity - XRD <220> peak; (c) Si oxyhydride - FTIR peak at ~ 880 cm <sup>-1</sup> .....	105
6.1.1	Process flow for porous silicon LED fabrication using lift-off .....	111
6.1.2	Process flow for porous Si LED fabrication using shadow masking .....	112
6.1.3	Photographs of a porous silicon thin film obtained by stain etching of B-doped 6-8 Ω-cm (100) c-Si in HF:HNO <sub>3</sub> :H <sub>2</sub> O of 1:3:5 composition for 1 min plus 3 min incubation time .....	113
6.1.4	I-V characteristic of an ITO/p-porous silicon diode fabricated by stain-etching. The inset represents the diode structure under reverse bias .....	114
6.1.5	Ideality factor n of the ITO/p-Si diode extracted from its low voltage I-V curve .....	115
6.1.6	Ideality factor n of the ITO/p-porous silicon diode extracted from its low voltage I-V curve .....	115
6.1.7	Low bias I-V characteristics of ITO/p-porous silicon and ITO/p-Si heterojunctions .....	116
6.1.8	Dependence of series resistance on the applied bias for ITO/p-porous silicon diodes .....	117
6.1.9	Comparison of I-V characteristics of ITO/p-Si and ITO/p-porous silicon diodes indicating a significantly increased series resistance in ITO/p-porous silicon diode .....	118
6.1.10	EL topography from an ITO/p-porous silicon diode under a forward bias of 40 mA/cm <sup>2</sup> .....	119
6.1.11	EL intensity at a current density of 125 mA/cm <sup>2</sup> as a function of time for 60 min .....	119
6.1.12	Dependence of ITO/p-porous silicon electroluminescence intensity on bias .....	120

6.1.13 Dependence of stain-etched porous-silicon LED electroluminescence intensity on device current density .....	121
6.1.14 (a): PL spectrum under 365 nm UV line excitation; (b): EL spectrum at a bias of 125 mA/cm <sup>2</sup> .....	122
6.1.15 EL spectra as the function of device forward bias .....	123

# Chapter 1

## Introduction

The electronic revolution, which began in 1948 with the successful fabrication of the first transistor [Bardeen and Brattain (1948), Brattain and Bardeen (1948)], has made profound impact on almost every aspect of human life today. Being the most dominant material in microelectronics and one of the best-studied materials, semiconductor silicon has played a distinguished role in this tremendous historical event. However, while silicon is leading in many areas of microelectronics, its inability of emitting visible light and low luminescence efficiency at near infrared due to its indirect bandstructure and a bandgap energy of 1.11 eV (300°K), has prevented its applications in many areas of optoelectronics, which is one of the leading edges of the current information revolution.

The integration of both passive and active optical components onto a silicon-based chip allows further functional integration of electronics and optics. This will consequently lead to the realization of new concepts such as "Photonic Integrated Circuits". The use of semiconductor silicon and silicon technology in this new field is highly desirable because of the low cost of silicon material and the highly developed silicon technology. In the past four decades, efforts in achieving usable optical properties in silicon, such as efficient luminescence at energies different from its intrinsic bandgap with applications in integrated optoelectronics, has been focused mainly in four areas. These include defect engineering, band structure engineering, quantum confinement approaches and hybrid approaches [Iyer and Xie (1993)]. As a result and to a limited extent, optoelectronic integration has been achieved within the confines of the technology of III-V materials and their hybridization with silicon chips. More recently, there have been modest gains in the application of silicon processing to the fabrication of several optoelectronic components and their limited integration into silicon-based technology. These include detectors [Bassous, *et al.* (1991)], wave guides [Pesarick, *et al.* (1992)], modulators [Treyz, *et al.* (1991)], interferometers, and switches. However, these components are all optically passive and, therefore, there is no means to stimulate light emission from silicon.

Recent observations of the efficient room temperature photoluminescence (PL) by Canham [Canham (1990)] and the blue shifted optical absorption by Lehmann and Gösele [Lehmann and Gösele (1991)] in porous silicon in 1990 marked the beginning of a new era in silicon research and development. These newly discovered phenomena have generated a flurry of interest in the properties of this material and in its potential applications in Si-based integrated optoelectronics.

Porous silicon has been studied for over 30 years [Uhlir (1956)] mainly for its applications in electrical isolation technology in integrated circuits, particularly in silicon-on-insulator (SOI) devices [Bomchil, *et al.* (1988)]. Most visible light emitting porous silicon has been produced by anodic etching of crystalline silicon in HF-based solutions. Various kind of electrolytes have been used and each has a wide range of composition. These include concentrated (49%) hydrofluoric acid [Gardelis, *et al.* (1991)], HF in water [Pearsall, *et al.* (1992)], HF in ethanol [Cole, *et al.* (1992)], and HF in acetic acid [Searson, *et al.* (1992)]. Porous silicon films produced by pure chemical etching (stain-etching) in HF:HNO<sub>3</sub>:H<sub>2</sub>O have been shown to exhibit similar visible luminescence to that of electrochemically-etched porous silicon films [Fathauer, *et al.* (1992), Kidder, *et al.* (1992), Sarathy, *et al.* (1992), Aoyagi, *et al.* (1993)]. Stain films on silicon obtained by immersion in HF:HNO<sub>3</sub>-based solutions has been known for a comparable period of time [Turner (1958), Archer (1960)], and have been shown to consist of porous material similar to that produced by anodic etching [Beale, *et al.* (1986)]. Photoluminescence similar to that of anodized and stain-etched porous silicon has also been obtained from silicon subjected to spark erosion [Hummei and Chang (1992)] and to ion irradiation [Ochiai, *et al.* (1992)], from porous

silicon synthesized by visible light irradiation [Noguchi and Suemune (1993)], and from silicon nanoparticles or clusters produced by spark ablation [Saunders, *et al.* (1993)] and by gas phase synthesis from silane ( $\text{SiH}_4$ ) in a non-thermal microwave plasma [Zhang, *et al.* (1992)] and by photolysis of disilane ( $\text{Si}_2\text{H}_6$ ) using excimer laser [Heath and Jasinski (1992)].

Researches in luminescent porous silicon have also triggered great interests in other silicon-related materials. Several silicon-related compounds, alloy or other structures have been observed to exhibit similar visible photoluminescence as summarized below.

Siloxene ( $\text{Si}_6\text{O}_3\text{H}_6$ ) and its derivative, a kind of silicon compounds with over 70 years history [Kautsky (1921)], chemically synthesized from a reaction of  $\text{CaSi}_2$  powder with concentrated hydrochloric acid were first reported in 1992 by a group in Germany to have luminescence properties similar to that of porous silicon [Daek, *et al.* (1992), Fuchs, *et al.* (1992)]. It was once suggested that siloxene is the luminescent origin in porous silicon [Daek, *et al.* (1992), Fuchs, *et al.* (1992)]. However, this has been recently proven not to be the case experimentally [Friedman, *et al.* (1993)]. Nevertheless siloxene by itself and its optical properties are interesting topics to be further investigated.

Porous  $\text{Si}_{1-x}\text{Ge}_x$  alloys obtained by electrochemical anodization [Gardelis, *et al.* (1991)] and stain etching [Ksendzov, *et al.* (1993)] of molecular-beam-epitaxy (MBE) grown  $\text{Si}_{1-x}\text{Ge}_x$  alloys with  $x$  ranging from 0.04 to 0.41 were reported to exhibit visible photoluminescence similar to porous silicon, and its photoluminescence peak wavelength can be tuned by changing germanium composition  $x$ .

Visible photoluminescence with peak energy around 2.1 eV has been obtained in crystallized amorphous silicon:H/ $\text{SiN}_x$ :H multi-quantum-well (MQW) structures [Chen, *et al.* (1992)]. The MQW heterostructures consisting of 72 multilayers were formed by computer controlled plasma enhanced chemical vapor deposition (PECVD) from a gas mixture of  $\text{NH}_3/\text{SiH}_4=3.6$  and then crystallized by  $\text{Ar}^+$  laser annealing. No etching was involved in this process.

Carbon clusters embedded in  $\text{SiO}_2$  prepared by a RF co-sputtering of carbon and  $\text{SiO}_2$  combined target in  $\text{Ar}^+$  plasma [Hayashi, *et al.* (1993)] was recently observed to be photoluminescent in visible with peak energy around 2.2 eV. The photoluminescence, which was attributed to carbon clusters formed in the  $\text{SiO}_2$  matrices, can be tuned by changing carbon concentration.

Very recently, room temperature blue-green photoluminescence was reported [Matsumoto, *et al.* (1994)] for the first time from porous silicon carbide formed by electrochemical anodization of single crystal 6H-SiC in a HF-ethanol solution with conditions similar to that of porous silicon formation. In contrast to porous silicon, the porous SiC luminescence peak positions at  $\sim 500$  nm are below the band gap of the silicon carbide crystal (430 nm) and are similar with those generally observed in hydronated amorphous silicon carbide ( $\alpha$ -SiC:H). One advantage of porous silicon carbide is its very little luminescence degradation in air at room temperature under optical irradiation as compared to porous silicon.

Silicon-based zeolites were first observed [Mogul, *et al.* (1994)] to exhibit a strong PL signal at University of Cincinnati, with a peak centered at  $\sim 550$  nm, under UV excitation. Zeolites consist of a 3D network of  $\text{SiO}_4$  and  $\text{AlO}_4$  tetrahedral with each oxygen shared by two tetrahedra [Breck, *et al.* (1956)]. They posses a well defined crystal structure with a porous internal framework of molecular dimensions, with pore diameters ranging from 4 to 10 Å.

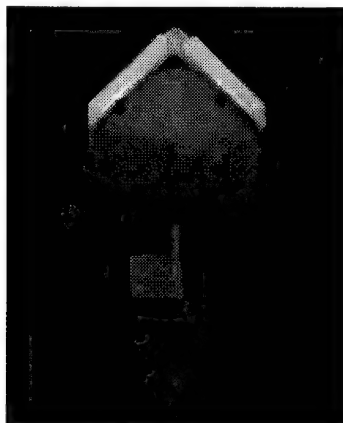


**FIGURE 1.1.1** Photograph of the first light emitting porous silicon wafer, under UV illumination, produced at University of Cincinnati.

At University of Cincinnati, researches seeking light emission from silicon started with silicon nanostructures fabrication in 1991 [Steckl, *et al.* (1992)] and with luminescing porous silicon obtained by stain-etching in May 1992 from this work. Figure 1.1.1 shows a color photograph of the first light emitting porous silicon at UC produced by stain etching of a 2-in *p*-type silicon wafer in a solution of HF:HNO<sub>3</sub>:H<sub>2</sub>O with 1:3:5 composition in volume. Since then researches in this area has extended into many areas of porous silicon research with the emphasis on the applications in optoelectronic devices.

The overall objective of this dissertation combines a study of the fundamental mechanisms of porous silicon with an investigation and development of fabrication techniques for porous silicon devices and ultimately with optoelectronic applications of porous silicon.

## REFERENCES

Aoyagi, H., Motohashi, A., Kinoshita, A., Aono, T. and Satou, A., "A comparative study of visible photoluminescence from anodized and from chemically stained silicon wafers", *Jpn. J. Appl. Phys.* **32**, L1 (1993).

Archer, R. J., "Stain films on silicon", *J. Phys. Chem. Solids* **14**, 104 (1960).

Bardeen, J. and Brattain, W. H., "The transistor, a semiconductor triode", *Phys. Rev.* **74**, 230-231 (1948).

Bassous, E., Scheuermann, M., Kesan, V. P., Ritter, M., Halbout, J.-M. and Iyer, S. S., "A high-speed silicon metal-semiconductor-metal photodetector fully integrable with (Bi)CMOS circuits", *Tech. Dig.* **1991**, 187 (1991).

Beale, M. I. J., Benjamin, J. D., Uren, M. J., Chew, N. G. and Cullis, A. G., "The formation of porous silicon by chemical stain etches", *J. Crys. Grow.* **75**, 408 (1986).

Bomchil, G., Halimaoui, A. and Herino, R., "Porous silicon: the material and its applications to SOI technologies", *Microelectronics Engineering* **8**, 293 (1988).

Brattain, W. H. and Bardeen, J., "Nature of the forward current in germanium point contacts", *Phys. Rev.* **74**, 231-232 (1948).

Breck, D. W., Eversole, W. G., Milton, R. M., Reed, T. B. and Thomas, T. L., *J. Chem. Soc.* **78**, 5963 (1956).

Canham, L., "Silicon quantum wire array fabrication by electrochemical and chemical dissolution of wafers", *Appl. Phys. Lett.* **57**, 1046 (1990).

Chen, K., Huang, X., Xu, J. and Feng, D., "Visible photoluminescence in crystallized amorphous Si:H/SiN<sub>x</sub>:H multiquantum-well structures", *Appl. Phys. Lett.* **61**, 2069 (1992).

Cole, M. W., Harvey, J. F., Lux, R. A., Eckart, D. W. and Tsu, R., "Microstructure of visibly luminescent porous silicon", *Appl. Phys. Lett.* **60**, 2800 (1992).

Daek, P., Rosenbauer, M., Stutzmann, M., Weber, J. and Brandt, M. S., "Siloxene: chemical quantum confinement due to oxygen in a silicon matrix", *Phys. Rev. Lett.* **69**, 2531 (1992).

Fathauer, R. W., George, T., Ksendzov, A. and Vasquez, R. P., "Visible luminescence from silicon wafers subjected to stain etches", *Appl. Phys. Lett.* **60**, 996 (1992).

Friedman, S. L., Marcus, M. A. and Adler, D. L., "Unimportance of siloxene in the luminescence of porous silicon", *Appl. Phys. Lett.* **62**, 1934 (1993).

Fuchs, H. D., Stutzmann, M., Brandt, M. S., Rosenbauer, M., Weber, J. and Cardona, M., "Visible luminescence from porous silicon and siloxene", *Physica Scripta* **T54**, 309 (1992).

Gardelis, S., Rimmer, J. S., Dawson, P., Hamilton, B., Kubiak, R. A., Whall, T. E. and Parker, E. H. C., "Evidence for quantum confinement in the photoluminescence of porous Si and SiGe", *Appl. Phys. Lett.* **59**, 2118 (1991).

Hayashi, S., Kataoka, M. and Yamamoto, K., "Photoluminescence spectra of carbon clusters Embedded in  $SiO_2$ ", *Jps. J. Appl. Phys.* **32**, L284 (1993).

Heath, J. R. and Jasinski, J. M., "Structural studies, surface properties, and photoluminescence behaviour of silicon nanocrystals", *Mat. Res. Soc. Symp. Proc.* **256**, 117 (1992).

Hummei, R. E. and Chang, S.-S., "Novel technique for preparing porous silicon", *Appl. Phys. Lett.* **61**, 1965 (1992).

Iyer, S. S. and Xie, Y.-H., "Light emission from silicon", *Science* **260**, 40 (1993).

Kautsky, H., Z. Anorg. Chemie **117**, 209 (1921).

Kidder, J. N., Williams, J., P. S., Pearsall, T. P., Schwartz, D. T. and Nosh, B. Z., "Comparision of light emission from stain-etch and anodic-etch silicon films", *Appl. Phys. Lett.* **61**, 2896 (1992).

Ksendzov, A., Fathauer, R. W., George, T., Pike, W. T., Vasquez, R. P. and Taylor, A. P., "Visible photoluminescence of porous  $Si_{1-x}Ge_x$  obtained by stain etching", *Appl. Phys. Lett.* **63**, 200 (1993).

Lehmann, V. and Gosele, U., "Porous silicon formation: A quantum wire effect", *Appl. Phys. Lett.* **58**, 856 (1991).

Matsumoto, T., Takahashi, J., Tamaki, T., Futagi, T., Mimura, H. and Kanemitsu, Y., "Blue-green luminescence from porous silicon carbide", *Appl. Phys. Lett.* **64**, 226 (1994).

Mogul, H. C., Xu, J., Steckl, A. J., Clarson, S. J., Stuart, J. O. and Hoffman, C. L., "Light emission and related materials properties of siloxene and Si-based zeolites", *Proc. 7th International Symp. Si Mat. Sci. Tech.* **99-10**, 563 (1994).

Noguchi, N. and Suemune, I., "Luminescent porous silicon synthesized by visible light irradiation", *Appl. Phys. Lett.* **62**, 1429 (1993).

Ochiai, Y., Ookubo, N., Watanabe, H., Matsui, S., Mochizuki, Y., Ono, H., Kimura, S. and Ichihashi, T., "Novel process for visible light emission from Si prepared by ion irradiation", *Jpn. J. Appl. Phys.* **31**, L560 (1992).

Pearsall, T. P., Adams, J. C., Wu, J. E., Nosh, B. Z., Aw, C. and Patton, J. C., "Time-resolved photoluminescence in anodically etched silicon", *J. Appl. Phys.* **71**, 4470 (1992).

Pesarcik, S. F., Treyz, G. V. and Iyer, S. S., "Silicon germanium optical waveguides with 0.5 dB/cm losses for singlemode fibre optic systems", *Electron. Lett.* **28**, 159 (1992).

Sarathy, J., Shih, S., Jung, K., C., T., Li, K.-H., Kwong, D.-L., Campbell, J. C., Yau, S.-L. and Bard, A. J., "Demonstration of photoluminescence in nonanodized silicon", *Appl. Phys. Lett.* **60**, 1532 (1992).

Saunders, W. A., Sercel, P. C., Lee, R. B., Atwater, H. A., Vahala, K. J., Flagan, R. C. and Escorcia-Aparcio, E. J., "Synthesis of luminescent silicon clusters by spark ablation", Appl. Phys. Lett. **63**, 1549 (1993).

Searson, P. C., Macaulay, J. M. and Ross, F. M., "Pore morphology and the mechanism of pore formation in n-type silicon", J. Appl. Phys. **72**, 253 (1992).

Steckl, A. J., Mogul, H. C. and Mogren, S., "Localized fabrication of Si nanostructures by focused ion beam implantation", Appl. Phys. Lett. **60**, 1833 (1992).

Treyz, G. V., May, P. G. and Halbout, J.-M., "Silicon Mach-Zehnder waveguide interferometers based on the plasma dispersion effect", Appl. Phys. Lett. **59**, 771 (1991).

Turner, D. R., "Electropolishing silicon in hydrofluoric acid solutions", J. Electrochem. Soc. **105**, 405 (1958).

Uhlir, A., "Electrolytic shaping of germanium and silicon", Bell System Tech. J. **35**, 333 (1956).

Zhang, D., Kolbas, R. M., Mehta, P., Singh, A. K., Lichtenwalner, D. J., Hsieh, K. Y. and Kingon, A. I., "Visible light emission from silicon nanoparticles", Mat. Res. Soc. Symp. Proc. **256**, 35-40 (1992).

## Chapter 2

### Literature Review

This chapter reviews the optoelectronic properties of semiconductor silicon, approaches to achieve efficient light emission from silicon, historic background of porous silicon, and the recent discovery of room temperature efficient light emission from porous silicon.

#### 2.1 Band Structure and Optical Properties of Crystalline Silicon

The interaction between a photon and a semiconductor, such as the absorption of a photon or the emission of a photon, can be reflected in the optical properties of the semiconductor. Single crystalline silicon (c-Si) is widely known as indirect semiconductor with a band gap of 1.11 eV at room temperature. Theoretically, the band gap of a semiconductor can be easily deduced from its band structure which, conventionally, is represented by a dispersion relation between the energy  $E(\mathbf{k})$  of an electron (or hole) and its wave vector  $\mathbf{k}$  in the first Brillouin zone. Band gap is the energy difference between the lowest conduction band minimum and the highest valence band maximum. The band structure of a material is ultimately determined by several factors, including crystal structure, lattice constant, chemical species, bonding and bond lengths, electronegativity, stiffness, and elasticity. Many of these factors are lumped into the crystal potential, which is then used in the crystal Hamiltonian to solve for the crystal wave equation.

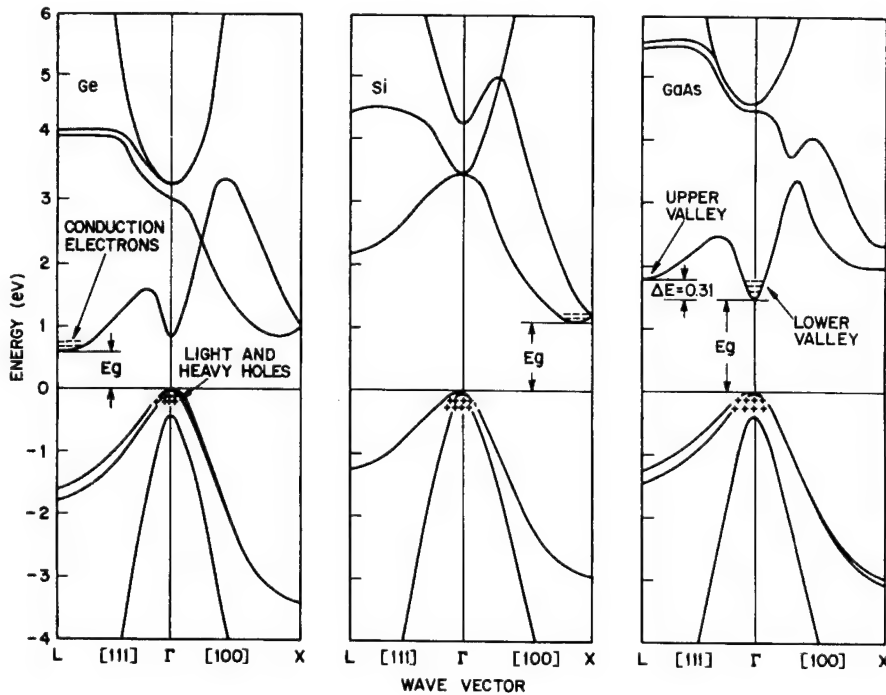


**FIGURE 2.1.1** Band structures of Si, Ge, and GaAs (after [Cohen and Bergstresser (1966)]).

Figure 2.1.1 represents the calculated band structures of three common semiconductors Si, Ge, and GaAs [Cohen and Bergstresser (1966)]. In silicon, as seen from its band structure, the momentum of an electron at the conduction band edge is quite different from that of a hole at the valence band edge. Since the momentum of a photon is very small compared to the range of wave vectors in the Brillouin zone, the probability of an optical transition is virtually zero, as required by

the momentum conservation law, unless a phonon with an appropriate momentum is involved. Such a transition is normally referred as indirect and silicon is therefore an indirect semiconductor.

Experimentally the most direct, and perhaps the simplest method for measuring the band structure of semiconductors, is to investigate the optical absorption spectrum. For an indirect semiconductor such as silicon, absorption of a photon is a two-step process and can involve both phonon emission and phonon absorption as described by equation (2-1) and illustrated in Fig. 2.1.2 (a),

$$\begin{aligned} h\nu_e &= E_f - E_i + E_p \\ h\nu_e &= E_f - E_i - E_p \end{aligned} \quad (2-1)$$

where  $h\nu_e$  is the photon energy absorbed,  $E_i$  and  $E_f$  represent the initial and final electron energy respectively,  $E_p$  is the phonon energy involved.

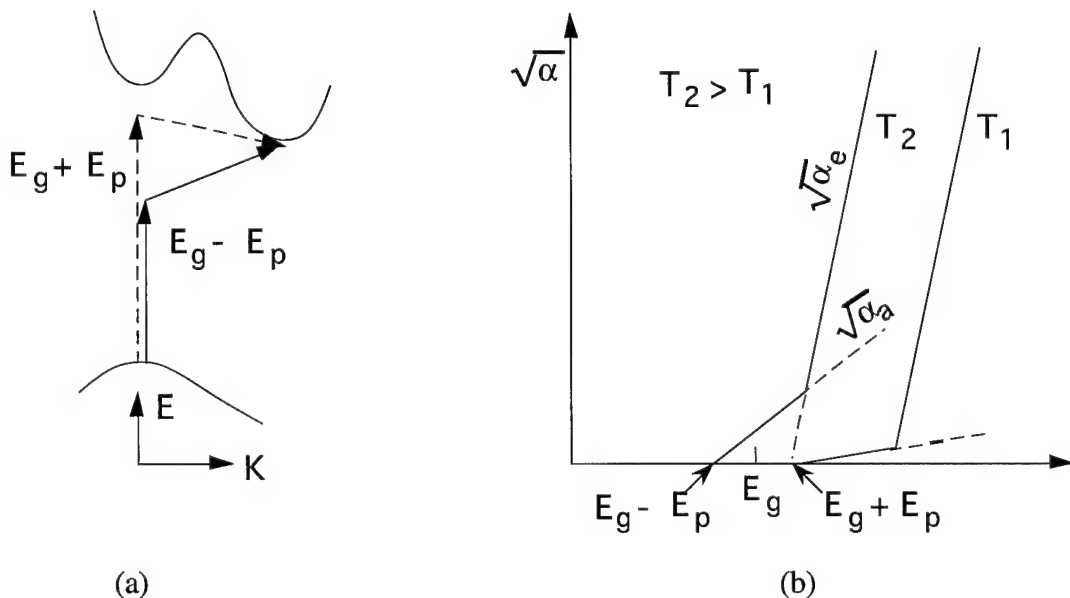


**FIGURE 2.1.2** Absorption process in indirect semiconductor (a), and relationship between absorption coefficient  $\alpha$  and incident photon energy  $h\nu$  (b) (after [Pankove (1971)]).

Figure 2.1.3 shows the silicon absorption-edge region obtained by Macfarlane *et al* [Macfarlane, *et al.* (1958), Macfarlane, *et al.* (1959)]. These data were taken with high resolution at a number of temperatures. There is considerable resemblance to the spectrum shown schematically in Fig. 2.1.2, indicating the occurrence of indirect transitions with the participation of both emission and absorption of a phonon. Another common technique for obtaining band gap energy is the photoluminescence excitation spectroscopy (PLE).

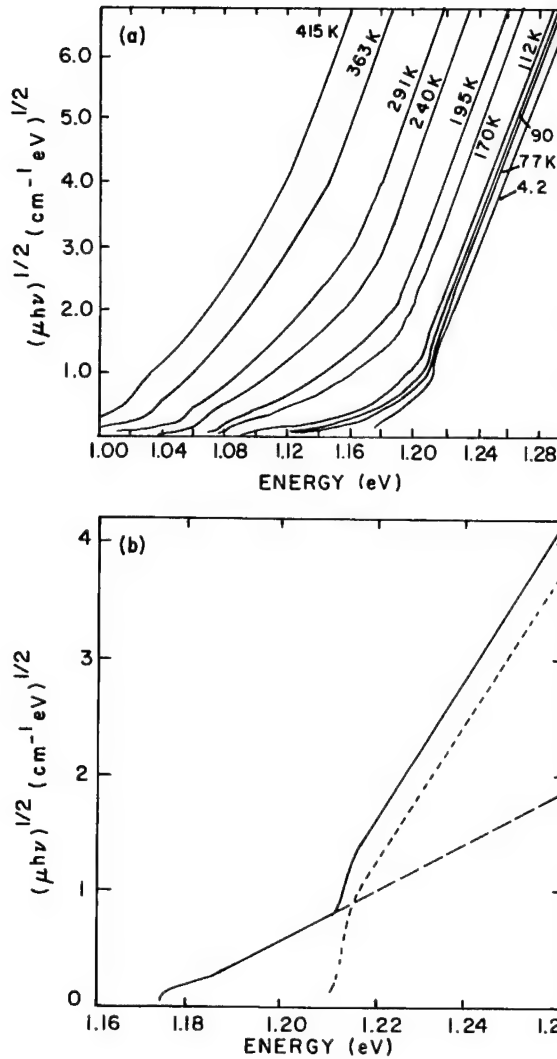


**FIGURE 2.1.3** Experimental absorption spectra for Si at several temperatures: (a) absorption-coefficient spectra for Si at the fundamental (indirect) edge at several temperatures and (b) decomposition of the 4.2°K spectrum into two components, phonon emission (dotted line beginning at higher energy) and phonon absorption (dashed line lying under the solid line, then leaving it.). The solid line is the spectrum from both components together (after [Palik (1985)]).

## 2.2 Optical Processes and Luminescence Efficiency in Semiconductors

Efficient luminescence from semiconductors requires primary two conditions: (1) the generation of a high concentration of charge carriers (electrons or holes) in their excited states by a variety of ways, such as photoluminescence by optical excitation, electroluminescence by an electrical current and cathodoluminescence by an electron beam; (2) the exist of an efficient radiative recombination process through which excited charge carriers can transfer their energy effectively to photons emitted. Table 2.1 lists some common radiative and nonradiative processes that occur in semiconductors and which compete with one another for excited carriers [Canham (1993)]. The internal radiative efficiency of a semiconductor is given by [Pankove (1971)]:

$$\eta = \frac{\tau_{nr}}{\tau_r + \tau_{nr}} \quad (2-2)$$

where  $\tau_r$  is the excess carrier lifetime that is limited by all radiative recombination processes and  $\tau_{nr}$  is that results from all nonradiative processes. This simple expression indicates that there are basically two ways that can be used to achieve high radiative efficiency: either minimizing all nonradiative processes (making  $\tau_{nr}$  very long) or creating a very fast radiative process (making  $\tau_r$  very short).

Table 2.1 Common radiative and nonradiative processes in semiconductors

Nonradiative processes	Radiative processes
Auger processes	Band-to-band electron-hole recombination
Surface recombination	Donor-acceptor pair recombination
Recombination through defects or inclusions	Free exciton recombination
Multiphonon recombination	Bound exciton recombination at "shallow" centers and isoelectronic traps

Table 2.2 shows the calculated  $\tau$  for band-to-band radiative transitions of various semiconductors [Pankove (1971)]. The intrinsic radiative efficiency of an undoped defect-free semiconductor is determined by its bandstructure and, in particular, whether its bandgap is direct or indirect. If direct (e.g., GaAs or InP), then the radiative recombination is a fast ( $\tau_r \sim \text{ns}$ ) and efficient process. If indirect (e.g., Si or GaP), then to conserve momentum, the electron and hole must interact with specific phonons to recombine. This three-particle process is a much slower process ( $\tau_r \sim \text{ms}$ ) and hence competes poorly with nonradiative processes and is therefore inefficient. The Auger process involves also three particles, but it is a nonradiative process which transfers the energy released from the electron-hole recombination to another electron or hole. That then thermalizes rapidly by phonon emission.

Table 2.2 Radiative recombination at 300°K

Material	$E_g$ eV	$n_i$ $\text{cm}^{-3} \times 10^{14}$	$\tau$ (intrinsic)	$\tau$ (for $10^{17}$ majority carriers/ $\text{cm}^3$ )
Si	1.08	0.00015	4.6 h	$2500 \mu\text{s}$
Ge	0.66	0.24	0.61 sec	$150 \mu\text{s}$
GaSb	0.71	0.043	0.009 sec	
InAs	0.31	16	$15 \mu\text{s}$	$0.37 \mu\text{s}$
InSb	0.18	200		
PbS	0.41	7.1	$0.62 \mu\text{s}$	$0.24 \mu\text{s}$
PbTe	0.32	40	$15 \mu\text{s}$	$0.12 \mu\text{s}$
PbSe	0.29	62	$2.4 \mu\text{s}$	$0.21 \mu\text{s}$
GaP	2.25		$2.0 \mu\text{s}$	$0.19 \mu\text{s}$
				$0.25 \mu\text{s}$
				$3000 \mu\text{s}$

Another important nonradiative process in all semiconductors is the surface recombination which is often quantified by a surface recombination velocity (SRV), where [Canham (1993)]

$$S \sim \sigma V_{th} N_t \quad (2-3)$$

$V_{th} \sim 10^7 \text{ cm/s}$  is the carrier thermal velocity,  $\sigma \sim 10^{-15} \text{ cm}^2$  is a typical recombination cross section, and  $N_t$  is the area density of surface traps that introduce levels in the bandgap of the semiconductor. If a surface is not well passivated it will become an effective nonradiative sink for excited carriers. This is an important issue for porous silicon light emission because the enormous surface area to volume ratio in porous silicon. Table 2.3 lists a few typical experimental values for three types of Si passivation [Canham (1993)]. As seen from the table, hydrogen termination reduces the surface nonradiative recombination by four orders of magnitude.

Table 2.3 Surface recombination velocities and area densities of traps for Si surface

Si surface passivation	SRV (cm/s)	N (cm <sup>-2</sup> )
"Native" oxide	$\sim 10^4$	$\sim 10^{12}$
Thermal oxide	$\sim 10^2$	$\sim 10^{10}$
Hydride	$\sim 1$	$\sim 10^8$

The luminescence efficiency of semiconductor structures are measured in a number of ways, but are basically ratios of output to input. The internal quantum efficiency (IQE) of an a light emitting diode, for example, is the number of photons created internally per the number of carries injected into the diode. The number of photons actually emitted out from the structure is determined by the so-called external quantum efficiency (EQE) which is invariably significantly lower than the IQE for bulk semiconductors, due to their large refractive indexes. For silicon, for example ( $n \sim 3.5$ ), only 2% of the light emitted internally avoids total internal reflection. The EQE of near infrared luminescence from bulk crystalline silicon typically lies in the  $10^{-5} - 10^{-3}$  percent range [Haynes and Westphal (1956), Michaels and Pilkuhn (1969)] under both optical and electrical excitations.

## 2.3 Engineering Luminescent Silicon

As a direct result of its indirect band structure and a gap energy of 1.11 eV silicon is not a natural candidate for photoemissive devices in the visible range for optoelectronic applications despite its overwhelming success in microelectronics. A number of avenues exit for the engineering of luminescing transitions in an indirect semiconductor, which can be grouped into four classes as discussed below.

### 2.3.1 Defect Engineering in Silicon

In so-called defect engineering, defects or impurities are introduced into the bulk of crystalline silicon as radiative mediators through which the electron-hole recombination process produces a photon and can take place at a relative high efficiency. The enhancement of the radiative process can be explained in a simplified manner as a consequence of the relaxation of  $\mathbf{k}$ -selection requirement caused by the localization of the electron-hole pairs near impurity centers. These optically active centers can be isolated impurities, impurity complexes, or defects induced by radiation damage or thermal processing. In silicon, the majority of defects are nonradiative through which the recombination of electron-hole pairs resulting in phonons instead of photons. Of the limited number of known radiative defects, only isoelectronic traps [Faulkner (1968)] created by substitutional impurities with the same number of valence electrons as of the hosting silicon (electronically neutral and therefore "iselectronic") and rare-earth metals [Ennen, *et al.* (1983)] have been successfully used to induce strong radiative transitions in silicon.

One example of radiative recombination in silicon through isoelectronic centers is the S-doped Si. S impurities are incorporated into silicon via either ion implantation or diffusion process followed by a high-temperature annealing at  $\sim 1200\text{C}^\circ$  and a rapid quench [Beale, *et al.* (1985)].

Two luminescent peaks are observed from Si-S, one broad peak at a wavelength of 1.32  $\mu\text{m}$  and one sharp peak near 1.50  $\mu\text{m}$ . However, those emissions exits only at low temperature below 170K and have a quantum efficiency of 2% to 5%. Another example of luminescence through isoelectronic centers in silicon is the Be doped silicon, with a cluster of peaks near 1.15  $\mu\text{m}$  from the BE-Be pair at temperature below 60K [Henry, *et al.* (1981)].

Luminescence through isoelectronic traps in silicon exhibits several common characteristics. These include [Iyer and Xie (1993)]: (1) it is extremely weak at room temperature and the luminescence intensity together with the quantum efficiency increase with decreasing temperatures as the result of reduced nonradiative recombination rates at low temperatures, among other reasons; (2) the quantum efficiency is a few percent at low temperatures; and (3) the radiative process is vulnerable to the competing nonradiative recombination due to the long spontaneous emission lifetime (milliseconds).

Rare-earth erbium ( $\text{Er}^{3+}$ ), once embedded in an appropriate electrical field such as the field generated by silicon crystal, can provide luminescence in the near infrared (1.54  $\mu\text{m}$ ). The fundamental mechanism of luminescence in rare-earth doped silicon is totally different from that of the isoelectronic traps. The characteristic feature of the Er-doped silicon is that the photon emission comes from an internal transition of the  $4f$  states of  $\text{Er}^{3+}$  [Hüfner (1978)], analogous to emission from a plasma. The  $4f$  to  $4f$  transitions is forbidden in the case of free  $\text{Er}^{3+}$  by the parity selection rule and is made possible for  $\text{Er}^{3+}$  in silicon by the crystal field. The emission at 1.54  $\mu\text{m}$  is very useful and important for optical communication because it matches to the low-loss region of silica-based optical fibers.

Ultimately, for optoelectronic applications, efficient electroluminescence (EL) at room temperature is the goal of the game. EL from Er-doped silicon has been demonstrated [Foll (1991)], although the quantum efficiency and the overall photon intensity needs to be improved. One of the limiting factors of low photon output from Er-doped silicon is the low solid solubility of Er in silicon, only  $\sim 10^{18}$  ions/ $\text{cm}^3$ . Along with the low solid solubility, the long spontaneous emission lifetime and small interaction cross section are serious hurdles for the use of Er-doped silicon in optoelectronic applications [Efimov and Erusalimchik (1963)].

The mechanisms for achieving radiative emission in silicon at energies differ from its bandgap, through incorporation of rare-earth impurities and isoelectronic centers, are fundamentally different. However, there are three most important common features as summarized by Iyer and Xie [Iyer and Xie (1993)].

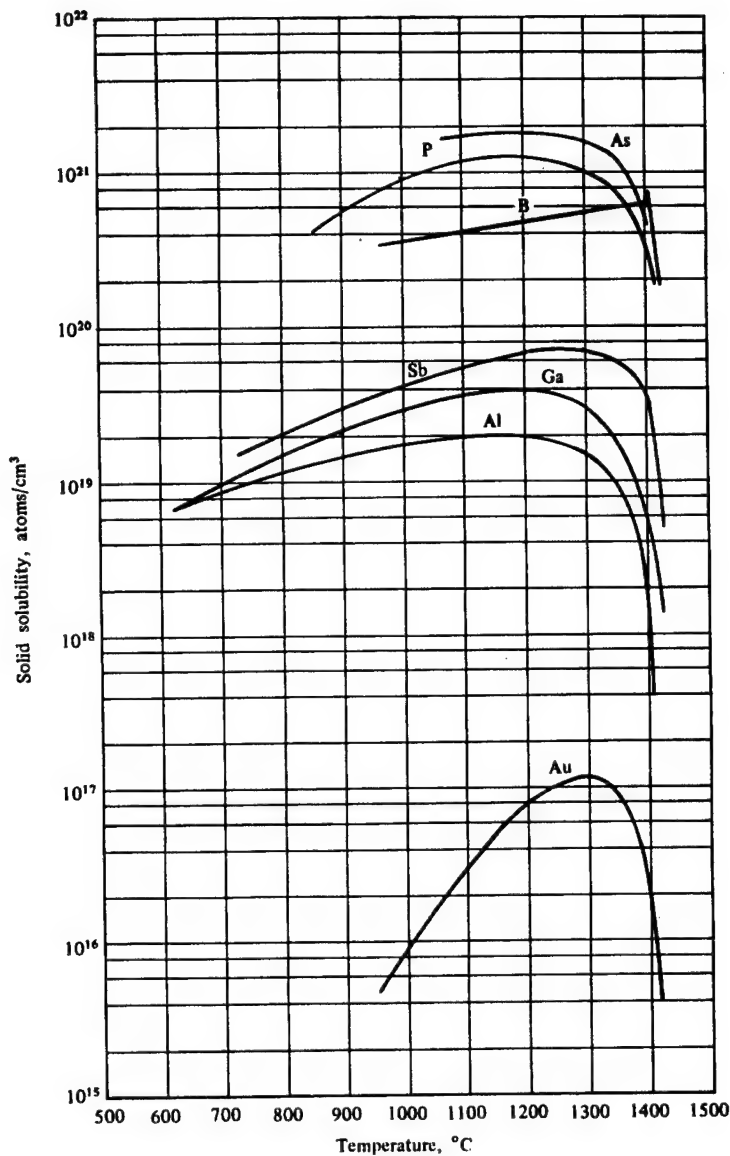


**FIGURE 2.3.1** Solid solubility of dopants in silicon (after [Gise and Blanchard (1979)]).

(1) Charge carrier localization due to the short-range potential associated with the radiative elements in Si enhances the zero-phonon transition probability for the injected electron-hole pairs. However the enhancement is generally moderate, leading the radiative recombination process vulnerable to nonradiative shunt paths from unwanted but ever-present deep-level defects. As a result, luminescence with acceptable quantum efficiency may only be obtained at low temperatures. To date, no radiative emission through impurity doping in silicon can reach a quantum efficiency at 300°K close to that of GaP-N (~0.1%) [Wight (1977)], which is one of the materials for commercial light-emitting diodes.

(2) The total amount of dopant incorporated into silicon via thermal diffusion or ion implantation is limited by the solid solubility  $C_s$ . The solubility  $C_s$  is a temperature-dependent parameter with a relatively known saturation value. Figure 2.3.1 plots the solubility  $C_s$  of certain common impurities as a function of temperature. [Gise and Blanchard (1979)]. For Er, the solid solubility in silicon is about  $10^{18}$  ions/cm<sup>3</sup>. As the result of solid solubility limitation the maximum

concentration of active impurity is also limited, therefore, this results in the saturation of the output optical intensity with pumping intensity.

(3) Questions remain as to the complete understanding of luminescence mechanisms for isoelectronic centers and Si-Er. For the case of isoelectronic centers, the details of the microstructures of the impurity complex and their associated short-range potential is still in question. In the case of Si-Er, the excitation mechanism is still under continuing investigation.

### 2.3.2 Band Structure Engineering

Semiconductor band structures can be changed significantly by alloying and quantum confinement effects in low-dimensional structures. For example, achievement in  $\text{Si}_{1-x}\text{Ge}_x$  alloys has produced remarkable results. Si/Ge strained layer superlattices (SLS) composed of alternating layers of silicon and germanium of only a few atomic monolayers (ML; 1 ML = 1.4 Å on  $\langle 100 \rangle$  Si) thick are both of fundamental and practical importance. This has been made possible by the highly developed molecular beam epitaxy (MBE) technique which allows the growth of ultrathin  $\text{Si}_m\text{Ge}_n$  superlattices on an either silicon or germanium substrate. When such superlattices consist of only a few monolayers of Si and Ge (m ML Si, n ML Ge and  $m+n \leq 40$ ) stacked on top of each other, they offer the opportunity to change the fundamental optical properties of silicon such as to convert the indirect bandgap of the silicon band structure to a direct bandgap via the so-called Brillouin zone (BZ) folding [Presting, *et al.* (1992)].

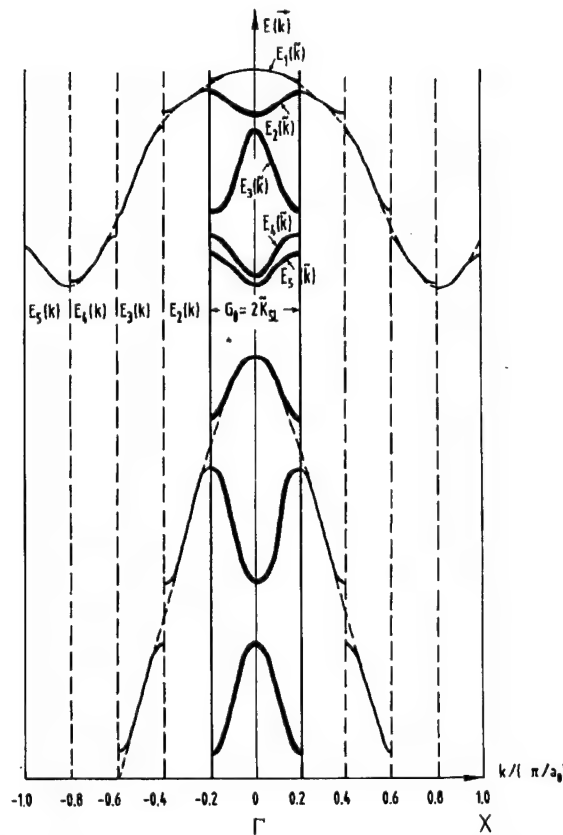


**FIGURE 2.3.2** Brillouin zone folding of a Si-like band structure introduced by a superlattice with a period of  $L = 5a$  (after [Presting, *et al.* (1992)]).

As early as 1974 Gnulzmann and Clausecker predicted that the folding of Brillouin zone could change the indirect characteristic of Si band structure [Gnulzmann and Clausecker (1974)]. The folding of Brillouin zone of superlattice is a direct consequence of the super-period imposed on the lattice of the host crystal and can be easily explained with reference to Fig. 2.3.2, which depicts the zone folding for a superlattice with a period length of  $L = 5a$  ( $a = 5.431 \text{ \AA}$ , bulk lattice constant of silicon). For an appropriate choice of the period length  $L$  the minimum of the conduction band in the  $\Delta$ -direction at  $k_z \sim (\pi/a)(0, 0, 0.8)$  [Froyen, *et al.* (1987)] folds back into the center of the BZ ( $k = 0$ ) as shown in the picture. This zone-folded band structure is commonly referred as quasi-direct because the conduction minimum is folded back to the center and a vertical transition can take place.

### 2.3.3 Quantum Confinement Approaches

Along with alloying and zone folding the use of quantum confinement effect in thin wires and small dots provides another way of engineering to achieve direct transition in silicon and germanium. Similar to a particle in a potential box the values of allowed energy level of free carriers in a semiconductor wire (or dot) increase as its physical size shrinks. As a result, the bandgap of a semiconductor that is a quantum wire or dot increases. Qualitatively, the physical confinement of the carriers in real space causes their wave functions to spread out in momentum space because of the uncertainty principle, which increase the probability of radiative recombination. In addition, scattering at the wire or dot boundaries, a very likely event, can supply the needed momentum more readily in a confined structure [Iyer and Xie (1993)].

### 2.3.4 Hybrid Approaches

A seemingly straight-forward way to fabricate light emitting devices on a silicon chip is to integrate direct bandgap materials, such as a III-V material GaAs, onto silicon substrate. However this type of integration, as in previously described approaches, is also a challenging task, only with issues fundamentally different. The main objective here is to reduce material defects and hence to increase the device reliability other than to increase the luminescence efficiency and to understand the luminescence mechanism. As in general, the radiative recombination processes in direct bandgap semiconductor is well understood and the luminescence efficiency is relatively high, about tens of percent.

Heteroepitaxy of GaAs on Si [Fischer, *et al.* (1985)] using techniques such molecular beam epitaxy and GaAs epitaxy lift-off [Yablonovitch, *et al.* (1990)] by wet chemical etching and Van der Waals bonding are two of the various approaches developed to integrate device quality GaAs thin films onto Si substrates.

One of the fundamental problems with heteroepitaxy of GaAs on Si is high density defects generation, such as dislocations, due to the large mismatch of lattice constants between GaAs ( $5.65 \text{ \AA}$ ) and Si ( $5.43 \text{ \AA}$ ). It is well known that dislocations can act as fast diffusion paths for impurities [Dash (1956)], short circuits in  $p-n$  junction [Klyatskina, *et al.* (1979)] and origins for the catastrophic breakdown of semiconductor lasers [Petroff and Hartman (1974)]. A variety of methods have been developed to reduce the dislocation density ( $\rho$ ) in the GaAs films on Si, including thermal annealing [Lee, *et al.* (1987)], thermal cycle growth [Shimizu, *et al.* (1986)], the use of strained layer superlattice [Fischer, *et al.* (1986)], and the use of a compositionally graded buffer layer [Fitzgerald, *et al.* (1991)]. By inserting a stained layer superlattice Nozawa and Horikoshi have successfully reduced the dislocation density down to a value of  $2.9 \times 10^4 \text{ cm}^{-2}$  as characterized by etch-pit count [Nozawa and Horikoshi (1991)]. The second problem associated with heteroepitaxy of GaAs on Si comes from the fact that GaAs crystal has two distinguishable elements in the lattice while Si has only element. This is the so-called polar-nonpolar mismatch and

can consequently cause the problems of antiphase boundaries (APBs) [Kroemer (1986)] and interface charge [Harrison, *et al.* (1978)].

In contrast to heteroepitaxy, epitaxial lift-off process utilizes wet etching to etch off the grown GaAs and/or  $Al_xGa_{1-x}As$  thin films and then to bond it onto an arbitrary substrate by the Van der Waals force [Yablonovitch, *et al.* (1990)]. In this approach the only step involving heteroepitaxy is the growth of  $Al_xGa_{1-x}As$ -GaAs ( $x < 0.4$ ) on GaAs substrates with a thin release layer of AlAs ( $\approx 50\text{\AA}$ ), therefore, the problems with heteroepitaxy of GaAs on Si previously discussed do not exist in the epitaxy lift-off approach. The key to success in this technique is the extremely high etching selectivity ( $>10^7$ ) between  $Al_xGa_{1-x}As$  and AlAs in HF acid, which was first observed by Konagi and co-workers in 1978 [Konagai, *et al.* (1978)].

Despite the obstacles encountered in the hybrid approaches discussed above, a variety types of GaAs devices have been successfully fabricated onto silicon substrates. These include transistors [Fischer, *et al.* (1985), Ren, *et al.* (1988), Hoof, *et al.* (1989)], light emitting diodes [Pollandier, *et al.* (1990)] and lasers [Yablonovitch, *et al.* (1989)]. However reliability and manufacturability are still the two major problems to be tackled before the GaAs-Si hybrid devices can be commercialized.

## 2.4 Porous Silicon

Porous silicon is usually obtained by anodic etching of crystalline silicon in hydrofluoric acid (HF) based electrolytes under certain conditions. It was first reported in 1956 by Uhlir in his study of the electrolytic shaping of Ge and Si [Uhlir (1956)]. Uhlir observed the existence of a threshold current density for obtaining smooth etching (polishing) of silicon in HF electrolyte, below which a matte black, brown or red deposit formed in stead of a shiny surface. Turner [Turner (1958)], in 1958, reported a more detailed study of electropolishing of silicon including the effect of HF concentration, viscosity, and temperature on the critical current condition and the nature of thick anode film prior to electropolishing (porous silicon film). Porous silicon can also be formed by pure chemical etching, the so-called stain-etch, of silicon in hydrofluoric and nitric acid (HF-HNO<sub>3</sub>) based solutions. Archer [Archer (1960)], in 1960, reported a detailed study of the properties of stain films (porous silicon) on silicon and of the staining process. Until 1990, researches in porous silicon had been concentrated in areas of formation mechanism, microstructure, oxidation, electrical and optical properties mainly for its potential applications in electrical isolation technology in integrated circuits, particularly in silicon-on-insulator (SOI) devices [Bomchil, *et al.* (1988)]. However, the observation of optical transmission and strong photoluminescence in porous silicon at energies considerably above the band gap of c-Si by Canham [Canham (1990)] and by Lehmann and Gösele [Lehmann and Gosele (1991)] in 1990 has triggered tremendous new interests and research efforts in porous silicon in search of the physical understanding of this newly discovered phenomenon and its potential applications in silicon-based optoelectronic devices. Since 1990, researches in photoluminescent porous silicon has exponentially increased and this trend is going to exist for years to come.

### 2.4.1 Porous Silicon Formation by Anodization

#### A. History Review

In the early days of research, porous silicon was considered to be a layer which was deposited during anodization [Turner (1958), Memming and Schwandt (1966)]. It was confirmed later that porous silicon contains mainly the starting monocrystalline material and is a result of inhomogenous dissolution. Despite the level of interest and effort in the past four decades, the fundamental formation mechanism of porous silicon is still not fully understood. Unagami

[Unagami (1980)] proposed that porous silicon formed as a result of formation of insoluble silicates that passivate the pore walls. Parkhutik and co-workers [Parkhutik, *et al.* (1983)] considered the formation of porous silicon similar in nature to that of porous alumina where a thin oxide layer, acting as an electrical barrier, exists at the bottom of each pore and results in localized electric field enhancement at the pore tips. Similarly, Theunissen and co-workers [Theunissen, *et al.* (1970), Theunissen (1972)] proposed that porous silicon formation in *n*-type silicon is due to reverse bias breakdown because of high fields concentrated at the pore tips. Beale *et al.* [Pickering, *et al.* (1984), Beale, *et al.* (1985), Beale, *et al.* (1985)] extended Theunissen's model into both *n*- and *p*-type silicon materials and implicated the semiconductor depletion layer as the parameter responsible for controlling the electric field density. Presently, the Beale model is the most widely accepted standard for porous silicon formation [Smith and Collins (1992)]. Recently, two other notable models have been proposed to explain porous silicon formation, a diffusion-limited model by Smith *et al* [Smith, *et al.* (1988)] and a quantum confinement model by Lehmann and Gösele [Lehmann and Gosele (1991)] and by Foll [Foll (1991)].

Table 2.4 Summarizes the proposed models for the formation of porous silicon by anodization of crystalline silicon HF based electrolyte.

Table 2.4 Porous silicon formation models by anodization

Mechanism	Reference
Insoluble porous film deposition	Unagami, 1980
Existence of oxide barrier layer	Parkhutik et al, 1983
Local break down of space charge layer	Theunissen, 1972
Depletion layer formation and Fermi level pinning	Beal et al, 1985
Charge exchange	Gaspard et al, 1989
Diffusion-limited model	Smith et al, 1988
Quantum wire effect	Lehmann et al, 1991

#### B. General Current-Voltage Characteristics of Si Anodization Process

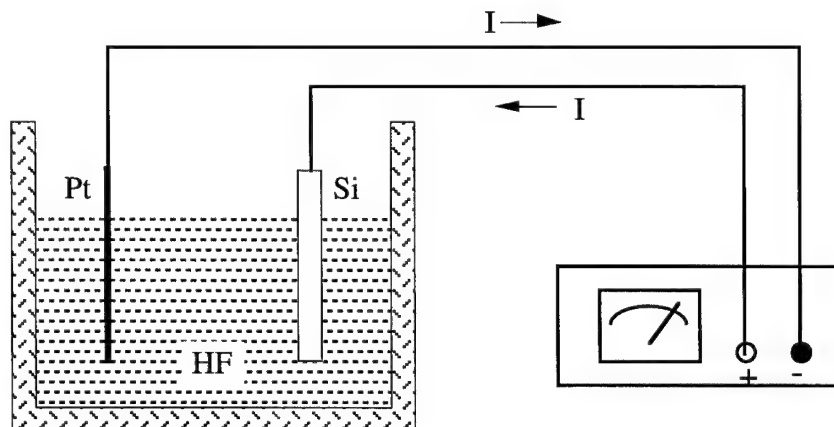
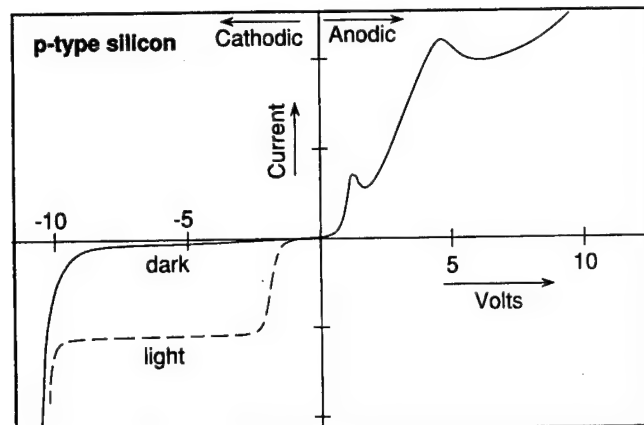


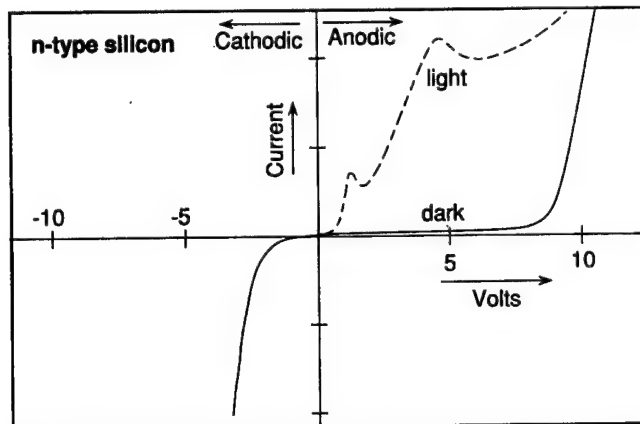
FIGURE 2.4.1 Schematic of an electrochemical cell for silicon anodization.

The basic experimental setup of anodization process of silicon is outlined in Fig 2.4.1. An electrochemical cell for silicon anodization consists of two electrodes immersed in an appropriate electrolyte, e.g. HF mixed with water, with silicon being the anode and a noble metal, usually platinum, being the cathode. Anodization takes place at the interface of electrolyte and anodes as result of current flow from anode to cathode through the electrolyte by applying a voltage across

the two electrodes. In the early days, almost all studies of porous silicon formation have been limited to an electrochemical characterization



(a)



(b)

**FIGURE 2.4.2** "Typical" current-voltage relationships for *n*- and *p*-type silicon. The solid line indicates the dark response and the dashed line shows a response under illumination (after [Smith and Collins (1992)] with original references from [Efimov and Erusalimchik (1963), Zhang, *et al.* (1989), Foll (1991)]).

of its *i*-*V* relationship of the Schottky diode formed at the semiconductor/electrolyte interface. Although additional analysis techniques have been recently employed to study porous silicon, the staple understanding of porous silicon formation comes from the studies of *i*-*V* characteristics. Figure 2.4.2 shows typical *i*-*V* characteristics of a *n*- and *p*-type silicon in HF solution [Efimov and Erusalimchik (1963), Zhang, *et al.* (1989), Foll (1991)].

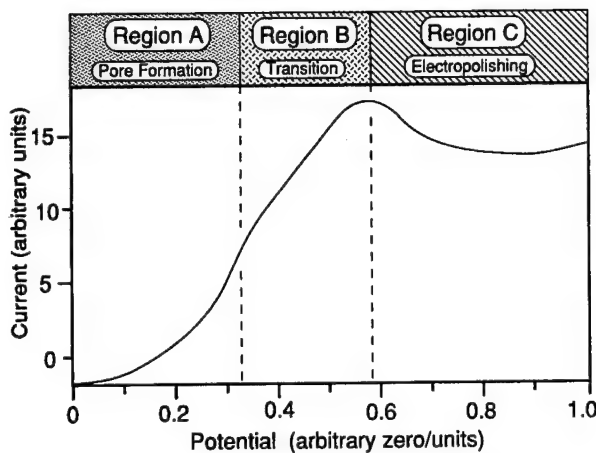
For simplicity, the *i*-*V* curves shown in Fig. 2.4.2 can be divided into four distinct regions depending on the sign of the applied potential and whether *n*- or *p*-type material is used, and Table 2.5 summarizes the salient electrochemical features that are predominant in each region [Smith and Collins (1992)].

Table 2.5. Breakdown of the different electrochemical regions for the Si/HF system summarizing the important features for each region.

Cathodic overpotentials		Anodic overpotentials
<i>p</i> -type Si	No silicon dissolution–Inert $H_2$ gas evolution High hydrogen overpotential Reverse-biased Schottky Photogenerated currents proportional to light intensity	Silicon dissolution –Pore formation at low potentials –Electropolishing at high potentials  Forward-biased Schottky $i$ - $V$ curve exponential Tafel slope $\sim 60$ mV No apparent illumination effects  Two current "peaks" –Lower potential, anodic electropolishing oxide –Oscillations at higher potential "peak"
<i>n</i> -type Si	No silicon dissolution–Inert $H_2$ gas evolution Low hydrogen overpotential Forward-biased Schottky No apparent illumination effects	Silicon dissolution –Pore formation at low potentials –Electropolishing at high potentials  Reverse-biased Schottky High breakdown voltage before significant pore formation Photogenerated currents, function of light intensity and voltage  Single current peak without illumination –Anodic oxide for electropolishing  Second current peak with illumination –Oscillations

When a bias is applied between silicon and cathode in an aqueous electrolyte, charge transfer occurs and a measurable current is induced in the system. However, in order for any current to pass through the silicon/electrolyte interface it must first change from electronic to ionic charge carriers. This charge carriers conversion process is accomplished through a specific chemical redox reaction at the silicon interface. Application of a potential then results in a precise interfacial reaction, which in turn is fundamental to the formation of porous silicon [Smith and Collins (1992)]. When a negative potential is applied to silicon (for both *n*- and *p*-type) the system is under reverse bias (cathodic polarization), no silicon dissolution occurs and silicon is stable. The current  $i$  under reverse bias is very small, as shown in Fig. 2.4.2, except when the bias reaches break-down voltage. For *p*-type materials at reverse breakdown, hydrogen gas liberation occurs due to the reduction of water, which is the only important cathodic charge transfer reaction in the silicon/HF system under cathodic polarization. Only under forward bias (anodic polarization) silicon dissolution can happen. However, drastically divergent surface morphologies can occur as a result of the magnitude of the bias. Above certain anodic overpotentials, the silicon surface electropolishes and the surface retains a relative smooth and planar morphology. In the contrast at low anodic overpotentials, a vast labyrinth of channels dominate the surface morphology and that can penetrate deep into the bulk of the silicon resulting the so-called "porous silicon". The size, shape, and the density of the channels are determined by the exact conditions of the anodization process, including such as HF concentration, temperatures, silicon type, dopant concentration, anodization time, etc. [Smith and Collins (1992)].

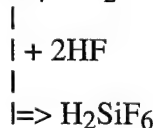
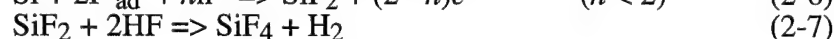
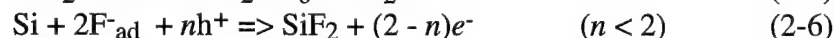
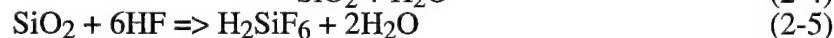
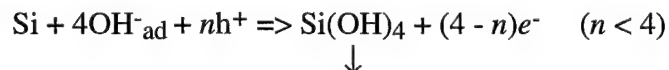
Figure 2.4.3 shows the anodic dissolution portion of a "typical" silicon *i*-*V* curve [Zhang, *et al.* (1989)] where three different regions are labeled A-C [Smith and Collins (1992)]. In region A pore formation occurs and in region C silicon electropolishes. Region B is a transition zone between porous silicon formation and silicon electropolishing.



**FIGURE 2.4.3** Typical anodic *i*-*V* relationship for silicon anodization in HF showing three different regions (after [Smith and Collins (1992)]).

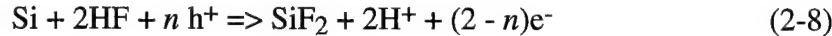
### C. Surface Dissolution Chemistries

The process of silicon dissolution in an aqueous hydrofluoric acid electrolyte involves two steps, silicon dioxide formation through electrochemical and chemical oxidation of silicon and the subsequent removal of silicon dioxide by forming silicon tetrafluoride through reaction with HF. The following reactions are considered possible [Memming and Schwandt (1966)],



where  $\text{OH}^-_{\text{ad}}$  and  $\text{F}^-_{\text{ad}}$  are the absorbed ions;  $h^+$  and  $e^-$  represent hole and electron respectively. Reaction (2-4) leads to oxidation of silicon. Reaction (2-6) leads to direct dissolution of silicon. The participation of hole and electron in these reactions depends on the doping type and concentration of silicon. In the case of *n*-type silicon, the absence of holes can be compensated by external illumination with UV or visible light. In non-HF containing solution, formation of a silicon dioxide film will result in a complete passivation of silicon surface. However, in HF solution, silicon dioxide is not stable and will be dissolved by HF according to reaction (2-5) [Tenney and Ghezzo (1973)]. In reaction (2-4) and reaction (2-6) charge transfer of four and two electrons occurs respectively, while no charge is involved in reaction (2-5) and reaction (2-7). These reactions are considered to proceed simultaneously on the silicon surface and compete with

each other in rate and coverage of the surface area. An overall electrochemical reaction of silicon in HF-based solution can be written as



#### D. Porous Silicon Formation Mechanism

There are two important and different issues regarding to the mechanism of porous silicon formation. The first issue is related to the initial stage of process: how the formation of porous silicon starts and why. The second issues is related to the progression of the process and the morphology of the porous silicon formed. Most of the studies done so far have been concentrated primarily on the second question. In general, it is widely agreed that the formation of porous silicon by electrochemical etching in HF-based solution is a result of inhomogeneous dissolution of silicon.

The formation of porous structures, as suggested by some authors [Beale, *et al.* (1985), Beale, *et al.* (1985), Zhang, *et al.* (1989)], is attributed to the inhomogenous distribution of various reaction rates at silicon surface. When the anodic potential is low, the limiting step is the rate of electrochemical oxidation at the silicon-electrolyte interface which is controlled by charge transfer at the interface and is low compared to the rate of oxide dissolution by HF. Therefore no oxide film can be formed. At the same time different reactions, as summarized in equations (2-4 to 7), proceed simultaneously at all possible sites on the silicon surface at their own pace. Since the rate is different for each reaction at a given potential, the sites where slower reaction proceeds will be dissolved slower as if they were passivated compared to the sites where quicker reaction proceeds [Zhang, *et al.* (1989)]. Porous silicon formation results from such inhomogeneous dissolution of the silicon surface. However, the underline mechanism which determines the initial inhomogeneous distribution of such sites with different reaction rates is less investigated and remains an open question. Once a thin layer of porous silicon is formed, the process will continue to be porous structure formation as long as the critical condition, i.e. the potential is below the critical point, is fulfilled and pores will grow and propagate in the direction of current flow. The critical condition can also be expressed in current density  $J_{ps}$  which is given the following equation [Lehmann (1992)]:

$$J_{ps} = Ae^{(-E_a/kT)}C^{3/2} \quad (2-9)$$

where:  $J_{ps}$  is current density in  $\text{A}/\text{cm}^2$ ,  $c$  is HF concentration in wt.%,  $T$  is temperature in K,  $E_a = 0.345 \text{ eV}$ ,  $k = 8.6171 \times 10^{-5} \text{ eV/K}$  and  $A = 3300 \times (\text{wt. \% HF})^{-3/2} \text{ A}/\text{cm}^2$ .

A surface area which is depleted of holes is passivated and silicon dissolution is stopped. Continuous silicon dissolution will only occur at areas where holes are available for electrochemical reaction. Many authors found the interface between porous silicon and the bulk silicon to be depleted of holes during porous silicon formation [Beale, *et al.* (1985), Gaspard, *et al.* (1989), Zhang, *et al.* (1989)]. It was widely suggested that the basic conditions for electrochemical pore formation and pore propagation are a passive state of the pore walls and an active state, which promotes further dissolution, at the pore tip. The propagation of pores in the direction of current flow due to continuous dissolution of pore tip can be explained in terms of field enhancement at pore tip resulting in a localized charge (hole or electron) transfer through tunneling mechanism [Beale, *et al.* (1985)].

There are two different mechanisms responsible for the holes depletion at the silicon surface:

(1) A space charge region forms as the result of a potential barrier, which is a Schottky barrier, between the semiconductor surface and the electrolyte when a semiconductor electrode is in contact with an electrolyte [Beale, *et al.* (1985), Gaspard, *et al.* (1989), Zhang, *et al.* (1989)]. Under anodic bias this layer is thick (several  $\mu\text{m}$ ) for low doped *n*-type, is thin for lightly doped *p*- or *n*-type and does not exist for *p*-type silicon [Lehmann and Gösele (1993)]. Pores formed in this case will have sizes resemble to the depletion region width and are designated as macro- or meso-porous according to sizes.

(2) A depletion of holes is also expected as the result of quantum confinement if the dimensions of a semiconductor particle, wire or sheet is below the Bohr radius of an exciton (a few nm). In this case there is no dependence of the depletion layer thickness on the doping concentration of the semiconductor and these small pores are designated as microporous [Lehmann and Gösele (1993)].

Both mechanisms (1) and (2) are independent of each other and therefore are usually coexist, resulting in a superposition of microporous, and meso- or macro-porous silicon structures. Figure 2.4.4 summarizes the kind of porous structures formed under given conditions [Lehmann and Gösele (1993)].

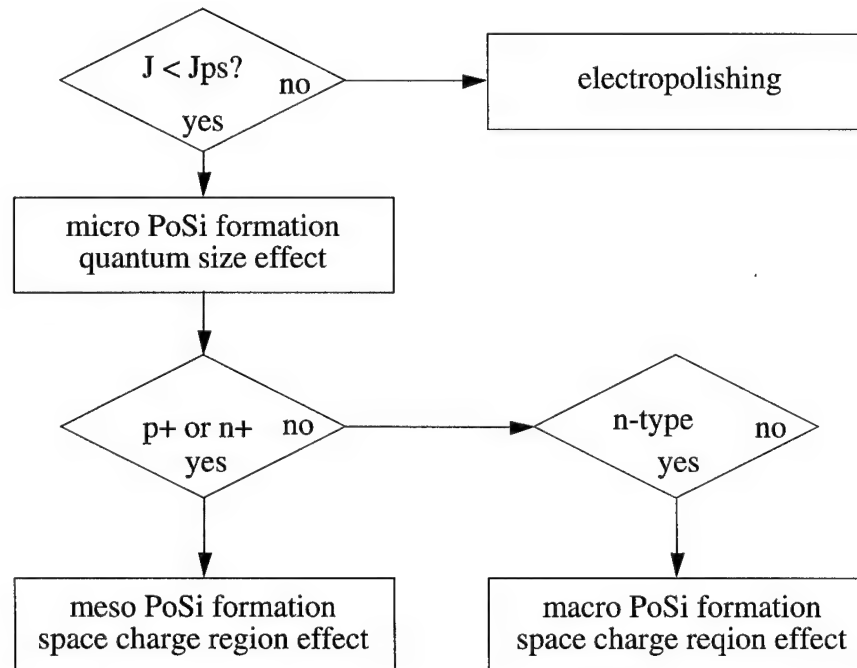


**FIGURE 2.4.4** Porous silicon formed under different conditions (after [Lehmann and Gösele (1993)]).

## 2.4.2 Porous Silicon Formation by Stain-Etch

Stain films on silicon obtained by immersion in HF:HNO<sub>3</sub>-based solutions has been known for over 30 years [Turner (1958), Archer (1960)], and have been suggested [Archer (1960)] to be similar in nature to the anodically-etched porous silicon films first observed by Uhlir [Uhlir (1956)]. More recently, in addition to HNO<sub>3</sub>, NaNO<sub>2</sub> in HF and CrO<sub>3</sub> in HF were utilized as the oxidation agent to produce Si stain films and it was demonstrated that the stain films produced were similar in structure to that of porous silicon produced by anodic etching [Beale, *et al.* (1986)]. After Canham [Canham (1990)] reported the first observation of strong visible photoluminescence from anodized porous silicon film at room temperature, porous silicon films

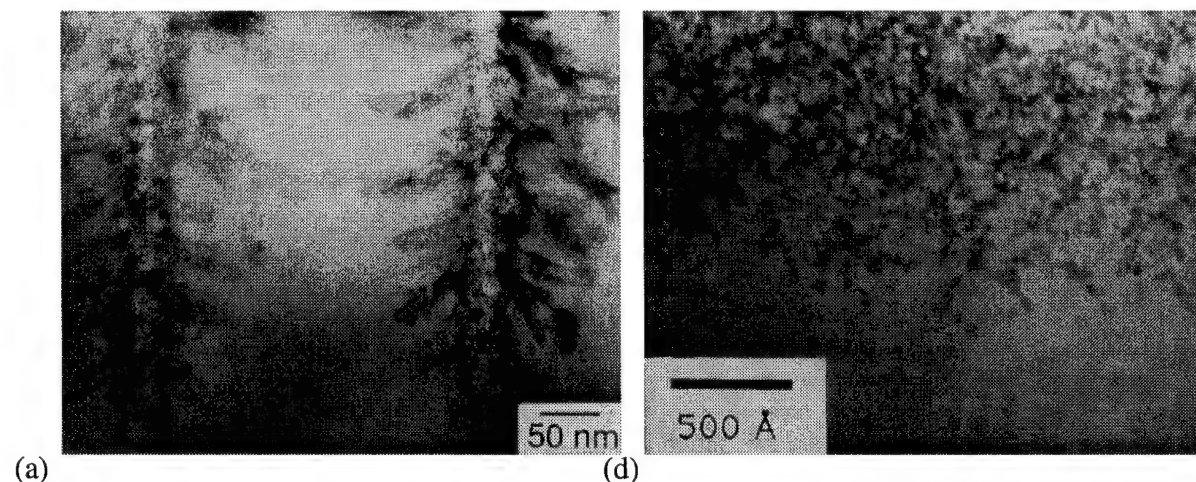
produced by stain-etching have been shown to exhibit similar photoluminescence [Fathauer, *et al.* (1992), Kidder, *et al.* (1992), Sarathy, *et al.* (1992), Aoyagi, *et al.* (1993)]. The most commonly used stain-etch solutions, which produce luminescent porous silicon films, are mixtures of HF:HNO<sub>3</sub>:H<sub>2</sub>O with a variety compositions and mixture of NaNO<sub>2</sub>:HF [Fathauer, *et al.* (1992)]. Stain films obtained from immersion in CrO<sub>3</sub>:HF were found non-luminescent [Fathauer, *et al.* (1992)].

As discussed by Beale *et al.* [Beale, *et al.* (1986)] that the similarity between the anodically and chemically formed films suggests that their formation processes are similar. The main difference is that during stain film formation, the current is driven by reduction of the oxidizing species present in the etchant rather than by the application of a potential to external electrodes. Stain-etching of silicon can be considered as localized electrochemical process. Microscopically, local anode and local cathode sites form on the etched surface with local cell currents flowing between the sites during the etch. The local anode and local cathode sites are not necessarily fixed during the etching process. Unlike porous silicon fabricated by conventional anodization techniques, the chemically etched porous silicon film thickness is self-limited [Beale, *et al.* (1986)].

## 2.5 Properties of Porous Silicon

### 2.5.1 Morphology and Microstructure of Porous Silicon

Porous silicon has a variety of different morphologies. The morphology is determined primarily by the dopant concentration in the silicon and, to a lesser extent, by the etching condition for both anodized [Beale, *et al.* (1986), Searson, *et al.* (1992)] and stain-etched porous silicon. Figure 2.5.1(a) through (h) attempts to illustrate this variety of morphologies by a select sampling of transmission electron microscopy (TEM) and secondary electron microscopy (SEM) micrographs of porous silicon obtained by anodizing silicon of both *n*- and *p*-types with various doping concentrations in HF under different conditions [Smith and Collins (1992)]. Although the appearance of the porous silicon samples may differ, the recurrent motif is the formation of vast labyrinth of permeating pores [Smith and Collins (1992)].



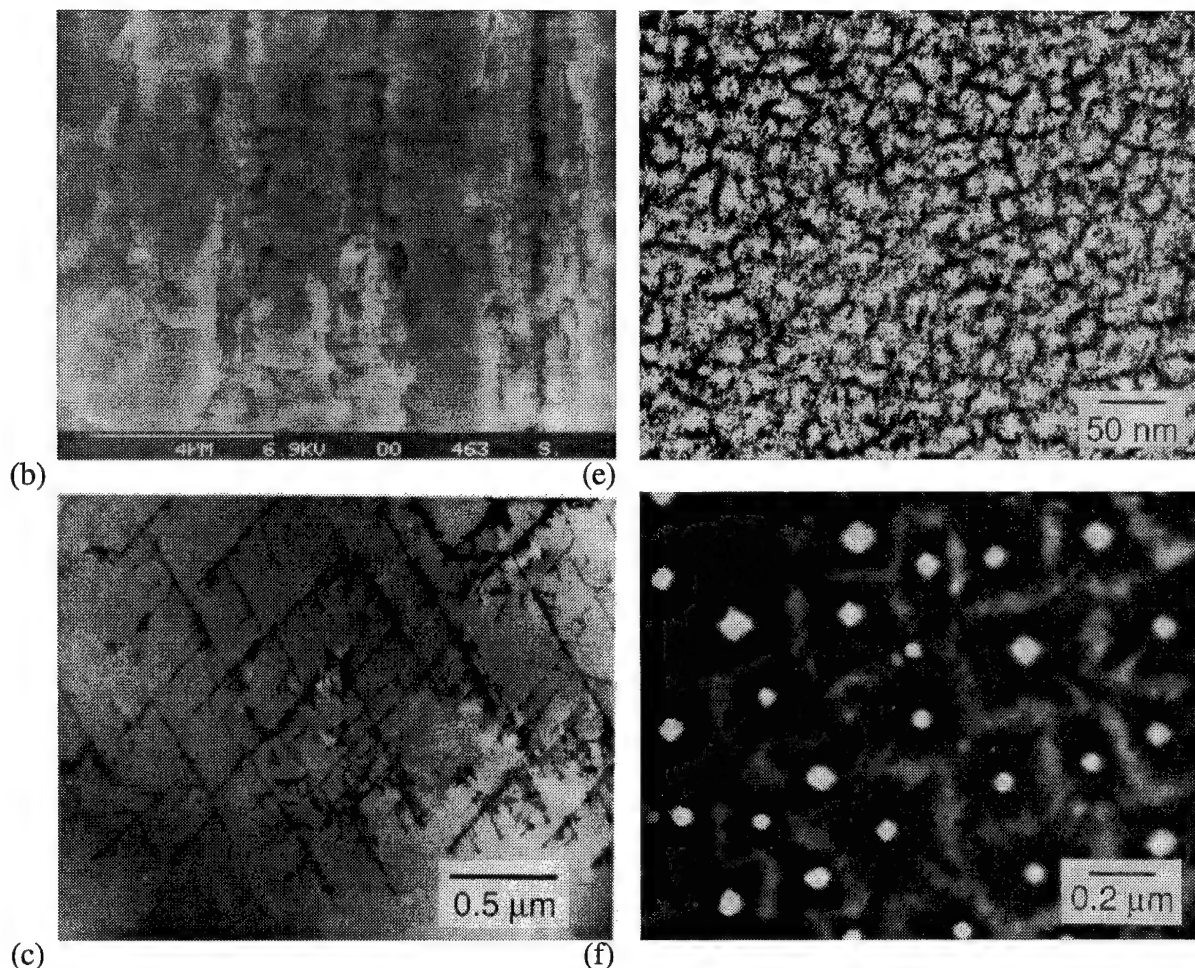


**FIGURE 2.5.1** A select sampling of porous silicon samples showing the distinctive pore morphologies. Except for (e) & (f), the direction of current for all samples is from bottom to top. (a) Two pore tips with numerous side branches. Cross-section transmission electron microscopy (XTEM) of (100), arsenic-doped, 0.09  $\Omega$ -cm silicon anodized in 10% HF at 10 mA/cm $^2$ . (b) Large channel formation. SEM of (100), phosphorous-doped, 5  $\Omega$ -cm silicon anodized in 49% HF at 100 $^+$  mA/cm $^2$  with ambient illumination. (c) Preferential crystallographic pore propagation at the pore tips. XTEM of (110), phosphorus-doped, 0.82  $\Omega$ -cm silicon anodized in 49% HF at 80 mA/cm $^2$ . (d) Preferential crystallographic pore propagation at the pore tips. XTEM of (110), boron-doped, 0.01  $\Omega$ -cm silicon anodized in 49% HF at 2 mA/cm $^2$ . (e) Plan view of pore structure in *p*-type silicon. Boron-doped, 0.01  $\Omega$ -cm, and anodized in 10% HF at 10 mA/cm $^2$ . (f) Plan view of pore structure in *n*-type silicon near the silicon/HF surface. Notice the tendency to form square pores with distinct pore branching domains. Arsenic-doped, (100), 0.09  $\Omega$ -cm silicon anodized in 10% HF at 10 mA/cm $^2$  (after [Smith and Collins (1992)]).

As summarized by Smith and Collins in their recent review article on the porous silicon formation mechanisms [Smith and Collins (1992)], porous silicon morphologies are usually grouped into four basic groups, primarily determined by the substrate dopant concentrations and types, *n*, *p*, *n* $^+$ , and *p* $^+$ . Figure 2.5.2, after [Smith and Collins (1992)], shows representative samples from each group. For *p*-type silicon both the pore diameters and interpore spacing are extremely small, generally between 1 and 5 nm, with a highly interconnected and homogeneous pore network as shown in Fig. 2.5.2(a). As the dopant concentration increases slightly, the pore diameters and interpore spacings also increase slightly, resulting in a clear channel formation for *p* $^+$  materials as indicated in Fig. 2.5.2(c). For the case of *n*-type silicon the effect of dopant concentration is complicated by the so-called "piping" phenomenon [Smith and Collins (1992)].

However, generally, both the pore diameter and average interpore spacing decrease with increasing dopant concentration as shown in Fig. 2.5.2(b) and (d). The pore diameters in *n*-type silicon are considerably larger than that in *p*-type silicon and show a strong tendency to form straight channels at low doping concentrations, as shown in Fig. 2.5.1 and 2.5.2(b), rather than the randomly directed pore network of *p*-type silicon [Smith and Collins (1992)].

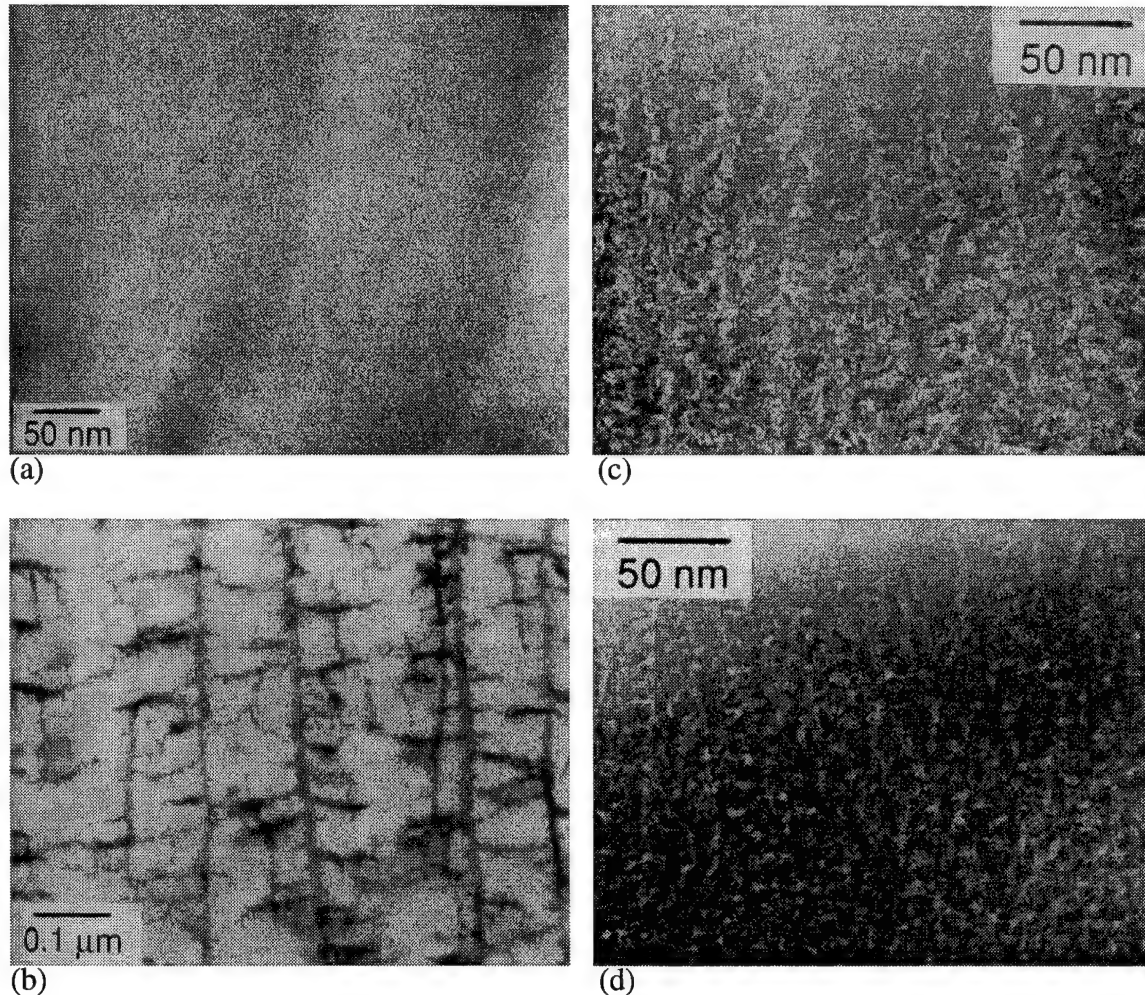


**FIGURE 2.5.2** XTEM micrographs showing the basic differences in the morphology among *n*, *p*, *n*<sup>+</sup>, and *p*<sup>+</sup> samples. (a) *p*-type silicon. Pore diameters are extremely small and highly interconnected. (b) *n*-type silicon. Strong tendency to form straight channels. (c) *p*<sup>+</sup>-type silicon. Tendency to form small 5-10 nm channels with numerous, "budding," side branches. (d) *n*<sup>+</sup>-type silicon. Virtually identical with *p*<sup>+</sup>-type silicon. The current direction for all samples is from bottom to top and the anodization conditions are 49% HF at 10 mA/cm<sup>2</sup> (after [Smith and Collins (1992)]).

As mentioned above, Beale *et al.* first reported the observation of similarity of the morphology between anodized and stain-etched silicon [Beale, *et al.* (1986)]. Figure 2.5.3 shows a XTEM micrograph of stain film formed by chromium trioxide and hydrofluoric acid etching of 0.01 Ω-cm *p*-type silicon [Beale, *et al.* (1986)]. It is very clear from the picture that the pore morphology, pore diameter and interpore spacing of this stain-etched silicon is almost identical to that of anodized *p*<sup>+</sup>-type silicon shown in Fig. 2.5.2(c).

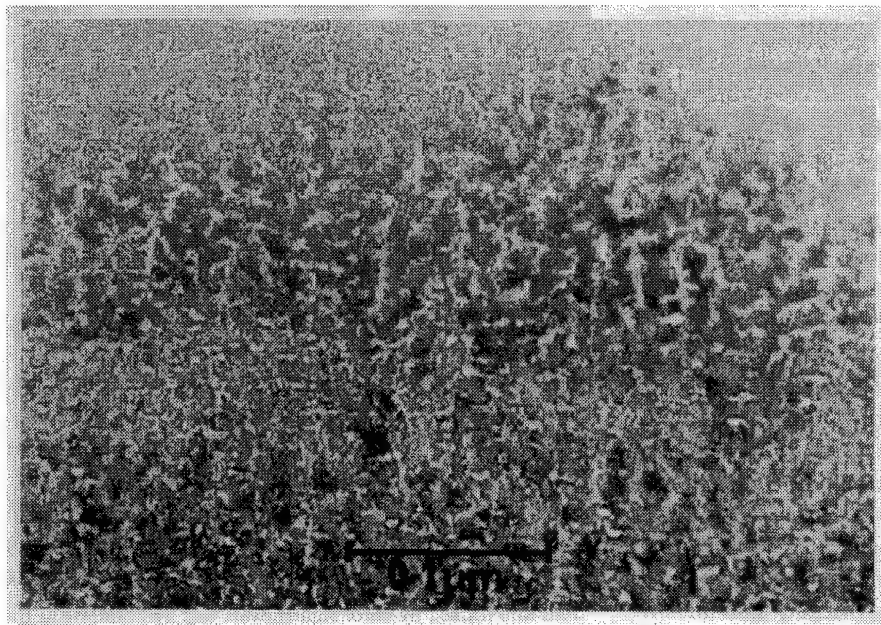


**FIGURE 2.5.3** XTEM of stain film formed by chromium trioxide and hydrofluoric acid on 0.01  $\Omega\text{-cm}$  *p*-type silicon. Image shows the structure of individual pores. The sample surface is uppermost. (after [Beale, *et al.* (1986)]).

## 2.5.2 Luminescence of Porous Silicon

Since the observation of room temperature visible photoluminescence from porous silicon, a wealth of literature has already been published in searching of the underlying mechanism or mechanisms of this interesting phenomenon. A very good review article by Jung and co-workers [Jung, *et al.* (1993)] published recently detailed the proposed luminescence mechanisms of luminescent porous silicon. Table 2.6 summarizes the evidence and issues for the basic mechanisms which have been frequently reported and discussed in recent literature [Jung, *et al.* (1993)]. However, despite the significant achievements made in light emitting porous silicon, the search for fundamental luminescence mechanism continues.

Table 2.6 Summary of proposed porous silicon luminescence mechanism

Mechanism	Evidence	Issues under debate
Quantum confinement in c-Si	Quantum sizes observed by Raman and TEM PL blue shifts with processing designed to reduce feature sizes μc-Si known to luminesce	Lack of depth/spatial information in TEM evidence PL blue shift does not always happen μPL and XTEM show light emitting areas are amorphous
Surface passivation	SiH <sub>2</sub> desorption/passivation parallels PL decay/recovery SiH passivation kills PL	SiH <sub>2</sub> and PL signal changes do not perfectly coincide Changes in dangling bond density
Si-H <sub>x</sub> alloys	Significant amorphous phases observed by micro-Raman, TEM, XPS, and XRD Similar to PL from a-SiH SiH <sub>x</sub> observed in porous Si	Amorphization due to TEM preparation Porous Si can luminesce without H No PL observed from porous Si made from a-Si
Molecular electronics	Numerous strong parallels between PL from siloxene and porous Si	Annealing porous Si at 400°C kills PL, siloxene still luminesce Porous Si can luminesce without H

## REFERENCES

Aoyagi, H., Motohashi, A., Kinoshita, A., Aono, T. and Satou, A., "A comparative study of visible photoluminescence from anodized and from chemically stained silicon wafers", Jpn. J. Appl. Phys. **32**, L1 (1993).

Archer, R. J., "Stain films on silicon", J. Phys. Chem. Solids **14**, 104 (1960).

Beale, M. I. J., Benjamin, J. D., Uren, M. J., Chew, N. G. and Cullis, A. G., "An experimental and theoretical study of the formation and microstructures of porous silicon", J. Crys. Grow. **73**, 622 (1985).

Beale, M. I. J., Benjamin, J. D., Uren, M. J., Chew, N. G. and Cullis, A. G., "The formation of porous silicon by chemical stain etches", J. Crys. Grow. **75**, 408 (1986).

Beale, M. I. J., Uren, M. J., Chew, N. G., Cullis, A. G. and Benjamin, J. D., "Microstructure and formation mechanism of porous silicon", Appl. Phys. Lett. **46**, 86 (1985).

Bomchil, G., Halimaoui, A. and Herino, R., "Porous silicon: the material and its applications to SOI technologies", Microelectronics Engineering **8**, 293 (1988).

Canham, L., "Progress toward crystalline-silicon-based light emitting diodes", MRS Bulletin/July , 22 (1993).

Canham, L., "Silicon quantum wire array fabrication by electrochemical and chemical dissolution of wafers", *Appl. Phys. Lett.* **57**, 1046 (1990).

Cohen, M. L. and Bergstresser, T. L., "Band structures and pseudopotential form factors for fourteen semiconductors of the diamond and zinc-blend structures", *Phys. Rev.* **141**, 789 (1966).

Dash, W. C., "Copper precipitation on dislocations in silicon", *J. Appl. Phys.* **27**, 1193 (1956).

Efimov, E. A. and Erusalimchik, I. G., "Electrochemistry of Germanium and Silicon", (Sigma, London, 1963).

Ennen, H., Schneider, J., Pomerenke, G. and Axmann, A., "1.54- $\mu$ m luminescence of erbium-implanted III-V semiconductors and silicon", *Appl. Phys. Lett.* **43**, 943 (1983).

Fathauer, R. W., George, T., Ksendzov, A. and Vasquez, R. P., "Visible luminescence from silicon wafers subjected to stain etches", *Appl. Phys. Lett.* **60**, 996 (1992).

Faulkner, R. A., "Toward a theory of isoelectronic impurities in semiconductors", *Phys. Rev.* **175**, 991 (1968).

Fischer, R., Chand, N., Kopp, W., Morkoc, H., Erikson, L. P. and Youngman, R., "GaAs bipolar transistors grown on (100) Si substrates by molecular beam epitaxy", *Appl. Phys. Lett.* **47**, 397 (1985).

Fischer, R., Neuman, D., Zabel, H., Morkoc, H., Choi, C. and Otsuka, N., "Dislocation reduction in epitaxial GaAs on Si (100)", *Appl. Phys. Lett.* **48**, 1223 (1986).

Fitzgerald, E. A., Xie, Y.-M. and Green, M. L., "Totally relaxed GexSil-xlayers with low threading dislocation densities grown on si substrates", *Appl. Phys. Lett.* **59**, 811 (1991).

Foll, H., "Properties of silicon electrolyte junctions and their application to silicon characterization", *Appl. Phys. A* **53**, 8 (1991).

Froyen, S., Wood, D. M. and Zunger, A., "New optical transitions in strained Si-Ge superlattices", *Phys. Rev. B* **36**, 4547 (1987).

Gaspard, F., Bsiey, A., Ligeon, M., Muller, F. and Herino, R., "Charge Exchange Mechanism Responsible for P-Type Silicon Dissolution during Porous Silicon Formation", *J. Electrochem. Soc.* **136**, 3043 (1989).

Gise, P. E. and Blanchard, R., "Semiconductor and integrated circuit fabrication techniques", (Reston Publishing Company, Reston, VA, 1979).

Gnulzmann, U. and Clausecker, K., *Appl. Phys.* **3**, 9 (1974).

Harrison, W. A., Kraut, E. A., Waldrop, J. R. and Grant, R. W., "Polar heterojunction interfaces", *Phys. Rev. B* **18**, 4402 (1978).

Haynes, J. R. and Westphal, W. C., "Radiation resulting from recombination of holes and electrons in silicon", *Phys. Rev.* **101**, 1676 (1956).

Henry, M. O., Lightowers, E. C., Killoran, N., Dunstan, D. J. and Caventt, B. C., *J. Phys. C* **14**, L225 (1981).

Hoof, C. V., Raedt, W. D., Rossum, M. V. and Borghs, G., "MESFET lift-off from GaAs substrate to glass host", *Electron. Lett.* **25**, 136 (1989).

Hüfner, S., "Optical spectra of transparent rare-earth compounds", (Academic Press, New York, 1978).

Iyer, S. S. and Xie, Y.-H., "Light emission from silicon", *Science* **260**, 40 (1993).

Jung, K. H., Shih, S. and Kwong, D. L., "Developments in luminescent porous Si", *J. Electroch. Soc.* **140**, 3046 (1993).

Kidder, J. N., Williams, J., P. S., Pearsall, T. P., Schwartz, D. T. and Nosh, B. Z., "Comparison of light emission from stain-etch and anodic-etch silicon films", *Appl. Phys. Lett.* **61**, 2896 (1992).

Klyatskina, I. V., Kozhukh, M. L., Ryvkin, S. M., Trunov, V. A. and Shlimak, I. S., *Sov. Phys. Semicon.* **13**, 638 (1979).

Konagai, M., Sugimoto, M. and Takahashi, K., "High efficiency GaAs thin film solar cells by peeled film technology", *J. Cryst. Growth* **45**, 277 (1978).

Kroemer, H., Mater. Res. Soc. Symp. Proc. **67**, 3 (1986).

Lee, J. W., Shichijo, H., Tsai, H. L. and Matyi, R. J., *Appl. Phys. Lett.* **50**, 31 (1987).

Lehmann, V., "Research news: In microporous silicon...", *Adv. Mater.* **4**, 762 (1992).

Lehmann, V. and Gosele, U., "Porous silicon formation: A quantum wire effect", *Appl. Phys. Lett.* **58**, 856 (1991).

Lehmann, V. and Gosele, U., "Formation mechanism of microporous silicon: predictions and experimental results", *Mat. Res. Soc. Symp. Proc.* **283**, 27-32 (1993).

Macfarlane, G. G., McLean, T. P., Quarrington, J. E. and Roberts, V., "Exciton and phonon effects in the absorption spectra of germanium and silicon", *J. Phys. Chem. Solids* **8**, 388 (1959).

Macfarlane, G. G., McLean, T. P., Quarrington, J. E. and Roberts, V., "Fine structure in the absorption-edge spectrum of Si", *Phys. Rev.* **111**, 1245 (1958).

Memming, R. and Schwandt, G., "Anodic dissolution of silicon in hydrofluoric acid solutions", *Surf. Sci.* **4**, 109 (1966).

Michaels, W. and Pilkuhn, M. H., "Radiative recombination in silicon p-n junctions", *Phys. Status Solidi* **36**, 311 (1969).

Nozawa, K. and Horikoshi, Y., "Low threading dislocation density GaAs on Si(100) with InGaAs/GaAs strained-layer superlattice grown by migration-enhanced epitaxy", *Jpn. J. Appl. Phys.* **30**, L668 (1991).

Palik, E. D., "Handbook of optical constants of solid", (Academic Press, Inc., 1985).

Pankove, J. I., "Optical process in semiconductors", (Prentice-Hall, Inc., Englewood Cliffs, New Jersey, 1971).

Parkhutik, V. P., Glinenko, L. K. and Labunov, V. A., *Surf. Technol.* **20**, 265 (1983).

Petroff, P. and Hartman, R. L., "Rapid degradation phenomenon in heterjunction GaAlAs-GaAs lasers", *J. Appl. Phys.* **45**, 3899 (1974).

Pickering, C., Beale, M. I. J., Robbins, D. J., Pearson, P. J. and Greef, R., "Optical studies of the structure of porous silicon films formed in p-type degenerate and non-degenerate silicon", *J. Phys. C* **17**, 5535 (1984).

Pollentier, I., Demeester, P., Ackaert, A., Buydens, L., Daele, P. v. and Baets, R., "Epitaxial lift-off GaAs LEDs to Si for fabrication of opto-electronic integrated circuits", *Electron. Lett.* **26**, 193 (1990).

Presting, H., Kibbel, H., Jaros, M., Turton, R. M., Menczgar, U., Abstreiter, G. and Grimmeiss, H. G., "Ultrathin  $Si_m Ge_n$  strained layer superlattices - a step towards Si optoelectronics", *Semicond. Sci. Technol.* **7**, 1127 (1992).

Ren, F., Chand, N., Garbinski, P., Pearton, S. J., Wu, C. S., Urbanek, L. D., Fullowan, T., Shah, N. and Feuer, M. D., "GaAs MESFETs, ring oscillators and divide-by-2 integrated circuits fabricated on MBE grown GaAs on Si substrates", *Electron. Lett.* **24**, 1037 (1988).

Sarathy, J., Shih, S., Jung, K., C., T., Li, K.-H., Kwong, D.-L., Campbell, J. C., Yau, S.-L. and Bard, A. J., "Demonstration of photoluminescence in nonanodized silicon", *Appl. Phys. Lett.* **60**, 1532 (1992).

Searson, P. C., Macaulay, J. M. and Prokes, S. M., "The Formation, Morphology, and Optical Properties of Porous Silicon Structures", *J. Electrochem. Soc.* **139**, 3373 (1992).

Shimizu, M., Sugawara, K. and Sakurai, T., *J. Jpn. Assoc. Cryst. Growth* **13**, 253 (1986).

Smith, R. L., Chuang, S.-F. and Collons, S. D., "A theoretical model of the formation morphologies of porous silicon", *J. Elec. Mat.* **17**, 533 (1988).

Smith, R. L. and Collins, S. D., "Porous silicon formation mechanisms", *J. Appl. Phys.* **71**, R1 (1992).

Tenney, A. S. and Ghezzo, M., J. Electrochem. Soc. **120**, 1091 (1973).

Theunissen, M. J. J., J. Electrochem. Soc. **119**, 351 (1972).

Theunissen, M. J. J., Appels, J. A. and Verkuulen, W. H. C. G., J. Electrochem. Soc. **117**, 959 (1970).

Turner, D. R., "Electropolishing silicon in hydrofluoric acid solutions", J. Electrochem. Soc. **105**, 405 (1958).

Uhlir, A., "Electrolytic shaping of germanium and silicon", Bell System Tech. J. **35**, 333 (1956).

Unagami, T., "Formation mechanism of porous silicon layers by anodization in HF solution", J. Electrochem. Soc. **127**, 476 (1980).

Wight, D. R., "Green luminescence efficiency in gallium phosphide", J. Phys. D **10**, 431 (1977).

Yablonovitch, E., Hwang, D. M., Gmitter, T. J., Florez, L. T. and Harbison, J. P., "Van der Waals bonding of GaAs epitaxial liftoff films onto arbitrary substrates", Appl. Phys. Lett. **56**, 2419 (1990).

Yablonovitch, E., Kapon, E., Gmitter, T. J., Yun, C. P. and Bhat, R., IEEE Photonics Technol. Lett. **1**, 41 (1989).

Zhang, X. G., Collins, S. D. and Smith, R. L., "Porous silicon formation and electropolishing of silicon by anodic polarization of HF solution", J. Electrochem. Soc. **136**, 1561 (1989).

## Chapter 3

### Experimental Techniques

#### 3.1 Focused Ion Beam Implantation Technology

##### 3.1.1 System Specification and Operation

Focused ion beam (FIB) fabrication techniques have been widely used in many fields of microelectronics and optoelectronics because of its ability to produce well focused ion beam of selected species with controllable energies and doses. These includes [Mengailis (1987)] maskless implantation for device and micro- and nano-structures fabrication; ion milling for mask repair and circuit microsurgery; ion induced surface chemistry for localized in-suit etching and deposition; FIB lithography; microanalysis for integrated circuits (IC) failure analysis, FIB-induced compositional mixing in multiple quantum well. Table 3.1 outlines the applications of FIB technology and researches done at UC involving the use of FIB. The use of FIB technology in this work are primarily in the area of maskless/resistless doping for the fabrication Si micro- and nano-structures and selective photoluminescent porous silicon patterns and nanostructures [Steckl, *et al.* (1992), Steckl, *et al.* (1993), Xu, *et al.* (1994), Xu and Steckl (1994)].

Table 3.1 Summary of FIB applications and related research directions at NanoLab

FIB applications	Researches done at NanoLab
<ul style="list-style-type: none"><li>• Implantation:<ul style="list-style-type: none"><li>device fabrication</li><li>micro- and nanostructure</li></ul></li><li>• Ion milling:<ul style="list-style-type: none"><li>mask repair</li><li>circuit microsurgery</li></ul></li><li>• Ion induced surface chemistry:<ul style="list-style-type: none"><li>etching</li><li>deposition</li></ul></li><li>• FIB lithography:<ul style="list-style-type: none"><li>organic resist - PMMA</li><li>inorganic resist</li></ul></li><li>• Microanalysis:<ul style="list-style-type: none"><li>micro SIMS</li><li>secondary electron microscopy</li><li>secondary ion microscopy</li></ul></li></ul>	<p>Earlier work:</p> <ul style="list-style-type: none"><li>• STM and AFM tip fabrication</li><li>• Direct write lithography</li><li>• Si p-n shallow junction</li><li>• GaAs/AlGaAs 3rd order surface emitting laser</li><li>• Ion beam assisted Al deposition</li></ul> <p>This work:</p> <ul style="list-style-type: none"><li>• Si micro- and nanostructures</li><li>• Si light emitting nanostructures</li></ul>

The FIB system employed in this work was the NanoFab-150 system developed by MicroBeam Inc. The system is able to produce atomically pure beams of singly- or multiply-charged ions, over a wide range of acceleration voltages, of various elements from elemental or alloy liquid metal ion sources (LMISs). Figure 3.1.1 shows the electrical schematic of the MicroBeam NanoFab-150 system and Figure 3.1.2 is the schematic of the ion column. Ions extracted from the source pass through a beam-defining aperture (1, 3, or 5 mil in diameter), which sets the beam size, and then focused by the upper lens onto the plane of the mass-separation aperture. The mass filter deflects the un-wanted species and selects only the desired ions from the beam by using an appropriate electric and magnetic ( $E \times B$ ) fields. The beam can be turned on and off by applying voltages to the beam blanker. The lower lens focuses the beam onto the target surface and accelerates or decelerates the beam to its final energy. The main octopole deflector moves the beam across the target

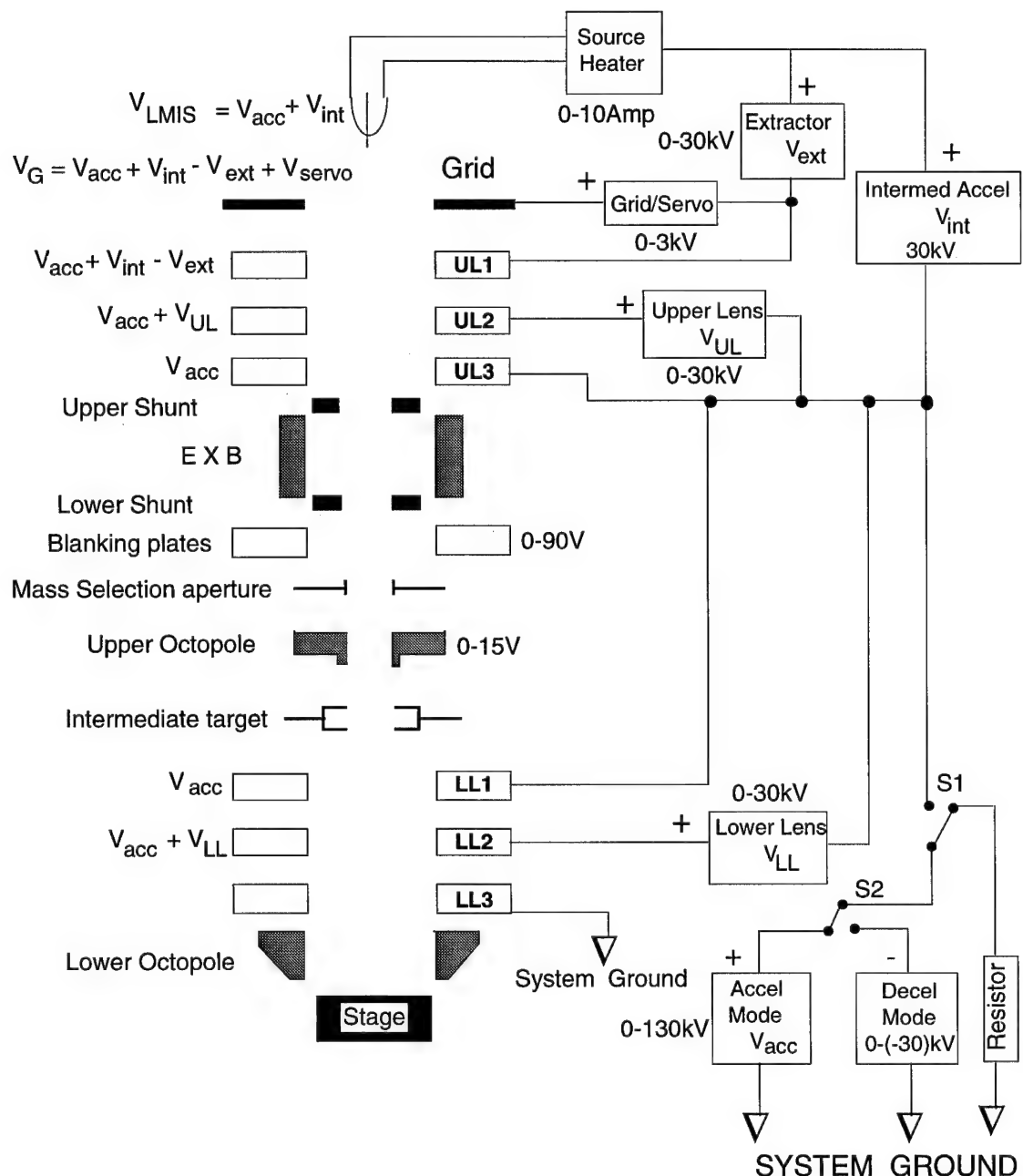


**FIGURE 3.1.1** Electrical schematic of NanoFab 150 system.

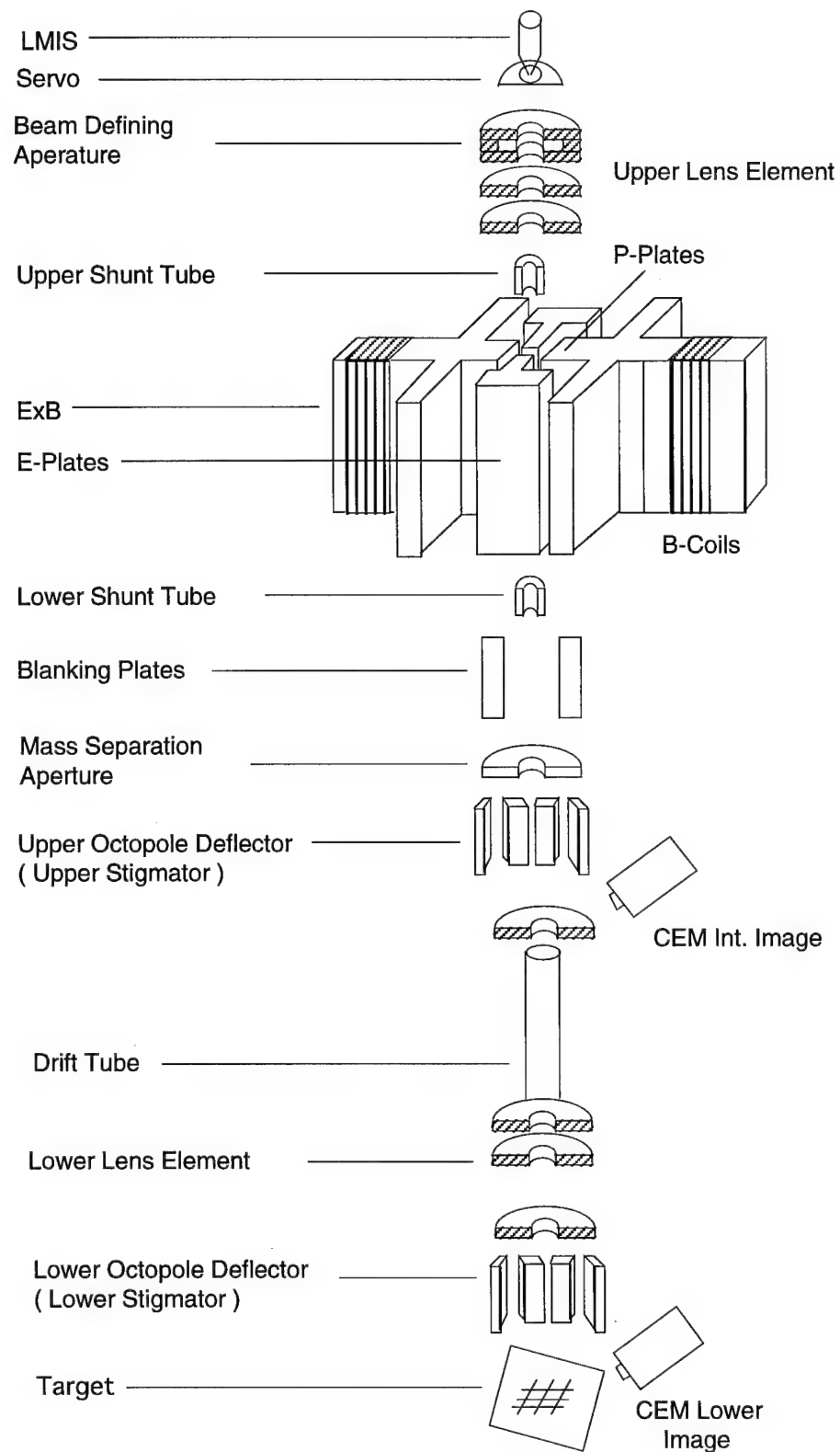


**FIGURE 3.1.2** Schematic of the ion column in NanoFab-150 FIB system.

surface under the control of a deflection controller using a set of user-supplied pattern data. Target motion is accomplished with a high precision mechanical X, Y stage with optical encoder and laser interferometer readout. Secondary particles ejected by the primary ion beam from the target are collected and used to form an image of the target. The system vacuum is achieved by using two cryopumps and one mechanical pump which can provide a base pressure up to  $2 \times 10^{-7}$  Torr in both the column and the target chamber. The whole system operation is controlled by a semi-automatic console with a PC 486 microprocessor. Most of the communications between the computer and the electro-mechanical actuators are optical communications through optical fiber bundle.

The major system specifications are listed under Table 3.2. The system operation mechanism and operation are documented in detail in the NanoFab-150 Operator's Manual.

Table 3.2 Focused ion beam system specifications

Parameter	Specification
Accelerating energy range:	2 - 150 KeV
Beam diameter range:	50 - 2000 nm
Beam current :	few pA to several nA
Minimum beam position step:	8 nm
Stage movement accuracy:	150 nm (laser interferometer)
Primary ion species:	Ga, Au, Be, In, and Si
Primary ion mass separation:	$E \times B$ filter, $M/\Delta M \geq 50$
Computer control:	IBM PC/AT
Substrate handling:	Up to $8 \times 8$ inches
Off-axis implantation:	3 - 30° (small area)
Localized gas delivery system:	currently not used
Base pressure:	$2 \times 10^{-7}$ Torr

### 3.1.2 Fabrication of Liquid Metal Ion Sources (LMIS)

The primary ion specie used in this work is singly charged  $\text{Ga}^+$  from either a GaIn alloy LMIS or an elemental Ga LMIS.  $\text{Ga}^+$  ion sources have also recently become commercially available at a relatively high cost.

A technique was adopted and modified, at Nanoelectronics Laboratory, to fabricate  $\text{Ga}^+$  and  $\text{Si}^{++}$  liquid metal ion sources, which are the two most common species for FIB implantation. The high melting temperature of silicon element (1414°C) prevents it from becoming potential liquid metal material. Therefore Si alloys with low eutectic melting points, such as AuSi and AuBeSi, are usually good candidates for making Si ion sources. The melting temperature for AuSi alloy with eutectic composition is ~370°C. This operation temperature is much more practical and can be achieved with tungsten ribbon and regular heater without causing noticeable side effects. In contrast to Si element, pure Ga has a melting temperature of 29.8°C and GaIn alloy is in liquid phase even at room temperature. Therefor  $\text{Ga}^+$  ion sources can be made easily from those two materials and the operation conditions of  $\text{Ga}^+$  LMIS is also readily obtained.

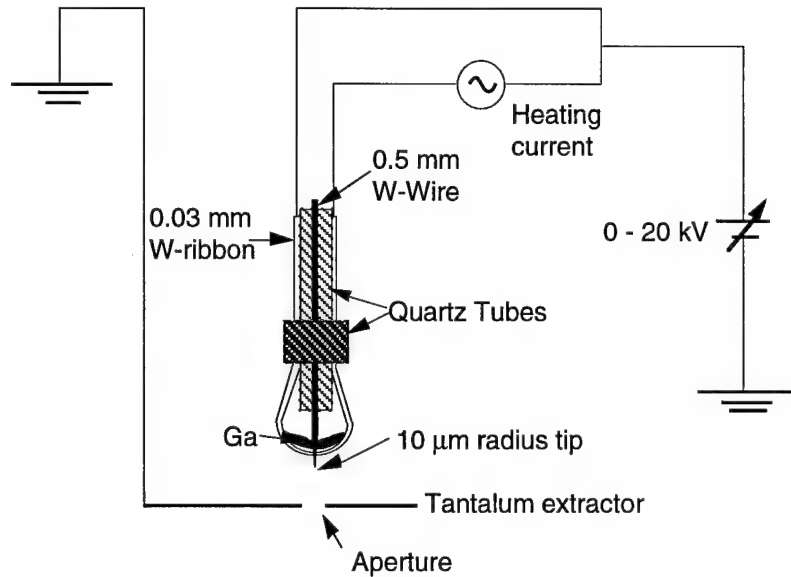


**FIGURE 3.1.3** Schematic of liquid metal ion source for NanoFab-150 FIB system.

The configuration of liquid metal ion sources designed for use in the NanoFab-150 system is shown in Fig. 3.1.3. A tungsten ribbon of 0.03 mm thickness is held between two quartz tubes to form a U-shape reservoir for holding liquid metal material. Through a small hole in the middle of the reservoir, the LMIS tip is supported by a bunch of tungsten wires inserted in the inner quartz tube.

The fabrication process of a LMIS is usually consisting of five steps: (1) reservoir formation; (2) tip fabrication; (3) source assembly; (4) source material loading and melting/alloying, and (5) testing. The procedure is described in the following a few sections.

#### *(1) Reservoir formation*

A tungsten ribbon with a width of 2.5 - 3 mm and a length of 50 - 60 mm is cut from tungsten foil of 0.03 mm thickness. The ribbon is then taped on to a copper disk of 1.5 inch, which has a pre-drilled guiding hole of 0.5 mm diameter in the center, and is aligned to the center of the disk. A small hole with 0.5 mm diameter is drilled in the middle of the ribbon through the guiding hole. The ribbon is bent over to form a U-shape with a reasonably small radius. The bending of the ribbon is conducted while the ribbon is being heated using a torch. This heat assisted bending helps to avoid the breaking of ribbon and the shape thus formed is nearly permanent. The ribbon is then cleaned by electrolytic etching in a NaOH solution to remove any oxide layer formed during the heated shaping process. Two quartz tubes with different diameters are used to hold the U-shaped ribbon and a reservoir is then formed. The length for larger diameter tube should be about 7 mm and the length for core tube is about 36 mm-40 mm. Finally, all the parts are assembled together as shown in Fig. 3.1.3.

#### *(2) Tip fabrication*

The tungsten tip is made from a piece of straight tungsten wire of a 0.5 mm diameter. First, one end of the wire from which the final tip is formed is electrolytically sharpened in a 2 M NaOH electrolyte with a 2 volts of ac voltage using the setup illustrated in Fig. 3.1.4. To obtain symmetric and straight tip, the W-wire must be carefully positioned in the center of the beaker, and perfectly vertical. During this process about 1 cm of the wire is immersed in the NaOH and etched,

thus a smooth and sharpened tip is formed. Fresh NaOH should be used because NaOH decomposes gradually. After the sharpening, the tip is roughened in a  $\text{HNO}_3:\text{HF}$  (1:3) solution. Normally about 10 quick dips in the solution is appropriate for producing a suitable roughness. The radius of tip is desired to be smaller than  $10 \mu\text{m}$  and the tip is evaluated by SEM to check its size, symmetry and roughness.

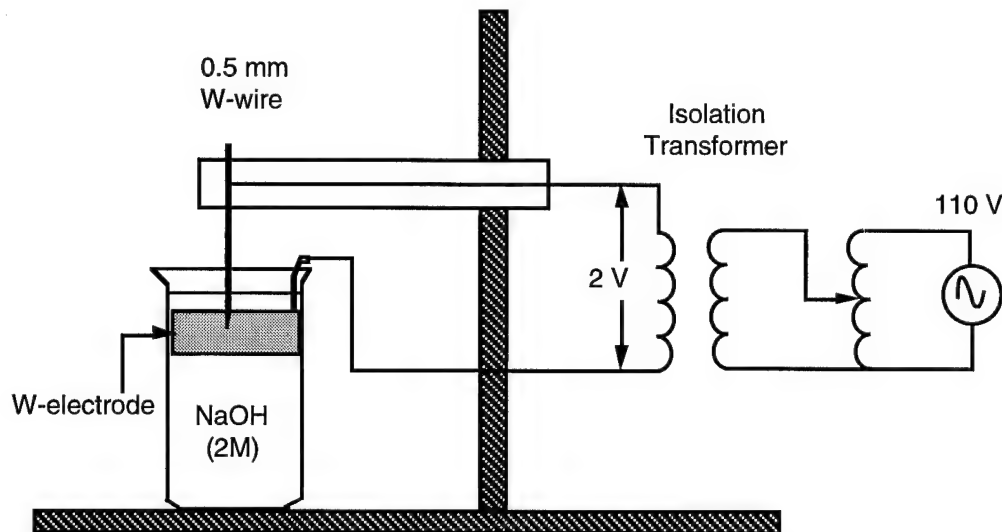


**FIGURE 3.1.4** Experimental setup for LMIS tip fabrication.

### (3) Assembly

The tip fabricated is assembled with reservoir in the manner shown in Fig. 3.1.3. The length of tip outside the ribbon is approximately 0.06 inch, and the ribbon length below the wider quartz tube is 0.44 inch. Extreme care must be taken during the handling.

### (4) Alloy melting and LMIS formation

A home-made test station has been used for alloy melting and LMIS testing. A schematic diagram of the test station is shown in Fig. 3.1.5.

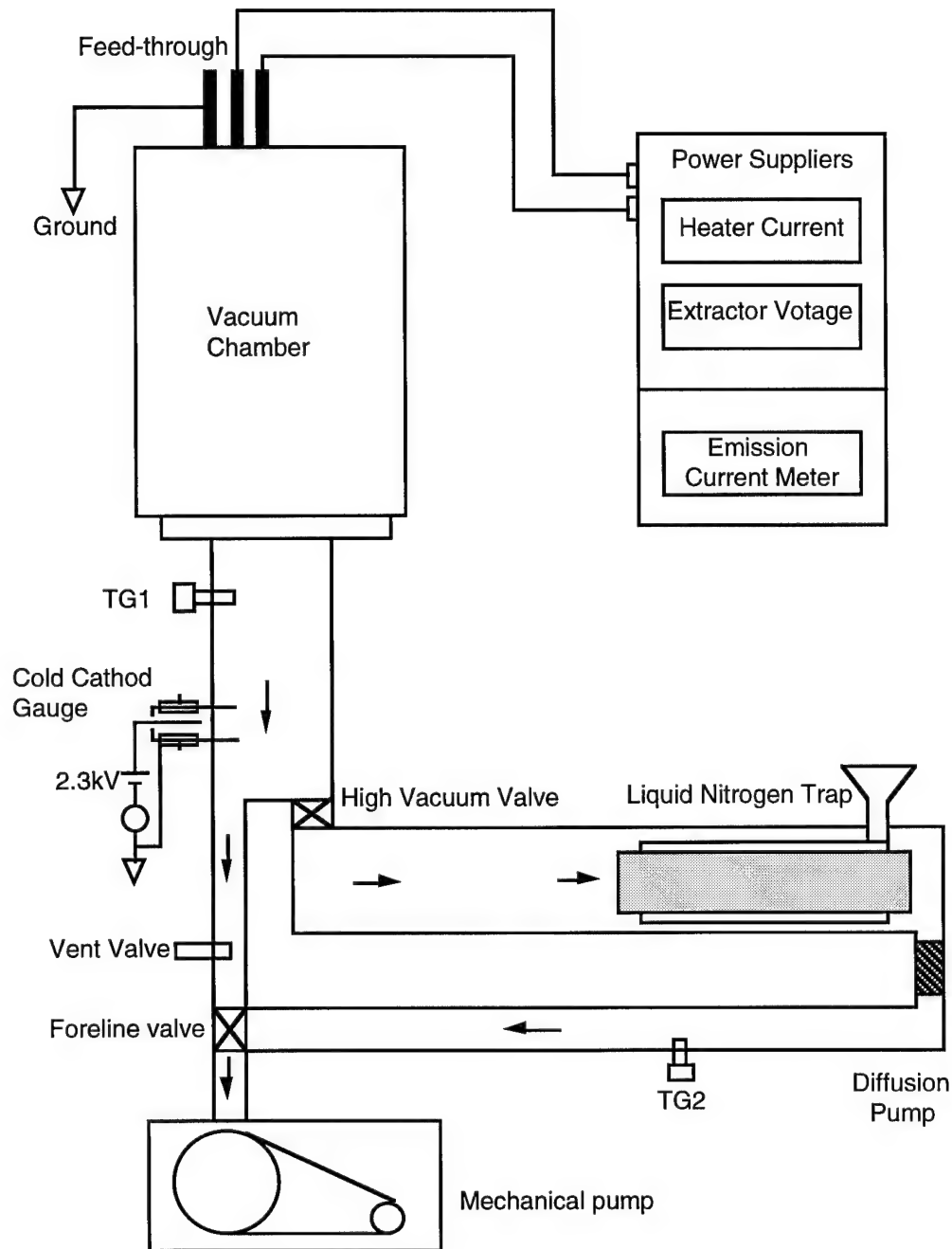


**FIGURE 3.1.5** Schematic of the home-made vacuum working station for LMIS fabrication and testing.

Before loading the source material to the reservoir, a bake of the assembled tip and reservoir in high vacuum is recommended to further clean the ribbon and tip surface by thermal evaporation. In this process the source assembly is heated to "red hot" for two-three minutes and cooled down gradually. A low pressure of  $< 10^{-6}$  is necessary for this bake and for all the heating processes.

After the pre-baking, the source material are loaded into the reservoir. For  $\text{Ga}^+$  source fabrication, two small pieces of Ga pallet are cut from the supplied pallet and put into the reservoir.

For AuSi source fabrication, a short piece of AuSi wire is bend to a U-shape, then placed around the tip within the ribbon.

A heating current is applied to melt the source material. The current for  $\text{Ga}^+$  source is usually in the range of 3-5 A, and the current required for melting AuSi alloy is about 8-10 A. A close observation is necessary and the current is to be adjusted during the heating process. Once a visible melting is observed, the current should be lowered immediately and slowly to avoid an excess heating. Meantime, the extract voltage should be applied to ultimately form a liquid metal tip.

#### *(5) Testing*

The home-made sources are first tested in the test station to check the stability of the ion emission using similar conditions of FIB operation. Until a stable emission current with reasonable value at those conditions is reached the source is then loaded in to FIB system for additional testing of the beam quality. Only after a source passes those two tests the source fabrication is considered successful.

### **3.2 Rapid Thermal Processing for Annealing and Oxidation**

Thermal annealing is normally performed on samples after ion implantation to activate the dopants and to reduce/eliminate any damage, and on samples after metallization to form specific type of contact (such as aluminum silicide for ohmic contact). In this work a rapid thermal annealing (RTA) was chosen for the above mentioned purposes over the conventional furnace annealing due to its simplicity and versatility.

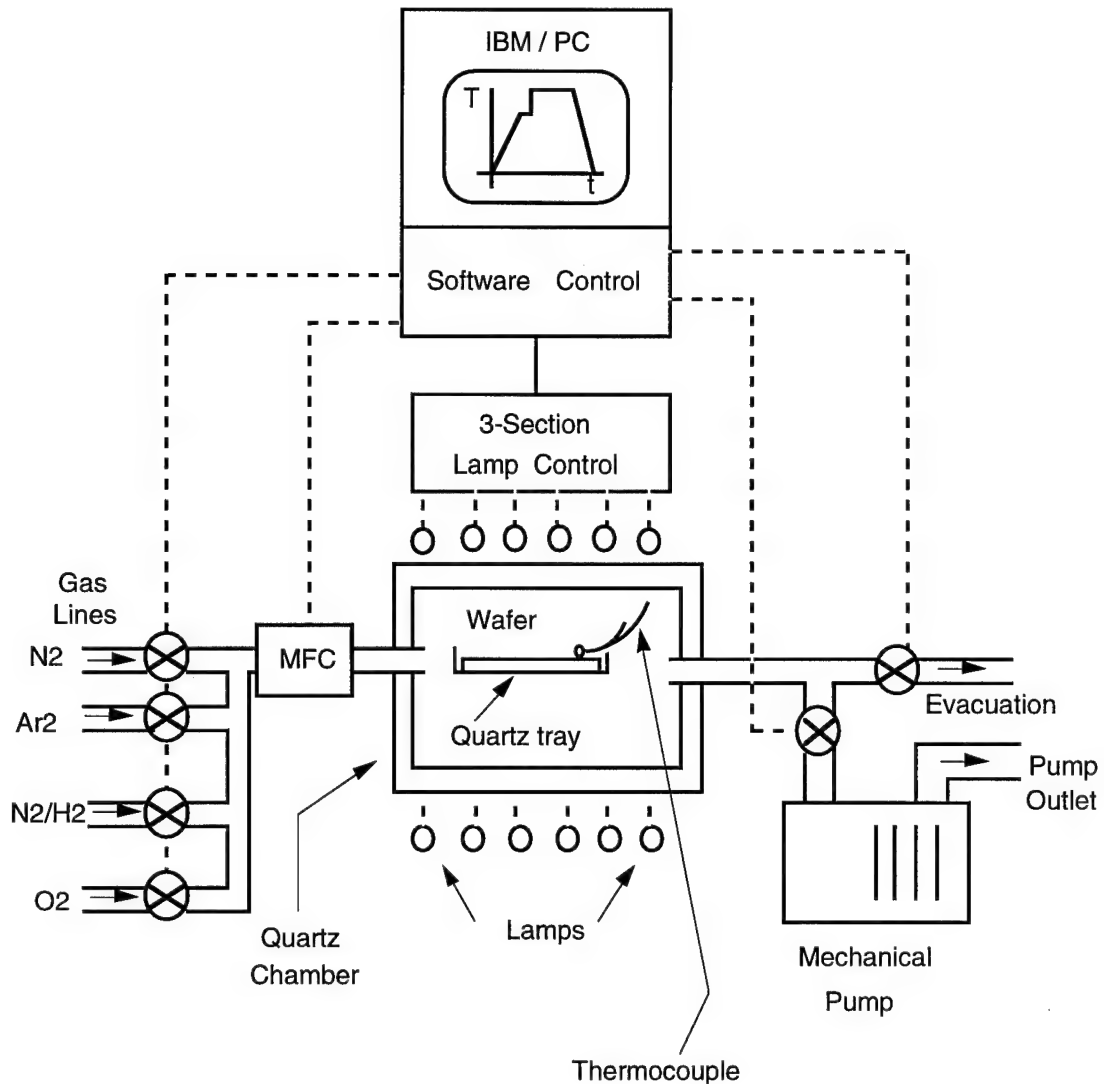


**FIGURE 3.2.1** Schematic diagram of the NanoLab RV1003 RTA system.

The annealing system used in this study was a AET/ADDAX RV1003 system, which is a semi-automatic rapid thermal processing system. Heating of the annealing quartz chamber is provided by the surrounding tungsten-halogen quartz lamps located inside a double-walled water cooled stainless steel chamber. The light sources and the reflector provide the chamber with a uniform light flow. A quartz tray in side the quartz chamber is used to support a wafer or a pill box. Vacuum in the quartz chamber is provided by a mechanical pump. The temperature control is performed by a thermocouple. All the desired cycles, including temperature, time, gas and gas flow, are specified and controlled by IBM/PC 386 computer.

The RTA system is routinely used for implant and silicide annealing of Si wafers. The process time runs from a few seconds to a few minutes. The annealing temperature routinely utilized ranges from 200 to 1000°C. A schematic of the RTA system is shown in Figure 3.2.1.

### 3.3 Wet Etching of Silicon

Wet etching was one of the most used processes in this work which included anisotropic etching of silicon in KOH for nanostructures fabrication, electrochemical etching and stain-etching

for porous silicon formation, and metal/ITO etching for devices patterning. The following a few sections describe the experimental setups for those various etching processes.

### 3.3.1 Anisotropic Etching of Silicon

Anisotropic etching of silicon in KOH solution at elevated temperatures is one of the most widely used techniques in silicon micromachining. It is relatively save and simple. One disadvantage with KOH is that it also etches  $\text{SiO}_2$  which is usually used as mask. Fortunately, in this work the so-called mask needed is obtained by FIB  $\text{Ga}^+$  implantation at very high dose ( $>5\text{E}15 \text{ ions/cm}^2$ ), and therefore KOH solution is a good choice as the anisotropic etchant. Figure 3.3.1 is the diagram of the automated experimental setup used through this work.

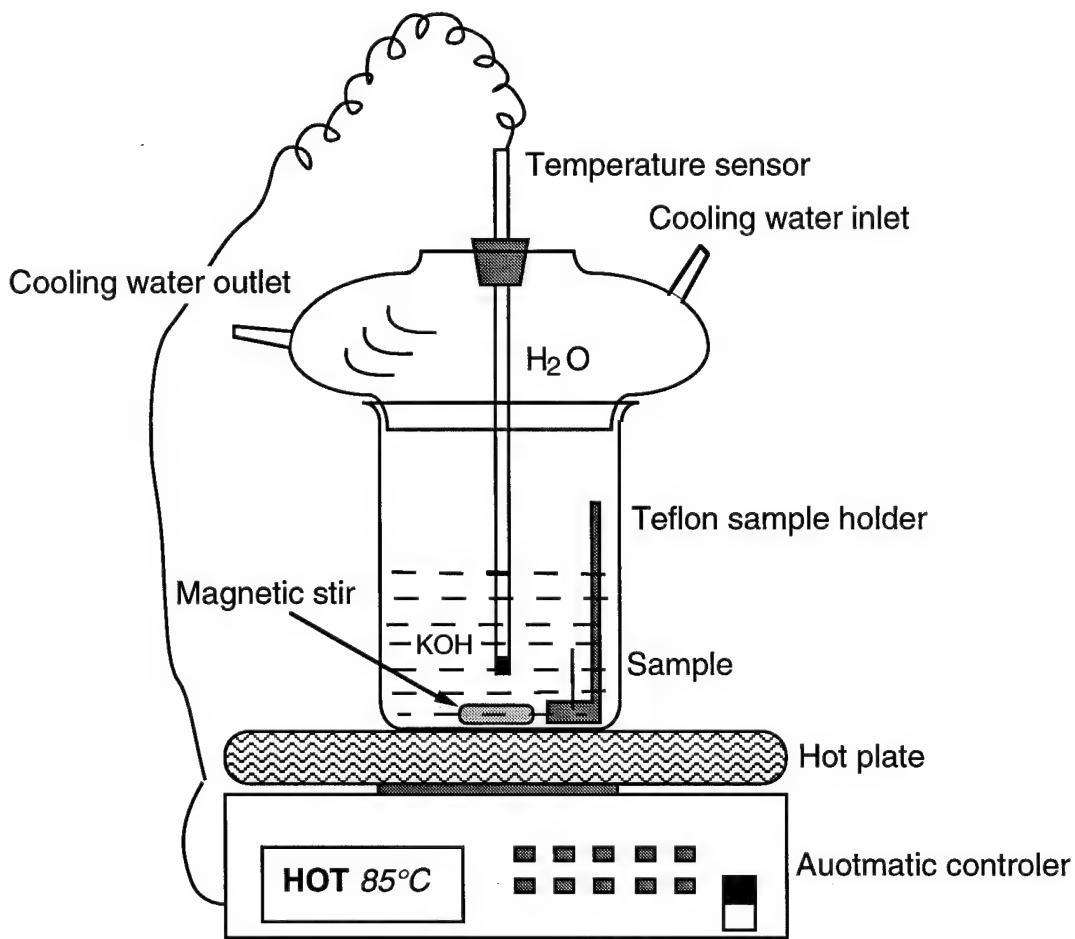


**FIGURE 3.3.1** Schematic of the automated silicon anisotropic etching setup.

The complete automatic silicon anisotropic etching system depicted in Fig. 3.3.1 consists of a Cole-Parmer's Digital Hot Plate/Stirrer and a large Teflon beaker covered with a glass condenser. The digital hot plate is a programmable hot plate with one magnetic stirrer located at the center. It has two thermal sensors for temperature monitor and control: one internal sensor monitoring the plate temperature and one external Teflon coated thermal couple probe for monitoring the temperature of etchant. Automatic temperature control is achieved by using either one of the two thermal sensors and can be set anywhere between 0 to 400°C. The stirrer speed may be set between 0 to 1500 rotation per minute (RPM). Once calibrated the system can stabilize and maintain at a selected temperature within  $\pm 1$  to 2°C.

A quartz condenser with cold circulating water is used to keep the etchant being evaporated away, so that the etching process may be taken as long as needed. The sample being etched is usually held vertically on a Teflon L-shaped holder as indicated in Fig. 3.3.1. For uniform micromachining, it is sometime necessary to rotate the sample position a few times during the etching process.

### 3.3.2 Electrochemical Anodization

The fabrication of porous silicon by electrochemical anodization is conducted in a Teflon electrochemical cell depicted in Fig. 3.3.2. The cell was made out of a Teflon rod with 1.0 in inner diameter. The Si substrate to be anodized was attached to the bottom of the cell serving as the anode, and secured by a brass plate with four set screws. A Teflon O-ring was put between the substrate and the cell to provide the necessary ceiling. A platinum wire was used as the cathode which is inserted into the HF based electrolyte. A variable DC power supply was used to provide the needed current flow for electrochemical etching. The electrolyte was always freshly mixed and consumed right away. Anodization was usually conducted under room light.

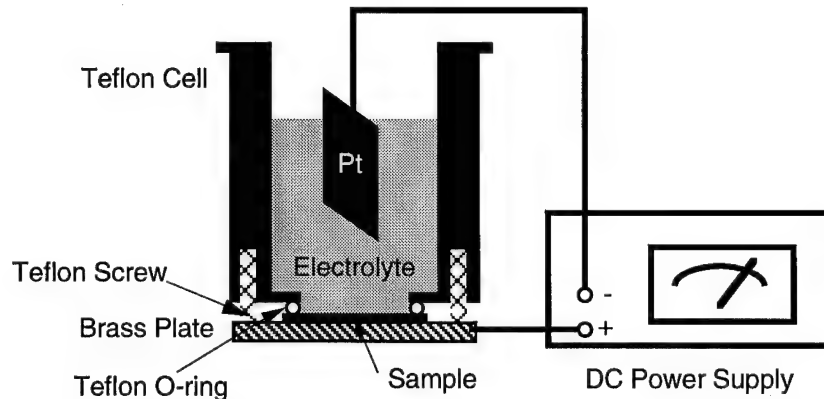


**FIGURE 3.3.2** Schematic of a single cell electrochemical etching setup.

### 3.3.3 Stain Etching

The experimental setup for stain etching of silicon is much simpler than that for anodization as shown in the sketch below in Fig. 3.3.3. Stain-etching solution made of either HF:HNO<sub>3</sub>:H<sub>2</sub>O with 1:3:5 volume ratio or HF:HNO<sub>3</sub> with 200:1 volume ratio was contained in a Teflon beaker. Normally the solutions were freshly made and consumed right way though the mixture could be stored in a Teflon bottle for later use with a self-life time of around a few months. Most stain-etching was performed under room light with no intentional heating. Sometimes UV illumination only was used such as in the study of doping effect on the porous silicon formation.

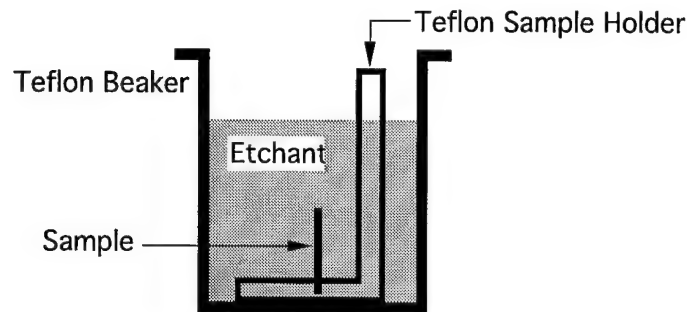


**FIGURE 3.3.3** Stain etch setup for fabrication of porous silicon.

### 3.4 Metallization and Solid Contact by DC & RF Sputtering

Sputter deposition of metal, oxide and semiconductor is routinely performed in this work for the formation of ohmic contact or electrode (Al, W), Schottky contact (indium tin oxide, Au), lift-off mask or protection mask (SiC, SiO<sub>2</sub>, and Si<sub>3</sub>N<sub>4</sub>). The system employed is a DV-602 sputter deposition system from Denton Vacuum. An illustration of the sputtering system is shown schematically in Fig. 3.4.1. The system consists of primarily three units: (1) a processing chamber; (2) a vacuum system; and (3) the control units. Located inside the process chamber are a heatable (up to 600°C) rotating sample stage, a crystal thickness monitor, a processing gas supply nozzle, and two water cooled magnetron sputtering cathodes. Etch cathode can be supplied with either DC or RF power depending on the processing target (for single target processing, the spare cathode is protected by covering it with Al thin foils). Most depositions were carried out under pure Ar<sup>+</sup> plasma though occasionally mixture of Ar with O<sub>2</sub> and/or H<sub>2</sub>O vapor were used. The use of magnetic field greatly increases the possibility of ionizing collisions with the Ar<sup>+</sup> gas molecules. This, in turn, increases the Ar<sup>+</sup> concentration, and hence the deposition rate. The chamber vacuum is obtained through two pumps; a Leybold D8A mechanical roughing pump and a CTI Cryogenics CTI-8 cryopump which could provide a base vacuum of  $\sim 10^{-7}$  Torr. The control unit provides an easy access to set the process conditions for power level, substrate temperature and film thickness etc.. It is also equipped with a computer system which provides a programmable interlock for operation safety, and the choice of automatic or manual procedures for pumping/venting and cryopump re-generation.

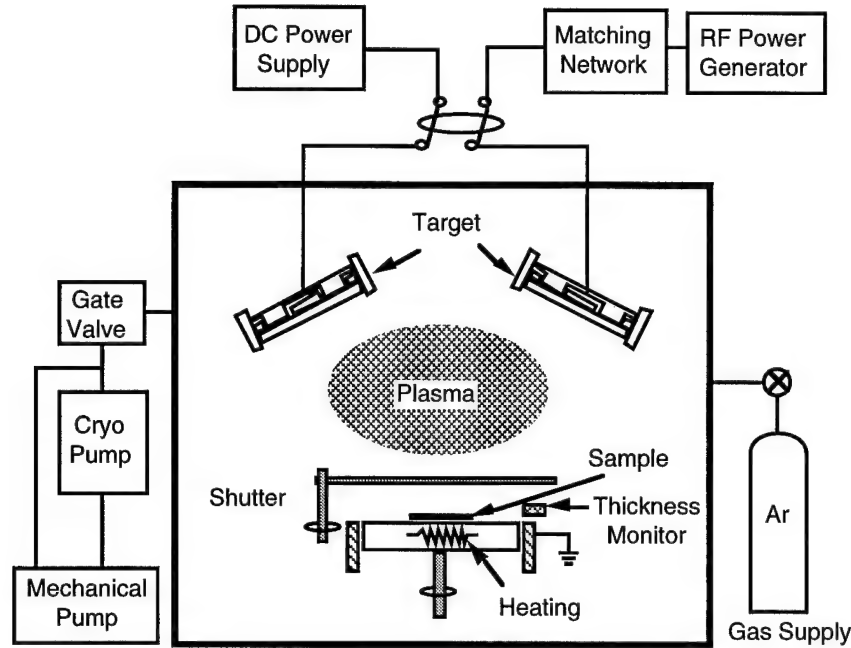


**FIGURE 3.4.1** Schematic of the Denton Vacuum DC-602 sputter deposition system.

### 3.5 Optical Characterization

Optical characterization is one of the most used techniques for porous silicon related researches due to its nondestructive nature and versatility. It has been used to study a number of properties of porous silicon, including: (1) bandgap energy; (2) optical properties such as refraction index and absorption; (3) photoluminescence; and (4) structural properties. During this work a multi-functional optical characterization system was designed and implemented. The system can be used either as an optical spectroscopy or a fluorescence microscopy. As a spectroscopy, it can be used to study photoluminescence (visible and near infrared), optical transmission or absorption (from UV to near infrared), Raman scattering, and electroluminescence. As a microscope it can take light emission micrographs as well as conventional optical reflection micrographs.

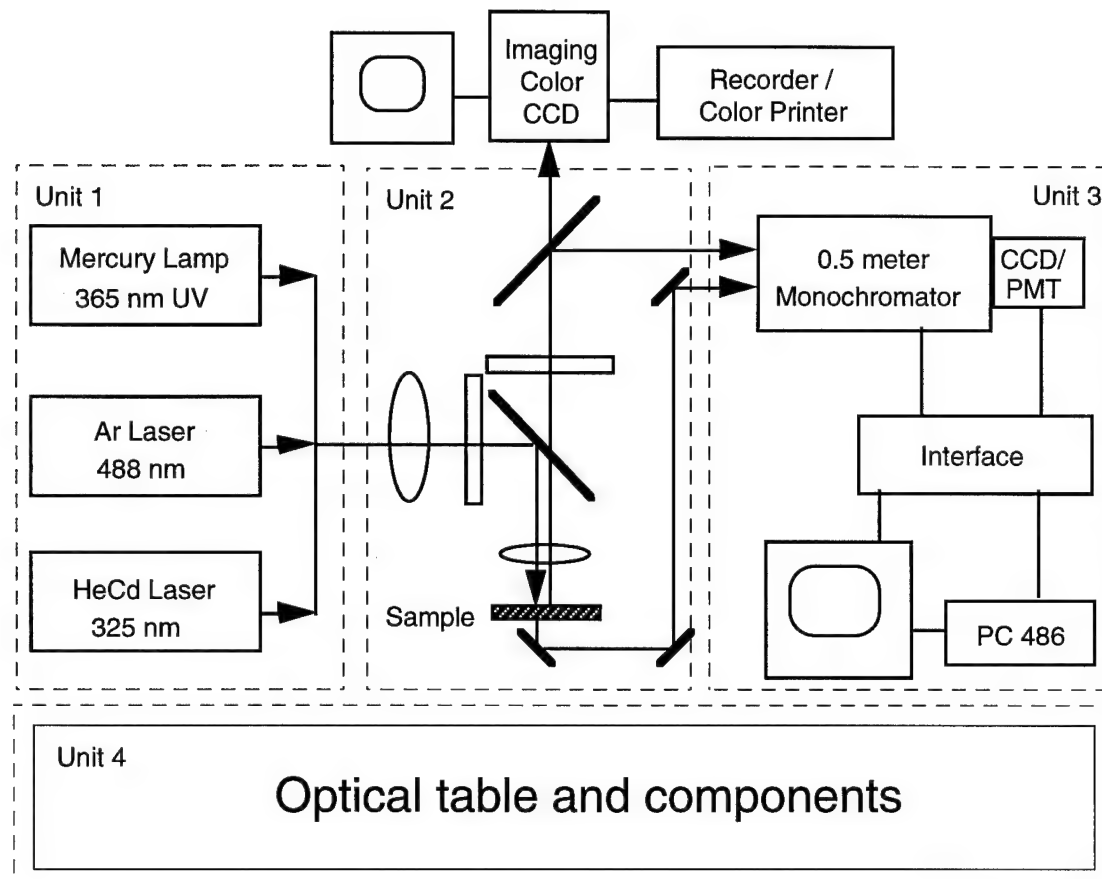


**FIGURE 3.5.1** Block diagram of the optical characterization system.

Figure 3.5.1 is a block diagram of the system. It contains four basic units identified as: light sources (unit 1), fluorescence microscope (unit 2), controller and data acquisition (unit 3), and optomechanical components (unit 4). The major components and functions are summarized below.

**Unit 1:** This unit currently contains two different types of light sources, a 100W mercury (Hg) lamp, a 100 mW Ar<sup>+</sup> laser at 488 nm and a HeCd UV laser. The Hg lamp gives an easy access to broad UV of 200-500 nm as well as visible light. This is used for either color imaging documentation and luminescence spectroscopy. A set of optical filters with three different working ranges were used to select a desired wavelength range which can produce a UV light source at centered 365 nm, a blue light source centered at 488 nm and a white light source. However, since the filtering obtained by these specially desired optics do not provide a 100% blocking of those light of un-desired wavelength, care must be taken when analyzing the resulting luminescence spectra to eliminate any contributions in the emission spectra due the un-complete filtering. The Ar<sup>+</sup> laser provides a single wavelength (at 488 nm) pumping source for photoluminescence measurement, and it can also be used for Raman scattering measurement. Additional light sources, including a 5 W single line tunable Ar<sup>+</sup> laser and a 50 mW multiline He-Cd laser will soon be added to the system, further extending its luminescence measurements capability.

**Unit 2 :** This part contains mainly a fluorescence microscope equipped with special optics allowing both UV and visible light comes in but only visible light goes out to be coupled either by optical lens or optical fiber bundle to unit 3 for spectrum analysis or a color imaging system for

documentation. The microscope is capable of focusing to micrometer spot size such that the microscale spectrum analysis and microstructure color imaging are readily obtained.

**Unit 3:** This unit currently contains a 0.5 meter monochromator along with computerized controller and data acquisition system, two interchangeable gratings, and two detectors: a photomultiplier tube and an AlGaAs photodiode. With proper combination of grating and detector, the system can be used to perform spectroscopic analysis in both visible (400 to 900 nm) and near infrared (800 to 15000 nm) range. In addition, liquid N<sub>2</sub> cooled CCD detector will soon be added to this system which will enhance the capability of the current system. Equipped with CCD detection, not only the spectrum measurement can be done quickly but also the time dependence of the spectrum can be obtained easily.

**Unit 4:** This optical table and its components provide a necessary isolation and stable support for the whole set up.

### 3.6 Structural Characterization

A number of material characterization techniques are employed to analyze crystallinity, morphology, molecular and atomic structures, and porosity of the materials used in this work, including amorphous- and poly-silicon, porous silicon and indium tin oxide. These characterizations provide structural and compositional information of the materials under investigation, and are essential to the understanding of the mechanisms of light emission from porous silicon as well as to the applications of this phenomena. The following paragraphs discuss briefly each of the techniques used and the specific applications in this work.

#### 3.6.1 X-Ray Diffraction Spectrometry (XRD)

X-Ray diffraction spectrometry (XRD) was used in this work to study and to compare the crystallinity of various materials at various processing stages. These include low pressure chemical vapor deposited (LPCVD) amorphous and poly-silicon thin films, porous polycrystalline silicon thin films, and sputter deposited indium tin oxide thin films. For most of the measurements, XRD was performed with the Cu K<sub>α</sub> line on a Siemens D-500 spectrometer

#### 3.6.2 Secondary Electron Microscopy (SEM)

Secondary Electron Microscopy (SEM) is a very handy tool for studying surface morphology of both conducting and nonconducting materials. Secondary electron (SE) imaging generates a high resolution, large depth of field image (compared to optical microscopy images) depicting the surface morphology of the specimen under investigation, and this is the most commonly used imaging mode of the SEM. SEs are defined as those electrons emitted from the surface with energies of 50 eV or less after primary electron exposure. SE image contrast is generated by differences in SE emission efficiency with topography. Sample charging from absorbed electrons on nonconducting and/or semiconducting surfaces, such as porous silicon surface, can be eliminated by coating the sample with a thin conducting film (such as Au used in this work). The SEM system used in this work is an SX-40A Scanning Electron Microscope from ISI.

### 3.6.3 Atomic Force Microscopy (AFM)

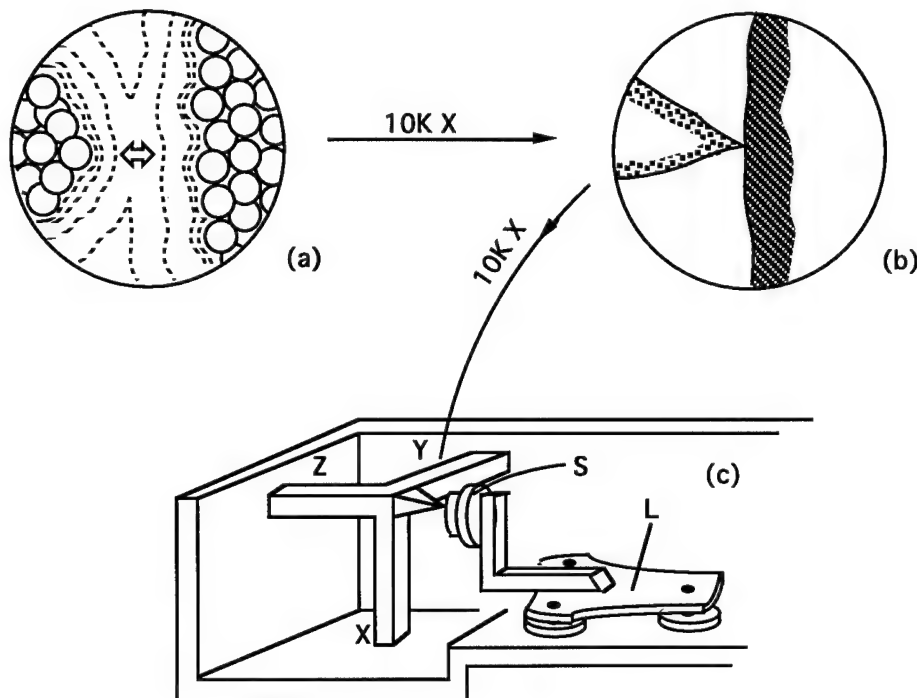


**FIGURE 3.6.1** Principle of scanning probe microscopy.

Atomic force microscopy (AFM) was invented in 1986 by Binnig, Quate and Gerber after Binnig and Rohrer invented scanning tunneling microscopy in 1982. Both microscopies (usually called scanning probe microscopy (SPM)) were developed to investigate surface topography at atomic scale. However both STM and AFM are very useful to provide a knowledge of the surface morphology on a larger scale which is important for many technological applications. Because of the ease of use and its versatility, such as the ability to work in air and no sample preparation requirement, SPM has become an ever growing popular surface analytical technique.

In both STM and AFM, as shown in Fig. 3.6.1, a very sharp tip is positioned at close proximity to the sample surface and moved in a raster fashion across the sample. Some type of interaction between the tip and the surface is measured to form an image in both techniques. In the case of AFM, the interacting quantity is primarily the force, while it is the tunneling current between the tip and the sample surface in the case of STM. For STM, samples must be conductive while AFM can be used to image samples of any conductivity. Table 3.3 summarizes the advantages of AFM. In this work, a NanoScope II AFM from Digital Instrument was used primarily for the study of surface morphology of amorphous and polycrystalline silicon and porous silicon thin films.

Table 3.3 Advantages of atomic force microscopy

---

- High magnification  $10^8\times$
- Works in air
- No sample preparation
- Compared to SEM => provides topographic contrast, direct height measurements, spatial resolution at least  $10\times$  better
- Compared to TEM => 3-D images yield far more complete information than the 2-D profiles available from cross-sectioned samples, cost effective since time consuming sample preparation avoided
- Compared to optical microscopy => provides at least 50 $\times$  better lateral resolution, direct height measurements
- Compared to STM => image any solid and some liquid materials

---

### 3.6.4 Fourier Transform Infrared Spectroscopy (FTIR)

Vibrational spectroscopy of surface species can provide information about structure and bonding directly and, when combined with the other surface analytical techniques available, yields a more complete picture of the chemistry and molecular structure of surfaces. Environments of hydrogen in porous silicon have been investigated extensively by infrared (IR) spectroscopy because of its high sensitivity to surface molecular structures. In this work FTIR spectroscopy was used to study silicon hydrides and silicon oxyhydrides in stain-etched amorphous and polycrystalline Si films. The data were obtained (vs. air as a reference) with  $4\text{ cm}^{-1}$  resolution using a Mattson Cygnus 100 Fourier transform system.

### 3.6.5 Raman Spectroscopy

The inelastic scattering of light by optical phonons or by a number of other elementary excitations (magnons, plasmons, electron-hole excitations, polaritons ...) with typical frequencies between 10 and  $5000\text{ cm}^{-1}$  is called Raman scattering [Cardona (1987)]. Raman spectroscopy is of great interest for basic investigations of semiconductors since it yields information about the vibrational and structural properties such as phonon frequencies, energies of electron states, and electron-phonon interaction. It is also a powerful nondestructive tool for the characterization of semiconducting materials and devices. It has been used to determine their temperature, strain, carrier concentration and scattering time, impurity content, composition in the case of mixed crystals, degree of crystallinity in particular after ion implantation, crystallite size in polycrystals, crystal orientation, amorphicity, surface electric fields, and impurity passivation by hydrogen (see reference [Cardona (1987)] and references therein). In this work, Raman spectroscopy was employed to study crystallite size in polycrystalline silicon thin films and the effect of chemical etching on the size. Figure 3.6.2 outlines the Raman system used in this work.

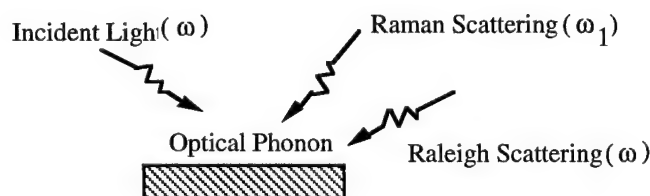
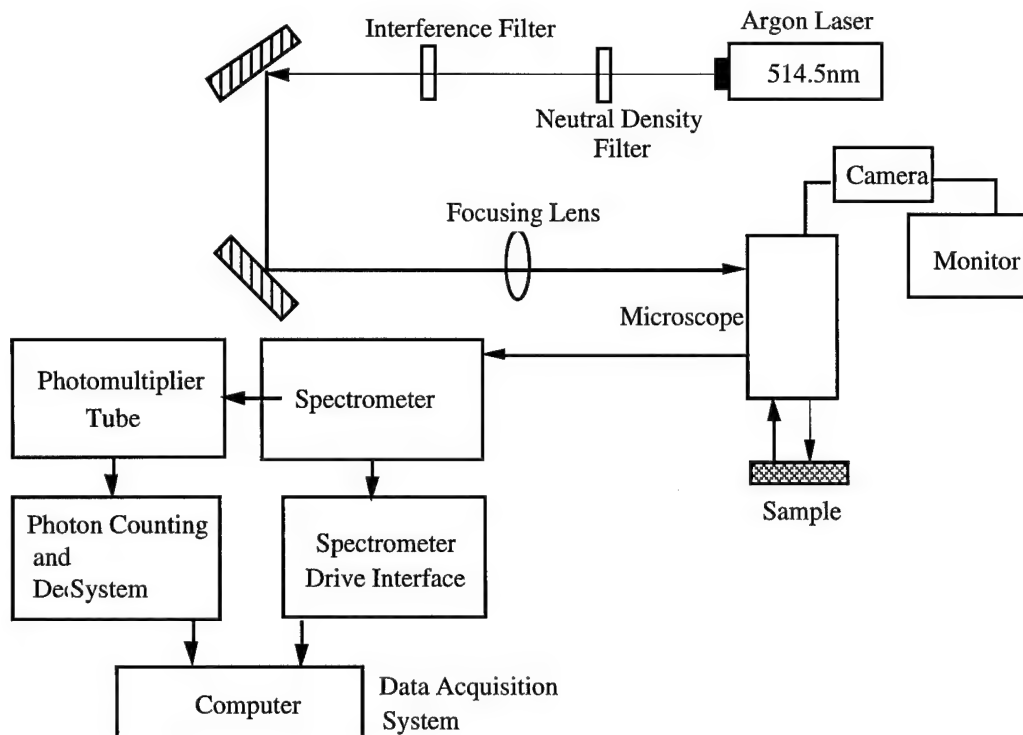


**FIGURE 3.6.2** Schematic of the Raman spectroscopy system used in this work.

### 3.7 Electroluminescence Characterization

To characterize the optical emission from porous silicon light emitting diodes, a system was implemented which combines a probe station and a high speed spectrometer with a CCD detector as outlined in Fig. 3.7.1. A constant current source was used to "pump" the LEDs. The emission was couple into the 0.25 monochromator by optical fiber bundle.

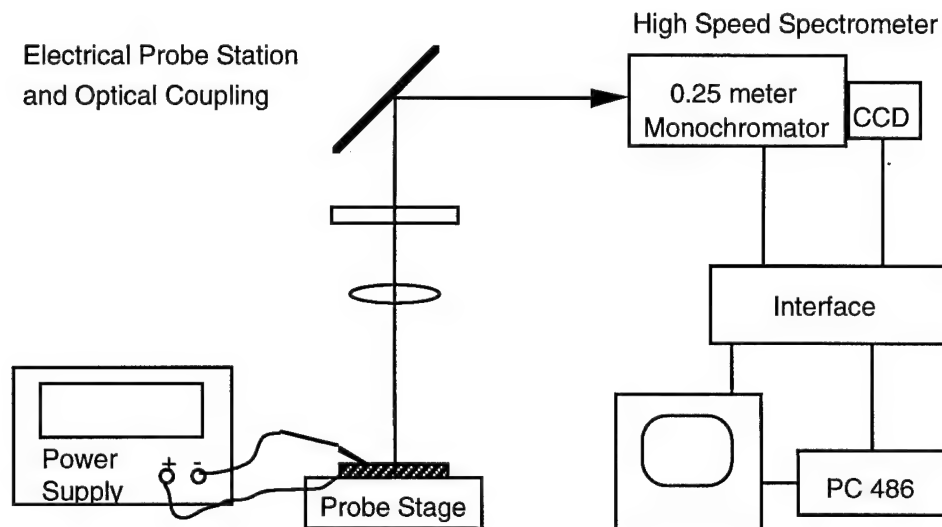


**FIGURE 3.6.3** Block diagram of the electroluminescence characterization system.

## REFERENCES

Cardona, M., "Raman spectroscopy applied to the characterization of semiconductors and semiconductor microstructures", SPIE Ramn and Luminescence Spectroscopy in Technology **822**, 2 (1987).

Melngailis, J., "Focused ion beam technology and applications", J. Vac. Sci. Technol. B **5**, 469 (1987).

Steckl, A. J., Mogul, H. C. and Mogren, S., "Localized fabrication of Si nanostructures by focused ion beam implantation", Appl. Phys. Lett. **60**, 1833 (1992).

Steckl, A. J., Xu, J., Mogul, H. C. and Mogren, S., "Doping-induced selective area photoluminescence in porous silicon", Appl. Phys. Lett. **62**, 1982 (1993).

Xu, J., Mogul, H. C. and Steckl, A. J., "Visible photoluminescence from stain-etched silicon nanostructures", Proc. of the 2nd International Symposium on Quantum Confinement **94-17**, 231 (1994).

Xu, J. and Steckl, A. J., "Fabrication of visibly photoluminescent Si microstructures by focused ion beam implantation and wet etching", Appl. Phys. Lett. **65**, 2081 (1994).

## Chapter 4

### Porous Si Light Emitting Patterns & Nanostructures

#### 4.1 Doping Effect on Porous Si Formation and Fabrication of Embedded Photoluminescent Porous Si Patterns with Sub-Micro Resolution

##### 4.1.1 Introduction

One of the major challenges in achieving porous-silicon-based optoelectronic devices is the integration of well-defined photoemissive porous silicon regions, with dimensions comparable to those provided by conventional microfabrication techniques, into a Si substrate where conventional devices can also be obtained. Conventional techniques of pattern transfer in Si, which usually involves photoresist and/or oxide as a mask, do not work readily because the process of porous silicon fabrication involves strong HF acid. Also, since porous silicon is susceptible to many chemicals and its photoluminescent property is chemically sensitive [Anderson, *et al.* (1993), Lauerhaas and Sailor (1993), Li, *et al.* (1993)], it is difficult to pattern the Si substrate using materials inert to HF, such as Si nitride, and remove those materials after porous silicon formation without damaging or changing the porous silicon properties. Therefore, development of novel techniques for selective fabrication of porous silicon is essential to the success of achieving Si optoelectronic devices. Two alternative porous silicon patterning methods have been reported recently using image projection during porous silicon anodic etching [Doan and Sailor (1992)] and multilayer-photoresist coating [Kalkhoran, *et al.* (1992)]. In the image projection method, positive and negative patterns of luminescent porous silicon are etched into *n*- and *p*-type Si substrates, respectively, by projecting a high-contrast image on the electrode surface during the anodic etching process. However this technique provides only a limited lateral resolution, on the order of 20  $\mu\text{m}$  [Doan and Sailor (1992)] and the technique is practically difficult to integrated into the existing Si technology. In the case of multilayer-photoresist coating, a standard photolithographic process is duplicated three times to coat the Si wafer with a triple-layer of photoresist and the best lateral resolution reported is about 3.0  $\mu\text{m}$  [Kalkhoran, *et al.* (1992)]. In addition the resolution obtained in both techniques is strongly process-dependent.

Previously work done at NanoLab on the fabrication of nanostructures in crystalline Si using focused ion beam (FIB) implantation followed by selective and crystallographically anisotropic chemical etching has been reported [Steckl, *et al.* (1992)]. In that process, shallow  $\text{Ga}^+$  FIB-implanted region with a dose of greater than  $1\text{E}15$  ions/ $\text{cm}^2$  has an almost zero etch rate in KOH solutions. This Si etch-stop is an extreme case of the well-known doping dependence of Si etch rate in many etchants including KOH, NaOH and ethylene-diamine pyrocatechol (EDP) solutions [Palik, *et al.* (1982)]. Subsequently, it was observed in this work that, if instead of KOH an HF:HNO<sub>3</sub>-based porous silicon stain-etchant is used, the onset of porous silicon formation can be significantly different in the implanted and unimplanted regions. This observation has led to the study of Si doping effect on the formation of porous silicon and its PL properties and its application in selective fabrication of light emitting porous silicon patterns [Steckl, *et al.* (1993)].

##### 4.1.2 Experimental Results

Materials used in this study of doping effect on the formation of porous silicon are Si dices of about  $1 \times 1 \text{ cm}^2$  cleaved from as-received CZ-grown *p*- and *n*-type (100) Si wafers with resistivity ( $\rho$ ) ranging from  $4 \times 10^{-3}$  to  $50 \Omega\text{-cm}$  using boron as *p*-type dopant and phosphorus as

*n*-type dopant. Table 4.1 details the type, doping concentration and hole concentration of the samples used in this study. The resistivities listed were measured using a four point probe. Doping concentrations were then obtained from the  $p$  vs.  $n/p$  chart assuming all impurities are ionized and neglecting the degeneracy of heavily doped substrates. For *n*-type samples, hole concentrations were then calculated from the known electron concentrations using the *mass-action law*:  $np = n_i^2$ , where  $n$  and  $p$  are electron and hole concentrations respectively and  $n_i$  is the intrinsic concentration, which is valid for both intrinsic and extrinsic materials under thermal equilibrium.

Table 4.1 Resistivity & doping (hole) concentrations of samples used

Type (n or p)	Resistivity ( $\Omega$ -cm)	Doping Concentration (ions/cm <sup>3</sup> )	Hole Concentration (holes/cm <sup>3</sup> )
n <sup>+</sup> (P)	0.13000	6.0000e+16	3504.2
n (P)	3.2000	1.5000e+15	1.4017e+05
n (P)	5.6000	8.0000e+14	2.6281e+05
n (P)	23.000	2.5000e+14	8.4100e+05
p <sup>+</sup> (B)	0.0043000	2.7000e+19	2.7000e+19
p <sup>+</sup> (B)	0.015000	6.5000e+18	6.5000e+18
p (B)	5.0000	2.5000e+15	2.5000e+15
p (B)	8.1000	1.6000e+15	1.6000e+15
p <sup>-</sup> (B)	32.400	4.1000e+14	4.1000e+14
p <sup>-</sup> (B)	49.800	2.6000e+14	2.6000e+14

The porous silicon was obtained by strictly chemical ("stain") etching [Fathauer, *et al.* (1992), Sarathy, *et al.* (1992), Shih, *et al.* (1992)], which was described in detail in chapter three, at room temperature in a solution of HF : HNO<sub>3</sub> : H<sub>2</sub>O with the composition of 1 : 3 : 5 by volume. The stain-etching technique was used instead of anodization because it is considerably easier to set-up than anodization and results in uniform porous silicon layers. The incubation time delay ( $t_1$ ) [Shih, *et al.* (1992)] which occurs between the insertion of the Si into the etching solution and the onset of porous silicon production was obtained under two conditions: (a) in normal "white" light ambient, the reflected color of the sample surface was monitored and the time at which the first change from metallic silver-gray to red-brown occurred was measured; (b) under UV (at 365 nm) illumination only, the time for first visible PL observation was noted.

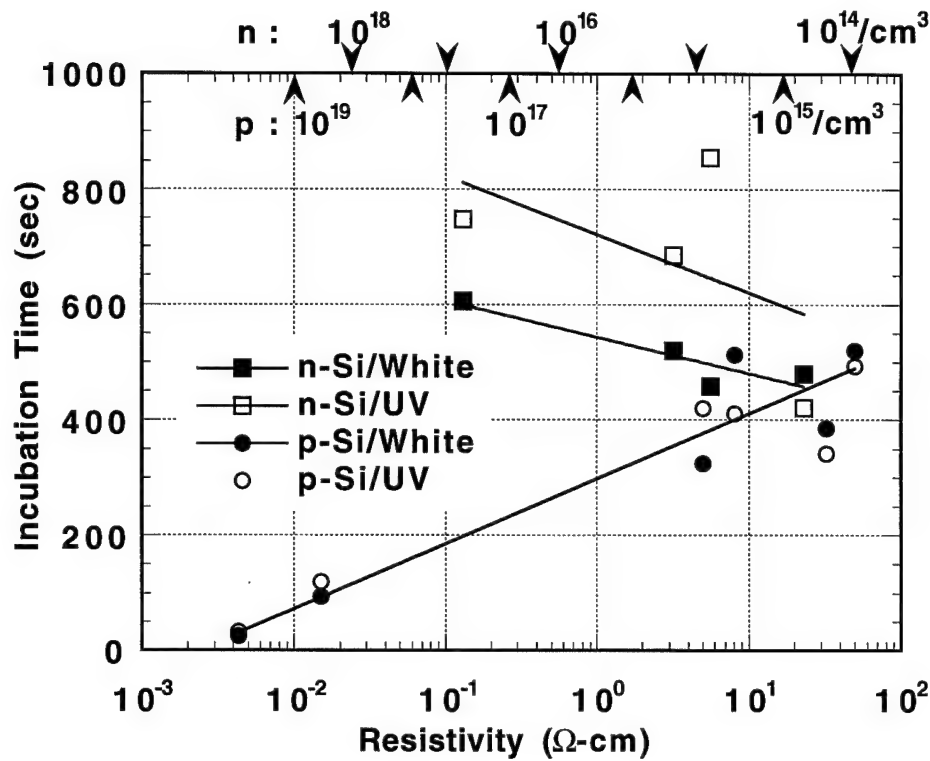


**FIGURE 4.1.1** Incubation time  $t_i$  as function of resistivity.

Shown in Fig. 4.1.1 are the average incubation time  $t_i$  of each sample as the function of resistivity for both  $n$ - and  $p$ -type materials obtained under either white light or UV illumination ambiance. The same general trend is obtained for both illumination conditions. Since all implantation experiments used stain-etching under white light ambient, quantitative discussion hereafter is restricted to  $t_i$  results obtained under this condition. The  $t_i$  for B-doped Si was generally smaller than for P-doped Si. The difference was increasingly pronounced for more heavily doped samples. For  $p$ -Si,  $t_i$  increased significantly with  $\rho$ , from  $\sim 0.5$  min for  $0.0043\ \Omega\text{-cm}$  to  $\sim 9$  min for  $50\ \Omega\text{-cm}$  with a transition resistivity at  $\sim 0.05\ \Omega\text{-cm}$  (doping concentration  $\sim 10^{18}/\text{cm}^3$ ). In contrast,  $n$ -Si substrates exhibited a weakly decreasing  $t_i$  with increasing  $\rho$ , from  $\sim 10$  min for  $0.13\ \Omega\text{-cm}$  to  $\sim 8$  min for  $\sim 20\ \Omega\text{-cm}$ . The values given in Fig. 4.1.1 represent averages over several samples at each data point. Occasionally, significant departures from the average  $t_i$  value was observed. The  $p^{++}$ -Si samples, however, always exhibited a very reproducible  $t_i$  of  $\leq 30$  sec.

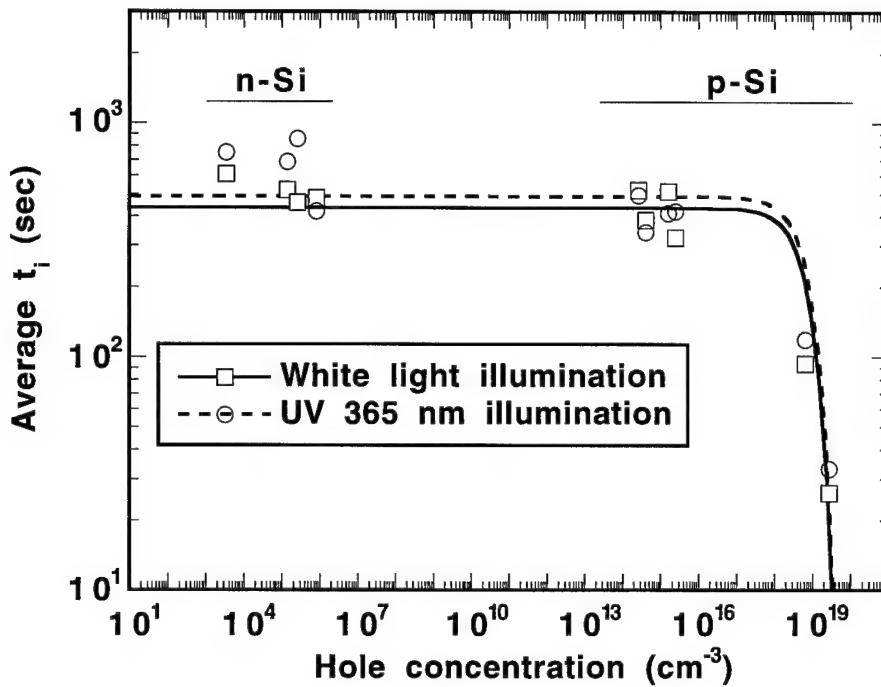


**FIGURE 4.1.2** Incubation time as a function of hole concentration of Si substrates.

Furthermore when we converted the samples' resistivity into their corresponding hole concentrations and plotted  $t_i$  as a function of hole concentration for both *n*- and *p*-type materials as shown Fig. 4.1.2, a more obvious trend was revealed indicating a strong dependence of the incubation time  $t_i$  on the hole concentration. It is clear from Fig. 4.1.2 that there exists a transition hole concentration between  $10^{18}$  and  $10^{19}/\text{cm}^3$ , above that concentration, the incubation time is very short and below that the  $t_i$  is much longer. This hole-dependent effect is consistent with the basic Si etching mechanism [Turner (1960), Nakagawa, *et al.* (1992)] which is initiated by the reaction of holes with Si atoms at the etching surface.

All samples etched under the above conditions show visible orange-red photoluminescence under UV or  $\text{Ar}^+$  488 nm excitation. The room temperatures photoluminescence spectra of stain-etched porous silicon, pumped by filtered UV radiation with emission at 365 nm from a 100 watts mercury (Hg) lamp through a fluorescence microscope, were measured with a 0.64 m monochromator equipped with photomultilayer tube (PMT) detector.

Typical photoluminescence spectra are shown in Fig. 4.1.3a for several Si substrates etched for  $t_i$  plus 2 min : 0.004  $\Omega\text{-cm}$   $p^{++}$ -Si; 5  $\Omega\text{-cm}$  *p*-Si; 3.2  $\Omega\text{-cm}$  *n*-Si; 10 kV  $\text{Ga}^+$  FIB-implanted *n*-Si. The photoluminescence spectrum for the  $p^{++}$  sample exhibits a symmetric signal in a broad band with a peak and full width at half-maximum (FWHM) of 660 nm (1.9 eV) and 133 nm, respectively. The other spectra have the major peak at 630 nm (1.95 eV). The minor peaks at 710 nm (1.75 eV) and at  $\sim 530$ -550 nm (2.3 eV) observed occasionally (from non-uniform areas) are due to contributions from the Hg source reflected by the non-etched Si surface. As shown in Fig. 4.1.3b, the photoluminescence spectrum of the  $p^{++}$  sample taken after only 14 sec past  $t_i$  also exhibits these additional features, which generally disappear if the process is continued for 2 min. The major peak at 1.9-1.95 eV (650 nm) is consistent with other reports [Fathauer, *et al.* (1992), Sarathy, *et al.* (1992), Shih, *et al.* (1992)] of photoluminescence from stain-etched porous silicon.

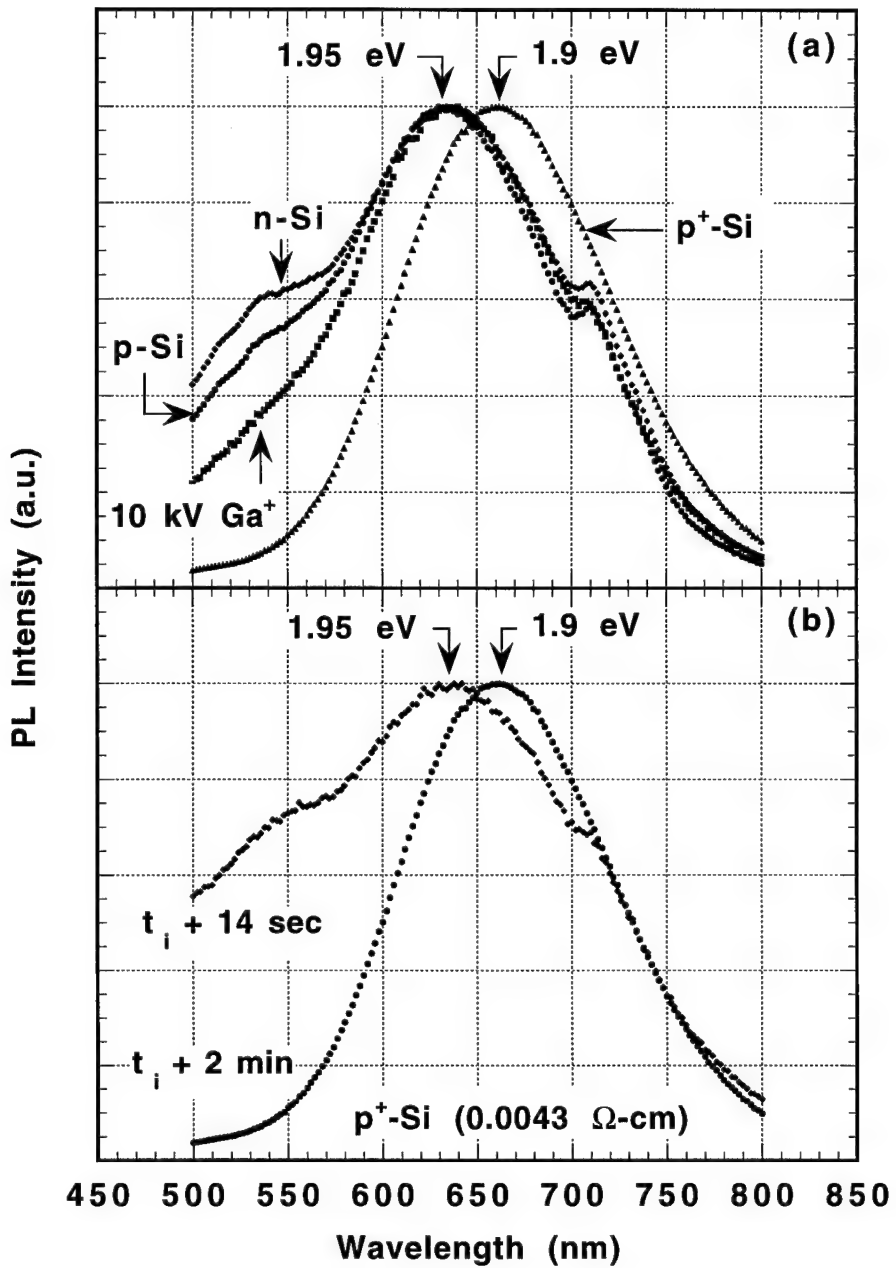


**FIGURE 4.1.3** Photoluminescence spectra of porous silicon on (a) *n*- and *p*-type substrates stain-etched for  $t_i$  plus 2 min:  $0.0043 \Omega\text{-cm } p\text{-Si}$ ;  $50 \Omega\text{-cm } p\text{-Si}$ ;  $3.2 \Omega\text{-cm } n\text{-Si}$ ;  $10 \text{ kV FIB Ga}^+ 10^{15}/\text{cm}^2$  into  $0.1 \Omega\text{-cm } n\text{-Si}$ ; (b)  $0.0043 \Omega\text{-cm } p\text{-Si}$  for 14 and 120 sec past  $t_i$ .

The PL peak energy and FWHM as a function of substrate resistivity for both *n*- and *p*-type Si etched for  $t_i$  plus 2 min is represented in Fig. 4.1.4. It is seen from Fig. 4.1.4 that despite the vast change in doping type and concentration the PL peak energy is almost same, which is quite in contrast to the incubation time  $t_i$  as seen from Fig. 4.1.1. This suggests that the photoluminescent property of porous silicon is not affected by Si doping. It was usually noted that, due to the differences in etch rate, usually  $p^{++}\text{-Si}$  show a stronger PL as compared to that of *n*- and *p*-Si etched for the same amount of time plus  $t_i$ . In addition, stronger PL were usually obtained for

samples etched longer. These are in consistent with the fact that heavily doped *p*-type materials have a short incubation time and faster etch rate so that for the same amount of etch time a thicker layer of porous silicon is formed on *p*<sup>++</sup> substrates. Also one can increase etching time to obtain a

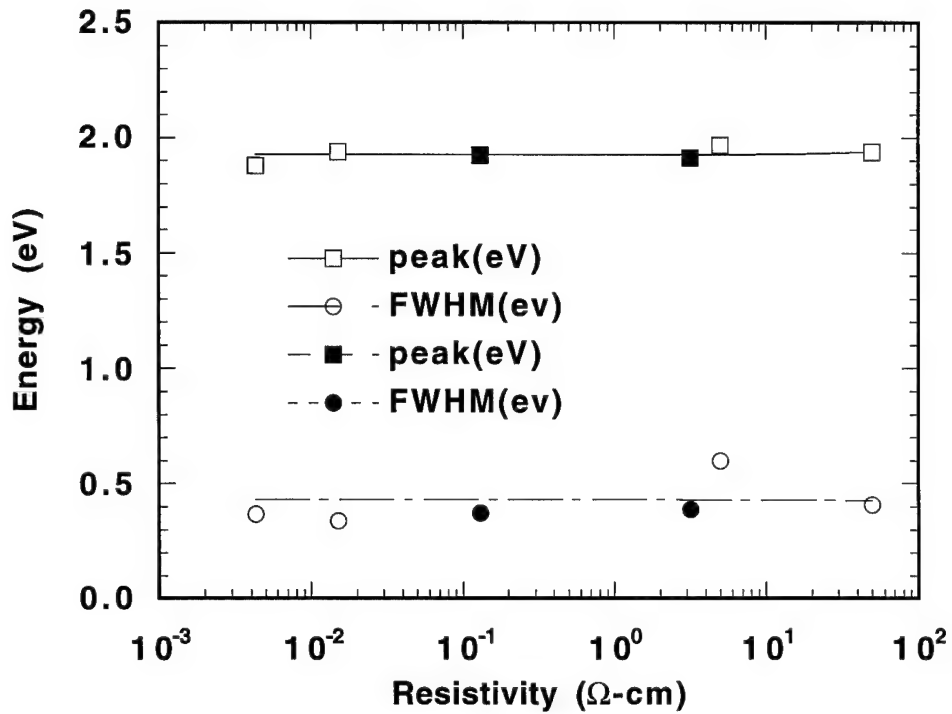


**FIGURE 4.1.4** PL peak and FWHM as a function of substrate resistivity for both *n*- and *p*-type Si etched for  $t_i$  plus 2 min.

thicker porous silicon layer and stronger photoluminescence. However, it was previously reported by Beale *et al.* [Beale, *et al.* (1986)], and was also observed in this work, that stain-etch is a self-limited process which tends to limit the ultimate thickness of porous silicon layer obtainable to be around  $\sim 1 \mu\text{m}$ . This is the result of thermodynamic equilibrium and can be qualitatively explained by the following two reasons: (1) the etchant which renders silicon porous will also etch porous silicon; (2) when the porous silicon layer becomes thicker, diffusion of both the oxidation agent ( $\text{NO}_2^-$ ) and oxide etchant ( $\text{F}^-$ ) into the porous silicon/Si interface becomes more difficult.

Scanning electron microscopy study of surface morphologies of porous silicon on substrates with different doping type and concentration reveal a wide range of porosities and pore sizes. For example, the surface morphologies of porous silicon on various substrates formed by stain-etching for 2 min past  $t_i$  are shown in Fig. 4.1.5 (a)-(f) for 0.13 and 3.2  $\Omega\text{-cm}$  *n*-Si, and for 50, 5, 0.015 and 0.004  $\Omega\text{-cm}$  *p*-Si. The *n*-Si samples exhibit only a minor degree of porosity. The *p*-Si samples show an increasing porosity level with decreasing  $\rho$ . The 0.004  $\Omega\text{-cm}$  *p*-Si sample stain-etched for only 14 seconds past  $t_i$  (Fig. 4.1.5 (g)) indicates that pores with  $\sim 100 \text{ nm}$  diameter have already formed. It is important to point out that these samples with different morphologies produce rather similar PL spectra, with only slight differences in the wavelength of peak emission.

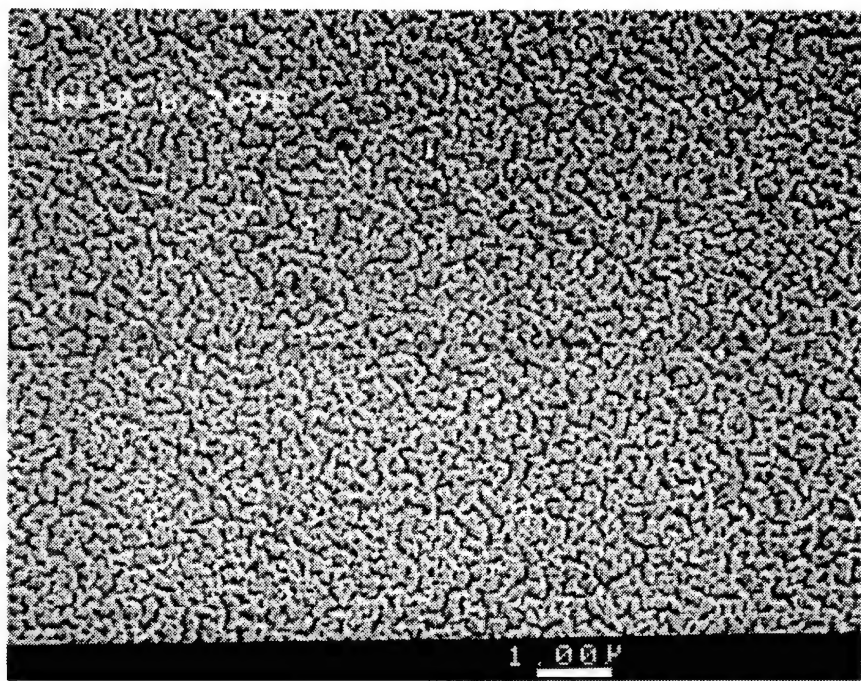


**FIGURE 4.1.5(a)** SEM micrograph (plan-view) of porous silicon regions of  $n^+$ -Si of  $0.13 \Omega\text{-cm}$  stain-etched for  $t_i$  plus  $\sim 2$  min.

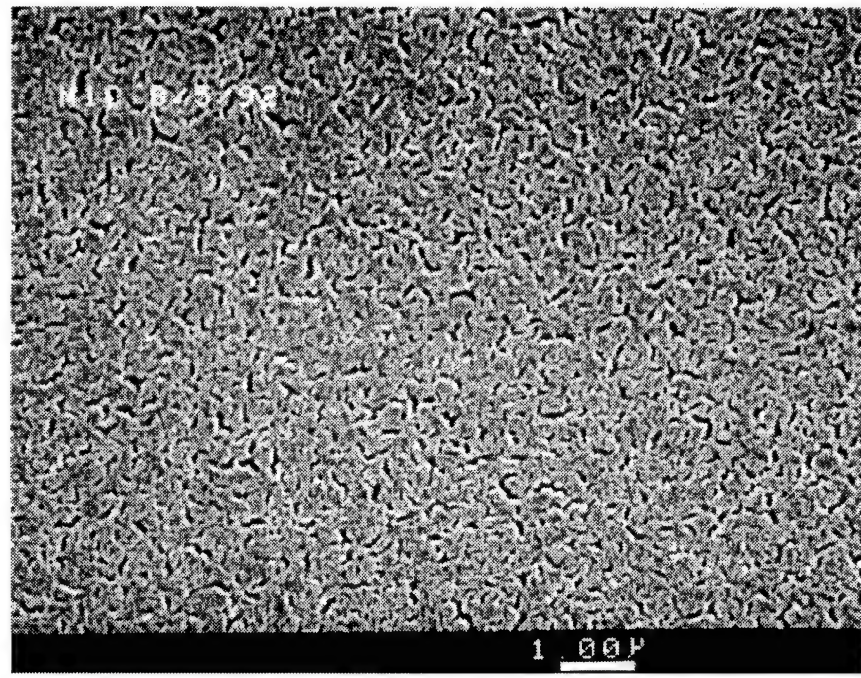


**FIGURE 4.1.5(b)** SEM micrograph (plan-view) of porous silicon regions of  $n$ -Si of  $3.2 \Omega\text{-cm}$  stain-etched for  $t_i$  plus  $\sim 2$  min.

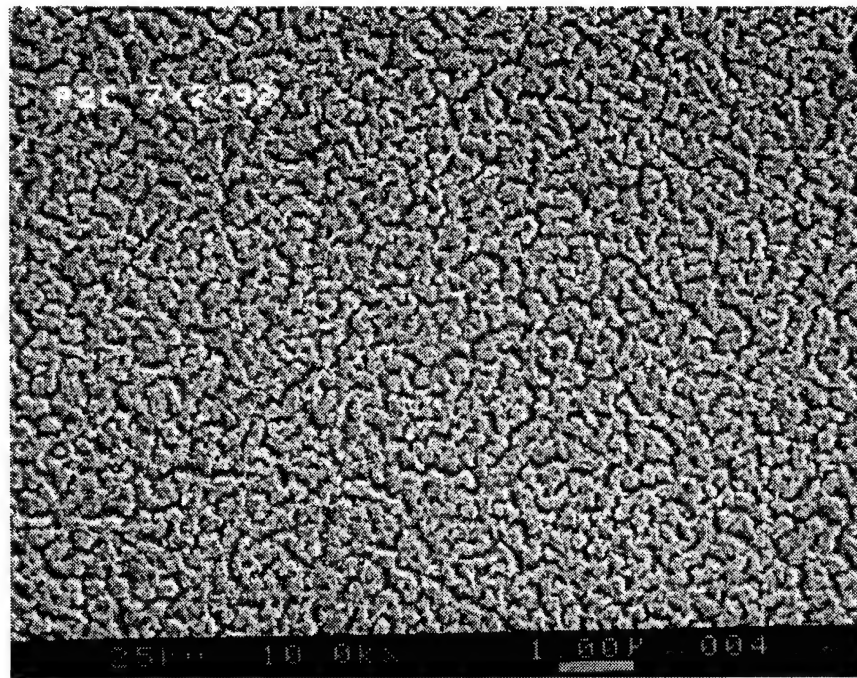


**FIGURE 4.1.5(c)** SEM micrograph (plan-view) of porous silicon regions of  $p^-$ -Si of  $50 \Omega\text{-cm}$  stain-etched for  $t_i$  plus  $\sim 2$  min.

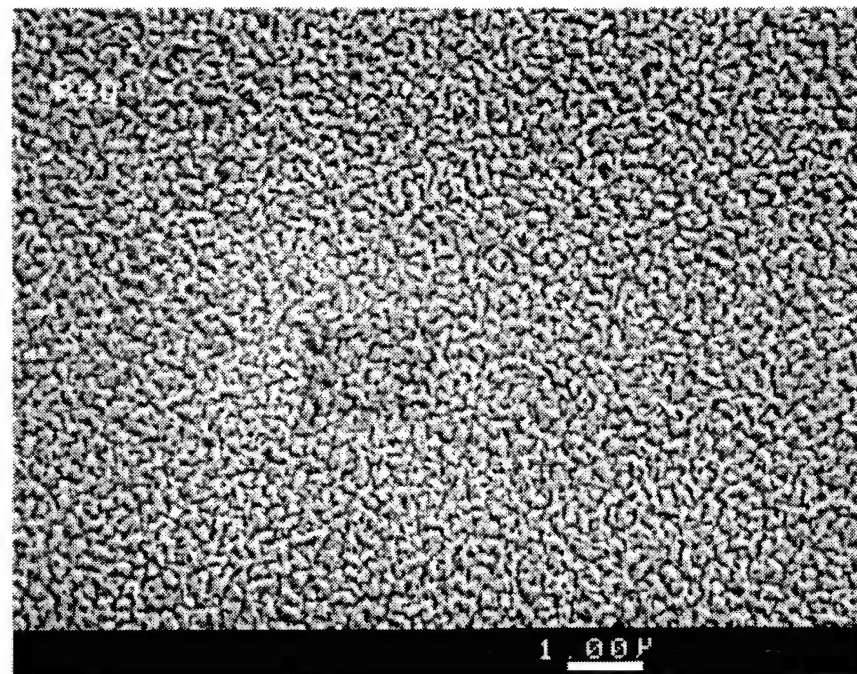


**FIGURE 4.1.5(d)** SEM micrograph (plan-view) of porous silicon regions of  $p$ -Si of  $5 \Omega\text{-cm}$  stain-etched for  $t_i$  plus  $\sim 2$  min.

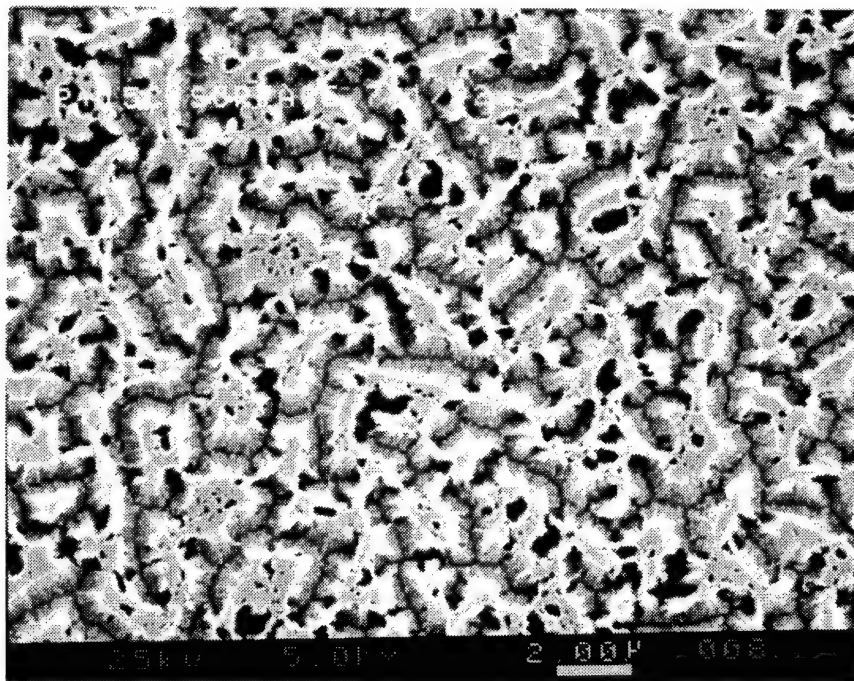


**FIGURE 4.1.5(e)** SEM micrograph (plan-view) of porous silicon regions of  $p^+$ -Si of  $0.015 \Omega\text{-cm}$  stain-etched for  $t_i$  plus  $\sim 2$  min.

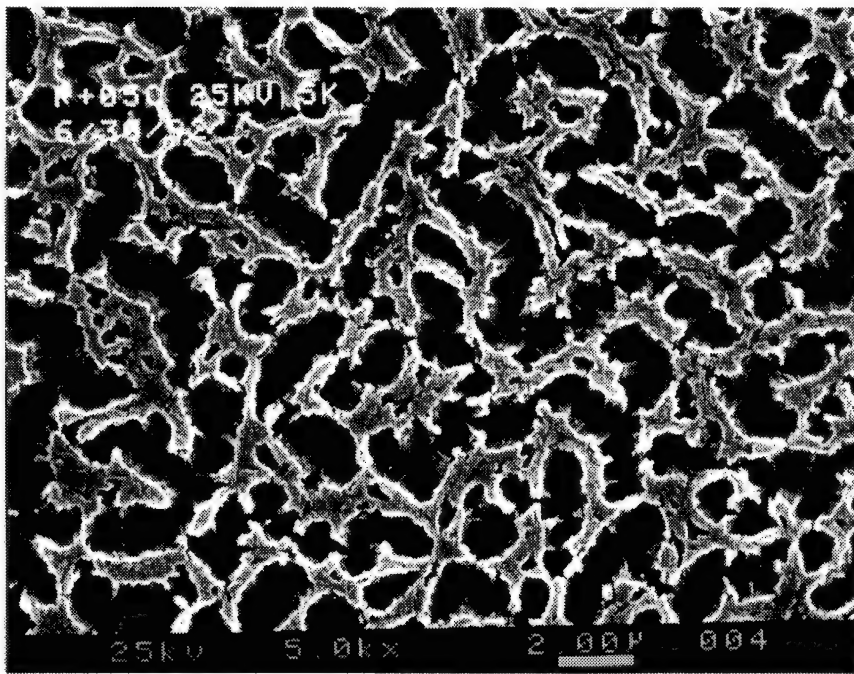


**FIGURE 4.1.5(f)** SEM micrograph (plan-view) of porous silicon regions of  $p^+$ -Si of  $0.004 \Omega\text{-cm}$  stain-etched for  $t_i$  plus  $\sim 2$  min.

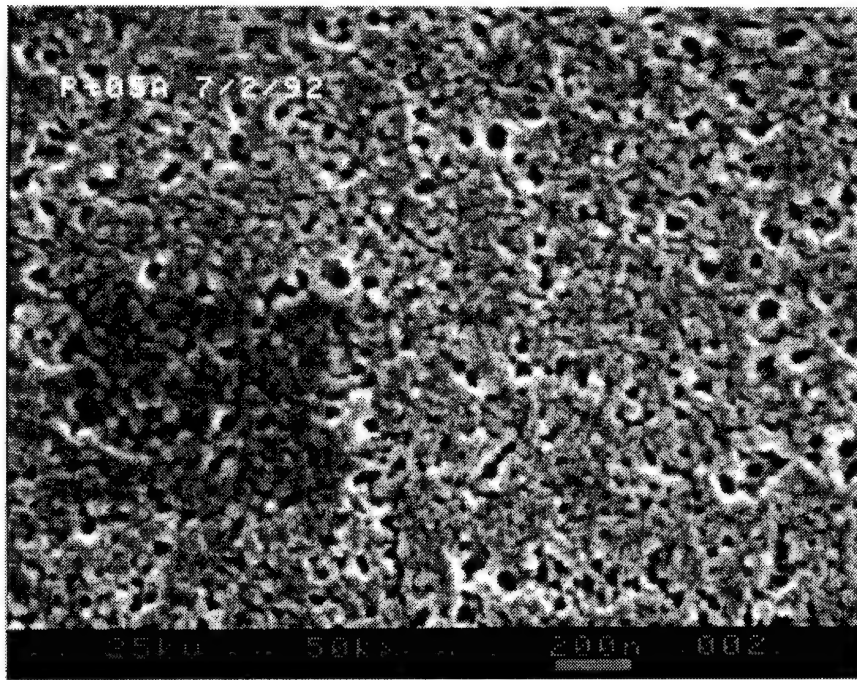


**FIGURE 4.1.5(g)** SEM micrograph (plan-view) of porous silicon regions of  $p^+$ -Si of  $0.004 \Omega\text{-cm}$  stain-etched for  $t_i$  plus  $\sim 14$  seconds.

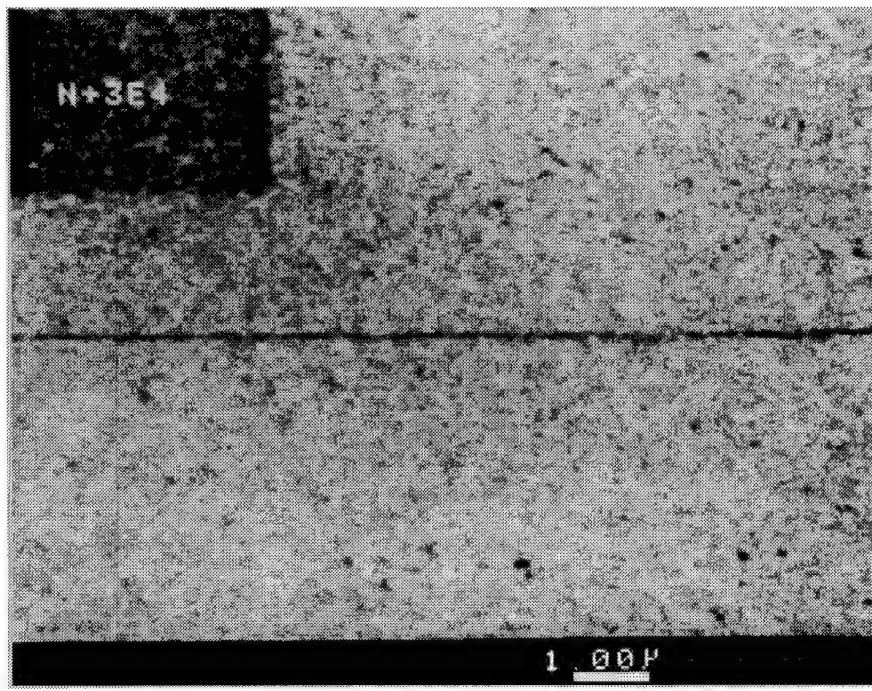


**FIGURE 4.1.5(h)** SEM micrograph (plan-view) of porous silicon regions of  $10 \text{ kV FIB Ga} + 10^{15}/\text{cm}^2$  into  $n\text{-Si}$  for  $t_i$  plus  $\sim 1$  min.

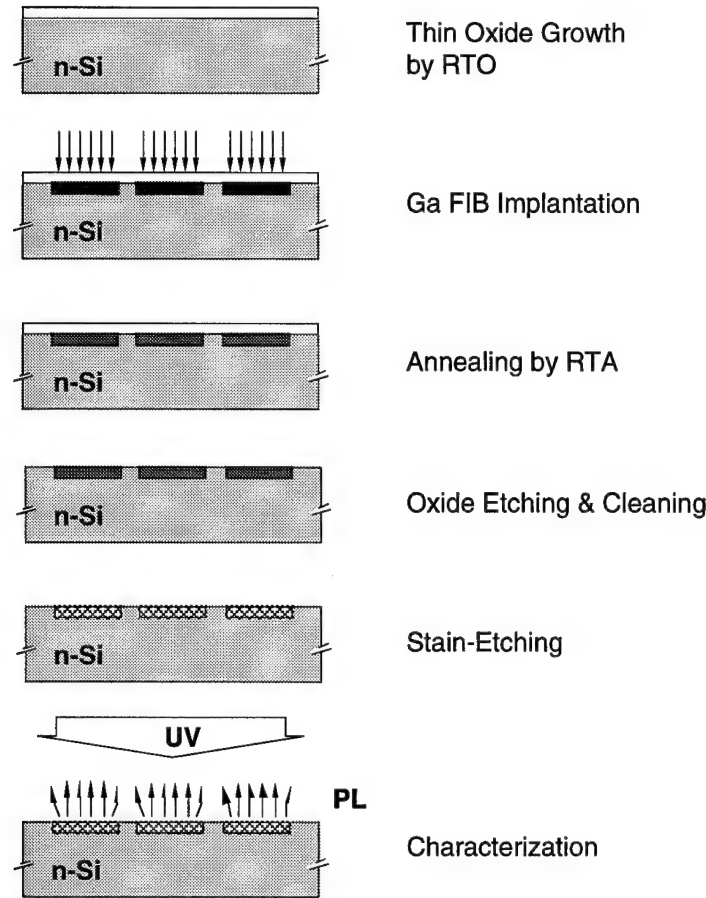


**FIGURE 4.1.6** Process flow for selective fabrication of light-emitting porous silicon pattern.

Utilizing the doping dependence on  $t_i$ , a process was developed to fabricate selective light emitting porous silicon patterns embedded in conventional Si. The process was outlined in Fig. 4.1.6, which combines localized Ga<sup>+</sup> FIB-implantation and masked B<sup>+</sup> broad beam (BB) implantation into *n*-type Si followed by rapid thermal annealing (RTA) and stain-etching in HF:HNO<sub>3</sub>:H<sub>2</sub>O solution. It was observed that the RTA can quench the  $t_i$  difference between *p*<sup>++</sup>-Si and *n*- or *p*-Si if the surface is not protected during annealing. The reason for the  $t_i$  of uncovered *n*- and *p*-Si being reduced after annealing may result from surface contamination. Therefore, for un-patterned Ga<sup>+</sup> FIB implantation, a protection thin layer of Si oxide  $\sim 100$  Å was grown using rapid thermal chemical vapor deposition of dry O<sub>2</sub> before implantation and was present during the RTA. The Ga<sup>+</sup> was implanted through the thin oxide layer. After RTA the SiO<sub>2</sub> layer was removed by dipping

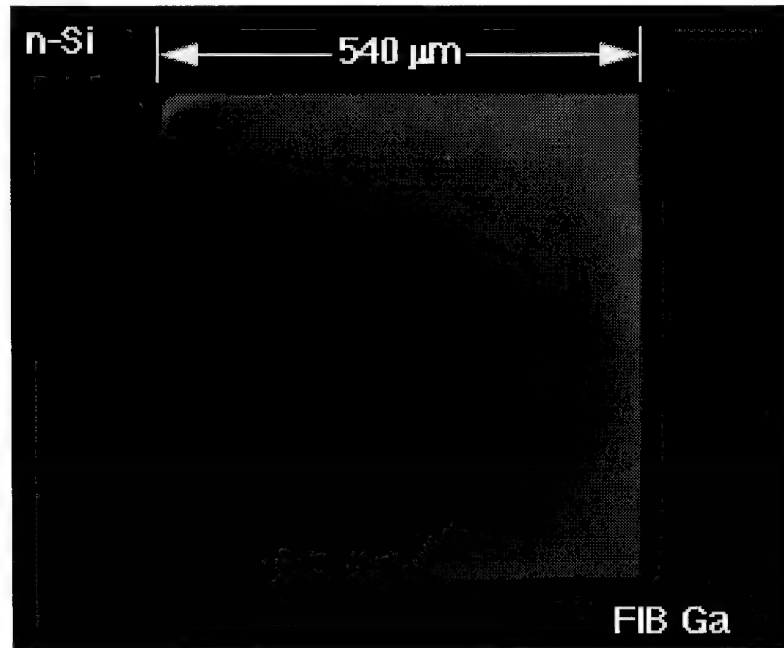


**FIGURE 4.1.7** PL micrograph of FIB  $\text{Ga}^+$  implantation-induced localized photoemission pattern of  $500 \times 500 \mu\text{m}^2$ .

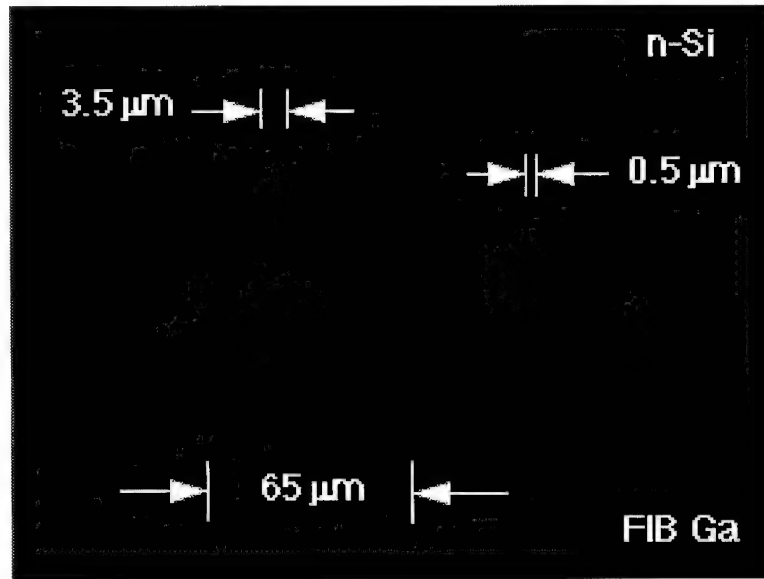


**FIGURE 4.1.8** PL micrograph of FIB  $\text{Ga}^+$  implantation-induced localized photoemission pattern. Line pattern with  $3.5$  and  $0.5 \mu\text{m}$  line widths implanted at  $30 \text{ kV}$  with  $10^{14}/\text{cm}^2$ .

in 10% HF for several minutes before stain-etching in  $\text{HF:HNO}_3:\text{H}_2\text{O}$ . These added steps prevented any possible surface contamination which might occur during the annealing process and therefore the initial incubation time difference between *n* - and *p*-type materials is preserved. During the stain-etching the total etching time was carefully controlled such that light emitting porous silicon was formed only in the  $\text{Ga}^+$  implanted regions. Examples of selective light emitting porous silicon pattern, using  $\text{Ga}^+$  FIB implantation into (100) *n*-Si and stain-etching, is shown by their photoluminescent imaging as in Fig. 4.1.7 and 4.1.8. The images were obtained by a color

CCD camera while the areas pictured were under UV 365 nm illumination through a fluorescent microscope. The larger orange-red square in Fig. 4.1.7, with dimensions of  $540 \times 540 \mu\text{m}^2$ , was  $\text{Ga}^+$  FIB implanted into  $\sim 0.1 \Omega\text{-cm}$  (100)  $n$ -Si at 10 kV with a dose of  $10^{15}/\text{cm}^2$  followed by RTA at  $550^\circ\text{C}$  for 60 sec. It was then stain-etched for a total time of  $t_i$  plus 1 min. The pattern of the UC logo ( $3.5 \mu\text{m}$ ) and  $0.5 \mu\text{m}$  lines in Fig. 4.1.8 was obtain by  $\text{Ga}^+$  FIB implantation into  $3 \Omega\text{-cm}$  (100)  $n$ -Si at 30 kV with  $10^{14} \text{ Ga}^+/\text{cm}^2$  followed by RTA at  $600^\circ\text{C}$  for 30 sec. This sample was also stain-etched for a total time of  $t_i$  plus 1 min. Upon UV excitation, photoemission from the implanted regions only was clearly observable.

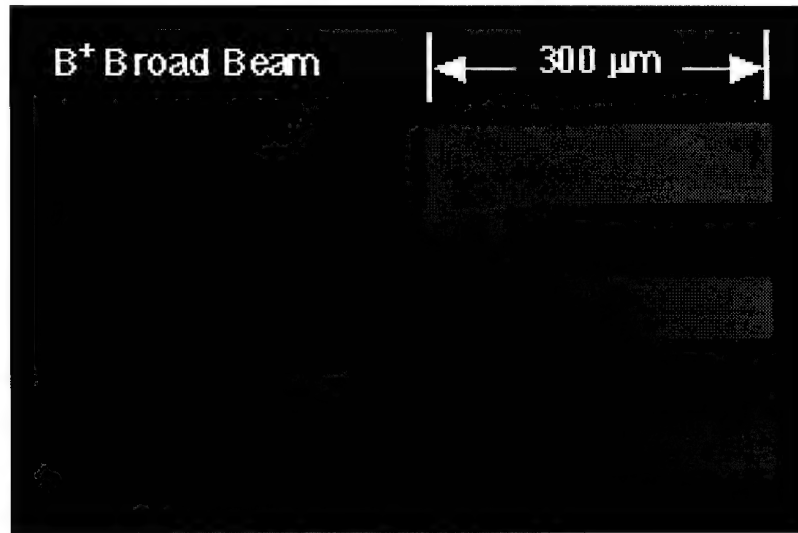


**FIGURE 4.1.9** PL micrograph of broad beam  $\text{B}^+$  implantation-induced localized photoemission patterns.

Similar results were also obtained from stain-etched masked  $\text{B}^+$  BB implanted  $3 \Omega\text{-cm}$   $n$ -type Si at 37 kV with a dose of  $10^{15}/\text{cm}^2$ . Shown in Fig. 4.1.9 is the PL image of  $\text{B}^+$  implanted pattern stain-etched for 1.5 min. The dark background surrounding each pattern is unimplanted  $n$ -Si. At these low implantation energies the  $\text{B}^+$  and, especially, the  $\text{Ga}^+$  have very shallow penetration depths of 130 nm and 9 nm, respectively. It can be, therefore, concluded that a nanometer-thin doped layer is sufficient for providing area selectivity in porous silicon formation and strong localized photoemission. The pattern of  $0.5 \mu\text{m}$  lines is quite sharp, indicating that sub-micrometer-scale resolution is easily achievable with this process.

During visual observation, the colors are the same for all samples: orange-red in the implanted regions and dark blue background. The PL spectrum obtained from the large  $\text{Ga}^+$ -implanted square is quite similar to those obtained from stain-etched unimplanted substrates, with a peak at 1.98 eV (see Fig. 4.1.3). The surface of the 10 kV  $\text{Ga}^+$  FIB-implanted sample (Fig. 4.1.4 (h)) is considerably smoother than that of stain-etched unimplanted samples. Only occasional pores, with dimensions  $\leq 100 \text{ nm}$ , are observed at higher magnification.

It was observed that if stain-etching was conducted on as-implanted samples without the RTA the implanted region had a much longer  $t_i$  than the surrounding area leading to a PL image complementary to the implantation pattern. For example, Fig. 4.1.10 is PL image taken from a stain-etched  $\text{B}^+$  BB implanted  $n$ -Si without RTA. After 5.5 min etching the implanted area, represented by the pattern "A4", is still not photoluminescent while the surrounding areas have

became photoluminescent. This suggests that amorphized area as in the implanted region can not be stain-etched to become light emitting porous silicon. This observation led to a systematic study on the relationship between crystallinity and photoluminescence in porous silicon which will be discussed in great detail in chapter 5.

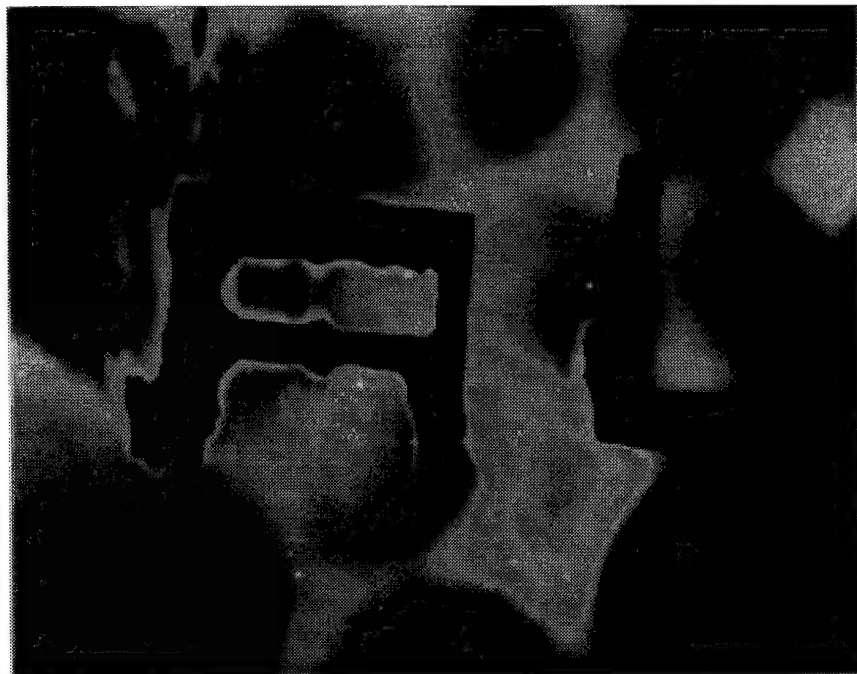


**FIGURE 4.1.10** PL micrograph of a stain-etched as-implanted pattern. The  $B^+$  BB implantation was done at 37 kV with  $10^{15} /cm^2$  into  $3 \Omega\text{-cm}$  n-Si. The sample was then stain-etched for a total of 5.5 min.

#### 4.1.3 Summary

In summary, Si doping effect on the incubation time of porous silicon formation by stain-etching of Si in HF:HNO<sub>3</sub>:H<sub>2</sub>O was systematically studied and a significant hole dependence was observed. The PL spectra of porous silicon of different doping type and concentration are very similar with a peak of  $\sim 1.94$  eV and FWHM of 0.5 eV despite significant difference in their incubation times and surface morphology. Combined with Ga<sup>+</sup> FIB- and B<sup>+</sup> BB-implantation doping, this effect has been utilized to produce selective-area photoemission in porous silicon. Using 30 kV FIB Ga<sup>+</sup> implantation, sub-micron photoemitting patterns have been obtained for the first time. This represents a considerably higher resolution than for the image projection lithography (20  $\mu\text{m}$ ) and multi-photoresist-layer coating (3  $\mu\text{m}$ ) processes previously reported for anodized porous silicon. The resolution is defined by FIB implantation and is not affected by the etching process. The process can be easily incorporated into conventional semiconductor fabrication technology.

#### REFERENCES

Anderson, R. C., Muller, R. S. and Tobias, C. W., "Chemical surface modification of porous silicon", *J. Electrochem. Soc.* **140**, 1393 (1993).

Beale, M. I. J., Benjamin, J. D., Uren, M. J., Chew, N. G. and Cullis, A. G., "The formation of porous silicon by chemical stain etches", *J. Crys. Grow.* **75**, 408 (1986).

Doan, V. V. and Sailor, M. J., "Photolithographic fabrication of micron-dimension porous Si structures exhibiting visible luminescence", *Applied physics letters* **60**, 619 (1992).

Fathauer, R. W., George, T., Ksendzov, A. and Vasquez, R. P., "Visible luminescence from silicon wafers subjected to stain etches", *Appl. Phys. Lett.* **60**, 996 (1992).

Kalkhoran, N. M., Namavar, F. and Maruska, H. P., "NP heterojunction porous silicon light-emitting diode", *Mat. Res. Soc. Symp. Proc.* **256**, 89 (1992).

Lauerhaas, J. M. and Sailor, M. J., "Chemical modification of the photoluminescence quenching of porous silicon", *Science* **261**, 1567 (1993).

Li, K.-H., Tsai, C., Sarathy, J. and Campbell, J. C., "Chemically induced shifts in the photoluminescence spectra of porous silicon", *Appl. Phys. Lett.* **62**, 3192 (1993).

Nakagawa, K., Nishida, A., Shimada, T., Yamaguchi, H. and Eguchi, K., "Fine structure of porous Si with visible photoluminescence", *Jpn. J. Appl. Phys.* **31**, L515 (1992).

Palik, E. D., J.W. Faust, J., Gray, H. F. and Greene, R. F., "Study of the etch-stop mechanism in silicon", *J. Electrochem. Soc.* **129**, 2051 (1982).

Sarathy, J., Shih, S., Jung, K., C., T., Li, K.-H., Kwong, D.-L., Campbell, J. C., Yau, S.-L. and Bard, A. J., "Demonstration of photoluminescence in nonanodized silicon", *Appl. Phys. Lett.* **60**, 1532 (1992).

Shih, S., Jung, K. H., Hsieh, T. Y., Sarathy, J., Campbell, J. C. and Kwong, D. L., "Photoluminescence and formation mechanism of chemically etched silicon", *Appl. Phys. Lett.* **61**, 1863 (1992).

Steckl, A. J., Mogul, H. C. and Mogren, S., "Localized fabrication of Si nanostructures by focused ion beam implantation", *Appl. Phys. Lett.* **60**, 1833 (1992).

Steckl, A. J., Xu, J., Mogul, H. C. and Mogren, S., "Doping-induced selective area photoluminescence in porous silicon", *Appl. Phys. Lett.* **62**, 1982 (1993).

Turner, D. R., "On the mechanism of chemically etching germanium and silicon", *J. Electroch. Soc.* **107**, 810 (1960).

## 4.2 Light Emitting Si Nanostructures

### 4.2.1 Introduction

The integration of optically active components onto a Si-based chip allows further functional integration of electronics and optics. This will consequently lead to the realization of new concepts such as "Photonic Integrated Circuits". The use of semiconductor Si and Si technology in this new field is highly desirable because of the low cost of Si material and the highly developed Si technology. However the inability of emitting visible light and the low luminescence efficiency at near infrared of conventional crystalline Si, due to the indirect bandgap (1.11 eV at 300°K), has limited its application in many aspects of optoelectronics while it is leading in many areas of microelectronics.

In order to achieve monolithic Si-based integrated optoelectronic devices, one needs to fabricate optically active Si structures with acceptable lithographic resolution embedded in the same substrate where conventional Si devices can also be fabricated. In the previous section, we have discussed in detail the fabrication of embedded Si light emitting pattern with sub-micron resolution using localized doping by  $\text{Ga}^+$  focused ion beam (FIB) implantation followed by stain etching in  $\text{HF:HNO}_3:\text{H}_2\text{O}$ . Previously in NanoLab, Si nanostructures in the form of cantilevers located at the top of truncated pyramids etched into the Si substrate [Steckl, *et al.* (1992)] have been fabricated by  $\text{Ga}^+$  FIB implantation followed by anisotropic etching in KOH. In this section the development of a process for fabrication of the first photoluminescent Si micro- and nano-structures is described and discussed.

### 4.2.2 Experimental Results

The overall fabrication process is outlined in Fig. 4.2.1. The process starts with CZ grown P-doped (100) *n*-type Si substrates with a resistivity of 5 - 7  $\Omega\text{-cm}$ . A high dose of

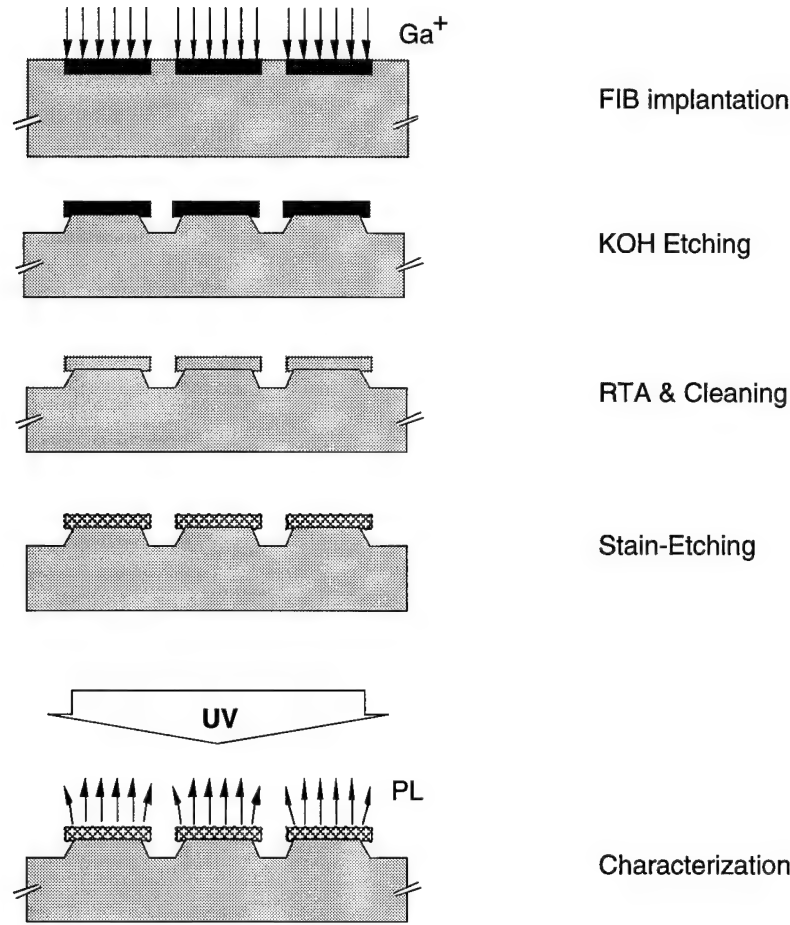


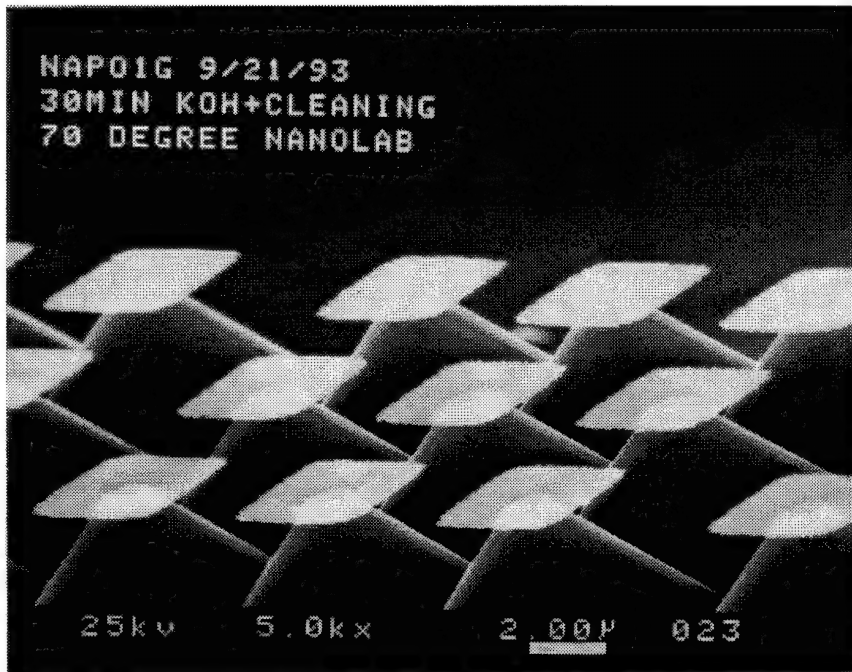
**FIGURE 4.2.1** Overall process schematic of the fabrication of optically active Si micro- and nano-structures.

$\text{Ga}^+$  ions ( $10^{16}/\text{cm}^2$ ) was first implanted locally into  $n$ -Si substrate at 30 kV using a NanoFab 150 FIB implanter, either on-axis or off-axis to varying degrees. This implantation produces a highly  $p$ -type doped region with a doping concentration high enough to introduce an etch-stop mechanism in some Si etchants such as KOH [Palik, *et al.* (1982)]. Nanostructures of various forms were then obtained by anisotropic etching of either as-implanted or annealed samples. The anisotropic etching was performed in a Teflon beaker containing KOH-based anisotropic etchant. The recipes used are KOH mixed with either isopropyl alcohol (IPA) and deionized water (DI) or with DI only in a volume composition of 16 : 11: 20 (recipe #1: "R1") and 1: 5 (recipe #2: "R2"), respectively. The etching temperature was automatically controlled to a constant value  $\pm 1^\circ\text{C}$  within the range of between  $70^\circ\text{C}$  and  $85^\circ\text{C}$ . To achieve etching uniformity, the solution was normally stirred at 150 rpm by a magnetic stirrer. Rapid thermal annealing (RTA), used to anneal the implantation damage and to activate the dopant, was performed in  $\text{N}_2$  ambient at  $600^\circ\text{C}$  for 30 sec either before or after the anisotropic etching. Immediately after the anisotropic etching and annealing (only for samples not annealed before KOH etching), the samples were carefully cleaned with a modified RCA (mRCA) process [Aslam, *et al.* (1993)] to eliminate the potassium contamination introduced during the previous step. The mRCA cleaning process includes soaking for twenty minutes in a fresh solution of  $\text{H}_2\text{SO}_4 : \text{H}_2\text{O}_2$  in the ratio of 4 : 1 (by volume) at room temperature followed by 2 min DI rinsing and dry in slow  $\text{N}_2$  flow. This cleaning step was found to be essential to the success of achieving localized photoemission from Si nanostructures upon stain-etching. Finally, the Si nanostructures were rendered porous by stain-etching in a solution of  $\text{HF} : \text{HNO}_3 : \text{H}_2\text{O}$  with a volume ratio of 1 : 3 : 5 for a few minutes under ambient light. Scanning electron

microscopy and photoluminescent spectroscopy and microscopy were used to study the structural and optical characterization of the Si nanostructures at different processing stages. PL measurements were done at room temperature using Ar<sup>+</sup> 488 nm excitation. The laser beam was focused to a spot of  $\sim 100 \mu\text{m}$  in diameter. The laser power at the sample was measured to be  $\sim 8.5 \text{ mW}$ . The PL signal was dispersed by a 0.5m monochromator and detected by a photomultiplier (PMT).

#### A. Si Nanostructures

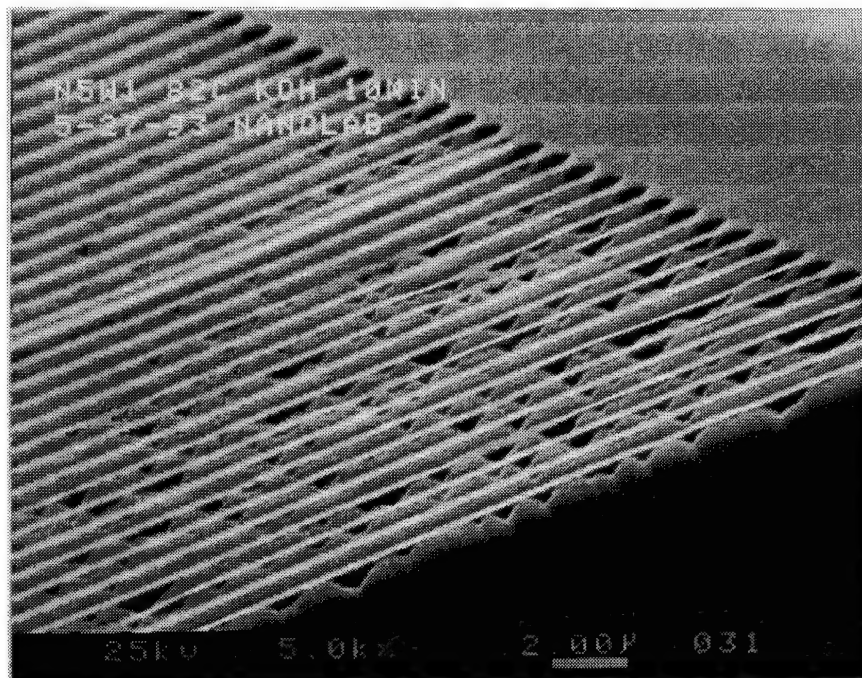
Si nanostructures in the form of cantilevers located at the top of truncated pyramids etched into the Si substrate and Si air bridges across two large cantilevers, with very high length-to-width aspect ratio (up to 100), were first fabricated by anisotropic etching the as-implanted or annealed samples. Off-axis implantation was studied and chosen to maximize the undercut effect [Bean (1978)] for obtaining complete-undercut air-bridges. Fig. 4.2.2 shows a tilted-view SEM picture of an array of Si cantilevers of  $4 \times 4 \mu\text{m}^2$  obtained by anisotropic etching in R1 solution of an implanted and annealed sample at 71°C for 30 min. In general, the cantilevers are very thin and uniform, with more than 1  $\mu\text{m}$  undercut on each side. The surfaces of the cantilevers are clean and free of redeposition after the mRCA cleaning. It is also worth noting that the edges of these cantilevers are not very smooth, possibly resulting from a combination of extended etching and slight misalignment of the on-axis implantation.



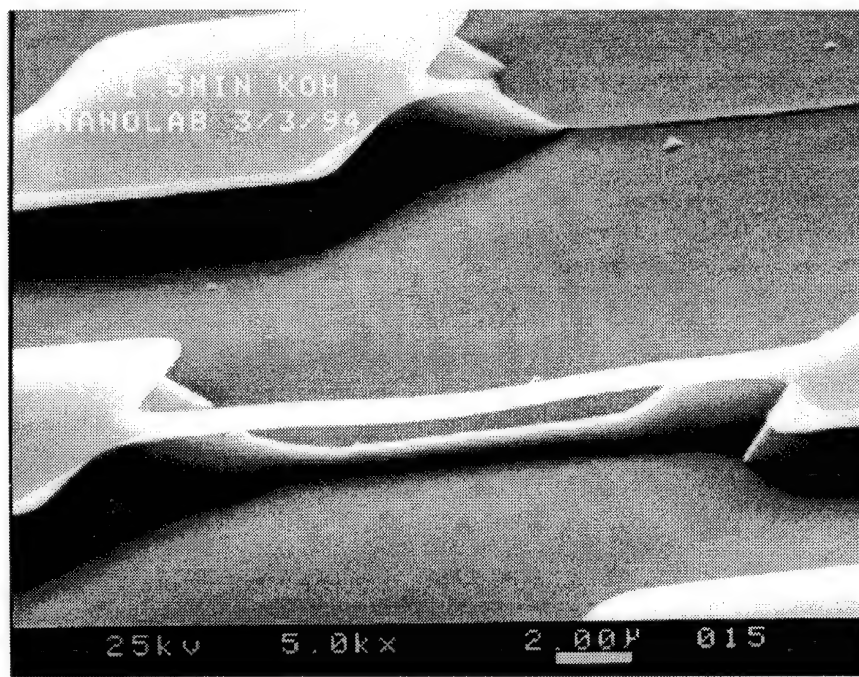
**FIGURE 4.2.2** SEM micrograph (tilted-view) of Si  $4 \times 4 \mu\text{m}^2$  cantilevers: on-axis FIB, 30 min KOH etching of annealed sample in R1 at 71°C.

Figure 4.2.3 shows an example of Si air bridges with dimensions of  $0.5 \mu\text{m} \times 50 \mu\text{m}$  produced by anisotropic etching (of an annealed sample) for 10 min in R1 solution at 82°C. The implantation was done at about 45° rotation off the  $<110>$  axis. It can be seen from the SEM picture that complete undercut, along most of the length, can be achieved by using this technique. For the implantation conditions utilized, the thickness of the nanostructures is estimated to be

around 10 nm. As seen from Figs. 4.2.2 & 3, these nanostructures are partially transparent to the 25 keV electrons used in the SEM.



**FIGURE 4.2.3** SEM micrograph (tilted-view) of Si  $0.5 \mu\text{m} \times 50 \mu\text{m}$  air-bridges: off-axis FIB and 10 min KOH etching of annealed sample in R1 at  $82^\circ\text{C}$ .



**FIGURE 4.2.4** SEM micrograph (tilted-view) of Si air-bridge of  $2 \mu\text{m} \times 20 \mu\text{m}$  obtained by:  $25^\circ$  off-axis FIB implantation into (100) *n*-Si and 1.5 min KOH etching of the as-implanted sample in R2 at  $81^\circ\text{C}$ .

Another example of Si nanostructures in the form of air-bridge etched in recipe R2 is shown in Fig. 4.2.4, which is a 2  $\mu\text{m}$  wide and 20  $\mu\text{m}$  long bridge hanging over two  $10 \times 10 \text{ mm}^2$  Si cantilevers. In this case the implantation was done at  $25^\circ$  off the  $\langle 110 \rangle$  axis and the etching was performed on the as-implanted sample. It is clear that the materials under the bridge was completely etched away. The fact that this sample was etched in recipe R2 for only 1.5 minutes and the narrower air-bridge of 1  $\mu\text{m}$  wide was already etched away as shown in the upper-left corner of Fig. 4.2.4 indicated that recipe R2 is a more aggressive anisotropic etchant with a faster undercut capability.

#### B. Undercut and Annealing Effect

It is well known that undercut, in anisotropic etching of (100) Si, normally occurs at the outside (convex) corners in masked (or implanted) structures [Bean (1978)]. This effect can be enhanced and utilized to obtain completely undercut air-bridges as shown in Fig. 4.2.3 & 4 by rotation of the substrate orientation with respect to the implantation direction [Berry and Caviglia (1983)]. To optimize the undercut enhancement by this off-axis implantation, an O-ring type of pattern was implanted and etched to observe the orientation dependence of the undercut. Figure 4.2.5 shows the tilted-view SEM picture of such a structure after 2 min etching using recipe R2. The anisotropic etching was carried out on the as-implanted sample. It is obvious that the undercut rate is orientation dependent and is fastest along the directions indicated by the eight-fold symmetric lines in Fig. 4.2.5, with the smallest angle towards to the [110] direction being  $\sim 22.5^\circ$ . As shown in the SEM some parts of the air-bridges had "collapsed" on to the bottom substrate. However, closer examination of the fallen bridges revealed that these bridges did not break and were laying on the ground. It was also observed that the undercut effect is more significant for as-implanted samples than for annealed ones. This can be explained by the reduction of  $\text{Ga}^+$  concentration due to out diffusion during RTA.



**FIGURE 4.2.5** SEM micrograph (tilted-view) of orientation dependence of undercut: 2 min etching of as-implanted sample in R2 at 82°C.

We also studied the effect of annealing and cleaning on the shape and stability of already formed nanostructures. Figures 4.2.6(a), (b) and (c) are tilted-view of SEM micrographs of part of the O-ring described above in its three different stages: (a) just after KOH etching of the as-implanted sample; (b) after RTA annealing of the etched sample at 600°C for 30 sec in N<sub>2</sub>; and (c) after annealing and modified RCA cleaning process (soaking in fresh-made H<sub>2</sub>SO<sub>4</sub>:H<sub>2</sub>O<sub>2</sub> solution). It was clear from Fig. 4.2.6(a) and (b) that, while the nanostructure maintained its overall shape and did not break after RTA, annealing of the nanostructure resulted in some stretch of the structures, primarily in the lateral direction, because of the out diffusion of implanted Ga<sup>+</sup> and the release of the stress. Since as-implanted area has a better etch-stop mechanism in KOH etchant because of higher Ga<sup>+</sup> concentration and built-in stress [Palik, *et al.* (1982)], it is often desirable to fabricate the nanostructure first and then to anneal it. Therefore, the capability of preserving the nanostructure during annealing is very important for some practical applications. As also can be seen from Fig. 4.2.6(b) and (c) that the cleaning process did not change the

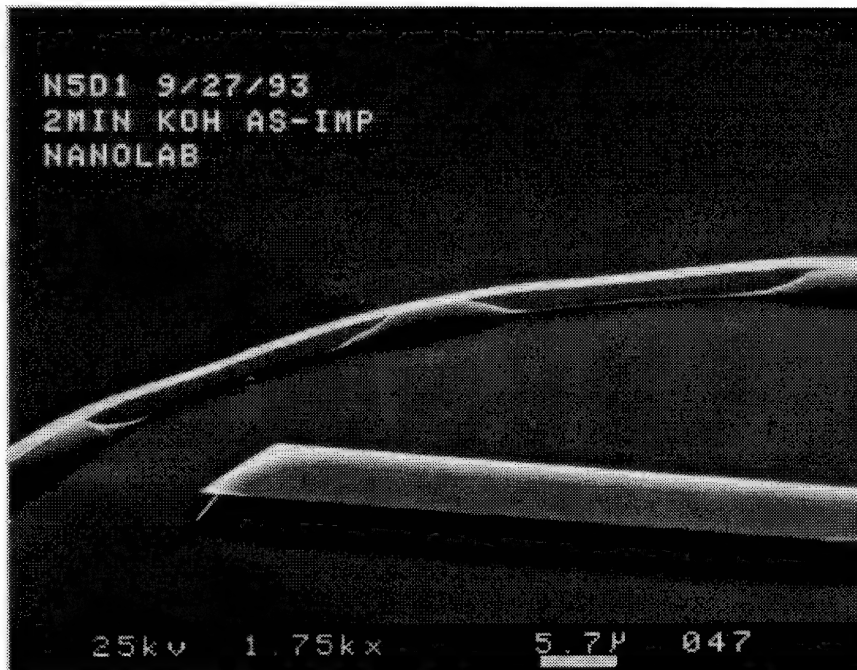


**FIGURE 4.2.6(a)** SEM micrograph (tilted-view) of Si O-ring nanostructure right after KOH etching of the as-implanted sample.

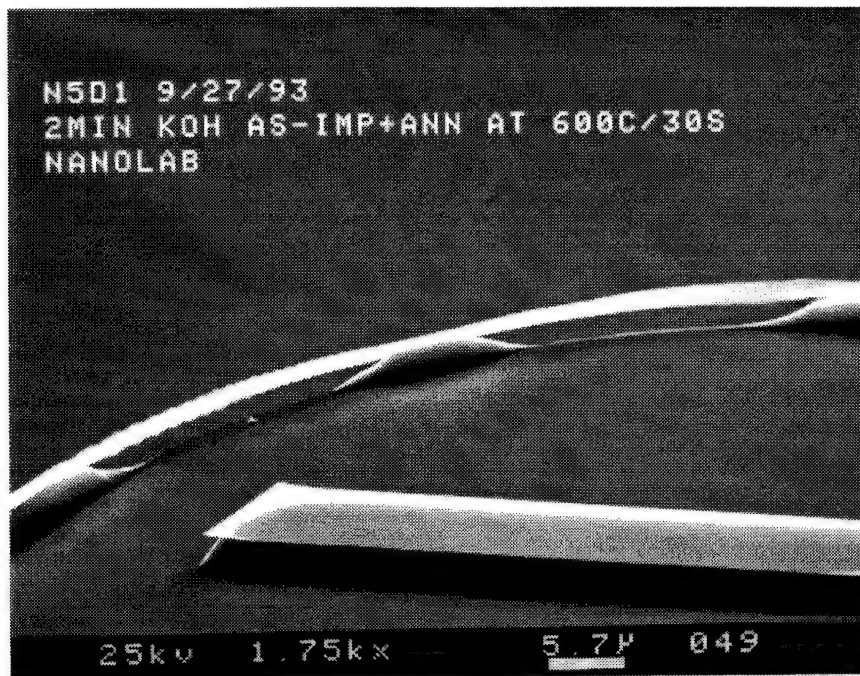


**FIGURE 4.2.6(b)** SEM micrograph (tilted-view) of Si O-ring nanostructure after KOH etching of the as-implanted sample plus RTA at 600°C for 30 sec.

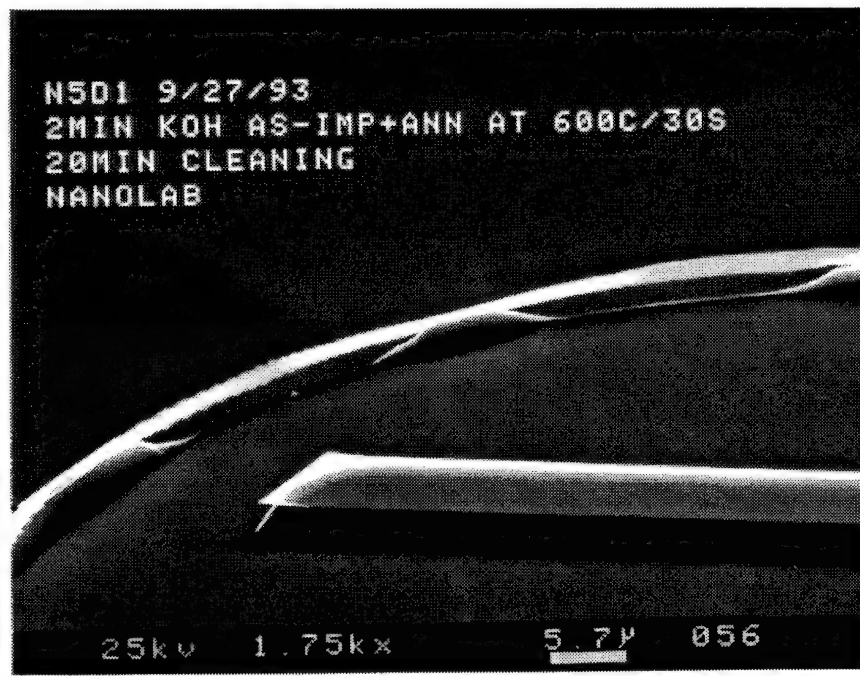


**FIGURE 4.2.6(c)** SEM micrograph (tilted-view) of Si O-ring nanostructure after KOH etching of the as-implanted sample plus RTA at 600°C for 30 sec plus 20 min modified RCA cleaning.

shape of the nanostructure at all nor did the process damage the nanostructure. This is also very important because the cleaning process is essential to the success of rendering the nanostructure porous selectively as discussed previously.

### C. Luminescing Si Nanostructures

Luminescence can be obtained by stain-etching the mRCA-cleaned Si nanostructures. Shown in Fig. 4.2.7 are tilted-view SEM pictures of photoluminescent Si nanostructures. Sample A, in Fig. 4.2.7(a), consists of an array of cantilevers with dimensions of  $4 \times 4$  and  $2 \times 2 \mu\text{m}^2$  obtained by stain-etching for 3.5 min after anisotropic etching of 5 min in R1 at 82°C. Sample B, in Fig. 4.2.7(b), consists of Si cantilevers of  $10 \times 10 \mu\text{m}^2$  and test lines of 0.5, 1, 2, and 5  $\mu\text{m}$  obtained by  $\text{Ga}^+$  off-axis FIB implantation, 1.5 min anisotropic etching in R2, and 2 min stain-etching. It is clear from Fig. 4.2.7(a) and (b) that smooth and uniform micro-cantilevers with small edge-undercut were obtained. High magnification SEM study of the porous silicon cantilever surfaces did not reveal an

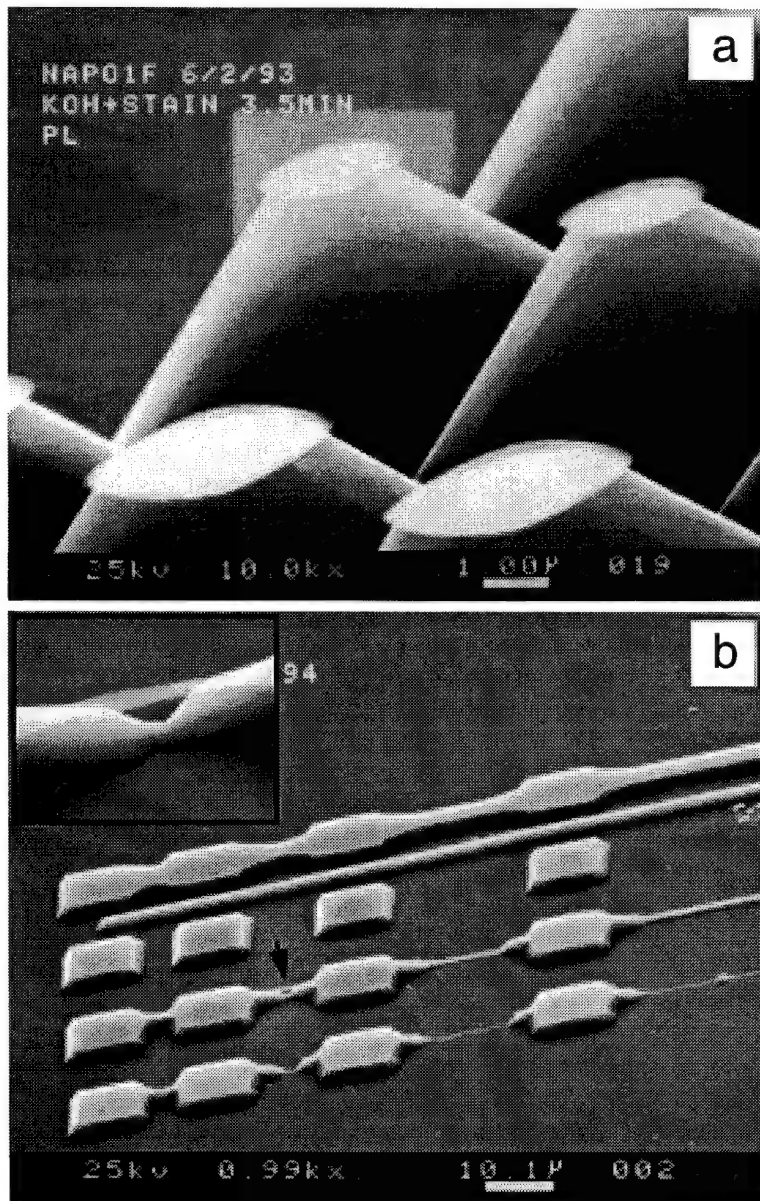


**FIGURE 4.2.7** SEM micrograph (tilted-view) of stain-etched Si nanostructures: (a) Sample A,  $2 \times 2 \mu\text{m}^2$  and  $4 \times 4 \mu\text{m}^2$  cantilevers: on-axis FIB, 5 min KOH etching of annealed sample in R1 at  $82^\circ\text{C}$  and 3.5 min stain-etching; (b) Sample B,  $10 \times 10 \mu\text{m}^2$  cantilevers and lines of 0.5, 1, 2, and 5  $\mu\text{m}$ , 1.5 min: off-axis FIB, KOH etching of as-implanted sample in R2 at  $82^\circ\text{C}$ , annealing and 2 min stain-etching. Inset of (b) shows a close-up of the 1 mm wide air-bridge.

obviously porous structure, which is in consistent with our previous observation of porous silicon stain-etched for short time periods. Air-bridges having at least some portion completely undercut were obtained (Fig. 4.2.7(b) and the inset) by choosing off-axis implantation, appropriate anisotropic etching and stain-etching conditions. The inset in Fig. 4.2.7(b) gives a close-up view of an air bridge of 1  $\mu\text{m}$  width across two cantilevers 10  $\mu\text{m}$  apart. It was noted that if stain-etched too long, the undercut cantilever edges and air bridges formed by KOH etching could be totally etched away. This is mainly due to a faster etch rate in these exposed areas.

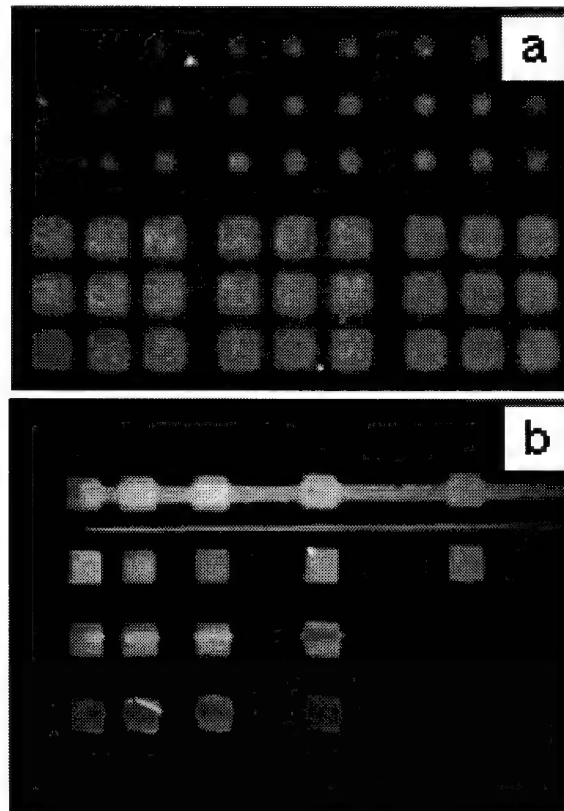


**FIGURE 4.2.8** Color microphotographs of photoemission image of stain-etched Si microstructures under UV excitation: (a) sample A; (b) sample B.

Upon UV 365 nm or Ar<sup>+</sup> 488 nm excitation, *localized visible PL was observed from the stain-etched Si nanostructures only*. The PL, orange-red to the naked eye, is similar to that of stain-etched c-Si. Fig. 4.2.8 shows two color microphotographs of PL imaging from samples A and B, taken with a color CCD camera from a fluorescent microscope with a filtered UV 365 nm source as excitation. It is obvious that luminescing porous silicon is formed only in the nanostructures and the rest of Si substrate is still non-luminescing. However, if one keeps the stain-etching long enough, PL will be obtained in both the nanostructure area and the substrate. Conversely, no PL was observed from the Si nanostructures before stain-etching, indicating that the dimensions of nanostructures defined by FIB implantation are not small enough to induce visible PL (as explained below) and stain-etching is necessary to render the nanostructure porous

and therefore to achieve PL. Also, since the FIB implantation introduces damage and amorphization to the implanted regions and PL can only be obtained from stain-etched crystalline or polycrystalline Si as reported in our previous works [Steckl, *et al.* (1993), Steckl, *et al.* (1994)], annealing of the samples by RTA is necessary to obtain PL from these nanostructures upon stain-etching. The relationship between crystallinity and PL will be discussed in detail in chapter 5.

Microphotoluminescence spectroscopy was performed on Si microstructures, both before and after stain etching, at room temperature using Ar<sup>+</sup> 488 nm excitation. The laser beam was focused onto sample through a Nikon fluorescent microscope with a 50 × objective, forming a circular spot with about 100  $\mu\text{m}$  diameter, and the laser power was

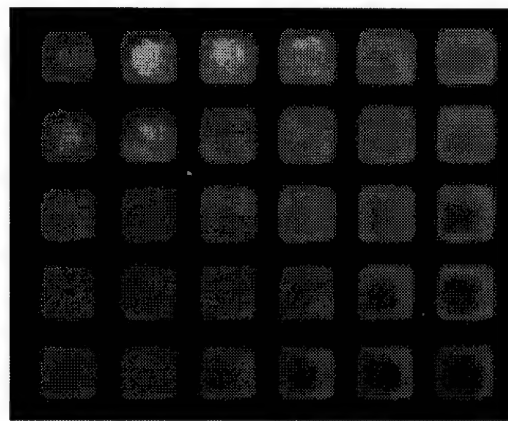


**FIGURE 4.2.9** Color microphotographs of photoemission image of stain-etched Si  $4 \times 4 \mu\text{m}^2$  under UV excitation with its PL spectrum shown in Fig. 4.2.10.

measured at the sample to be  $\sim 8.5$  mW. PL signal was collected through the microscope at 90 degree normal to the sample and was focused to the entry slit of a 0.5 Acton monochromator via an optical fiber. PL was detected from Si microstructures only after stain-etching. Figure 4.2.10 is the PL spectrum obtained from stain-etched Si  $4 \times 4 \mu\text{m}^2$  cantilever array (color microphotoluminescent picture in Fig. 4.2.9), with peak wavelength at  $\sim 670$  nm and a full width at half magnitude (FWHM) of  $\sim 130$  nm, similar to that of stain-etched porous silicon [Steckl, *et al.* (1993)]. The spectrum was equipment corrected by subtracting the background signal from non-PL area of the same sample taken at identical conditions.

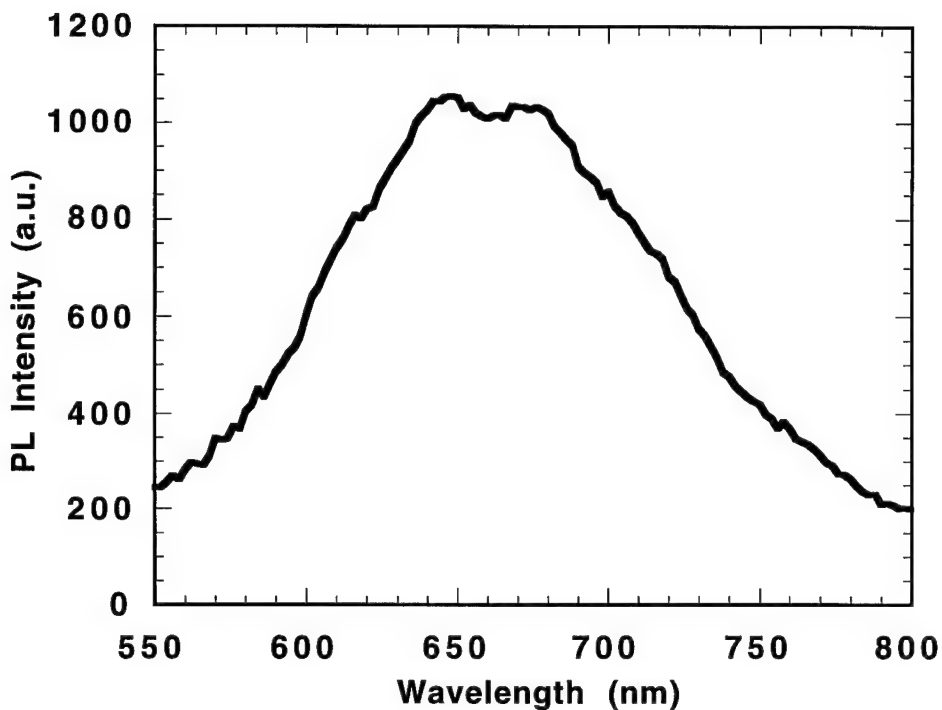


**FIGURE 4.2.10** Room temperature PL spectrum of sample A under  $\text{Ar}^+$  488 nm excitation.

#### 4.2.3 Summary

In summary, a process was successfully developed to fabricate three dimensional photoluminescent free standing Si nanostructures integrated on conventional Si substrate for the first time. The process combines anisotropic etching of  $\text{Ga}^+$  FIB implanted (100)  $n$ -Si in KOH-based solution and selective stain-etching in HF:HNO<sub>3</sub>:H<sub>2</sub>O mixture. The techniques developed here provide a capability of fabricating versatile, optically active Si micro- and nano-structures for potential applications in monolithic Si-based optoelectronics, such as intrachip optical communication, optoelectronic memory devices and light emitting devices.

#### REFERENCES

Aslam, M., Artz, B. E., Kaberline, S. L. and Prater, T. J., "A comparison of cleaning procedures for removing potassium from wafers exposed to KOH", IEEE Trans. Electron Devices **40**, 292 (1993).

Bean, K., "Anisotropic etching of silicon", IEEE Trans. Electron Devices **25**, 1185 (1978).

Berry, I. L. and Caviglia, A. L., "High resolution patterning of silicon by selective gallium doping", J. Vac. Sci. Technol. B. **1**, 1059 (1983).

Palik, E. D., J.W. Faust, J., Gray, H. F. and Greene, R. F., "Study of the etch-stop mechanism in silicon", J. Electrochem. Soc. **129**, 2051 (1982).

Steckl, A. J., Mogul, H. C. and Mogren, S., "Localized fabrication of Si nanostructures by focused ion beam implantation", Appl. Phys. Lett. **60**, 1833 (1992).

Steckl, A. J., Xu, J. and Mogul, H. C., "Photoluminescence from stain-etched polycrystalline Si thin films", Appl. Phys. Lett. **62**, 2111 (1993).

Steckl, A. J., Xu, J. and Mogul, H. C., "Relationship between crystallinity and photoluminescence in stain-etched porous Si", J. Electrochem. Soc. **141**, 674 (1994).

Steckl, A. J., Xu, J., Mogul, H. C. and Mogren, S., "Doping-induced selective area photoluminescence in porous silicon", Appl. Phys. Lett. **62**, 1982 (1993).

## Chapter 5

### Crystallinity, Photoluminescence & Si Oxyhydrides in Stain-Etched Porous Silicon Films

#### 5.1 Photoluminescent Polycrystalline Si Thin Film Patterns

##### 5.1.1 Introduction

For applications requiring large area of optically active Si material such as in flat panel display and solar cell, ploy-crystalline and/or amorphous silicon are desired materials for its easy processes, low thermal budget and low cost. Visible photoluminescence from hydrogenated partially-crystalline Si grown by plasma enhanced chemical deposition (PECVD) treated with two electrochemical processes was recently reported [Bustarret, *et al.* (1992)]. However, in that process, the film growth rate of PECVD is relatively slow (~25 nm/min) and the two-step anodization processes involved are relatively complex. Therefore we initiated the investigation of stain-etching of poly-crystalline Si thin films deposited by conventional low pressure chemical vapor deposition (LPCVD) and its optical properties. As a result, visible photoluminescence from stain-etched polycrystalline Si thin film was obtained for the first time.

##### 5.1.2 Experimental Results

In this experiment, undoped amorphous and polycrystalline silicon films of around 400 nm were deposited on oxidized Si substrates by LPCVD (180 mTorr) from SiH<sub>4</sub> at 560 and 600°C, respectively. The poly-Si films grown at 600°C had a sheet resistance ( $R_{sh}$ ) of ~ 1-10 MΩ/sq. Doped poly-Si films were produced by 30 kV P<sup>+</sup> ion implantation of the amorphous films grown at 560°C followed by annealing at 900°C for 30 min, yielding an  $R_{sh} \approx 20 \Omega/\text{sq}$ . Thicker (~2 μm) undoped poly-Si films were also deposited on quartz substrates at 630°C.

The poly-Si films were stain-etched in a 1:3:5 solution of HF:HNO<sub>3</sub>:H<sub>2</sub>O at room temperature in ambient light. The incubation times ( $t_i$ ) for the poly-porous silicon formation were uniformly small, 10-20 sec, for both doped and undoped poly-Si films. This is in contrast to the strong effect of the doping (hole) concentration observed [Steckl, *et al.* (1993)] on the  $t_i$  for stain-etching of single-crystalline Si as described in detail in section 4.1. Total stain etching times for the poly-Si films on oxidized silicon and on quartz were controlled to be 30 and 120 sec, respectively. Longer time etching tends to etch away the porous silicon/poly-Si film due to its small thickness. The surface morphologies of the doped and undoped poly-Si films on oxidized Si before and after stain-etching are studied using scanning electron microscopy and the results are shown in Fig. 5.1.1. The as-received doped poly-Si film has a relatively smooth surface (Fig. 5.1.1(a) & (b)), since it was amorphous as-grown and only became polycrystalline upon anneal. A slight surface texture can be observed in the tilt-view microphotograph (Fig. 5.1.1(b)). The undoped poly-Si film exhibited a grainy surface in the as-received condition (Fig. 5.1.1(c) & (d)) with a typical grain size of ~ 0.1 μm. The stain-etching process clearly reveals grains with ~ 0.2-0.4 μm and 0.1-0.2 μm average dimensions in the doped (Fig. 5.1.1(e) & (f)) and undoped (Fig. 5.1.1(g) & (h)) poly-Si films, respectively. The surface texture is considerably rougher after stain-etching for both doped and undoped films.

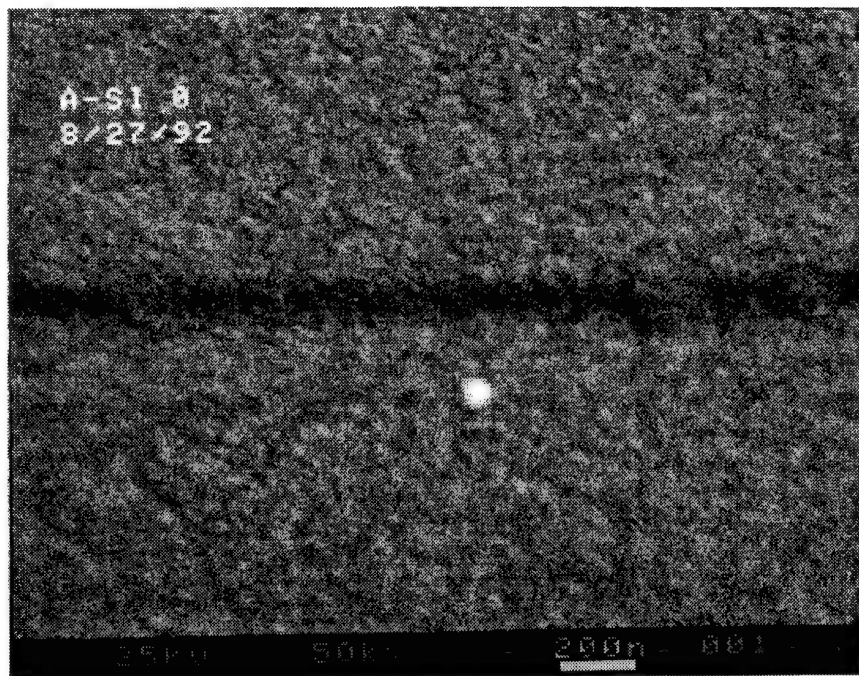


**FIGURE 5.1.1(a)** SEM micrograph (plan-view) of as-received doped polycrystalline Si film.

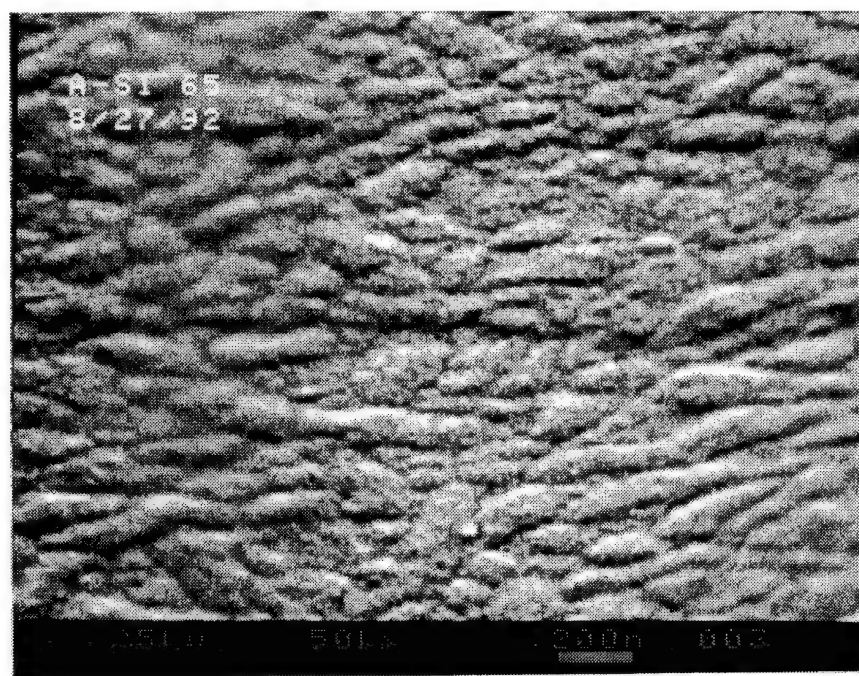


**FIGURE 5.1.1(b)** SEM micrograph (tilted-view) of as-received doped polycrystalline Si film.

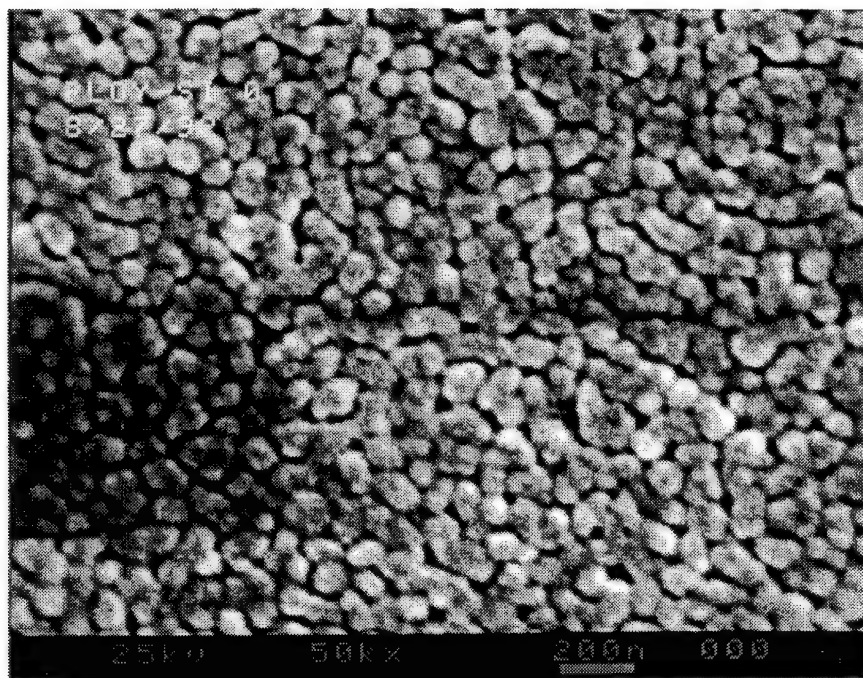


**FIGURE 5.1.1(c)** SEM micrograph (plan-view) of as-received undoped polycrystalline Si film.

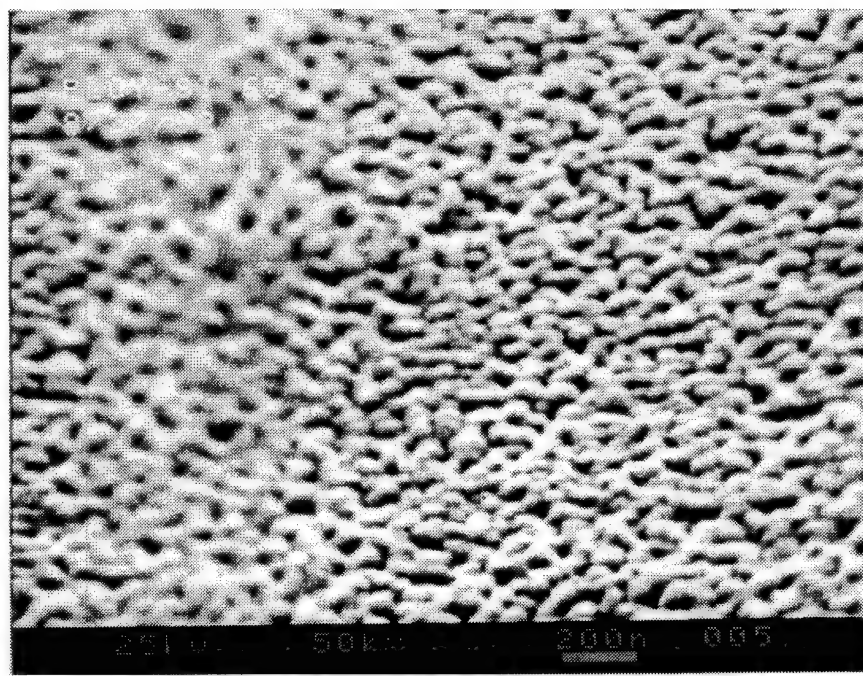


**FIGURE 5.1.1(d)** SEM micrograph (tilted-view) of as-received undoped polycrystalline Si film.

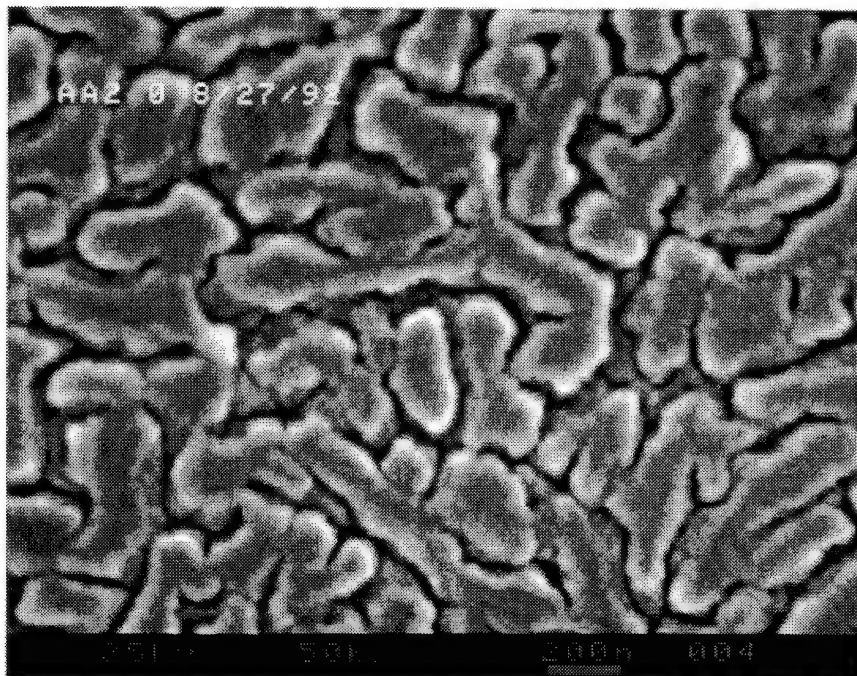


**FIGURE 5.1.1(e)** SEM micrograph (plan-view) of stain-etched doped polycrystalline Si film.

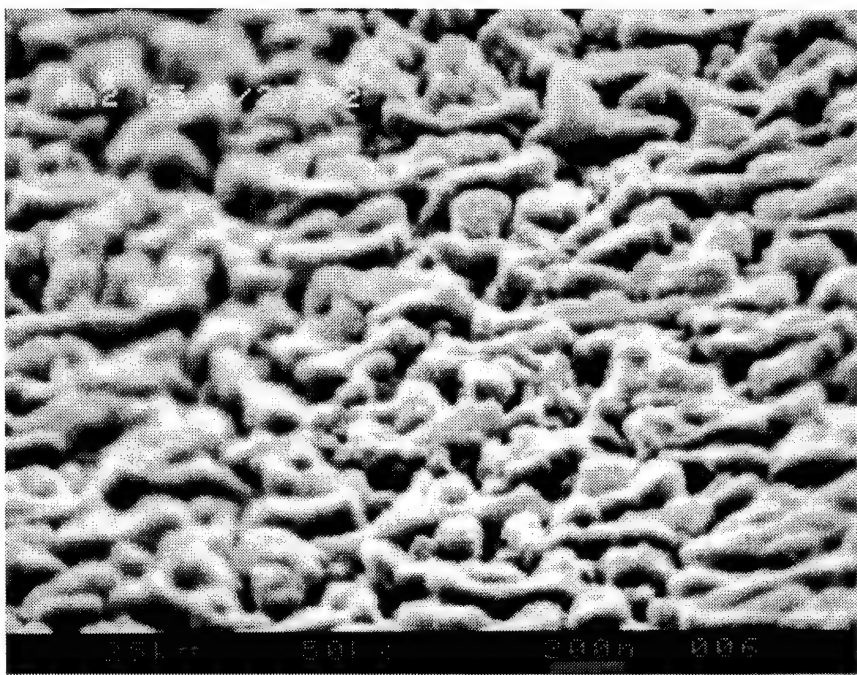


**FIGURE 5.1.1(f)** SEM micrograph (tilted-view) of stain-etched doped polycrystalline Si film.

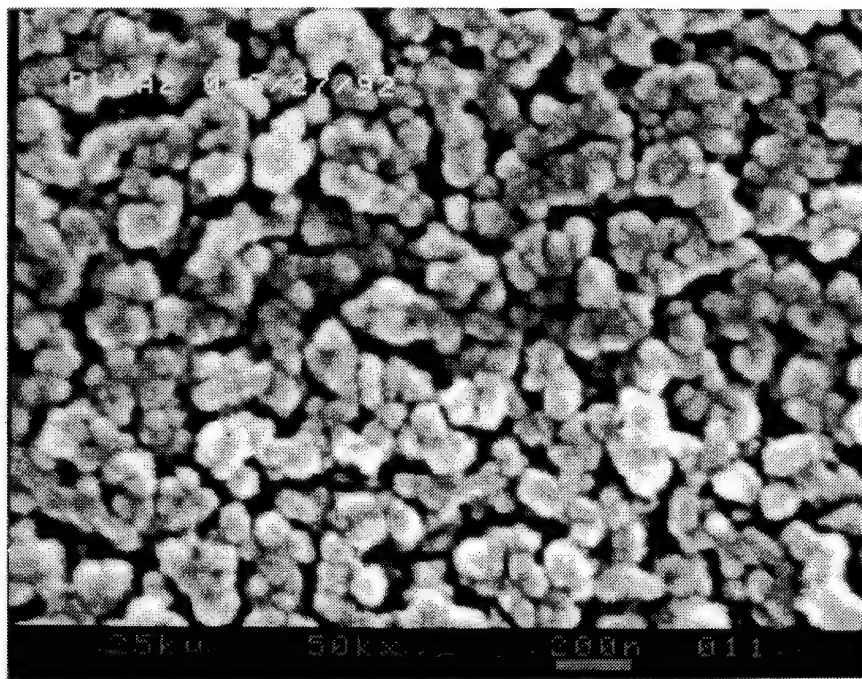


**FIGURE 5.1.1(g)** SEM micrograph (plan-view) of stain-etched undoped polycrystalline Si film.

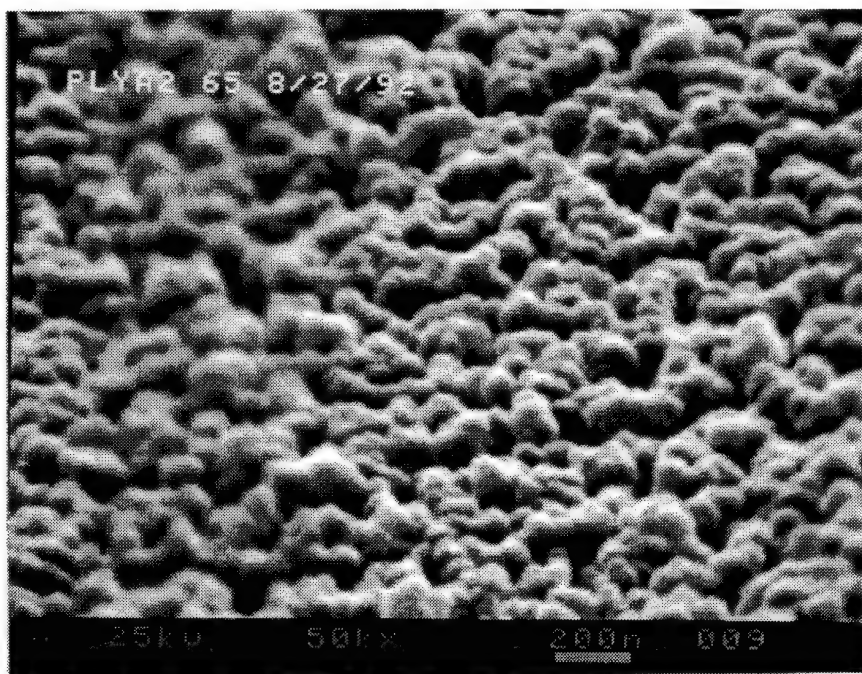


**FIGURE 5.1.1(h)** SEM micrograph (tilted-view) of stain-etched undoped polycrystalline Si film.

Atomic force microscopy (AFM) study of the poly-Si surface was used to provide a quantitative measure of the surface roughness ( $R_a$ ). For the doped film,  $R_a$  before and after stain-etching was 1.89 and 18.0 nm, respectively. As expected, the undoped film exhibited a rougher as-deposited surface, with an  $R_a$  of 5.65 nm. However, after stain-etching the roughness of the undoped (18.53 nm) and doped (18 nm) films was essentially the same.

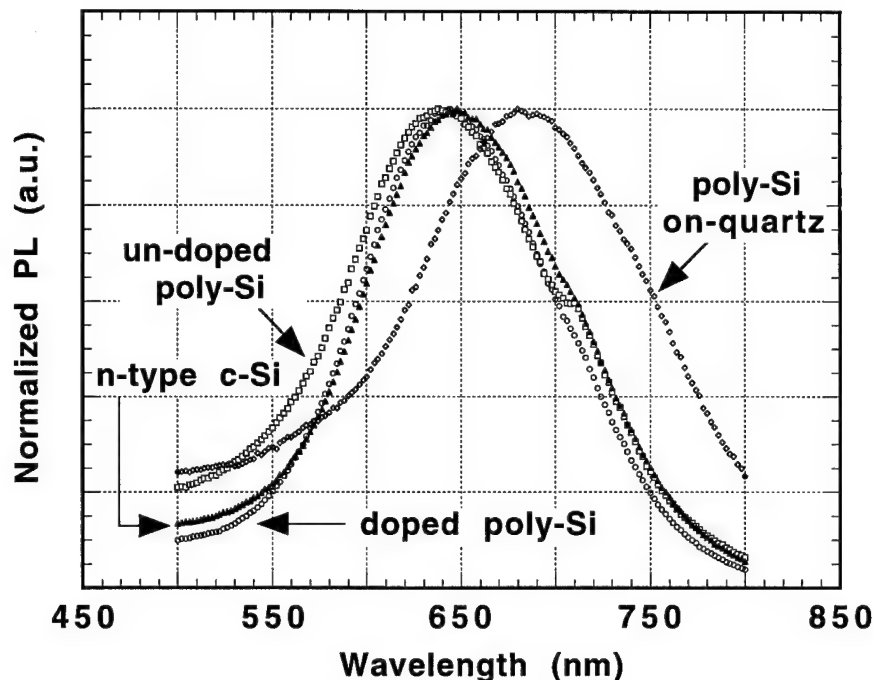


**FIGURE 5.1.2** Photoluminescence spectra: doped and undoped poly-Si on  $\text{SiO}_2/\text{Si}$  stain-etched for 30 sec; undoped poly-Si on quartz stain-etched for 120 sec; *n*-type c-Si stain-etched for  $t_i$  plus 120 sec.

PL spectra obtained from stain-etched poly-Si films revealed no significant difference between the doped and undoped poly-Si films. The emission from poly-Si layers on oxidized Si substrates, shown in Fig. 5.1.2, exhibits a broad signal with a peak at 640-645 nm. The poly-Si films deposited on quartz exhibited a slight red shift, with peak emission at  $\sim 680$  nm. The PL spectrum from an *n*-type (3.5 ohm-cm) c-Si (100) substrate, stain-etched for 2 min past  $t_i$  indicates almost identical characteristics to that of the poly-Si samples. Since quartz is transparent at these wavelengths, the emission of these poly-Si films was also measured through the quartz with no significant difference in the PL spectrum. Fig. 5.1.3 is the PL spectrum of stained poly-Si thin film on quartz measured from the other side of the quartz (the so-called transmission mode). For comparison the PL from the same film measured from the poly-Si side (the so-called reflection mode) is plotted again in Fig. 5.1.3. The spike at 710 nm from transmission mode spectrum is a contribution for the UV source due to the un-complete filtering. It is then clear from the plots that both spectra have the similar shape and an almost identical peak at 680 nm.

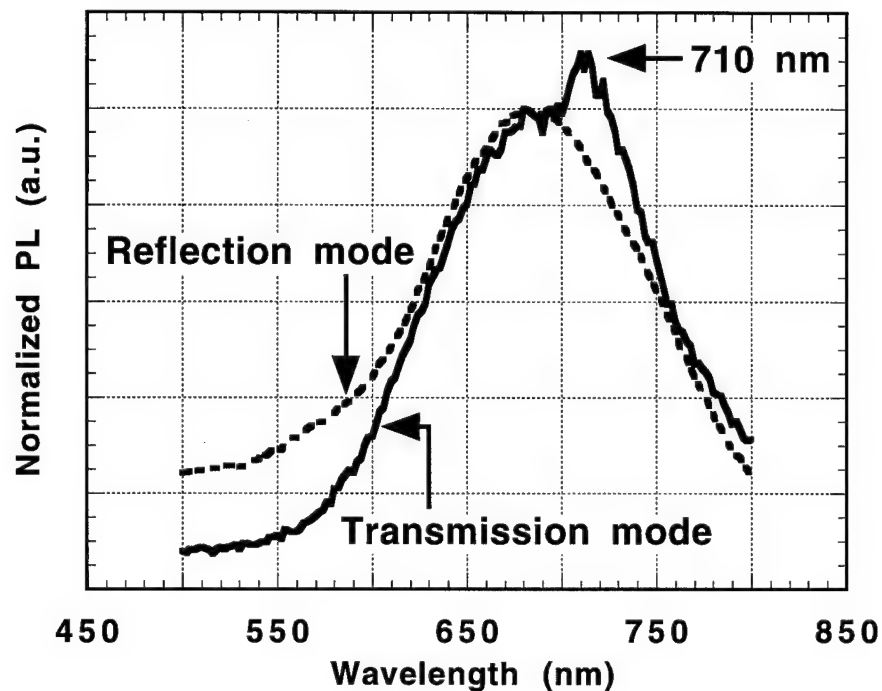


**FIGURE 5.1.3**

Photoluminescence spectra of porous poly-Si films on quartz measured from both front and back sides.

However, amorphous Si films which were also stain-etched did not exhibit a PL signal. This is consistent with the observation of non-PL from stain-etched FIB amorphized samples as discussed in the previous chapter. It, therefore, appears that for the deposited Si thin films the level of initial crystallinity plays a greater role than the doping level in obtaining a photoluminescent effect.

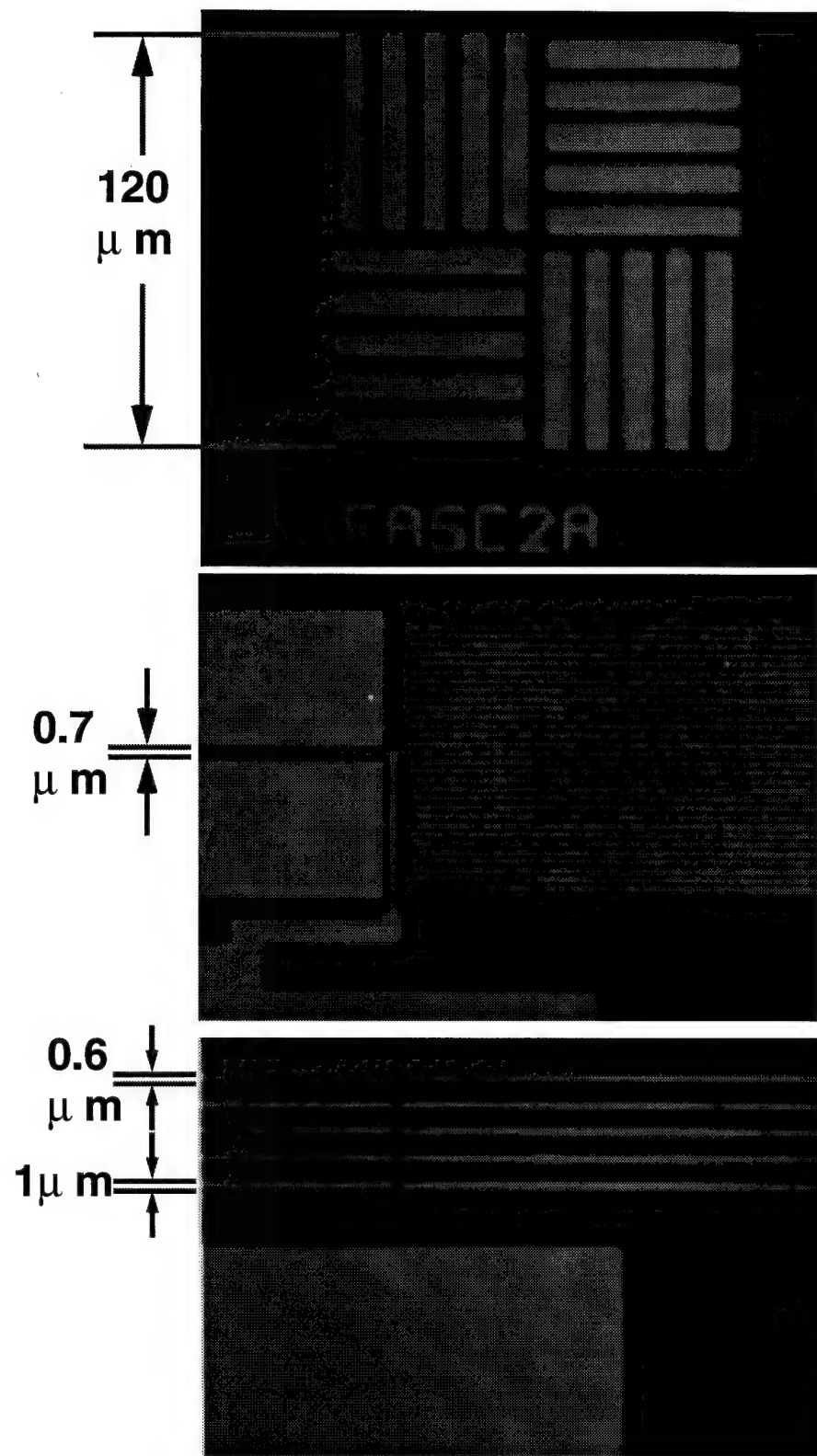


**FIGURE 5.1.4**

PL micrograph of light emitting patterns in stain-etched poly-Si on  $\text{SiO}_2/\text{Si}$ .

To investigate the feasibility of luminescing pattern formation using porous silicon thin films for flat panel display application, undoped poly-Si layers on oxidized Si wafers were first patterned by electron cyclotron resonance (ECR) reactive ion etching (RIE) [Dane, *et al.* (1992)] in Cl<sub>2</sub> at 2 mTorr with a wide range of feature sizes. After ECR RIE the samples were then stain-etched in HF:HNO<sub>3</sub>:H<sub>2</sub>O for a few minutes and porous silicon patterns were formed. Under UV excitation photoluminescent patterns with good uniformity were obtained over large areas and with high resolution in small features. In Fig. 5.1.4 several light-emitting poly-Si patterns are shown. The top pattern consists of 6  $\mu\text{m}$  wide lines on 12  $\mu\text{m}$  centers. The middle pattern combines relatively large porous silicon areas ( $45 \times 70 \mu\text{m}^2$ ) with fine light-emitting lines (0.7  $\mu\text{m}$ ). Finally, the bottom pattern consists of five parallel lines, ranging from 0.6 to 1.0  $\mu\text{m}$  in 0.1  $\mu\text{m}$  increments. It is interesting to point out that for these fine lines, the line width is only a factor of 3-5 times larger than the grain size shown in Fig. 5.1.1, yet a uniform and continuous photoemissive pattern is obtained.

### 5.1.3 Summary

In summary, room temperature visible photoluminescence was obtained from polycrystalline Si thin films upon stain-etching. Photoluminescent porous silicon patterns with sub-micron dimensions have been fabricated and have exhibited well-defined luminescence both as isolated features and in combination with much larger areas. It can be concluded from the experimental results that while complete long-range order in the starting material is not necessary for obtaining of photoluminescence in porous silicon some level of crystallinity is required. In addition it has been demonstrated for the first time that well defined light emitting porous silicon thin film patterns can be obtained by the stain-etch technique. This offers potential application in porous silicon-based flat panel display devices.

## REFERENCES

Bustarret, E., Ligeon, M., Bruyére, J. C., Muller, F., Hérino, R., Gaspard, F., Ortega, L. and Stutzmann, "Visible light emission at room temperature from anodized plasma deposited silicon thin films", *Appl. Phys. Lett.* **61**, 1552 (1992).

Dane, D., Gadgil, P., Mantei, T. D., Carison, M. A. and Weber, M. E., "Etching of polysilicon in a high-density electron cyclotron resonance plasma with collimated magnetic field", *J. Vac. Sci. Technol. B* **10**, 1312 (1992).

Steckl, A. J., Xu, J., Mogul, H. C. and Mogren, S., "Doping-induced selective area photoluminescence in porous silicon", *Appl. Phys. Lett.* **62**, 1982 (1993).

## 5.2 Crystallinity, Photoluminescence and Si Oxyhydrides in Stain-Etched Porous Si Films

### 5.2.1 Introduction

Considerable effort is being devoted to the exploration of the origin of PL of porous silicon (porous silicon) prepared by various techniques. The first model for the PL of porous silicon is the direct band to band radiative transition based on a quantum confinement effect in the narrow membranes between the channels of the etched Si [Canham (1990), Cullis and Canham (1991), Halimaoui, *et al.* (1991), Koshida and Koyama (1991), Lehmann and Gosele (1991), Nishida, *et al.* (1992)], which could lead to an effective bandgap substantially increased as compared to normal Si. For this effect to be significant, calculations indicate [Read, *et al.* (1992)] that the membrane width would have to be only a few nm thick. Since the initial introduction of quantum confinement model, two major alternative models have been proposed. The second model ascribes the PL to localized surface emission due to the existence of Si hydrides or polysilanes or Si oxyhydrides [Prokes, *et al.* (1992), Prokes, *et al.* (1992), Searson, *et al.* (1992)] formed by the bonding of Si surface atoms to hydrogen and/or oxygen, or to emission from a specific class of Si-O-H compounds (siloxene) and related derivatives [Brandt, *et al.* (1992), Daek, *et al.* (1992)]. Finally, a third model considers a combination of quantized states in the interior of small crystallites with discrete surface states [Koch (1993)]. All of these models for the optical properties of porous silicon are continuing to be intensively studied. However to date, the explanation for photoluminescence in porous silicon still remains an open topic due to the lack of unambiguously designed experiments.

Recently, it has been shown, as described in the previous section, that long range order in the starting Si is not necessary for the appearance of strong photoluminescence in the porous silicon. PL, with a spectrum similar to that of porous silicon prepared from c-Si, has been reported from anodized [Bustarret, *et al.* (1992)] and from chemically stained [Jung, *et al.* (1992), Steckl, *et al.* (1993)] polycrystalline Si (poly-Si) films. Since poly-Si can be deposited at quite low temperatures, this opens the door for many optoelectronic applications of porous silicon which integrate photoemissive poly-Si thin films with existing device structures. For example, poly-Si photoemitters can be deposited on Si VLSI circuits for inter- and intra-chip optical communications and on glass substrates for flat panel displays. It is important to point out, however, that Si films with an amorphous structure [Jung, *et al.* (1992), Steckl, *et al.* (1993)] did not exhibit a PL response upon stain-etching.

In this experiment, the effect of deposition temperature ( $T_D$ ) on the correlation among the level of crystallinity of Si thin films, the subsequent photoluminescence and Si oxyhydrides obtained after rendering the Si porous by stain-etching was systematically studied. Understanding of this relationship can hopefully provide additional insight into the basic mechanisms for the optical and electronic properties of porous silicon. Another goal for this investigation is to establish some important guidelines for the fabrication of devices incorporating poly-porous silicon elements.

### 5.2.2 Experimental Procedures

Si thin films were deposited by low pressure chemical vapor deposition (LPCVD) using silane pyrolysis at temperatures ranging from  $540^\circ\text{C}$  to  $640^\circ\text{C}$ . Two types of substrates were used: quartz and oxidized Si wafer (with about  $5000\text{\AA}$  of  $\text{SiO}_2$  on both sides of the wafer). The quartz substrates used are 1 inch square and 1/8th inch thick in size and are electrical graded fused silica. The half micron thick oxide on both sides of the silicon wafer was grown by wet oxidation. The Si deposition process was carried out using undiluted silane with a flow rate of 25 sccm at 0.5 Torr. The deposition time was decreased with increasing deposition temperature, such that the thickness

of the deposited Si films was around 1  $\mu\text{m}$  for all temperatures. Film thickness was measured by Dektak IIA surface micro-profile after a step was etched by KOH. The crystallinity of the as-deposited thin films was studied by X-ray diffraction spectroscopy (XRD) and room temperature Raman spectroscopy. XRD was performed with the Cu  $\text{K}\alpha$  line on a Siemens D-500 spectrometer and the Raman analysis used the Ar laser line at 496.5 nm.

The deposited Si films were converted to porous silicon by stain-etching in an HF:HNO<sub>3</sub>:H<sub>2</sub>O solution at room temperature for various periods of time. In most of the experiments described here, the ratio of these three reagents is 1:3:5 by volume and the etching time is 2 min. In certain cases, times as long as ~40 min were utilized. In addition to the standard stain-etching solution mentioned above, other etching solutions which provide a much shorter incubation time were also studied, for reasons discussed below. After etching, the crystallinity of the porous silicon films was again evaluated by XRD and Raman spectroscopy. The surface morphology of the as-deposited and etched films was studied by SEM and atomic force microscopy (AFM). PL spectroscopy was performed at room temperature with ultraviolet (UV) excitation at 365 nm from a filtered Hg source. As described below, Si samples prepared on quartz and on oxidized Si substrate both yielded nearly identical photoluminescence spectra after being rendered porous. Infrared (IR) transmission measurements were performed from 500 to 3000  $\text{cm}^{-1}$  on as-deposited and stain-etched amorphous and polycrystalline Si films on oxidized Si substrate to study the chemical structures. The data were obtained (vs. air as a reference) with 4  $\text{cm}^{-1}$  resolution using a Mattson Cygnus 100 Fourier transform system. IR transmittance spectra from a Si wafer and an oxidized Si wafer were also recorded in order to separate the Si and oxide-related IR absorption lines from the other spectra. Transmission electron microscopy (TEM) [Wei, *et al.* (1995)] and electron spin resonance (ESR) spectroscopy [Steckl, *et al.* (1995)] were performed on some samples to study the defects and dangling bond density.

### 5.2.3 Results and Discussions

Table 5.1 summarizes the information on substrate used, deposition temperature, film thickness and crystallinity by XRD. From the measured thickness and deposition time the deposition rate in angstrom per second was calculated and plotted in Fig. 5.2.1 as a function of the inversed deposition temperature.

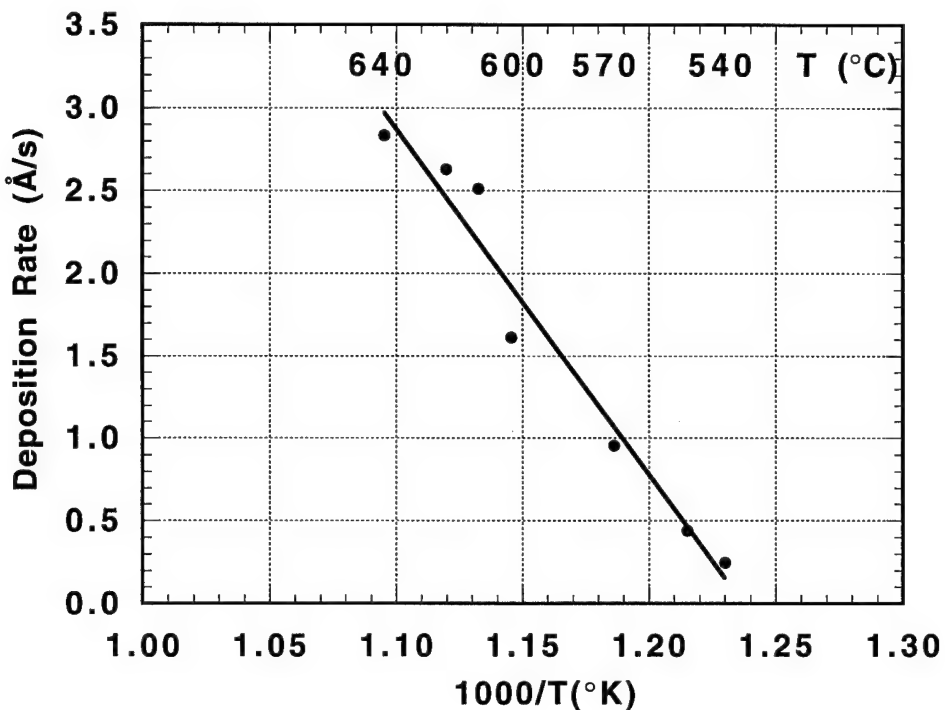
Table 5.1 Summary of the LPCVD films used in this work

Samples	Deposition T (°C)	Substrate	Thickness ( $\mu\text{m}$ )	Crystallinity
T540Q/W	540	Quartz & Oxidized Si	0.92	amorphous
T550Q/W	550	Quartz & Oxidized Si	1.35	amorphous
T560Q/W	560	Quartz & Oxidized Si	2.42	amorphous
T570Q/W	570	Quartz & Oxidized Si	1.80	amorphous
T580Q/W	580	Quartz & Oxidized Si	1.86	amorphous
T590Q/W	590	Quartz & Oxidized Si	1.73	poly
T600Q/W	600	Quartz & Oxidized Si	1.50	poly
T610Q/W	610	Quartz & Oxidized Si	1.81	poly
T620Q/W	620	Quartz & Oxidized Si	1.50	poly
T630Q/W	630	Quartz & Oxidized Si	0.82	poly
T640Q/W	640	Quartz & Oxidized Si	0.70	poly

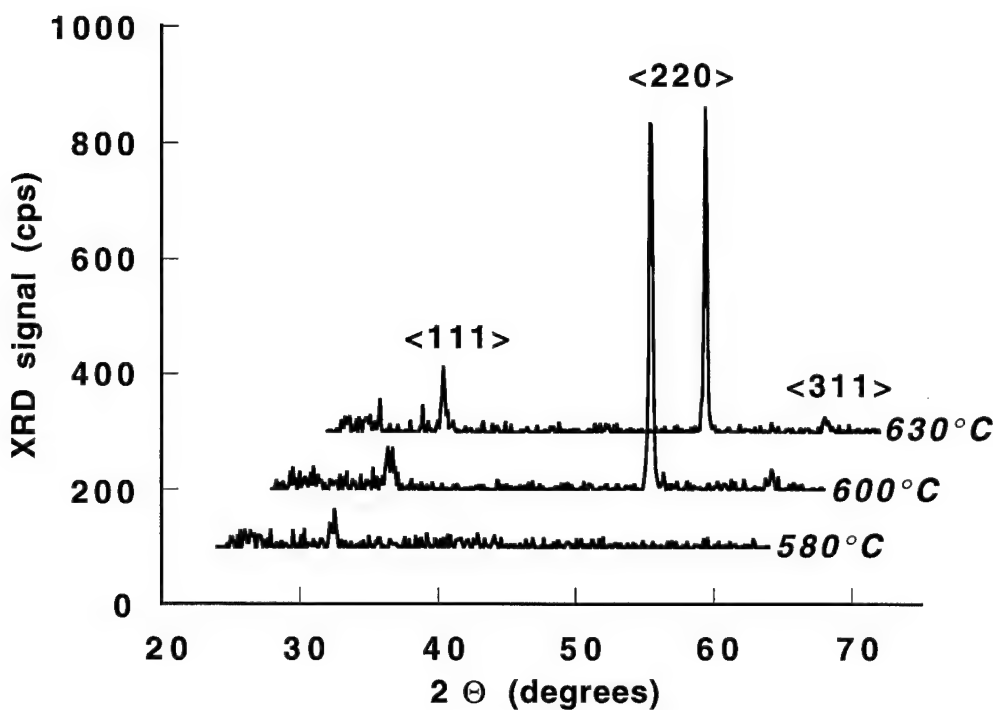
In general, the properties of the as-deposited Si films used in this experiment are similar to those previously reported [Kamins, *et al.* (1978), Harbecke, *et al.* (1984)] for the structural properties of LPCVD Si. XRD of the Si films indicates an amorphous structure for deposition temperatures of 580°C and below. For deposition temperatures above 580°C, X-ray peaks of

varying intensity are observed corresponding to the  $<111>$ ,  $<220>$  and  $<311>$  directions with a dominant  $<220>$  texture. For deposition temperatures between 580°C and 600°C, the Si films undergo a structural transition from amorphous to polycrystalline.

As mentioned previously films deposited at 590°C and above are polycrystalline while films deposited below 590°C are amorphous as revealed by XRD. Figure 5.2.2



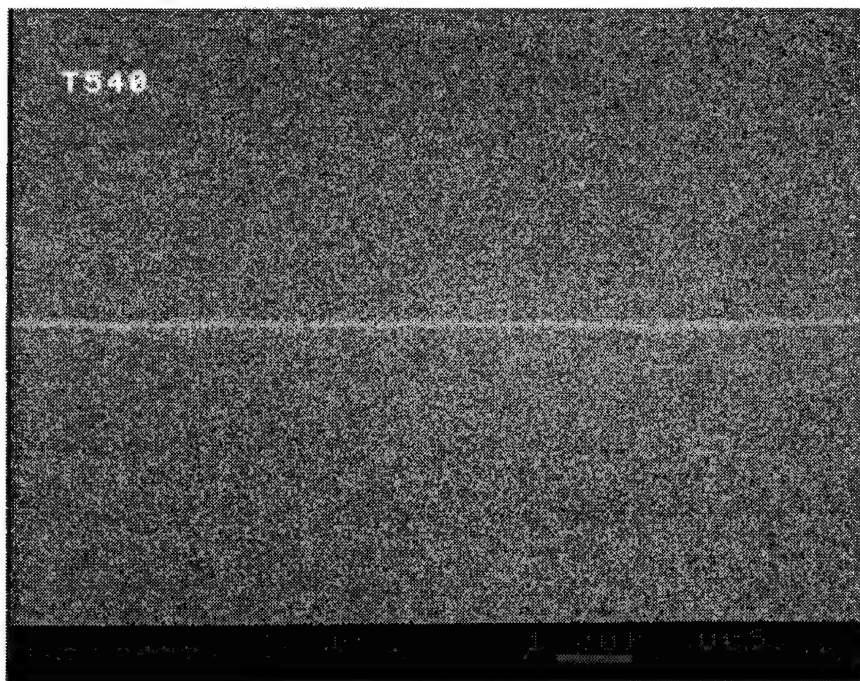
**FIGURE 5.2.1** Film deposition rate as a function of temperature.



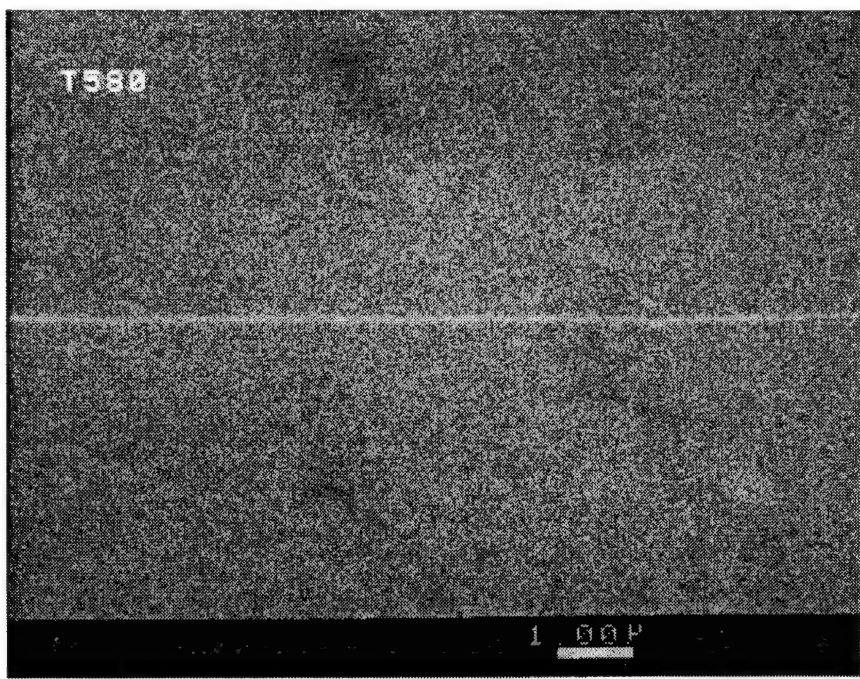
**FIGURE 5.2.2** X-ray diffraction spectra of as-deposited CVD Si films on quartz at temperatures of 580, 600 and 630°C.

shows three representative XRD spectra, obtained from Si films deposited at 580°C, 600°C and 630°C on quartz substrates. The polycrystalline films deposited at 600°C and 630°C exhibits a pronounced  $<220>$  texture as all the other polycrystalline films do. The grain size calculated from the  $<220>$  line width using the Scherrer formula [Cullity (1967)] yields a value of approximately 680 Å for  $T_D$  of 600°C.

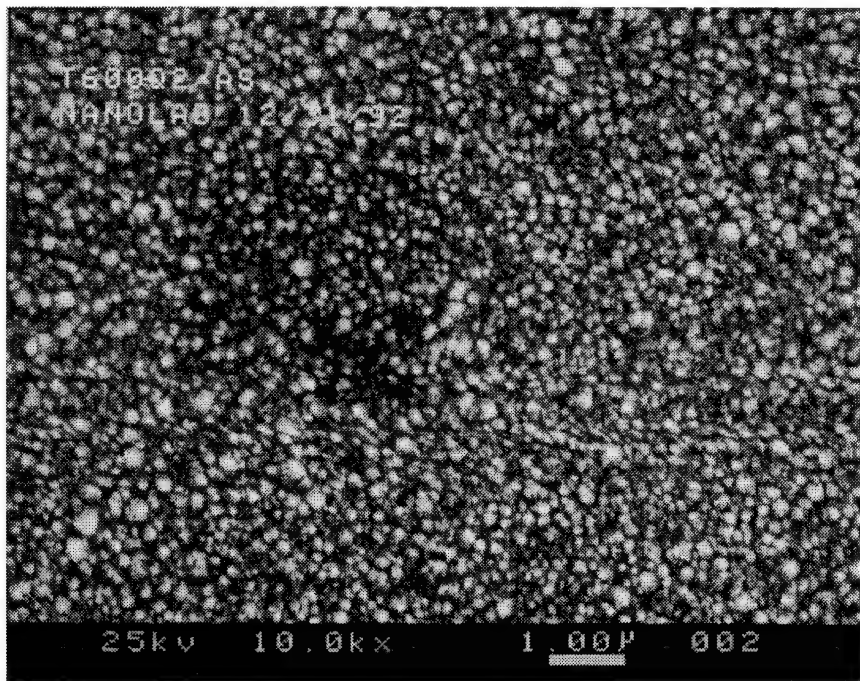
The surface morphology of as-deposited as well as stain-etched films was characterized using SEM and AFM. As shown in the SEM micrographs of as-deposited films in Fig. 5.2.3(a-d), as-deposited films with  $T_D$  of 540 and 580°C have a relatively smooth surface, while films deposited at  $T_D$  of 600 and 620°C display an significantly rougher surface. This dependence of surface morphology on deposition temperature of the films is very similar to that reported by H. Watanabe *et al.* [Watanabe, *et al.* (1992)] for Si films deposited under similar conditions.



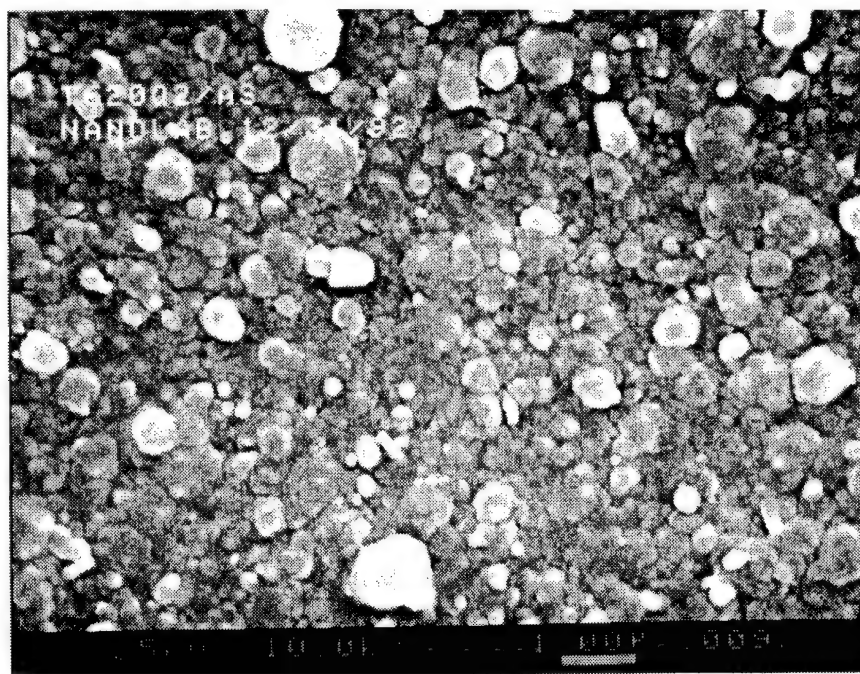
**FIGURE 5.2.3(a)** SEM micrograph (plan-view) of as-deposited amorphous Si at 540°C.



**FIGURE 5.2.3(b)** SEM micrograph (plan-view) of as-deposited amorphous Si at 580°C.



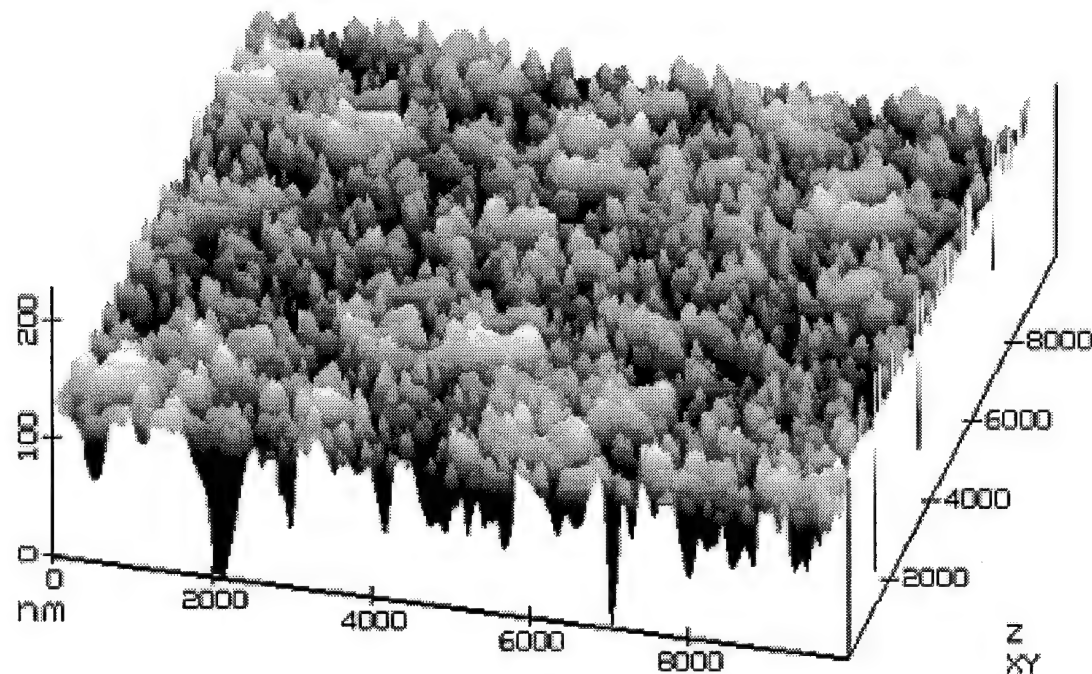
**FIGURE 5.2.3(c)** SEM micrograph (plan-view) of as-deposited polycrystalline Si at 600°C.



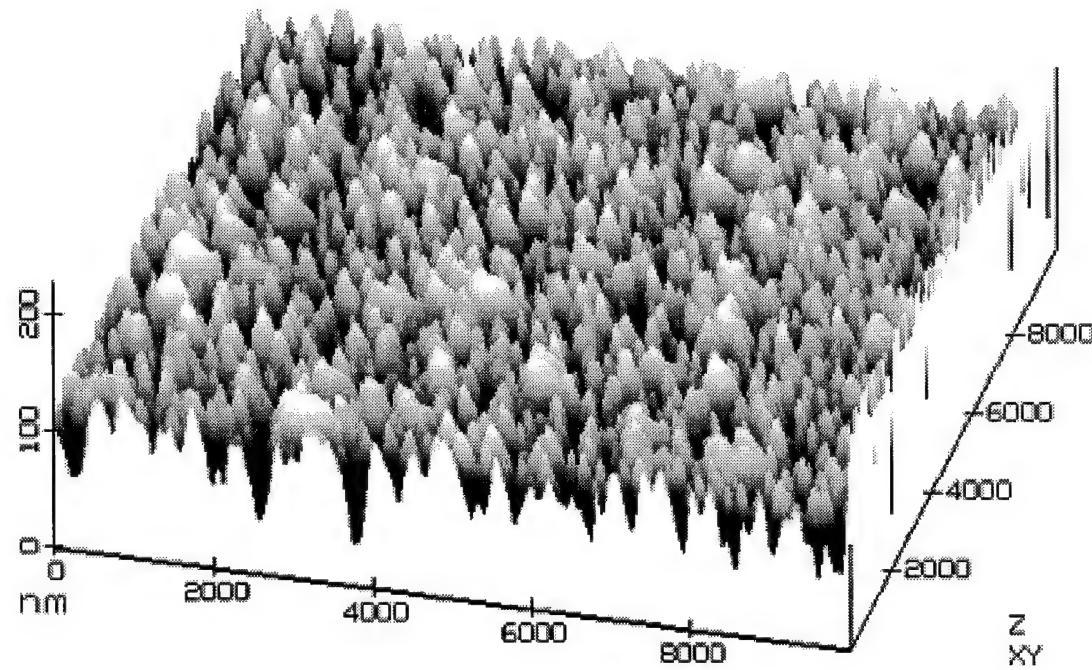
**FIGURE 5.2.3(d)** SEM micrograph (plan-view) of as-deposited polycrystalline Si at 600°C.

A more detailed surface structure of the as-deposited Si films was obtained by probing with AFM, using a Digital Instruments Nanoscope II with Si super-tips. The AFM provides a three-dimensional view of the surface which is easier to interpret as shown in Fig. 5.2.4(a) - (d), AFM area scan of films deposited at  $T_D$  of 540°C, 580°C, 600°C and 620°C. It can be seen from Fig. 5.2.4 that even at  $T_D$  of 540°C the surface exhibits a uniform and fairly significant level of roughness. The roughness increases slightly at  $T_D$  of 580°C, but retains its uniform distribution.

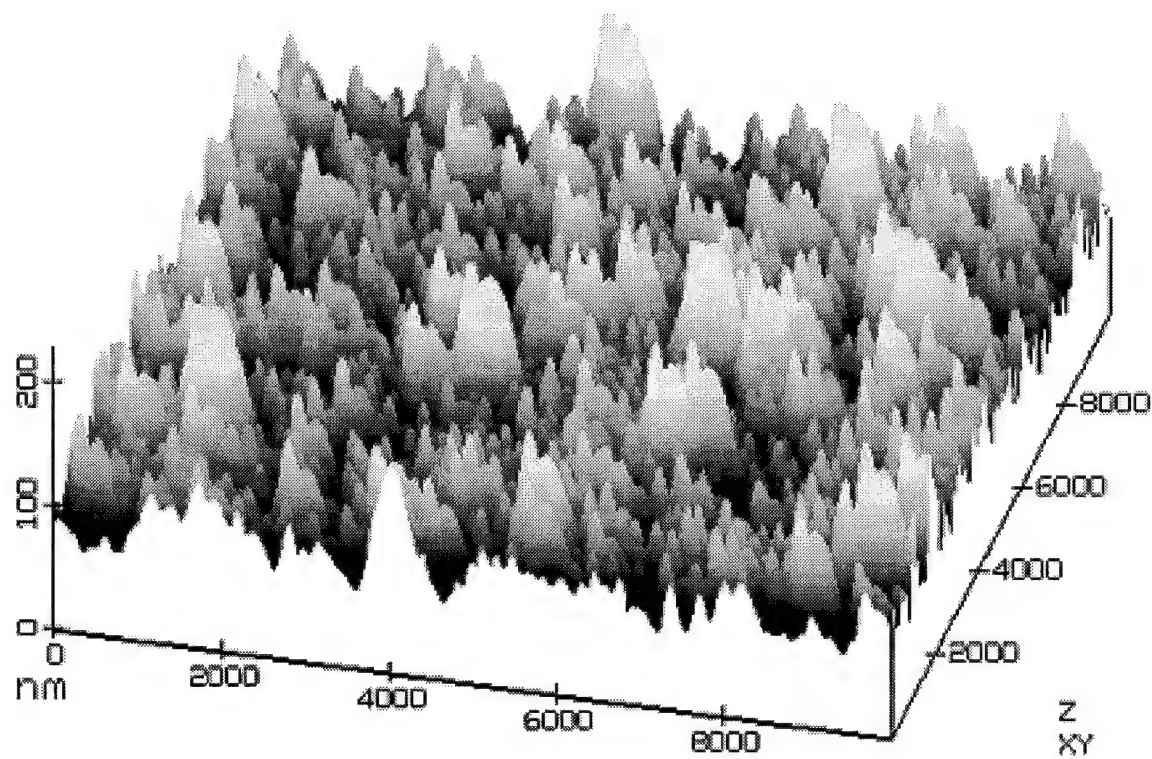
At  $T_D$  of  $600^\circ\text{C}$  considerably larger features (in all three dimensions) with a smaller density are observed in addition to the uniformly rough background surface. Finally, at  $T_D$  of  $620^\circ\text{C}$  very large features, with dimensions of one or more micrometers, dominate the surface morphology.



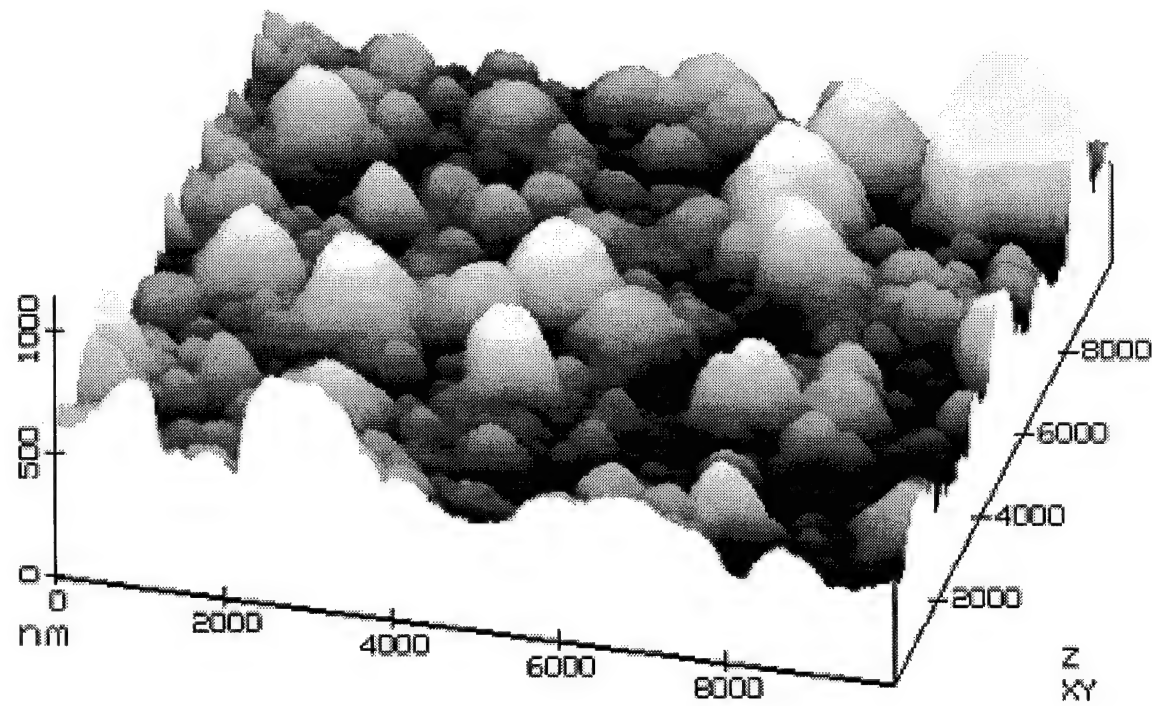
**FIGURE 5.2.4(a)** AFM area scan of as-deposited amorphous Si at  $540^\circ\text{C}$ .



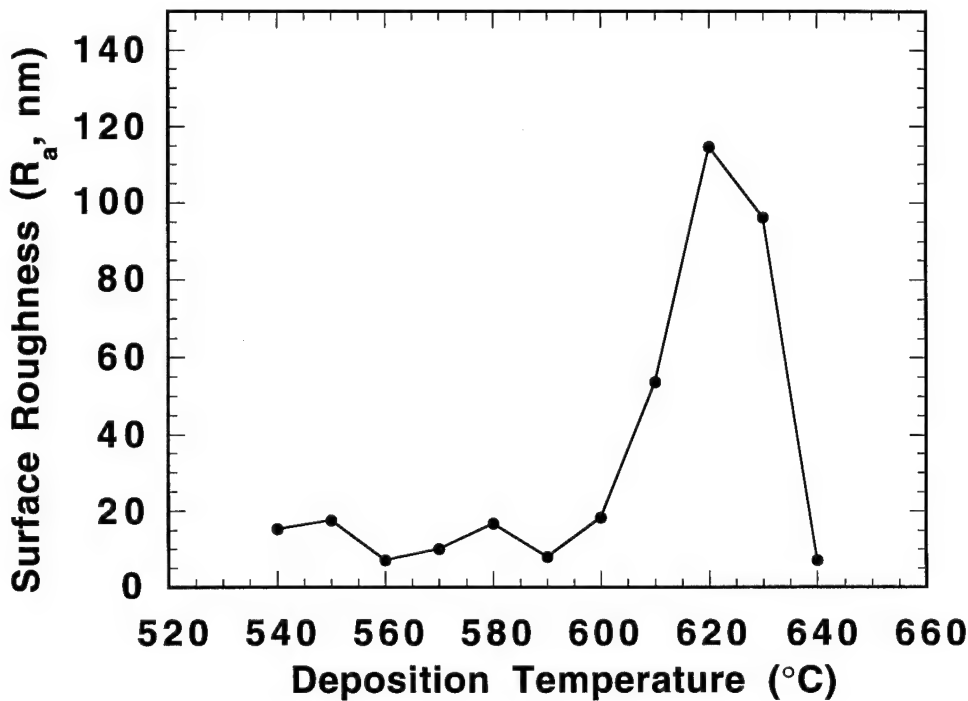
**FIGURE 5.2.4(b)** AFM area scan of as-deposited amorphous Si at  $580^\circ\text{C}$ .



**FIGURE 5.2.4(c)** AFM area scan of as-deposited polycrystalline Si at 600°C.



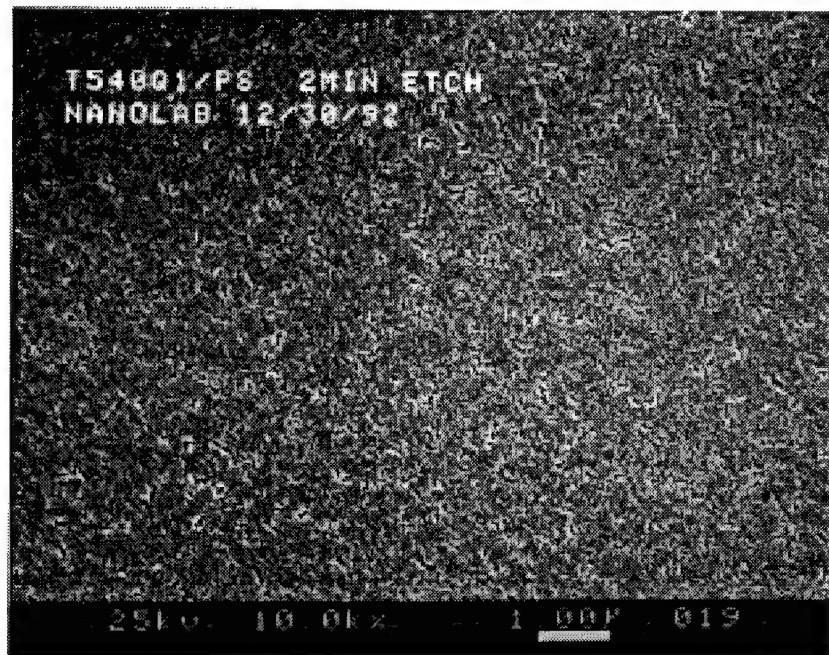
**FIGURE 5.2.4(d)** AFM area scan of as-deposited polycrystalline Si at 620°C.



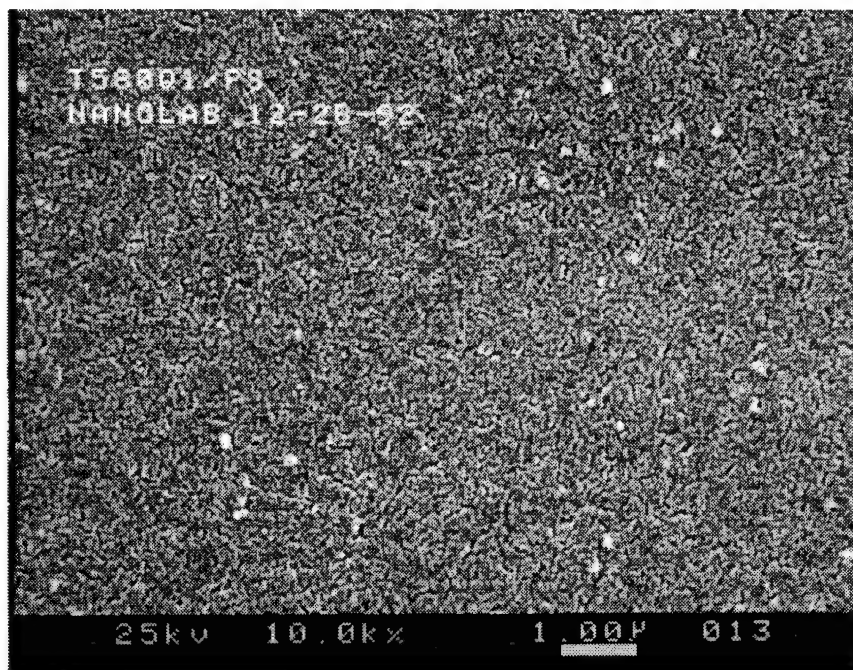
**FIGURE 5.2.5** Surface roughness of as-deposited films as a function of the deposition temperature  $T_D$ .

Figure 5.2.5 shows the surface roughness  $R_a$  obtained by AFM measurement as the function of deposition temperature. As shown in Fig. 5.2.5, the surface roughness of films deposited at  $T_D$ 's from 540°C to 590°C are uniformly smaller than that of films deposited at  $T_D$ 's from 600°C to 630°C. This trend of increasing roughness as the deposition temperature rises is consistent with the increase of crystallinity and grain size. However, as in Fig. 5.2.5, the polycrystalline film grown at 640°C is rather smooth with  $R_a$  of ~ 5 nm. This is an very interesting phenomenon and requires more studies (This sample was deposited last in the sequence of LPCVD while we run out of SiH<sub>4</sub> gas and the film is very thin).

After stain-etching for a period of 2 min, the Si films become porous with varying pore sizes and surface morphologies. We have first used SEM to obtain a qualitative comparison of the surface pore area density (SPAD) of films deposited at different temperatures. SPAD can be used as an indirect measure of the film porosity [Williams, *et al.* (1993)]. As shown by the SEM micrographs of 2 min stain-etched films in Figs. 5.2.6(a-d), the SPAD of films as-deposited at 540 and 580°C was much lower than that of films obtained at higher temperatures. The highest SPAD level was observed for  $T_D$  of 600°C, as seen in Fig. 5.2.6(c). The differences in SPAD and in morphology of the etched films, as seen from the SEM micrographs, are related to differences in etch rate and initial surface morphology of the films. They, in turn, are related to the crystallinity produced at various deposition temperatures. Of course, one can also alter the degree of porosity by adjusting the stain-etching time. For example, films deposited at the low end of the temperature range (540 and 580°C), which show low SPAD levels when stain-etched for 2 min (see Fig. 5.2.6(a) and 5.2.6(b)), developed significantly higher SPAD levels when stain-etched for 31 and 8 min, as shown in Fig. 5.2.7(a) and 5.2.7(b), respectively.



**FIGURE 5.2.6(a)** SEM micrograph (plan-view) of stain-etched amorphous Si at 540°C.



**FIGURE 5.2.6(b)** SEM micrograph (plan-view) of stain-etched amorphous Si at 580°C.

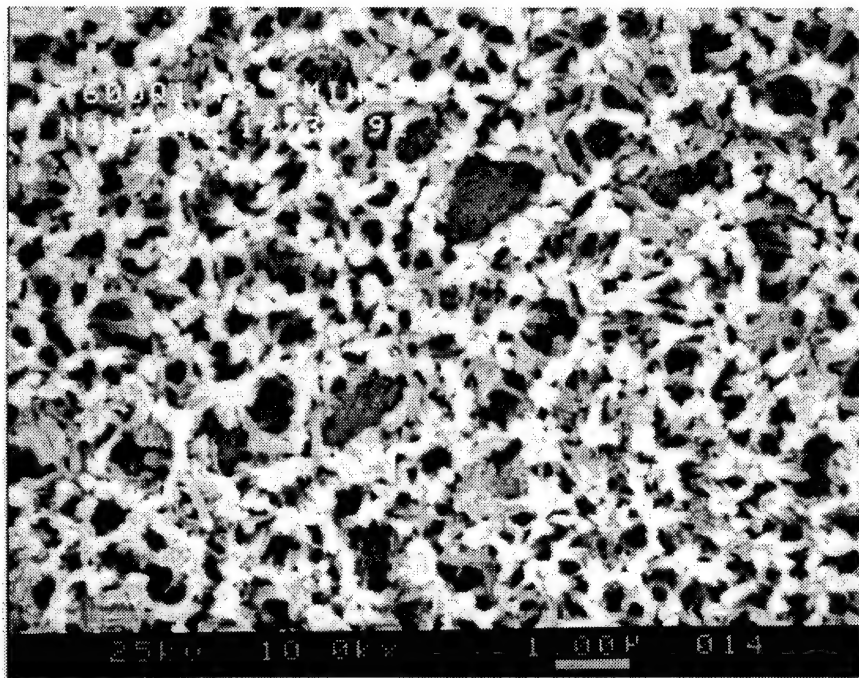


**FIGURE 5.2.6(c)** SEM micrograph (plan-view) of stain-etched polycrystalline Si at 600°C.

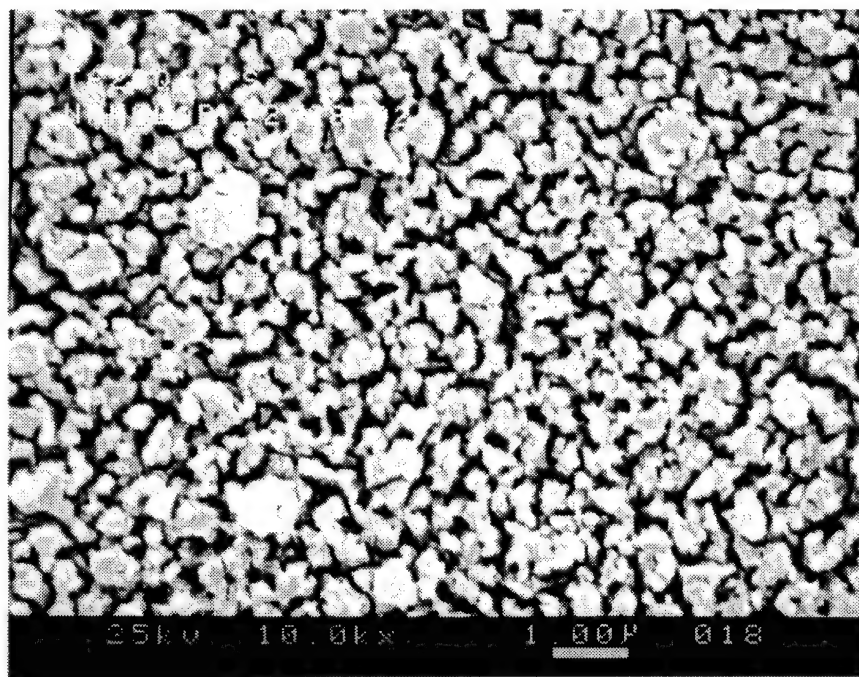


**FIGURE 5.2.6(d)** SEM micrograph (plan-view) of stain-etched polycrystalline Si at 620°C.

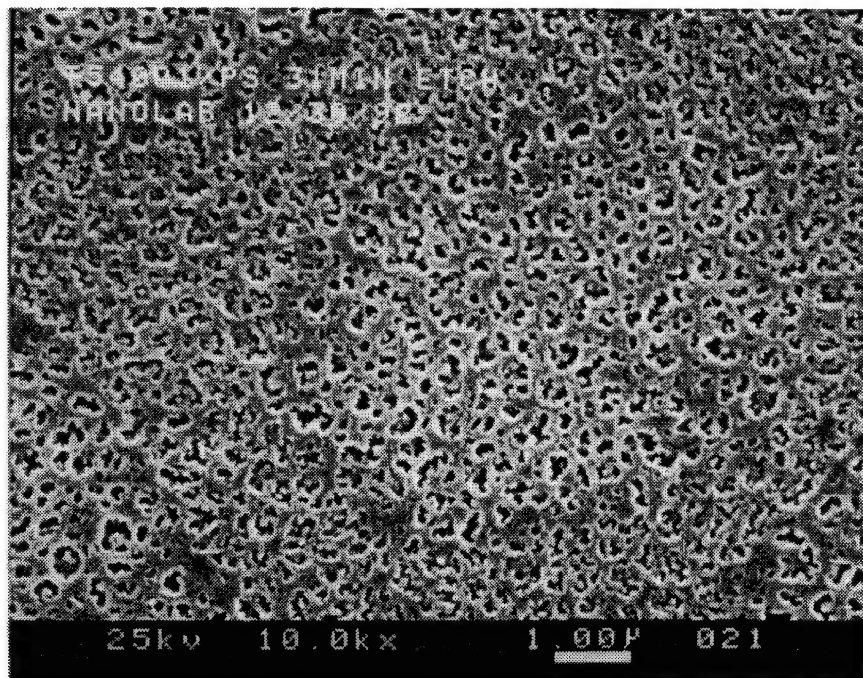


**FIGURE 5.2.7(a)** SEM micrographs (plan-view) of non-luminescent porous silicon with  $T_D$  of 540°C stained-etched for 31 min.

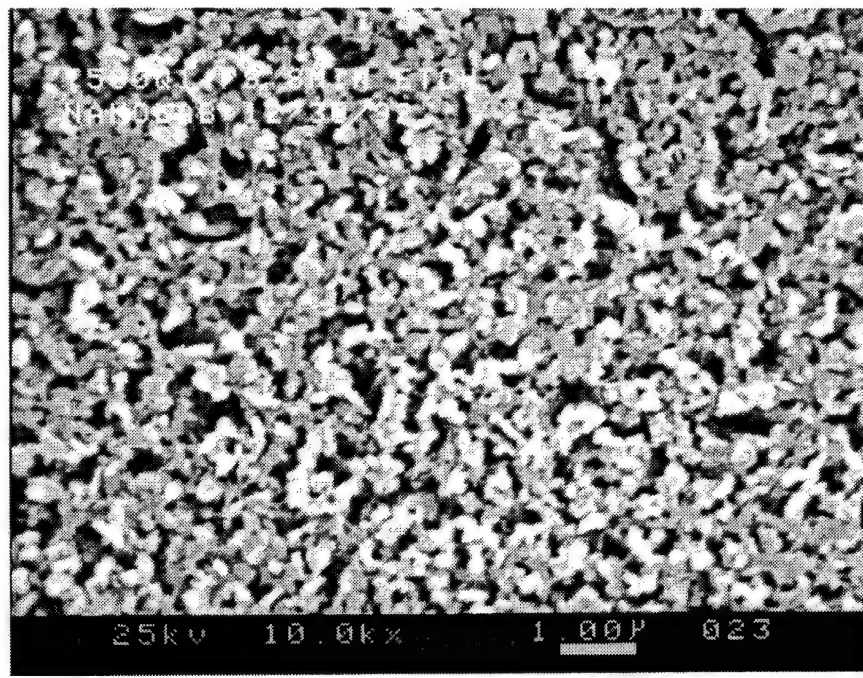


**FIGURE 5.2.7(b)** SEM micrographs (plan-view) of non-luminescent porous silicon with  $T_D$  of 580°C stained-etched for 8 min.

A more quantitative evaluation of the porosity of these samples was obtained by performing weight loss measurements. The weight of each sample was measured before and after stain-etching. The relative weight loss (normalized to the initial weight), which is defined as  $\Delta W\% = (W_1 - W_2)/W_1$ , where  $W_1$  is the initial weight of the sample and  $W_2$  is the weight after etching, is

shown in Fig. 5.2.8 as a function of deposition temperature. The weight loss of Si films deposited on both quartz (Fig. 5.2.8(a)) and oxidized Si substrates (Fig. 5.2.8(b)) and stain-etched for the standard 2 min was measured. The increase in weight loss for films with  $T_D \approx 600$ - $620^\circ\text{C}$  is a confirmation of higher levels of porosity for these films. It is also quite clear from Fig. 5.2.8(a) that by using longer etch times, the porosity of films deposited at low temperatures (in this case  $540^\circ\text{C}$ ) can reach, or exceed, that of films deposited at high  $T_D$  and etched for only 2 min.

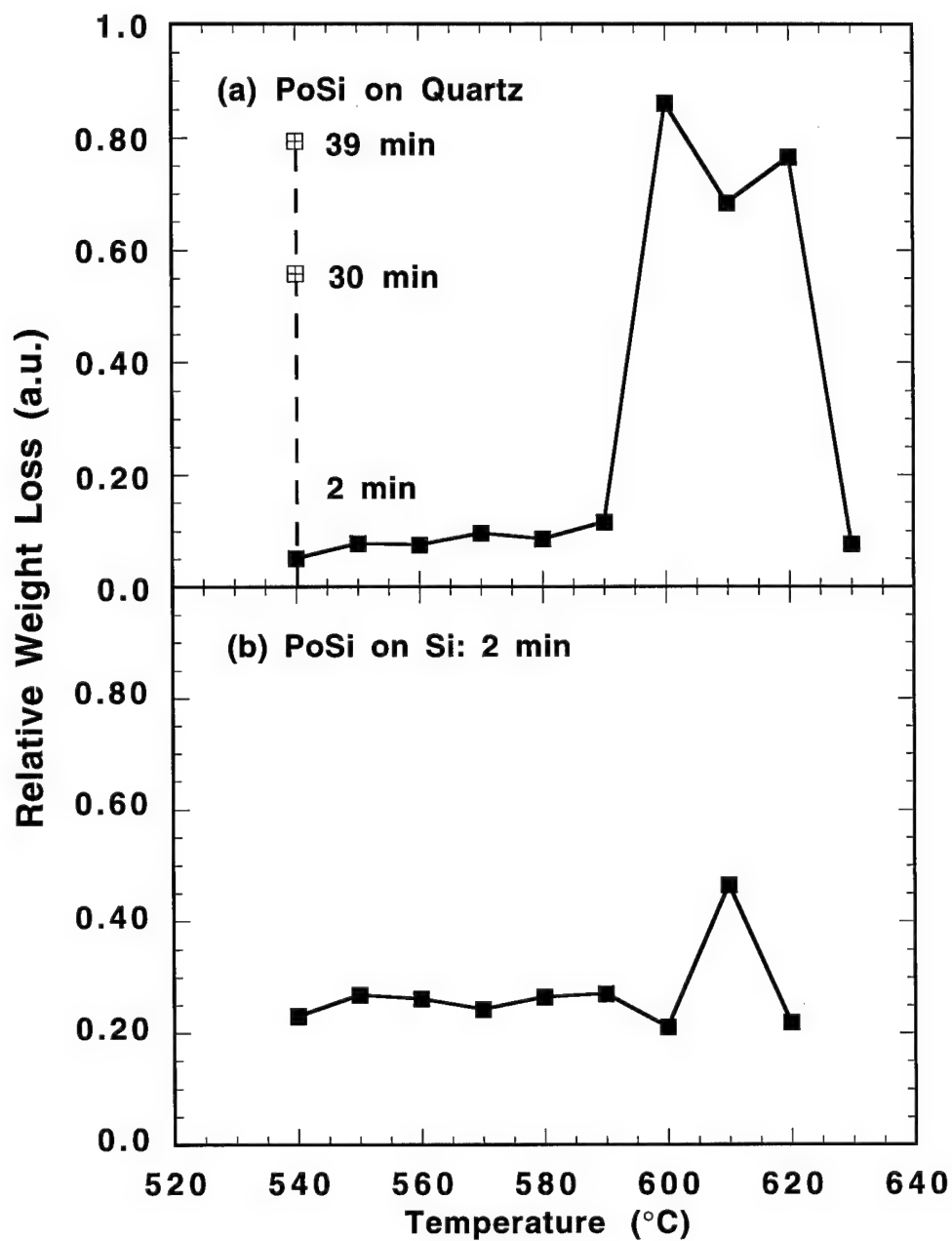


**FIGURE 5.2.8** Relative weight loss during stain etching of CVD Si films deposited at different temperatures: (a) Si on quartz,  $T_D = 540$  -  $630^\circ\text{C}$ , 2 min etch time; 30 and 39 min etch time for  $T_D = 540^\circ\text{C}$ ; (b) Si on oxidized Si,  $T_D = 540$  -  $620^\circ\text{C}$ , 2 min etch time.

The photoluminescence characterization of the Si films stain-etched for 2 min indicates that films deposited at 580°C (and below) do not exhibit a PL signal. For deposition temperatures of 590°C and higher, the porous silicon layers exhibit a broad PL signal with a peak at 660-670 nm and a full width at half-maximum (FWHM) of 120-140 nm. Shown in Fig. 5.2.9(a) is a comparison of the PL spectra obtained from three porous

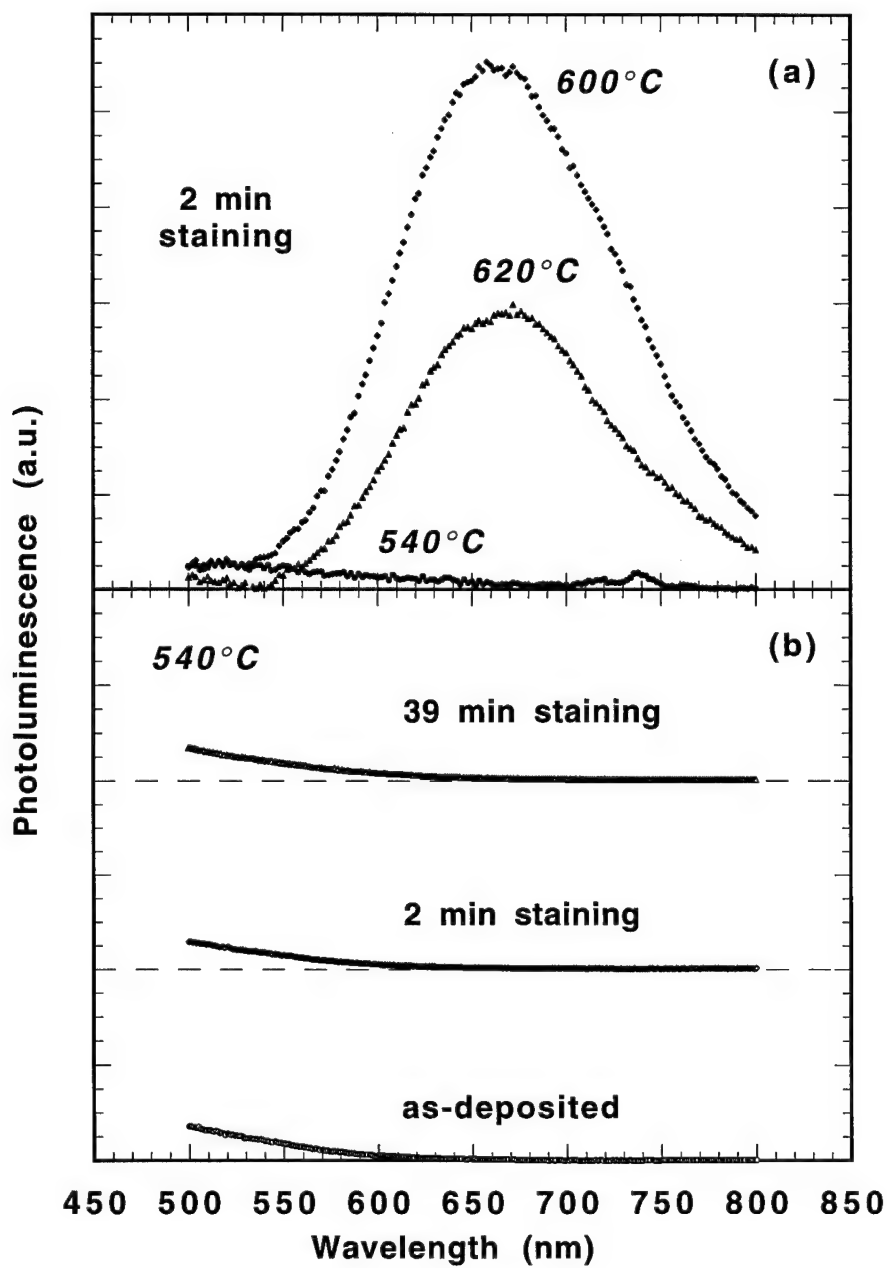


**FIGURE 5.2.9**

Room temperature PL spectra of porous silicon formed in Si films deposited at 580, 600, 620°C.

silicon films deposited at 580, 600, and 620 °C. Fig. 5.2.9(b) plots PL spectra obtained from the same Si sample deposited at 540°C when stain etched for 2 min and for 39 min, as well as in the as-deposited condition. The background PL level, due to the incomplete filtering of the UV source,

was subtracted for the data shown in Fig. 5.2.9. While arbitrary units are used for the PL signal in Fig. 5.2.9, the relative scale of all plots is the same. It is obvious from Fig. 5.2.9(b) that no PL can be obtained by stain-etching Si thin films which have been deposited at low temperature (and are therefore *amorphous*) even if they have a highly porous structure. For comparison, stain-etched *n*-type *crystalline* Si substrates, with a low SPAD level very similar to the 2 min stain-etched amorphous Si film deposited at 540°C, produced [Steckl, *et al.* (1993)] a copious room temperature PL signal.

A major issue regarding the mechanism for photoluminescence in porous silicon is the crystallinity of photoluminescent porous silicon, since its existence is essential for the quantum confinement effect to occur. Micro- and nano-crystalline clusters have been observed by many groups [Cole, *et al.* (1992), Kanemitsu, *et al.* (1992), Shih, *et al.* (1993)] in both anodized and stain-etched porous silicon formed from crystalline Si, using high resolution electron microscopy (HREM) or transmission electron microscopy (TEM). It is well known that the sample preparation for HREM and TEM inevitably introduces damage to the specimen under investigation. This sometimes gives rise to difficulties in obtaining unambiguous conclusions. For example, it was also reported [Jung, *et al.* (1992)] that photoluminescent porous silicon was obtained by stain-etching amorphous Si grown by MBE and subsequently annealed at temperature above 725°C. This porous silicon layer appeared amorphous under TEM observation.

We investigated the crystallinity of stain-etched porous silicon on several samples using XRD and Raman spectroscopy. In order to draw an unambiguous conclusion from XRD, one has to insure that the influence of non-porous silicon material (due to the presence of a Si substrate or of remaining poly-Si not rendered porous by etching) is eliminated or at least minimized. Therefore, we have modified the stain-etching recipe to consist of 200 parts HF and 1 part HNO<sub>3</sub> (by volume) in order to provide a more uniform porous silicon layer in a very short time. This combination has a very short incubation time (~10 sec) and faster etch rate than that of previously mentioned solutions.

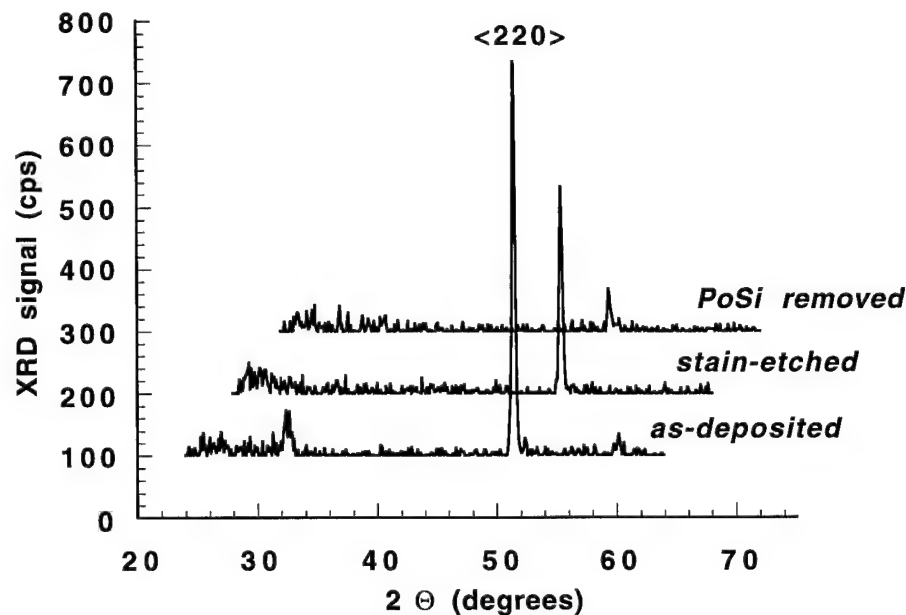


**FIGURE 5.2.10** XRD spectra of Si film deposited at 600°C: (a) as-deposited; (b) stain-etched for 50 sec in HF/HNO<sub>3</sub> with 200:1 ratio; (c) after porous silicon removal by etching in KOH for 30 sec.

Figure 5.2.10 shows the XRD spectra obtained at three different stages of processing for Si thin films deposited on quartz at 600°C: (a) as-deposited film; (b) after etching for 50 sec with the 200:1 solution to obtain a uniform layer of photoluminescent porous silicon; (c) after removal of the porous silicon layer by etching at room temperature in 1N KOH for 30 sec. The KOH solution etches porous silicon much more rapidly than poly-Si, thus removing it selectively from a poly-Si under-layer. The existence of crystallinity in the porous silicon layer is unambiguously deduced by comparing the X-ray spectra of Fig. 5.2.10, in particular the presence and intensity of the  $<220>$  line. By comparing first the as-deposited (Fig. 5.2.10(a)) and porous silicon films (Fig. 5.2.10(b)), we note that the  $<220>$  peak is still present after stain-etching. Its reduced intensity is probably due to the reduced effective Si volume after the poly-Si film is rendered porous by stain-etching. Next, we need to establish that the  $<220>$  peak in Fig. 5.2.10(b) is due to porous silicon and not to an unconverted poly-Si underlayer by selectively removing the porous silicon by KOH etching. As shown in Fig. 5.2.10(c), this results in the almost complete disappearance of the  $<220>$  peak, confirming that there remained very little unconverted poly-Si after stain-etching and that, therefore, the dominant contribution to the crystallinity of the film shown in Fig. 5.2.10(b) is from porous silicon. All the samples studied exhibited the same trend.

Raman spectroscopy was performed on photoluminescent porous silicon using the 496 nm line of an  $\text{Ar}^+$  laser. The Raman spectra shown in Fig. 5.2.11 compare an as-deposited (630°C) poly-Si film with a similar film after stain-etching for 2 min in the 1:3:5 solution. The similarity between the Raman peaks at 520.8  $\text{cm}^{-1}$  for the as-deposited and at

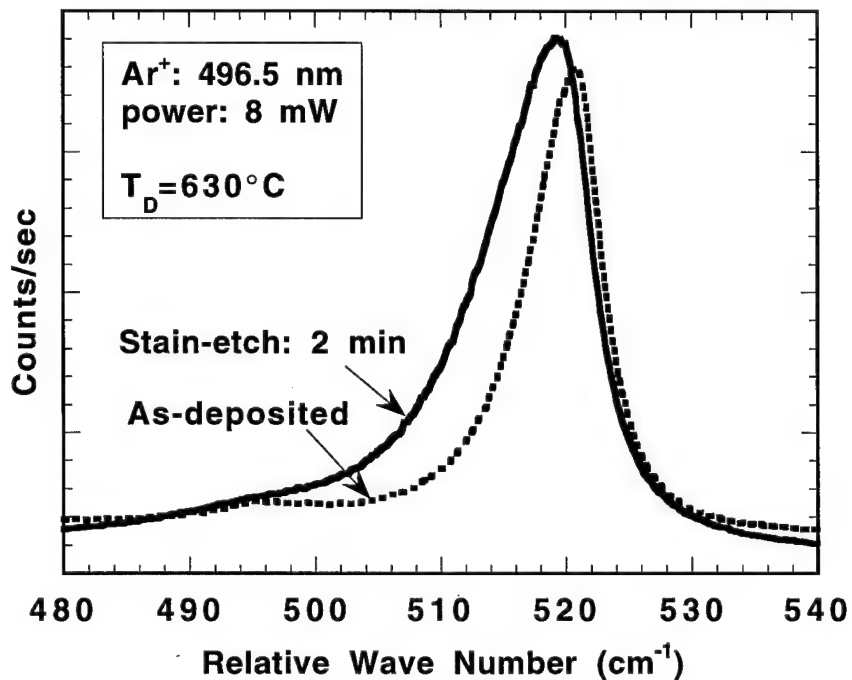


**FIGURE 5.2.11** Raman spectra of as-deposited (at 630°C) and stain-etched (for 2 min) poly-Si film.

519.4  $\text{cm}^{-1}$  for the stain-etched films provides another clear evidence that the crystallinity is preserved after the film is converted to porous silicon. The broader Raman peak for the porous silicon sample suggests that some reduction in crystallite size occurs during stain-etching.

Infrared (IR) transmission measurements revealed that above  $1000\text{ cm}^{-1}$ , both etched and unetched samples exhibited distinct periodic fringes which can be attributed to interference between the various layers of material present. These fringes differed somewhat in periodicity (with an average value of  $600\text{ cm}^{-1}$ ) from sample to sample, due to thickness variation. As a result, identification of specific absorption signals above  $1000\text{ cm}^{-1}$  was difficult. It was also difficult to compare  $\text{SiO}_2$ -related signals before and after stain etching, due to the thick oxide layers present on the Si wafers.

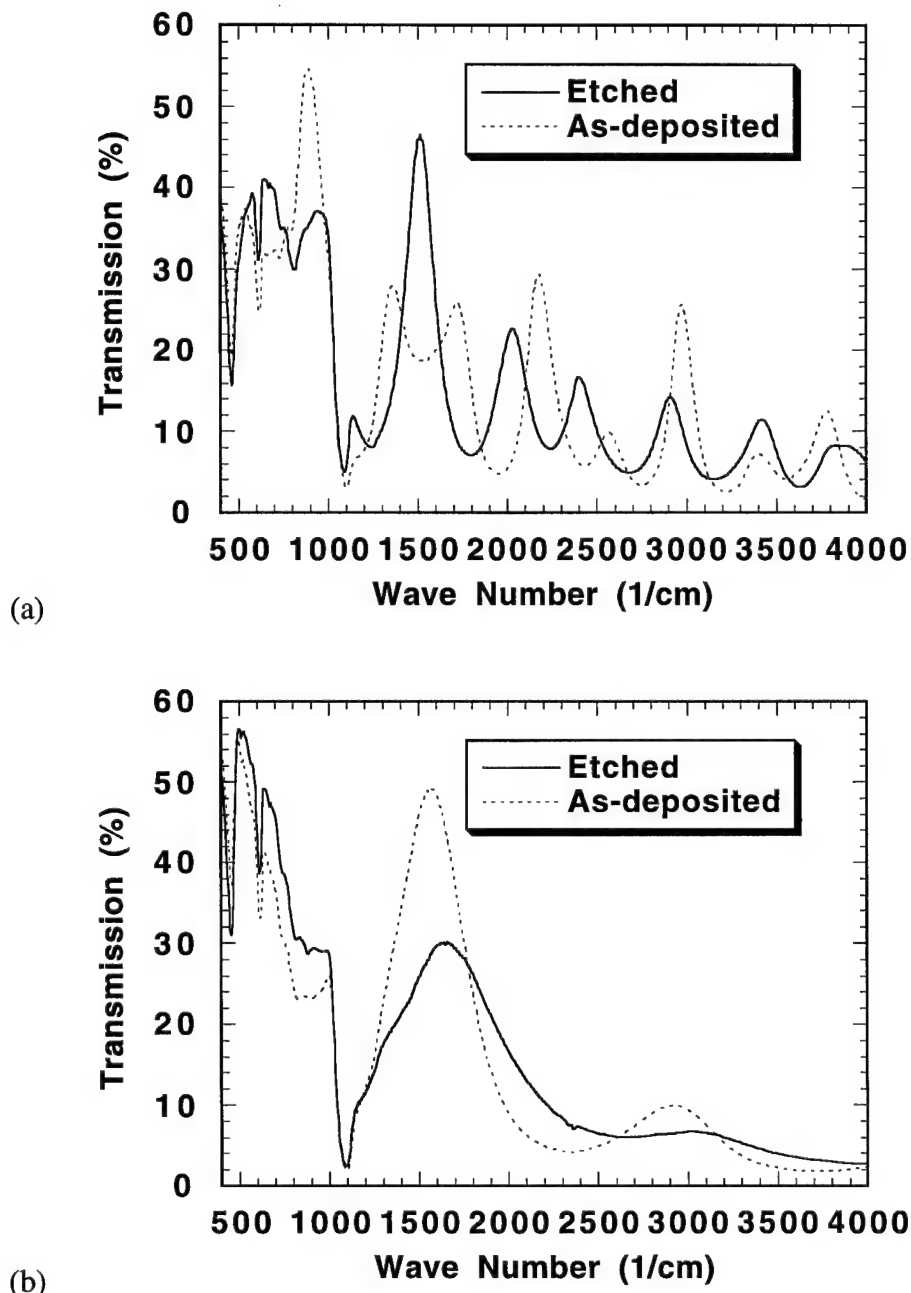


**FIGURE 5.2.12** Full range FTIR spectra showing distinct periodic fringes attributed to interference between the various layers of material present. (a): amorphous Si films deposited at  $540^\circ\text{C}$ ; (b) polycrystalline Si films deposited at  $630^\circ\text{C}$ .

Porous silicon samples formed from poly-Si deposited at  $T_D \geq 590^\circ\text{C}$ , exhibited a relatively weak peak at  $2260 \text{ cm}^{-1}$ , as indicated in Fig. 5.2.13 for films deposited at  $590^\circ\text{C}$  and  $600^\circ\text{C}$ . This peak can be attributed to Si-H stretching modes in which the Si is backbonded to one or more oxygen atoms [Sugiyama, *et al.* (1990), Gupta (1991)]. This assignment is supported by previous IR data for as-made and lightly oxidized porous silicon [Prokes, *et al.* (1992)]. The possibility of this  $2260 \text{ cm}^{-1}$  peak being assigned to a pure hydride peak specie corresponding to  $\text{SiH}_x$  stretching modes can be ruled out, since these modes occur at wavenumbers  $< 2260 \text{ cm}^{-1}$ .

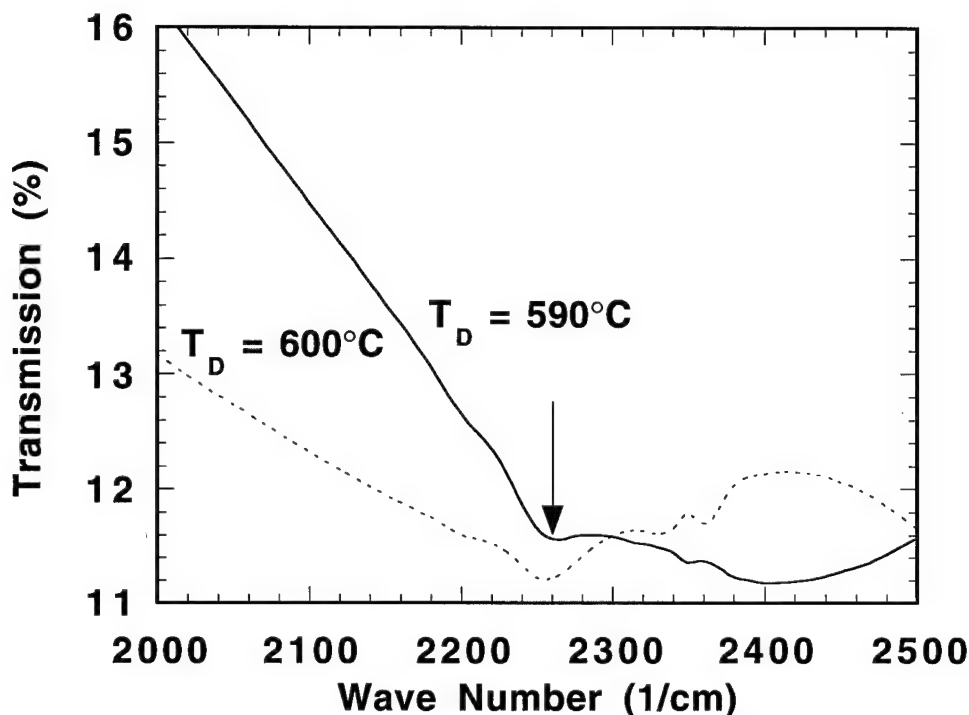


**FIGURE 5.2.13** FTIR spectra near the vicinity of  $2260 \text{ wavenumber}$  from stain-etched polycrystalline Si films showing distinct peak due to Si-H stretching mode.

IR spectra in the  $600\text{-}950 \text{ cm}^{-1}$  range are known to exhibit  $\text{SiH}_x$ -related bending and deformation modes [Gupta, *et al.* (1988), Crowell and Lu (1990)], providing accurate data. Figure 5.2.14 shows the transmission in the range of  $500\text{-}1000 \text{ cm}^{-1}$  of two films deposited at  $630^\circ\text{C}$ : one was an as-deposited sample and the other was a stain-etched sample. The major absorption peak at  $610 \text{ cm}^{-1}$  in both films is due to the two phonon (acoustic and optic) line of bulk silicon [Temple and Hathaway (1973)], and it is not related to the thin porous silicon layers.

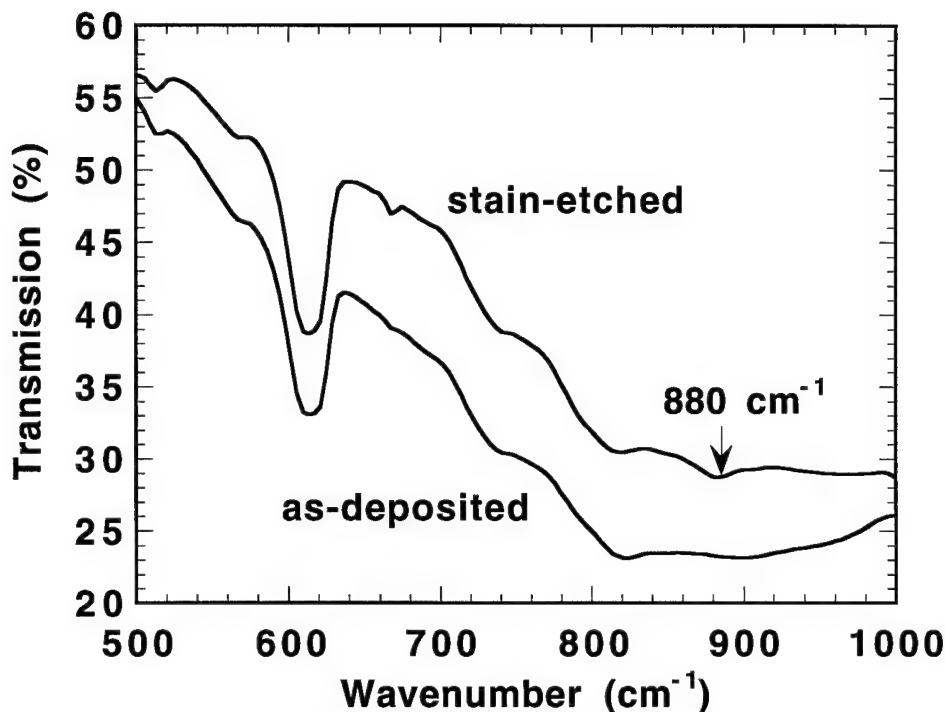


**FIGURE 5.2.14** FTIR spectra in the range of 500 - 1000  $\text{cm}^{-1}$  from both as-deposited and stain-etched poly-Si films with  $T_D$  of 630°C.

A small but distinct absorption region appears in a range centered at 880  $\text{cm}^{-1}$  for the stain-etched films. This feature was present only for samples prepared at  $T_D \geq 590^\circ\text{C}$ . Figure 5.2.15 shows the transmission in the vicinity of the 880  $\text{cm}^{-1}$  region for cases of luminescent ( $T_D \geq 590^\circ\text{C}$ ) as well as non-luminescent ( $T_D < 590^\circ\text{C}$ ) porous silicon films. Unetched samples and those produced at  $T_D < 580^\circ\text{C}$  do not exhibit this feature, regardless of the length of stain etching time. This absorption appears to be hydride related, since anneals to temperatures above 500°C lead to its disappearance, similar to earlier results [Prokes (1993)]. The bending or deformation modes of pure  $\text{SiH}_x$ -type species have been reported [Gupta (1991)] above 910  $\text{cm}^{-1}$ , at 666  $\text{cm}^{-1}$  and at 625  $\text{cm}^{-1}$ , but none of these appear to be present in our samples. Thus, the absorption observed at 880  $\text{cm}^{-1}$  absorption is unlikely to originate from pure hydrides. This absorption peak could be possibly due to a  $\text{SiH}_2\text{O}$  structural unit [Daek, *et al.* (1992)] or from a combination Si-OH stretch and SiO-H bend modes [Koch (1993)]. In addition, it should be pointed out that no N-H<sub>2</sub> nor N-H stretching modes (in the 3460  $\text{cm}^{-1}$  range) [Dillon, *et al.* (1990)] were detected for any of the samples. Thus, the 880  $\text{cm}^{-1}$  line cannot be due to  $\text{Si}_3\text{N}_4$ , since this stable complex forms only at temperatures above 650°C, and the samples studied in this work were etched at room temperature.

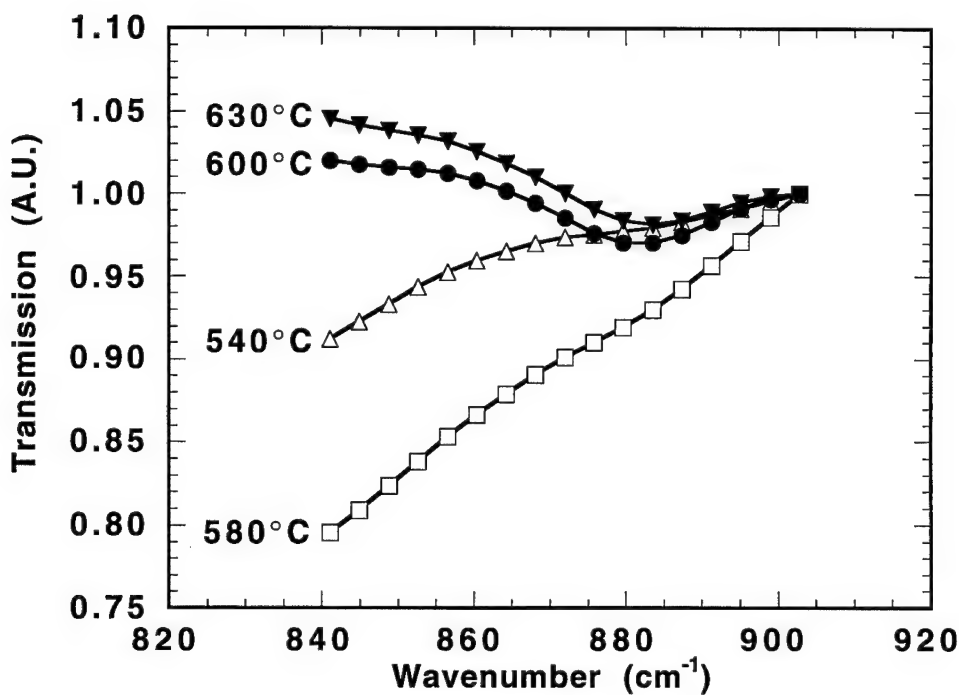


**FIGURE 5.2.15** FTIR spectra ( $800\text{-}900\text{ cm}^{-1}$ ) in the vicinity of Si oxyhydride peak ( $880\text{ cm}^{-1}$ ) from porous silicon films deposited at several temperatures ( $540, 580, 600, 630^{\circ}\text{C}$ ).

To determine possible correlation between the luminescence properties of amorphous and polycrystalline porous silicon films and the corresponding surface dangling bond density, the spin density of several etched films was measured using electron spin resonance (ESR). Comparing first films etched for same time of 2 min, the polycrystalline Si film deposited at  $620^{\circ}\text{C}$  yields a spin density of  $1.9 \times 10^{18}/\text{cm}^3$  vs. a value of  $1.2 \times 10^{19}/\text{cm}^3$  for the amorphous film deposited at  $580^{\circ}\text{C}$ . These values are consistent with the spin concentrations reported [Friederich and Kaplan (1980)] previously for CVD Si films as a function of temperature. More relevant is the fact that the amorphous porous silicon film deposited at  $580^{\circ}\text{C}$  and etched for 30 min to provide a high porosity level, but which was nevertheless *non-luminescent*, exhibits a spin density of only  $8.3 \times 10^{17}/\text{cm}^3$  or  $2.3 \times$  less than the *photoluminescent* polycrystalline Si film deposited at  $620^{\circ}\text{C}$ . Therefore, it can be concluded that there is no simple correlation between the dangling bond density and PL activity in these porous silicon films.

The presence of PL only in stain etched Si films deposited at  $T_D > 580^{\circ}\text{C}$  indicated that crystallinity is a necessary requirement for achieving optical emission. It is interesting to introduce the presence of the Si-O-H species in these films into this relationship. The integrated PL intensity (500 to 800 nm) of stained films, the  $\langle 220 \rangle$  X-ray diffraction peak of as-deposited films, and the IR signal at  $880\text{ cm}^{-1}$  from stained films are plotted as a function of deposition temperature in Fig. 5.2.16. To provide a meaningful comparison, the PL signal was normalized to the percent weight loss of each sample, thus effectively compensating for samples of different porosities. The XRD signal was normalized to the as-deposited film thickness to compensate for differences in film thickness with deposition temperature. A common transition temperature in film deposition occurs between 580 and  $590^{\circ}\text{C}$ . Above this transition temperature the films deposited are polycrystalline, and are light emitting, as well as exhibiting Si oxyhydrides, upon stain etching. Therefore, it appears that a certain level of crystallinity in the starting material is essential to produce both PL

and Si oxyhydrides in porous silicon rendered by stain etch. However, since both crystallinity and Si oxyhydride are present in all porous silicon films exhibiting PL, this commonality does not lead us to draw an unambiguous conclusion regarding the origin of PL. In addition, one should not be confused by previous reports on PL from anodized "a-Si:H" films, since these materials were actually partially crystallized with 45% crystalline volume fraction [Bustarret, *et al.* (1992)].

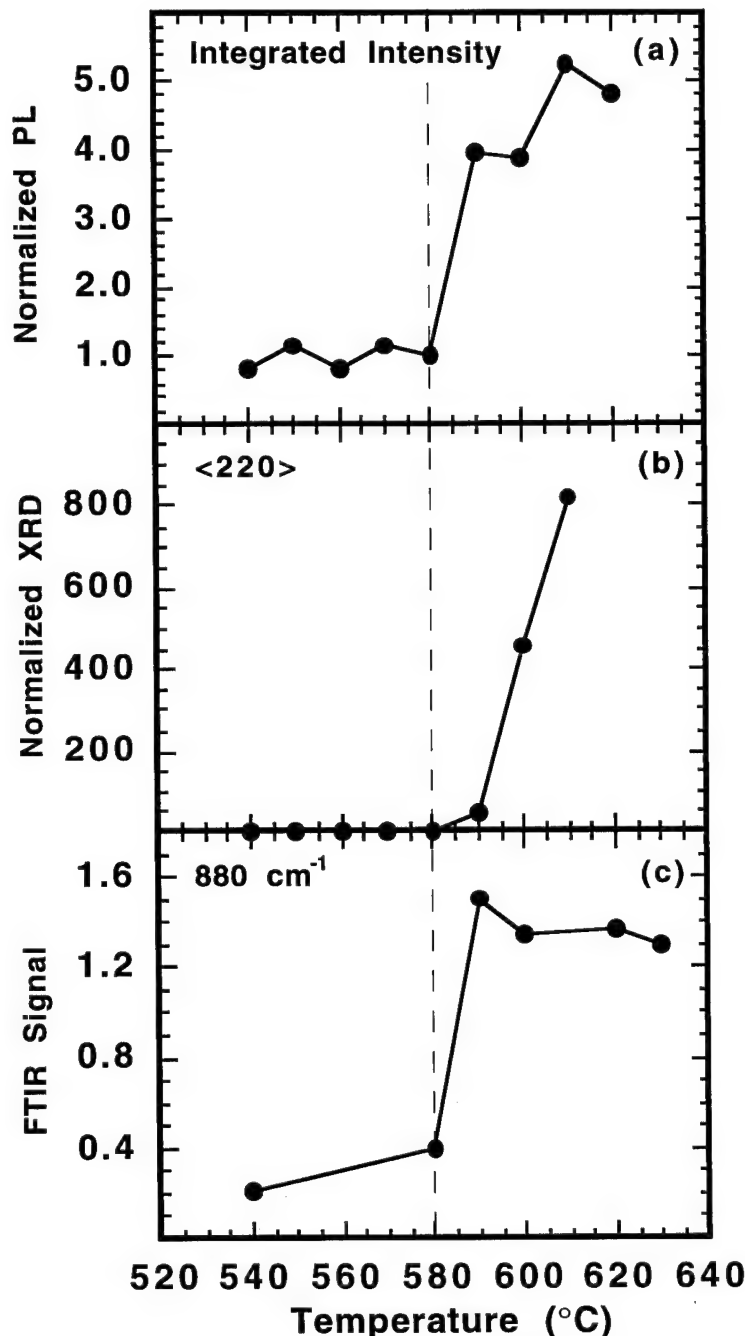


**FIGURE 5.2.16** Effect of deposition temperature on porous silicon materials properties: (a) photoluminescence - UV pumping at 365 nm ; (b) crystallinity - XRD  $<220>$  peak; (c) Si oxyhydride - FTIR peak at  $\sim 890 \text{ cm}^{-1}$ .

There exist at least three possible explanations. Firstly, the crystallinity and only the crystallinity in the starting material, which is retained after stain-etching [Steckl, *et al.* (1994)], is directly responsible for the PL in porous silicon. This would support the quantum confinement model. Secondly, the crystallinity is important only for Si oxyhydride formation and the Si oxyhydride is the origin of the PL. In this case, one possible way to interpret the above result is as follows. It has been previously suggested that the source of the orange-red PL in porous silicon is due to non-bridging oxygen hole centers (NBOHCs) [Nishijimi, *et al.* (1986), Prokes (1993)], which exhibit very similar optical characteristics to porous silicon PL. An NBOHC is simply an Si-O unit, in which the oxygen is missing an electron. At room temperature, in the presence of hydrides or OH, the defect becomes H-stabilized, and the PL efficiency has been noted to significantly increase. Thus, it is possible that this defect may relate to the absorption at 880 cm<sup>-1</sup>. If that is the case, the amorphous porous silicon lacks this structure and thus may exhibit no visible PL. Thirdly, it is possible that a combination of effects is responsible for the observed effects. However, whatever the PL origin is, crystallinity in the initial materials is essential to produce PL in porous silicon.

#### 5.2.4 Summary

In summary, porous silicon from stain-etched Si thin films deposited on oxidized Si substrates at temperatures ranging from 540 to 640°C, designed to provide varying levels of crystallinity, have been investigated by XRD, PL and IR transmission spectroscopy. We have observed that a minimum level of crystallinity in the as-deposited Si film is required for the subsequent porous silicon layer to exhibit visible photoluminescence. Simply providing a high level of SPAD in initially amorphous Si films does not produce photoluminescent layers. We have also determined that initially polycrystalline films, which yield light-emitting porous silicon, also retain their crystallinity during the stain-etching process. Concomitantly with the presence of photoluminescence and crystallinity, an absorption peak at 880-890 cm<sup>-1</sup> was observed in all etched poly-porous silicon films which were deposited at  $T_D \geq 590^\circ\text{C}$ . This absorption line, due to SiH<sub>2</sub>O structural unit [Daek, *et al.* (1992)] or possibly from a combination Si-OH stretch and Si-O-H bend modes [Koch (1993)], is not exhibited in any non-PL samples, either the etched a-porous silicon films grown at  $T_D \leq 580^\circ\text{C}$  or in any of the as-deposited films. Therefore, it appears that there exists a unique correlation between the level of crystallinity of the starting Si film, and the presence of surface oxyhydrides and photoluminescence after stain-etching.

#### REFERENCES

Brandt, M. S., Fuchs, H. D., Stutzmann, M., Weber, J. and Cardona, M., "The origin of visible luminescence from "porous silicon": a new interpretation", Solid State Comm. **81**, 307 (1992).

Bustarret, E., Ligeon, M., Bruyére, J. C., Muller, F., Hérino, R., Gaspard, F., Ortega, L. and Stutzmann, "Visible light emission at room temperature from anodized plasma deposited silicon thin films", Appl. Phys. Lett. **61**, 1552 (1992).

Canham, L., "Silicon quantum wire array fabrication by electrochemical and chemical dissolution of wafers", Appl. Phys. Lett. **57**, 1046 (1990).

Cole, M. W., Harvey, J. F., Lux, R. A., Eckart, D. W. and Tsu, R., "Microstructure of visibly luminescent porous silicon", Appl. Phys. Lett. **60**, 2800 (1992).

Crowell, J. E. and Lu, G., "The adsorption of hydrogen, digermane and disilane on Ge(111): a multiple internal reflection infrared spectroscopy study", J. Electron Spectrosc. Rel. Phenom. **54/55**, 1045 (1990).

Cullis, A. G. and Canham, L. T., "Visible light emission due to quantum size effects in highly porous crystalline silicon", Nature **353**, 335 (1991).

Cullity, B. D., "Elements of X-ray Diffraction", (Addison-Wesley, Reading, MA, 1967).

Daek, P., Rosenbauer, M., Stutzmann, M., Weber, J. and Brandt, M. S., "Siloxene: chemical quantum confinement due to oxygen in a silicon matrix", Phys. Rev. Lett. **69**, 2531 (1992).

Dillon, A. C., Gupta, P., Robinson, M. B., Bracker, A. S. and George, S. M., "FTIR studies of water and ammonia decomposition on silicon surfaces", J. Electron. Spectrosc. Relat. Phenom. **54/55**, 1085 (1990).

Friederich, A. and Kaplan, D., "Light-induced ESR quenching in a-Si", J. Non-Cryst. Solids **35&36**, 657 (1980).

Gupta, P., "FTIR studies of  $H_2O$  and  $D_2O$  decomposition on porous silicon surfaces", Surface science **245**, 360 (1991).

Gupta, P., Colvin, V. L. and George, S. M., "Hydrogen desorption kinetics from monohydride and dihydride species on silicon surfaces", Phys. Rev. B **37**, 8234 (1988).

Halimaoui, A., Oules, C., Bomchil, G., Bsiesy, A., Gaspard, F., Herino, R., Ligeon, M. and Muller, F., "Electroluminescence in the visible range during anodic oxidation of porous silicon films", Appl. Phys. Lett. **59**, 304 (1991).

Harbecke, G., Krausbauer, L., Steigmeier, E. F., Widmer, A. E., Kapper, H. F. and Neugebauer, G., "Growth and physical properties of LPCVD polycrystalline silicon", J. Electrochem. Soc. **131**, (1984).

Jung, K. H., Shih, S., Kwong, D. L., Cho, C. C. and Gnade, B. E., "Visible photoluminescence from porous Si formed by annealing and chemically etching amorphous Si", Appl. Phys. Lett. **61**, 2467 (1992).

Kamins, T. I., Mandurah, M. M. and Saraswat, K. C., "Structures and stability of low pressure chemically vapor-deposited silicon films", J. Electrochem. Soc. **125**, 927 (1978).

Kanemitsu, Y., Suzuki, K., Uto, H., Masumoto, Y., Matsumoto, T., Kyushin, S., Higchi, K. and Matsumoto, H., "Visible photoluminescence of silicon-based nanostructures: Porous silicon and small silicon-based clusters", Appl. Phys. Lett. **61**, 2446 (1992).

Koch, F., "Models and mechanisms for the luminescence of porous Si", MRS Symp. Proc. **298**, 319 (1993).

Koshida, N. and Koyama, H., "Efficient Visible Photoluminescence from Porous Silicon", Jpn. J. Appl. Phys. **30**, L1221 (1991).

Lehmann, V. and Gosele, U., "Porous silicon formation: A quantum wire effect", Appl. Phys. Lett. **58**, 856 (1991).

Nishida, A., Nakagawa, K., Kakibayashi, H. and Shimada, T., "Microstructure of Visible Light Emitting Porous Silicon", Jpn. J. Appl. Phys. **31**, L1219 (1992).

Nishijimi, M., Edamoto, K., Kubota, Y., Tanaka, S. and Onchi, M., "Vibrational electron energy loss spectroscopy of the Si (111) (7×7)- $H_2O$  ( $D_2O$ ) system", J. Chem. Phys. **84**, 6458 (1986).

Prokes, S. M., "Light emission in thermally oxidized porous silicon: Evidence for oxide-related luminescence", Appl. Phys. Lett. **62**, 3244 (1993).

Prokes, S. M., Carlos, W. E. and Bermudez, V. M., "Luminescence cycling and defect density measurements in porous silicon: Evidence for hydride based model", Appl. Phys. Lett. **61**, 1447 (1992).

Prokes, S. M., Glembocki, O. J., Bermudez, V. M., Kaplan, R., Friederhof, L. E. and Searson, P. C., "SiHx excitation: An alternate mechanism for porous Si photoluminescence", Physical review. b, condensed matter v **45**, 13788 (1992).

Read, A. J., Needs, R. J., Nash, K. J., Canham, L. T., Calcott, P. D. J. and Qteish, A., "First-principles calculations of the electronic properties of silicon quantum wires", Phys. Rev. Lett. **69**, 1232 (1992).

Searson, P. C., Macaulay, J. M. and Prokes, S. M., "The Formation, Morphology, and Optical Properties of Porous Silicon Structures", J. Electrochem. Soc. **139**, 3373 (1992).

Shih, S., Jung, K. H., Qian, R.-Z. and Kwong, D. L., "Transmission electronmicroscopy study of chemically etched porous Si", Appl. Phys. Lett. **62**, 467 (1993).

Steckl, A. J., Xu, J. and Mogul, H. C., "Photoluminescence from stain-etched polycrystalline Si thin films", Appl. Phys. Lett. **62**, 2111 (1993).

Steckl, A. J., Xu, J. and Mogul, H. C., "Relationship between crystallinity and photoluminescence in stain-etched porous Si", J. Electrochem. Soc. **141**, 674 (1994).

Steckl, A. J., Xu, J., Mogul, H. C. and Mogren, S., "Doping-induced selective area photoluminescence in porous silicon", Appl. Phys. Lett. **62**, 1982 (1993).

Steckl, A. J., Xu, J., Mogul, H. C. and Prokes, S. M., "Si oxyhydrides on stain-etched porous Si thin films and correlation with crystallinity and photoluminescence", J. Electrochem. Soc. **142**, L69 (1995).

Sugiyama, K., Igarashi, T., Moriki, K., Nagasawa, Y., Aoyama, T., Sugino, R., Ito, T. and Hattori, T., "Silicon-hydrogen bands in silicon native oxides formed during wet chemical treatments", Jpn. J. Appl. Phys. **29**, L2401 (1990).

Temple, P. A. and Hathaway, C. E., "Multiphonon Raman spectrum of silicon", Phys. Rev. B **7**, 3685 (1973).

Watanabe, H., Sakai, A., Tatsumi, T. and Niino, T., "Hemispherical grain silicon for high density DRAMs", Solid State Technology, **29** (1992).

Wei, L., Vaudin, M., Hwang, C. S., White, G., Xu, J. and Steckl, A. J., "Heat conduction in silicon thin films: effect of microstructure", J. Mat. Res. , (1995).

Williams, P. S., Kidder, J. N., Yun, H., Crain, D., Pearsall, T. P. and Schwartz, D. T., "Variations in the photoluminescence intensity of chemically and anodically etched silicon films", MRS Symp. Proc. **298**, 313 (1993).

## Chapter 6

### Porous Si Optoelectronic Devices

#### 6.1 Porous Si Light Emitting Diodes

##### 6.1.1 Introduction

Current induced visible luminescence at room temperature from Si was first reported, more than three decades earlier than the observation of visible photoluminescence from porous Si, by Allen Gee in 1960 [Gee (1960)]. Gee observed reddish glow at a silicon anode in contact with an electrolyte (the so-called electrochemiluminescence) while studying stain films on single-crystal silicon chemically formed by the method of Archer [Archer (1960)]. Apparently the so-called Type I stain films as designated by Archer are stain-etched porous silicon films as often quoted in recent literature. In Gee's experiment only *p*-type silicon coated with Type I films were found to glow at current densities greater than  $5 \text{ mA/cm}^2$ . Since the report of strong visible photoluminescence from anodized porous silicon by Canham in 1990 [Canham (1990)], a few authors have reported current-induced visible light emission from electrochemically etched porous silicon. These include electroluminescence from porous silicon in contact with electrolyte during anodic oxidation [Halimaoui, *et al.* (1991)] and solid-state Schottky contacts between a porous silicon layer obtained from anodically etched c-Si and a thin film of Au [Richter, *et al.* (1991), Kolmakova, *et al.* (1993), Steiner, *et al.* (1993)], Al [Shi, *et al.* (1993)], indium tin oxide (ITO) [Kalkhoran, *et al.* (1992), Koshida and Koyama (1992), Kalkhoran, *et al.* (1993)], or conducting polymer (polypyrrole) [Koshida, *et al.* (1993)]. EL was also reported from an anodized porous silicon *p-n* homojunction [Chen, *et al.* (1993)] and a SiC/porous silicon heterojunction [Futagi, *et al.* (1992), Futagi, *et al.* (1993)]. The available device characteristics of anodized porous silicon light emitting diodes (LED's) reported to date are summarized in Table 6.1 below. The table indicates the materials used for the top contact, the thickness of the porous silicon layer, the leakage current density at a given reverse bias voltage, the current rectification ratio obtained between given forward and reverse bias voltages, the current density (bias) required for onset of EL (both visually observable and photodetector measured), and the peak wavelength of the EL spectrum. While the results are still sketchy, it is clear that reproducible photoemission at orange to red wavelengths can be obtained from anodized porous silicon.

Table 6.1 Summary of porous silicon LED characteristics

Contact Material	Porous silicon Layer ( $\mu\text{m}$ )	Leakage		Rectification		Observable EL		EL peak Wavelength (nm)	Reference First Author year
		Current (nA/cm <sup>2</sup> )	Rev. Bias (V)	Ratio	Vol. (V)	Current (mA/cm <sup>2</sup> )	Forward Bias (V)		
Au	7.5	-	-	-	-	14	200	650	Richter '91
Au	5.5	-	-	-	-	133	30	480, 540, 650	Steiner '93
Au	1-10	-	-	-	-	$10^4 \text{ V/cm}$ (field)	-	650	Kolmakova '93
Au	3-7	$2 \times 10^5$	7	420	$\pm 7$	90	7	680	Koshida '92
Al	-	177	10	-	-	30	-	-	Shi '93
ITO	-	-	-	-	-	-	-	650	Namavar '92
Polymer	4	$2 \times 10^5$	10	1000	$\pm 15$	-	-	593	Koshida '93
Polymer	7	-	-	-	-	5	12	630	Li '94
p-n	-	-	-	-	-	600	-	640	Chen '93
SiC	-	$4 \times 10^3$	1	$2.5 \times 10^4$	$\pm 1$	$2 \times 10^4$	20	670	Futagi '92
SiC	-	$10^4$	5	100	$\pm 5$	12	18	700	Futagi '92
ITO	0.2	538	10	$1.6 \times 10^5$	$\pm 15$	40	10	640	This work

While porous silicon produced by *purely chemical etching* (stain-etching) [Fathauer, *et al.* (1992)] of crystalline silicon (c-Si) or poly crystalline silicon (poly-Si) in HF:HNO<sub>3</sub>-based solutions exhibits similar PL to that of prepared by anodization in HF-based electrolytes, the stain-etching process possesses some unique advantages over anodization in addition to its much greater simplicity. This includes sub-micron porous silicon pattern formation [Steckl, *et al.* (1993)] and fabrication of poly-porous silicon thin films on glass [Steckl, *et al.* (1993)]. The capability of fabricating luminescing porous silicon patterns embedded in conventional Si is very important for monolithic integration of optically active Si components onto a Si substrate. In addition, for application in flat panel display devices, the stain-etching technique might well be the only practical method to produce luminescent thin poly-Si films on quartz and glass [Steckl, *et al.* (1993)], because stain-etching is performed without the electrode and electrolytic bath required by anodization. However, to date there has been a scarcity of information regarding electroluminescence (EL) in stain-etched porous silicon. We recently reported the fabrication and characterization of ITO/porous silicon *n-p* heterojunctions using *stain-etched* porous silicon thin films [Xu and Steckl (1994)].

### 6.1.2 Experimental Procedures

#### A. Fabrication Process

The process starts with 3" *p*-type (100) Si substrates with a resistivity of 6-16 Ω-cm. Two different types of process, lift-off process and shadow masking process, were developed to fabricate the porous Si LED as outlined in Figure 6.1.1 and Figure 6.1.2. The process depicted in Figure 6.1.1 employs a photolithographic lift-off step for defining the diode size and contacting area while the process shown Figure 6.1.2 uses a shadow mask to define the contact area. In either one of the processes an aluminum film of ~ 400 nm was first sputter-deposited on to the back side of the wafer at room temperature to form an ohmic contact. The Al deposition was carried out in a DV-602 sputter deposition system from Denton Vacuum using pure Ar<sup>+</sup> plasma and aluminum target. A base pressure of less than 6×10<sup>-6</sup> Torr and a plasma pressure of about 10 mTorr were used for the deposition. Because of the high conductivity of aluminum target both d.c. and a.c. sputtering can be used for the deposition. However, a.c. sputtering was usually chosen over d.c. sputtering since the former method tends to produce more uniform sputtering of the target. Typical a.c. sputter power are between 250 W to 300 W. The Al thickness was controlled by a quartz monitor which automatically closes the shutter once the set thickness is reached. After the aluminum deposition the sample was then annealed in N<sub>2</sub> at 450°C for 5 min using rapid thermal annealing to form the ohmic contact.

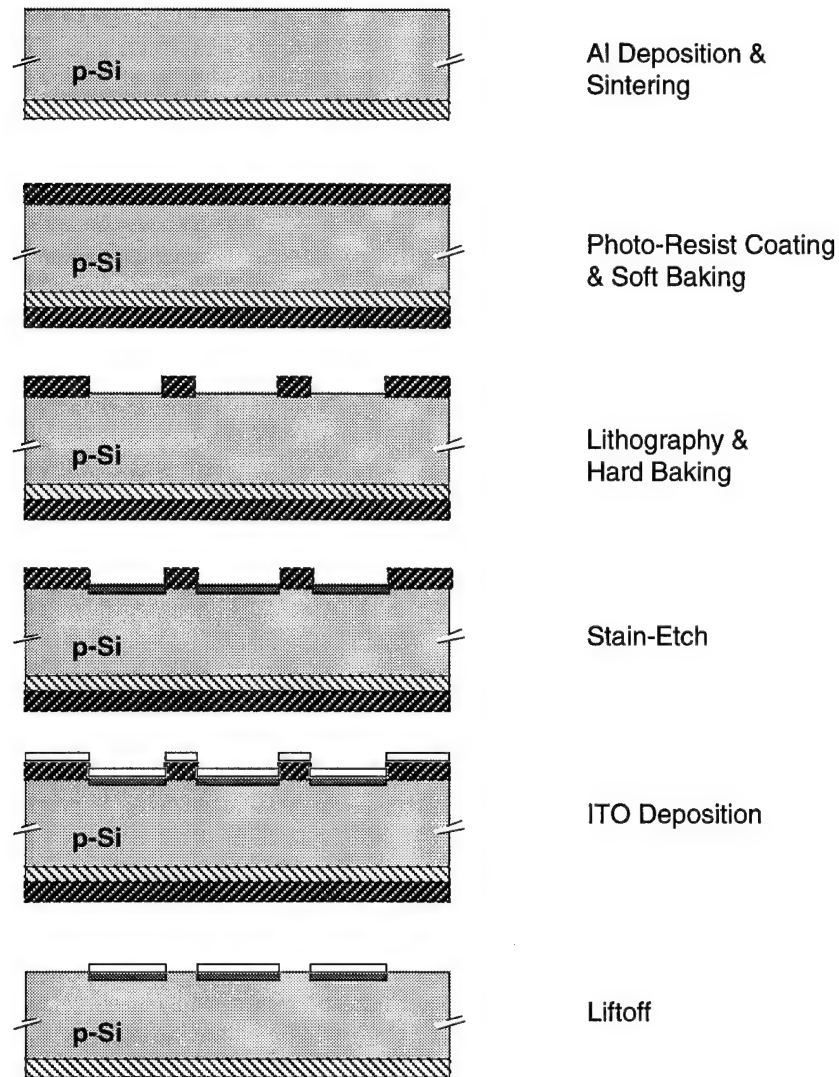


**FIGURE 6.1.1** Process flow for porous Si LED fabrication using lift-off.

After Al sintering a photoresist layer of about  $2\text{ }\mu\text{m}$  is spin-coated on to the aluminum film and oven-baked at  $100^\circ\text{C}$  for 30 min to serve as a protection layer during the stain-etching. For the lift-off process as shown in Figure 6.1.1 photoresist of about  $1\text{ }\mu\text{m}$  was then deposited onto the front side and soft-baked at  $80^\circ\text{C}$  for 30 min. Windows in circular shape with 5 mm in diameter were then opened on the front side photoresist using conventional lithography.

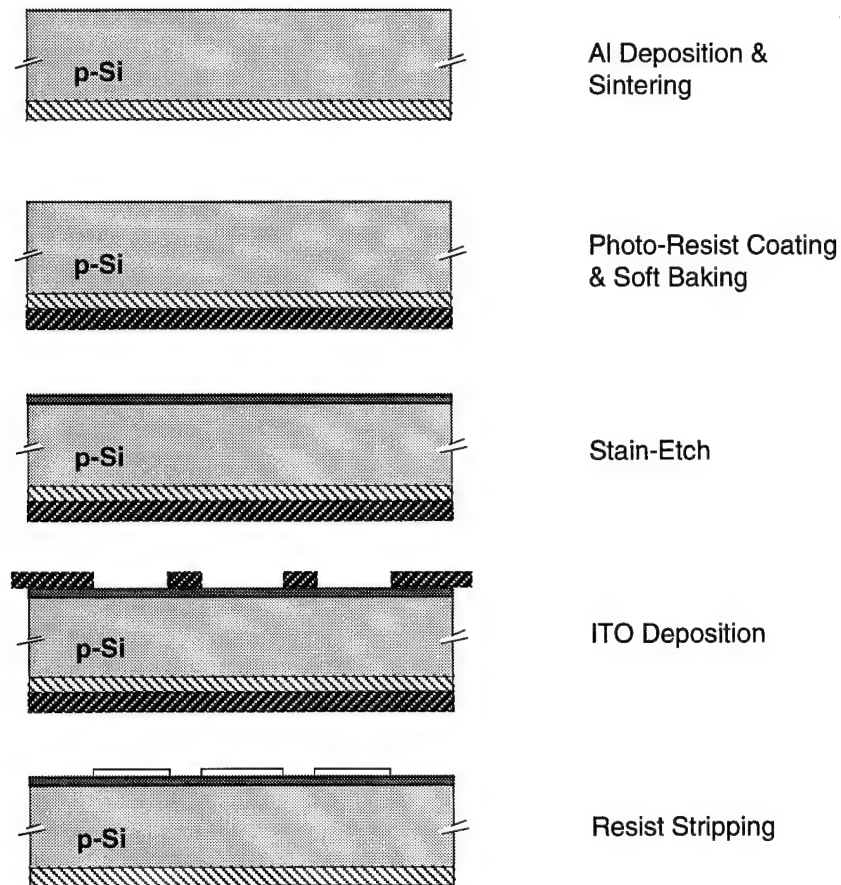


**FIGURE 6.1.2** Process flow for porous silicon LED fabrication using shadow masking.

The front side of the sample was then rendered porous in a solution of HF:HNO<sub>3</sub>:H<sub>2</sub>O with 1:3:5 volume ratio for ~ 1 min beyond the incubation time. An alternative stain-etching process uses a solution of HF:HNO<sub>3</sub> with 200:1 volume ratio for less than 1 min. The stain-etching was performed in ambient light at room temperature with no intentional heating. The sample was then rinsed in deionized water and blown dry with nitrogen. An indium tin oxide (ITO) thin film of ~1000Å was sputter deposited from an ITO target (90%In<sub>2</sub>O<sub>3</sub>+10%SnO<sub>2</sub>) onto the porous silicon. For the process using lift-off the ITO film was uniformly deposited on the wafer while, in the other process, the deposition was through a shadow mask. For the shadow masking process, this results in *n-p* heterojunctions with a top transparent circular electrodes of ~ 0.08 cm<sup>2</sup> area. Alternately, a Au thin layer of ~ 100Å is evaporated through the shadow mask onto the porous silicon forming Schottky contacts with same device area. After ITO (or Au) deposition, the back side photoresist was removed by rinsing in acetone. ITO/p-Si heterojunctions were also fabricated simultaneously with ITO/porous silicon using the same process except for the stain-etching step.

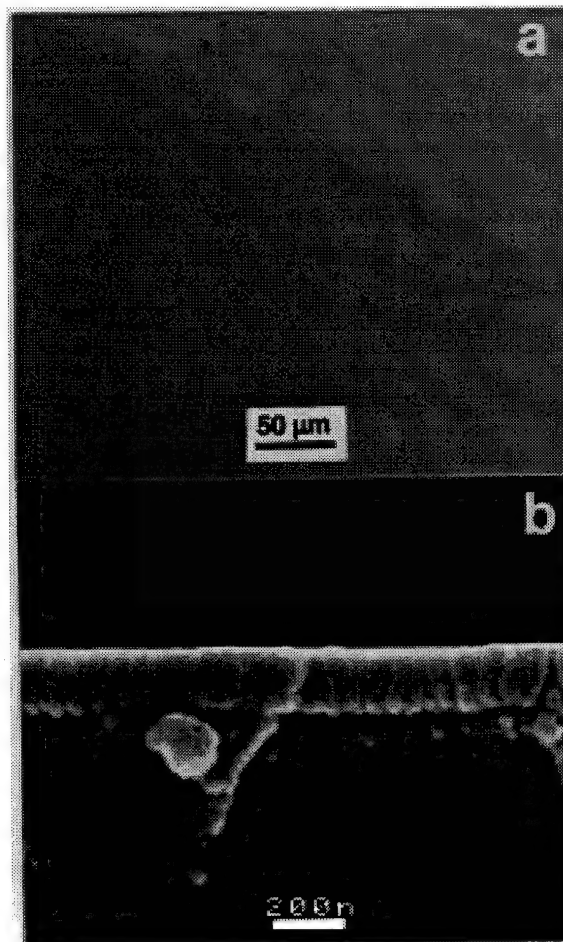
#### B. Characterization

Electrical and optoelectronic measurements were conducted to characterize the device performance. These include I-V characterization, PL and EL measurements. The I-V characteristic was studied using an HP 4140B pA/DC voltage source. The photoluminescence characterization was described in detail in a previous chapters. Electroluminescence spectra are obtained using a 0.25 meter monochromator and a photomultiplier detector as well as a CCD detector. In the study

of EL intensity versus bias current, the photoemission is coupled into the photomultiplier directly using an optical fiber bundle.

### 6.1.3 Results and Discussions

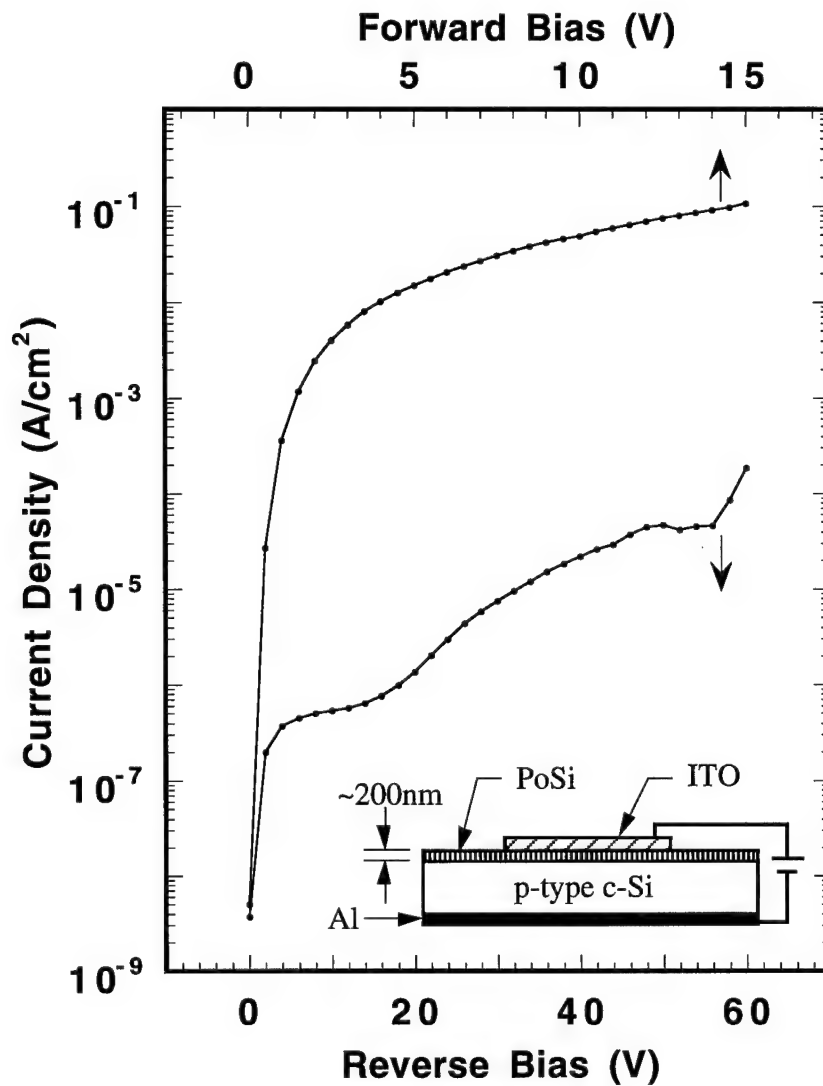
The porous silicon film obtained by stain-etching in this study was very smooth and showed a shiny, mirror-like dark-blue interference color. The surface morphology and pore sizes were studied by optical and scanning electron microscopy (SEM). Figure 6.1.3a is an optical plan-view microphotograph of a porous silicon film etched for a total of 4 min, including a 3 min incubation time. The top surface is clearly observed to be very smooth and uniform. Figure 6.1.3b is a cross-section SEM microphotograph of the same sample which indicates that the porous silicon film has a uniform thickness of about 200 nm. Figure 6.1.3b also reveals the presence of vertical pores (with diameters of 10-20 nm) existing through the entire thickness of the porous silicon layer. No obvious modification of the surface morphology (such as bubbling) was observed during the stain-etch.



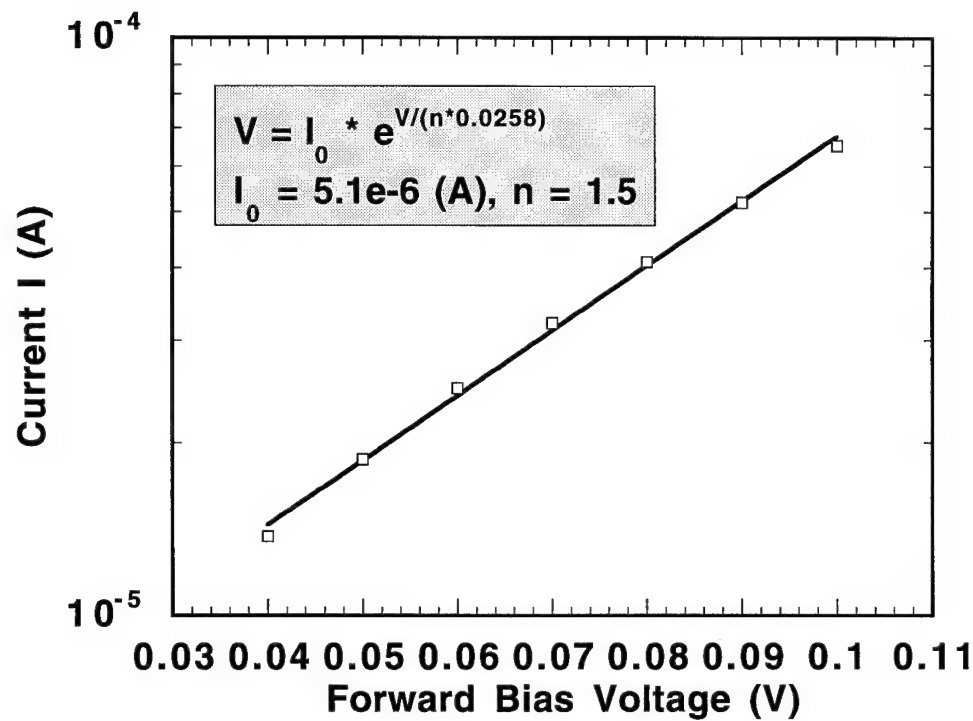
**FIGURE 6.1.3** Photographs of a porous silicon thin film obtained by stain etching of B-doped 6-8  $\Omega$ -cm (100) c-Si in HF:HNO<sub>3</sub>:H<sub>2</sub>O of 1:3:5 composition for 1 min plus 3 min incubation time: (a) plan-view optical microscope image; (b) cross-section SEM image.

All heterojunctions of ITO to porous Si and to conventional Si exhibited strongly rectifying I-V characteristics. The ITO/p-porous silicon diode typically turned on at a forward bias (negative voltage on ITO electrode) of less than 1.5 V and had a reverse breakdown voltage in excess of 50

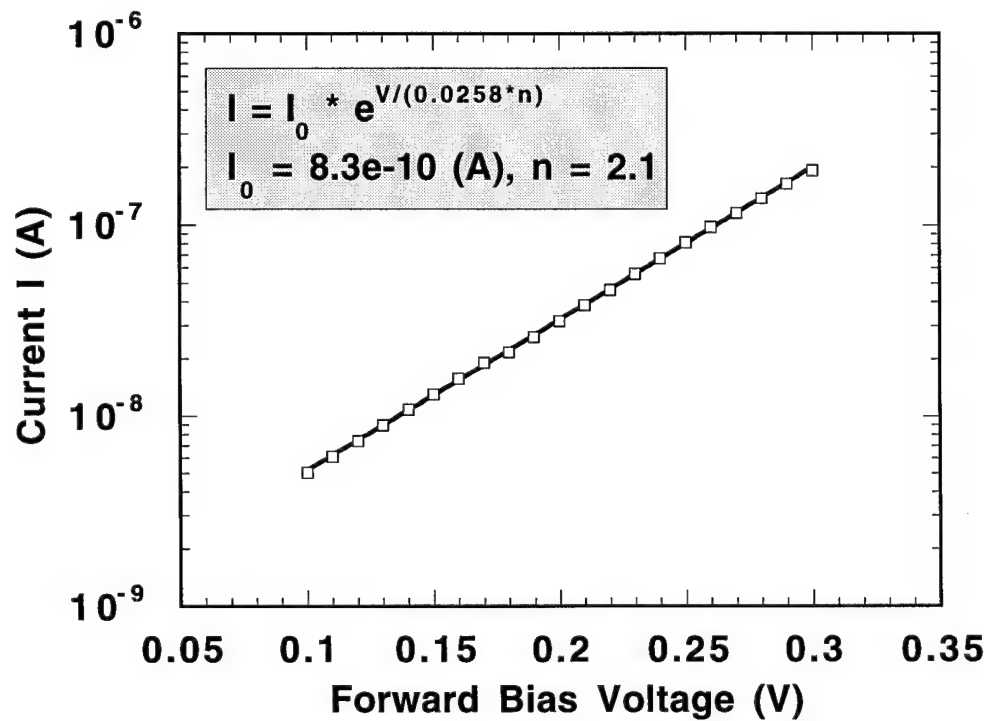
V. Figure 6.1.4 shows a typical I-V characteristic of the ITO/p-porous silicon heterojunction, with the device structure illustrated in the inset and under a reverse bias. The leakage current density of the diode at a reverse bias of -10 V is  $\sim 538 \text{ nA/cm}^2$ , which is close to the lowest reported values [Shi, *et al.* (1993)]. The diode has a rectifying ratio of  $\sim 1.6 \times 10^5$  at  $\pm 15 \text{ V}$ , which is the highest value reported to date [Futagi, *et al.* (1992), Koshida, *et al.* (1993)].



**FIGURE 6.1.4** I-V characteristic of an ITO/p-porous silicon diode fabricated by stain-etching. The inset represents the diode structure under reverse bias.



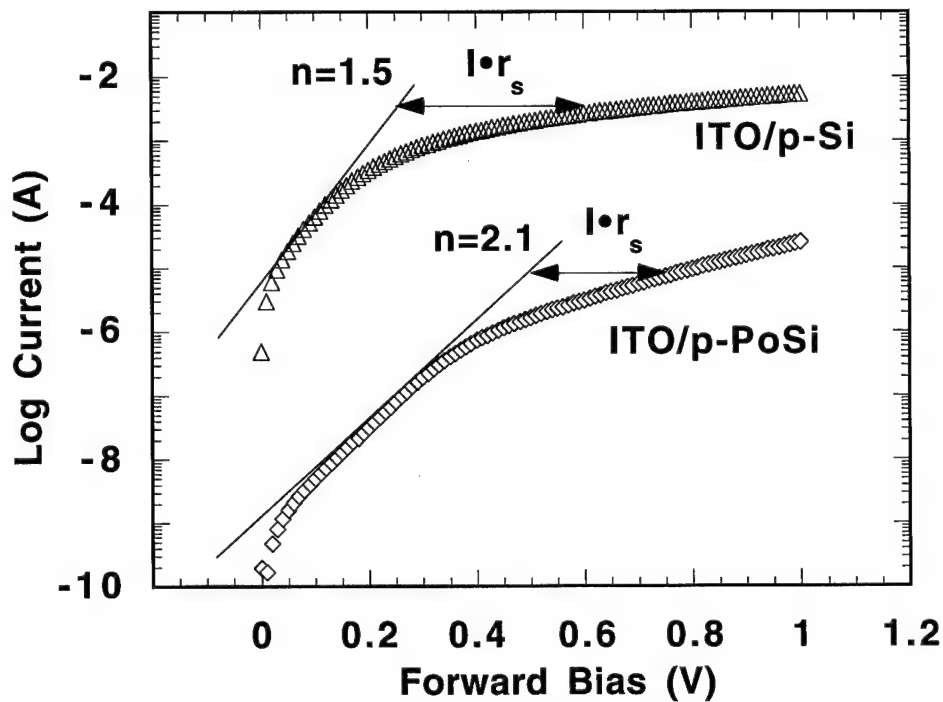
**FIGURE 6.1.5** Ideality factor  $n$  of the ITO/p-Si diode extracted from it's low voltage I-V curve.



**FIGURE 6.1.6** Ideality factor  $n$  of the ITO/p-porous silicon diode extracted from it's low voltage I-V curve.

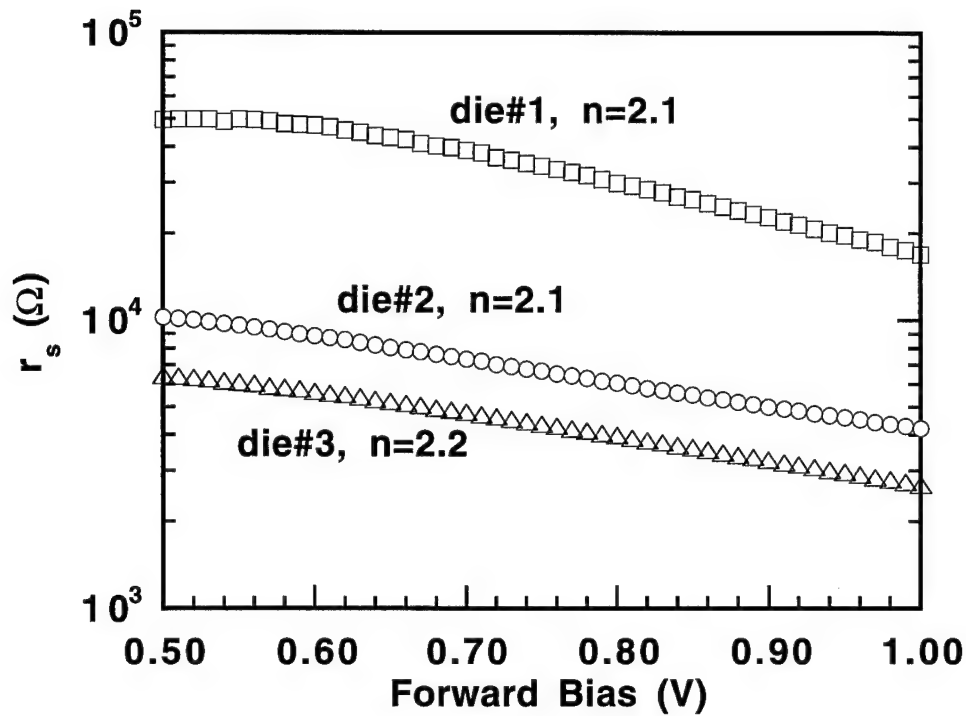
Low voltage measurements of the I-V characteristics revealed an ideality factor (n) of  $\sim 1.5$  for ITO/p-Si and  $\sim 2.1$  for ITO/p-porous silicon heterojunctions, as shown in Figure 6.1.5 and Figure 6.1.6 respectively. The ideality factor of 2.1 for our *stain-etched* ITO/p-porous silicon diode is significantly better than the previously reported values of 3.8 for an anodized ITO/p-porous silicon diode [Maruska, *et al.* (1992)] and of 3 for an anodized porous silicon  $p^+-n^+$  homojunction [Chen, *et al.* (1993)].

Figure 6.1.7 plots the extended low voltage I-V characteristics for both ITO/p-Si and ITO/p-porous silicon diodes. It is also obvious from Fig. 6.1.7 that a series resistance exists for both ITO/p-Si and ITO/p-porous silicon diodes. Using the method illustrated in Fig. 6.1.7, an  $r_s$  of  $\sim 135 \Omega$  is calculated for the conventional ITO/p-Si diodes ( $r_s = 136 \Omega$  at 1 V and  $r_s = 134 \Omega$  at 0.5 V).



**FIGURE 6.1.7** Low bias I-V characteristics of ITO/p-porous silicon and ITO/p-Si heterojunctions.

However, when the same method is applied to the ITO/p-porous silicon I-V curve, the  $r_s$  obtained is roughly 10 to 100 times higher than that of ITO/p-Si diodes and the series resistance has a strong dependence on the applied bias and varies significantly from diode to diode as indicated in Fig. 6.1.8. The increase in  $r_s$  in the porous silicon diodes as compared to conventional Si diodes could be a combination of several factors: (a) an effective area which is much smaller than the ITO area because of the columnar nature of the porous silicon; (b) the presence of a thicker native oxide layer on the porous silicon [Maruska, *et al.* (1993)] than on conventional Si; (c) carrier depletion [Anderson, *et al.* (1991)] in the  $p$ -porous silicon layer. It is clear from Fig. 6.1.8 that the  $r_s$ -V dependence does exist and the three diodes tested have roughly the same slope. The high values of  $r_s$



**FIGURE 6.1.8** Dependence of series resistance on the applied bias for ITO/p-porous silicon diodes.

from die #1 probably represents an extreme case. The dependence of  $r_s$  on forward bias voltage could be the result of one or more mechanisms: (a) increased tunneling through the oxide at the ITO/porous silicon interface at higher forward bias; (b) reduction in the carrier depletion in the porous silicon due to injection. Further study is needed to fully understand the effect of voltage dependence of  $r_s$  and to reduce the  $r_s$ .

One of the major effects of series resistance is the reduction of carrier injection efficiency resulted from the reduced effective junction bias due to a voltage drop across the resist. Therefore higher bias is needed to obtain the same current for a device with higher series resistance as illustrated in Fig. 6.1.9, which plots forward current vs. forward voltage for both ITO/p-Si and ITO/p-porous silicon diodes.

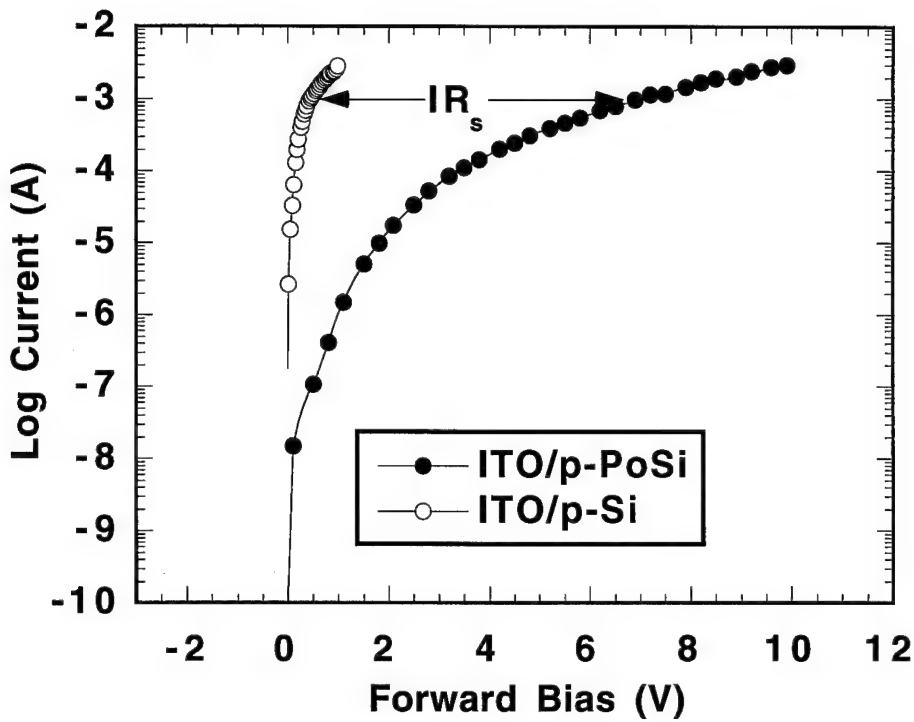


**FIGURE 6.1.9** Comparison of I-V characteristics of ITO/p-Si and ITO/p-porous silicon diodes indicating a significantly increased series resistance in ITO/p-porous silicon diode.

Under forward bias, visible EL was readily observed with the naked eye in a dark background when a current larger than  $\sim 10$  mA/cm $^2$  was applied. Figure 6.1.10 shows an EL topography of an ITO/p-porous silicon diode under a forward bias of  $\sim 40$  mA/cm $^2$  taken by a color CCD camera mounted on top of the probe station. It can be seen that uniform light emission is produced only from the area where the porous silicon is in contact with the ITO electrode, in other words where electron injection occurs under forward bias. The sharp black spike is the tip shadow of the mechanic probe where electrical contact was made to the ITO. When the sample is under UV illumination, PL is observed from both the electrode region and the surrounding area, with PL from the surrounding area being actually brighter because of the finite ITO absorption in the center. No EL was observed under reverse bias indicating that the photoemission is a result of carrier injection. No EL is observed from the ITO/p-Si heterojunction under similar condition which supports the fact that the EL from porous silicon diode comes from the porous Si layer. The EL color (reddish-orange) is very similar to that of PL under UV (365 nm) excitation.

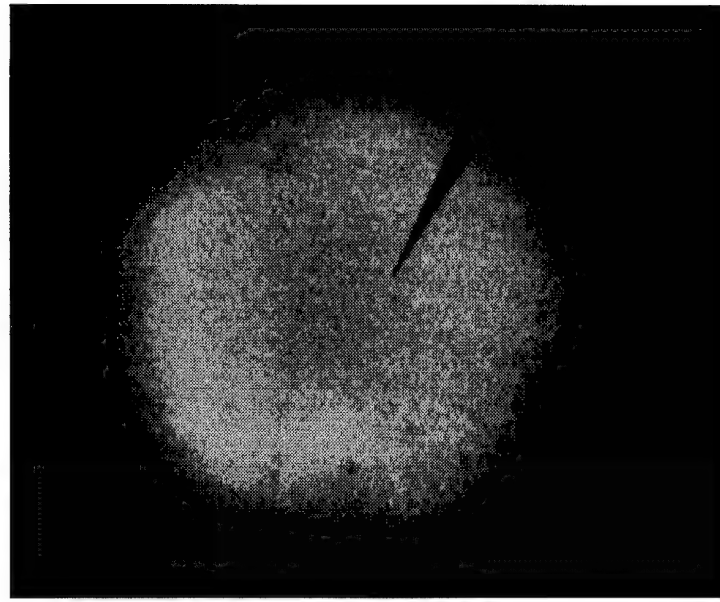


**FIGURE 6.1.10** EL topography from an ITO/p-porous silicon diode under a forward bias of  $40 \text{ mA/cm}^2$ .

The EL intensity is stable and reproducible as monitored by a photomultiplier. For example, Figure 6.1.11 plots the EL intensity at a constant current of  $10 \text{ mA}$  as a continuous function of time for 1 hour. It is obvious from Fig. 6.1.11 that the EL is quite stable and a variation of only  $\sim 6\%$  was observed. The lowest EL onset measured with a photomultiplier was at a bias of  $\sim 3 \text{ mA/cm}^2$ . To the best of our knowledge, this represents the lowest EL onset reported to date for a non *p-n* homo-junction diode structure, and is comparable to the lowest EL onset obtained [Badoz, *et al.* (1994)] from a  $n^+-p$  porous silicon diode.

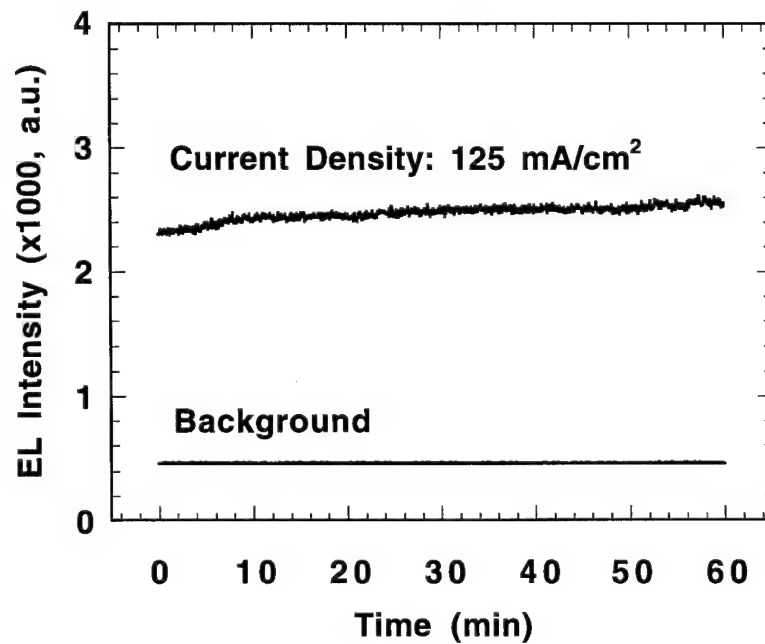


**FIGURE 6.1.11** EL intensity at a current density of  $125 \text{ mA/cm}^2$  as a function of time for 60 min.

The non-dispersed EL intensity increases monotonically with bias as shown in Fig. 6.1.12. At low bias, below a current density ( $J_D$ ) of 213 mA/cm<sup>2</sup>, the EL intensity scales with a power law dependence of  $EL \sim J_D^m$ , where  $m$  was calculated to be approximately 2.5. This nonlinear behavior at low bias is similar to that of reported by Maruska et al. [Maruska, *et al.* (1992)] for anodized ITO/*p*-porous silicon diodes. The onset current density of 213 mA/cm<sup>2</sup> for linear EL vs.  $J_D$  dependence obtained here is almost 10 times lower than that of the anodized ITO/porous silicon *n-p* heterojunction [Maruska, *et al.* (1992)].

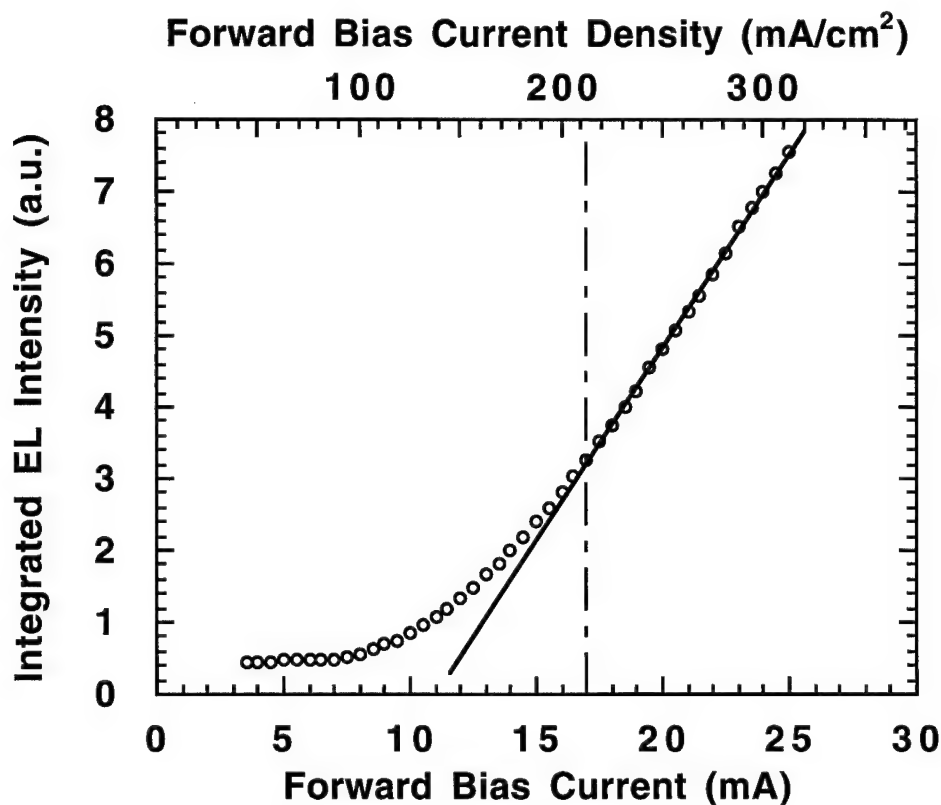


**FIGURE 6.1.12** Dependence of ITO/*p*-porous silicon electroluminescence intensity on bias.

To study the reproducibility of the porous Si light emitting diodes EL intensity from one device was measured twice and plotted in Fig. 6.1.13, where EL intensity is shown as a function of diode current. The two sets of data displayed are taken from the same diode, with two hours of electrical aging under continuous dc current of 10 mA (40 mA/cm<sup>2</sup>) between the two sets of measurements. It is clear from Figure 6.1.13 that the electroluminescence output is reproducible indicating the LED is stable and has good reliability.

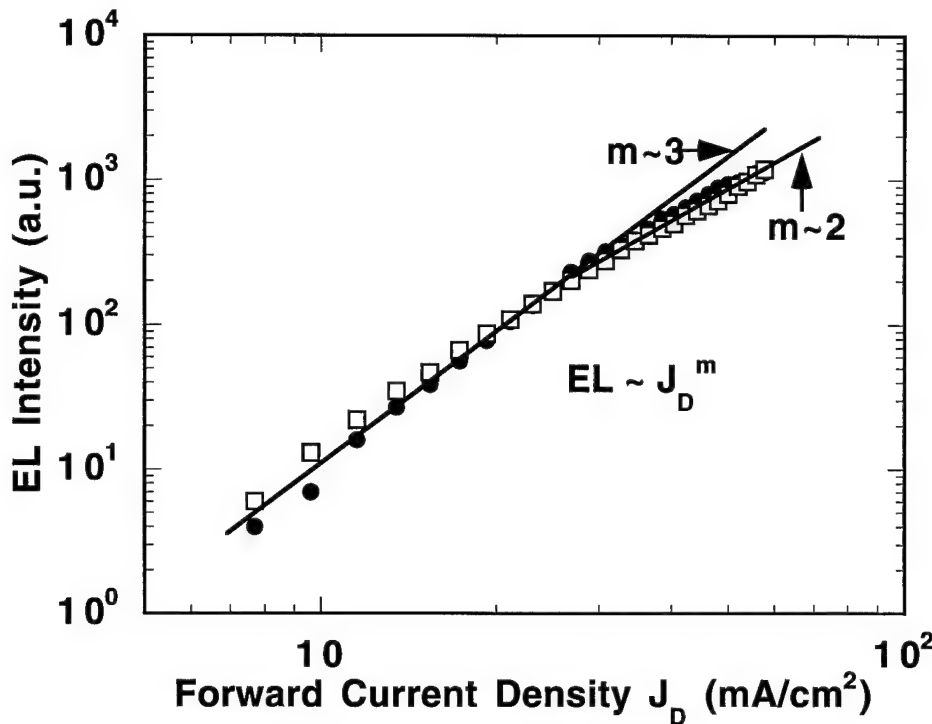


**FIGURE 6.1.13** Dependence of stain-etched porous-silicon LED electroluminescence intensity on device current density. The filled circles represents data from the first measurement and the open squares represents data from the second measurement after two hours electrical aging of the device under  $40 \text{ mA/cm}^2$  bias.

The PL spectrum, taken from porous silicon under UV 365 nm excitation, has a broad emission band, peaked at around  $\sim 635 \text{ nm}$  as shown in Fig. 6.1.14(a). The EL was measured under a forward dc bias at a constant current. Shown in Fig. 6.1.14(b) is the electroluminescence spectrum from an ITO/p-porous silicon diode at a forward current of  $10 \text{ mA}$  ( $125 \text{ mA/cm}^2$ ). The electroluminescence has a broad spectrum, similar to that of the photoluminescence but with a slightly blue shifted peak at  $\sim 625 \text{ nm}$ . While both electroluminescence and photoluminescence spectra are not equipment corrected, the similarity in these emission spectra suggests that the electroluminescence has the same luminescent center as that of the photoluminescence.

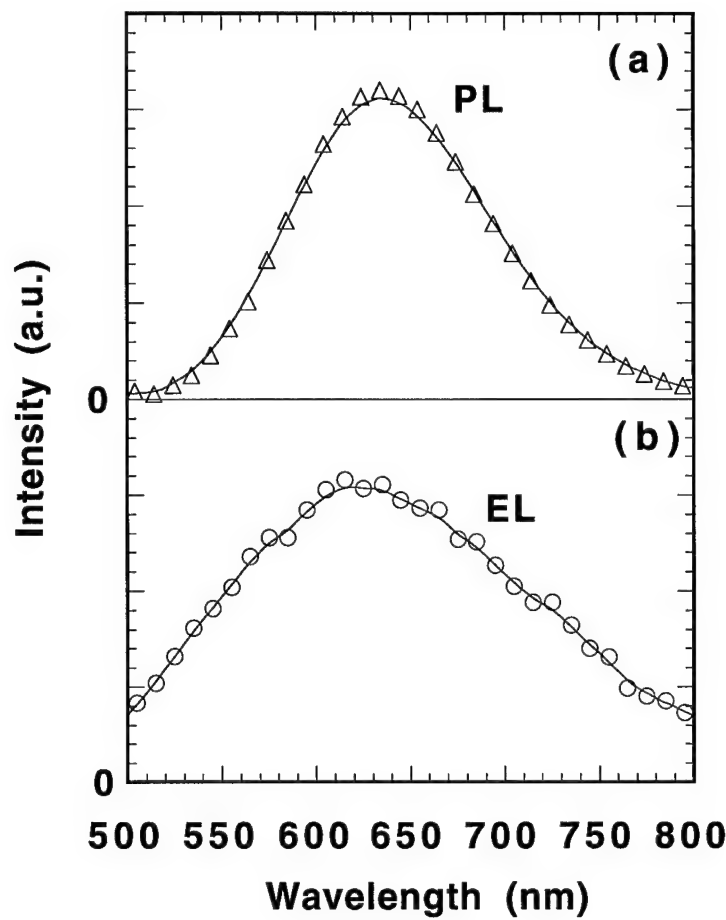


**FIGURE 6.1.14** (a): PL spectrum under 365 nm UV line excitation; and (b): EL spectrum at a bias of 125 mA/cm<sup>2</sup>.

We also studied the effect of bias current on its emission spectra on a porous Si LED and the results were plotted in Fig. 6.1.15. It can be seen from Fig. 6.1.15 that while the overall emission intensity increase as the bias is increased the shape of the EL spectra dose not change. This would, once again, strongly suggest that the emission is due to carrier injection rather than due to some other effects, such as thermal effect.

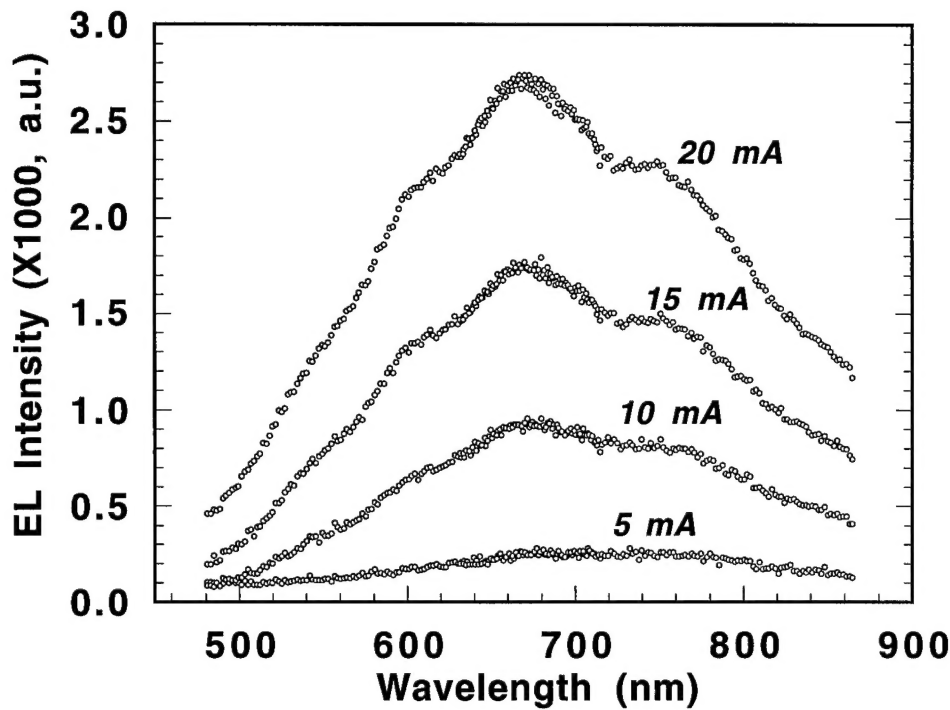


**FIGURE 6.1.15** EL spectra as the function of device forward bias.

In comparison with previously published anodized porous silicon LED's, the characteristics of the stain-etched porous silicon LED fabricated in this work here are significantly improved over the best reported value in aspects such as ideality factor [Maruska, *et al.* (1992), Chen, *et al.* (1993)], rectifying ratio [Futagi, *et al.* (1992)], EL onset current [Steiner, *et al.* (1993)] and EL linearity [Maruska, *et al.* (1992)]. The improvement obtained in porous silicon LED with stain-etch process could be attributed to the thinner porous silicon films and better uniformity. EL has also been obtained from stain-etched porous silicon Schottky diodes using Au thin films ( $\sim 100 \text{ \AA}$ ).

#### 6.1.4 Summary

In summary, visible light emitting diodes using stain-etched porous silicon thin films have been fabricated and characterized. The porous silicon film used in this work of only about 200 nm is the thinnest ever reported for a porous silicon LED. The devices have superior electrical characteristics and achieved the best ideality factor, the highest rectifying ratio and among the lowest EL onset current reported to date along with improved EL linearity. Since the stain-etch process is much simpler than anodization and can be used to form sub-micron luminescent porous silicon patterns and to produce luminescing poly-porous silicon films on quartz and glass, these results demonstrate a very promising and advantageous technique for fabrication of porous silicon-based LED's and poly-porous silicon-based electroluminescent devices.

#### REFERENCES

Anderson, R. C., Muller, R. S. and Tobias, C. W., "Investigations of the electrical properties of porous silicon", *J. Electrochem. Soc.* **138**, 3406 (1991).

Archer, R. J., "Stain films on silicon", *J. Phys. Chem. Solids* **14**, 104 (1960).

Badoz, P. A., Garchery, L. and Halimaoui, A., "Physical characterization of silicon and porous silicon based electroluminescent diodes", *Proc. 7th Int'l. Symp. Si Mat'l. Sci. and Tech., Electrochem. Soc.* **94-10**, 569 (1994).

Canham, L., "Silicon quantum wire array fabrication by electrochemical and chemical dissolution of wafers", *Appl. Phys. Lett.* **57**, 1046 (1990).

Chen, Z., Bosman, G. and Ochoa, R., "Visible light emission from heavily doped porous silicon homojunction pn diodes", *Appl. Phys. Lett.* **62**, 708 (1993).

Fathauer, R. W., George, T., Ksendzov, A. and Vasquez, R. P., "Visible luminescence from silicon wafers subjected to stain etches", *Appl. Phys. Lett.* **60**, 996 (1992).

Futagi, T., Matsumoto, T., Katsuno, M. and Ohta, Y., "Visible light emission from a pn junction of porous silicon and microcrystalline silicon carbide", *Appl. Phys. Lett.* **63**, 1209 (1993).

Futagi, T., Matsumoto, T., Katsuno, M., Ohta, Y., Mimura, H. and Kitamura, K., "Visible Electroluminescence from P-Type Crystalline Silicon/Porous Silicon/N-Type Microcrystalline Silicon Carbon PN Junction Diodes", *Jpn. J. Appl. Phys.* **31**, L616 (1992).

Gee, A., "Electrochemiluminescence at a silicon anode in contact with an electrolyte", *J. Electrochem. Soc.* **78**, 788 (1960).

Halimaoui, A., Oules, C., Bomchil, G., Bsiesy, A., Gaspard, F., Herino, R., Ligeon, M. and Muller, F., "Electroluminescence in the visible range during anodic oxidation of porous silicon films", *Appl. Phys. Lett.* **59**, 304 (1991).

Kalkhoran, N. M., Namavar, F. and Maruska, H. P., "NP heterojunction porous silicon light-emitting diode", *Mat. Res. Soc. Symp. Proc.* **256**, 89 (1992).

Kalkhoran, N. M., Namavar, F. and Maruska, H. P., "Optoelectronic applications of porous polycrystalline silicon", *Appl. Phys. Lett.* **63**, 2661 (1993).

Kolmakova, T. P., Baru, V. G., Malakhov, B. A., Ormont, A. B. and Tereshin, S. A., "Electro- and photoluminescence in thin films of porous silicon", *JETP Lett.* **57**, 411 (1993).

Koshida, N. and Koyama, H., "Visible electroluminescence from porous silicon", *Appl. Phys. Lett.* **60**, 347 (1992).

Koshida, N., Koyama, H., Yamamoto, Y. and Collins, G. J., "Visible electroluminescence from porous silicon diodes with an electropolymerized contact", *Appl. Phys. Lett.* **63**, 2655 (1993).

Maruska, H. P., Namavar, F. and Kalkhoran, N. M., "Energy bands in quantum confined silicon light-emitting diodes", *Appl. Phys. Lett.* **63**, 45 (1993).

Maruska, H. P., Namavar, F. and Kalkhoran, N. M., "Current injection mechanism for porous-silicon transparent surface light-emitting diodes", *Appl. Phys. Lett.* **61**, 1338 (1992).

Richter, A., Steiner, P., Kozlowski, K. and Lang, W., "Current-induced light emission from a porous silicon device", *IEEE Elec. Dev. Lett.* **12**, 691 (1991).

Shi, H., Zheng, Y., Wang, Y. and Yuan, R., "Electrically induced light emission and novel photocurrent response of a porous silicon device", *Appl. Phys. Lett.* **63**, 770 (1993).

Steckl, A. J., Xu, J. and Mogul, H. C., "Photoluminescence from stain-etched polycrystalline Si thin films", *Appl. Phys. Lett.* **62**, 2111 (1993).

Steckl, A. J., Xu, J., Mogul, H. C. and Mogren, S., "Doping-induced selective area photoluminescence in porous silicon", *Appl. Phys. Lett.* **62**, 1982 (1993).

Steiner, P., Kozlowski, F. and Lang, W., "Blue and green electroluminescence from a porous silicon devices", *IEEE Electron Device Lett.* **14**, 317 (1993).

Xu, J. and Steckl, A. J., "Visible electroluminescence from Stain-etched porous Si diode", *IEEE Electron Device Lett.* **15**, 507 (1994).

## Chapter 7

### Conclusions and Suggestions for Future Work

#### 7.1 Conclusions

Si doping effect on the incubation time of porous silicon nanostructure formation by stain-etching of Si in HF:HNO<sub>3</sub>:H<sub>2</sub>O was systematically studied along with surface morphology and photoluminescence. A significant dependence of the incubation time  $t_i$  on the hole concentration was observed. There exists a transition hole concentration between 10<sup>18</sup> and 10<sup>19</sup>/cm<sup>3</sup>. Above that concentration, the incubation time is very short and below it the  $t_i$  is much longer. This hole-dependent effect is consistent with the basic Si etching mechanism which is initiated by the reaction of holes with Si atoms at the etching surface. The nanostructure morphology was also observed to be a strong function of substrate doping type and concentration. However, the photoluminescence spectra of porous silicon of different doping type and concentration are very similar with a peak of ~ 1.94 eV despite significant difference in their incubation times and surface morphology. Utilizing the doping dependence on the incubation time, combined with Ga<sup>+</sup> FIB- and B<sup>+</sup> BB-implantation doping, a process was developed to fabricate selective light emitting porous silicon arrays embedded in conventional Si. Using 30 kV FIB Ga<sup>+</sup> implantation, sub-micron photoemitting patterns have been obtained for the first time. This represents a considerably higher resolution than for the image projection lithography (20  $\mu$ m) and multi-photoresist-layer coating (3  $\mu$ m) processes previously reported for anodized porous silicon. The resolution is defined by FIB implantation and is not affected by the etching process. The process can be easily incorporated into conventional semiconductor fabrication technology.

Anisotropic etching of single crystalline silicon was studied using Ga<sup>+</sup> FIB implantation and KOH etching at elevated temperatures. By choosing appropriate conditions, including such as off-axis implantation angle and etching conditions, completely undercut Si air-bridges were obtained. A process was successfully developed to fabricate three dimensional photoluminescent free standing Si nanostructures integrated on conventional Si substrate for the first time. The process combines anisotropic etching of Ga<sup>+</sup> FIB implanted (100) *n*-Si in KOH-based solution and selective stain-etching in HF:HNO<sub>3</sub>:H<sub>2</sub>O mixture. The techniques developed here provide a capability of fabricating versatile, optically active Si micro- and nano-structures for potential applications in monolithic Si-based optoelectronics, such as intrachip optical communication, optoelectronic memory devices and light emitting devices.

Room temperature visible photoluminescence was obtained from polycrystalline silicon thin films on both oxidized Si and quartz substrates using stain-etching in HF:HNO<sub>3</sub>:H<sub>2</sub>O (1:3:5) and HF:HNO<sub>3</sub> (200:1) mixtures. Photoluminescent porous silicon arrays with sub-micron dimensions were demonstrated for the first time and exhibited well-defined luminescence both as isolated features and in combination with much larger areas. This offers potential application in porous-silicon-based flat panel display devices.

Porous silicon from stain-etched Si thin films deposited on oxidized Si substrates at temperatures ranging from 540 to 640°C, designed to provide varying levels of crystallinity, was systematically studied by XRD, PL and IR transmission spectroscopy. It was observed that a minimum level of crystallinity in the Si nanostructures is required for the subsequent porous silicon layer to exhibit visible photoluminescence. Simply providing a high level of porosity in initially amorphous Si films does not produce photoluminescent layers. We have also determined that initially polycrystalline films, which yield light-emitting porous silicon, also retain their crystallinity during the stain-etching process. Concomitantly with the presence of

photoluminescence and crystallinity, an absorption peak at  $880\text{-}890\text{ cm}^{-1}$  was observed in all etched poly-porous silicon films which were deposited at  $T_D \geq 590^\circ\text{C}$ . This absorption line, due to a  $\text{SiH}_2\text{O}$  structural unit or possibly from a combination Si-OH stretch and SiO-H bend modes, is not exhibited in any non-PL samples, either the etched a-porous silicon films grown at  $T_D \leq 580^\circ\text{C}$  or in any of the as-deposited films. Therefore, it appears that there exists a unique correlation between the level of crystallinity of the starting Si film, and the presence of surface oxyhydrides and photoluminescence after stain-etching.

Visible light emitting diodes using stain-etched porous silicon nanostructures have been fabricated and characterized. The porous silicon film used in this work of only about 200 nm is the thinnest ever reported for a porous silicon LED. The devices have superior electrical characteristics and achieved the best ideality factor, the highest rectifying ratio and the lowest EL onset current reported to date along with improved EL linearity. Since the stain-etch process is much simpler than anodization and can be used to form sub-micron luminescent porous silicon patterns and to produce luminescing poly-porous silicon films on quartz and glass, these results demonstrate a very promising and advantageous technique for fabrication of porous-silicon-based LED's and poly-porous-silicon-based electroluminescent devices.

## 7.2 Suggestions for Future Work

Integrating optically active silicon components with conventional silicon electrical and optoelectronic devices onto a single silicon substrate is a very challenging and rewarding endeavor. The fabrication process developed in this work for silicon light emitting nanostructures and LED's embedded in conventional silicon provides a potential technique for integrating a host of optically active silicon devices onto to a silicon wafer, where other silicon devices can also be easily made. These devices can be either pure optical structures, such as gratings, wave guides and lasers, or optoelectronic devices including LED's and detectors. We strongly recommend that these optical and optoelectronic applications of porous Si be pursued.

The process for fabricating luminescent poly-Si thin films on quartz and glass substrate by LPCVD and stain-etching with a processing temperature as low as  $590^\circ\text{C}$  also finds porous silicon a very practical and promising application in the area of flat panel display devices. One possible such display device could be the cathodoluminescent display device using low energy electrons from cold cathode arrays such as silicon microcathode array fabricated by micromaching or tungsten microtips obtained by localized growth. The technology for fabrication of micro-cathode arrays is already in its maturing stage. Therefore, we also suggest the study of the cathodoluminescence of porous poly-Si thin films in order to evaluate its possible application to flat panel displays.